Phase-Dependent Energy Dissipation Processes in $La_{0.7}Sr_{0.3}MnO_3$ and $(La_{0.6}Pr_{0.4})_{0.7}Ca_{0.3}MnO_3$ after an Ultrashort Optical Excitation

Dissertation
for the award of the degree

”Doctor rerum naturalium”

of the Georg-August-Universität Göttingen

within the doctoral program "Physics"
of the Georg-August University School of Science (GAUSS)

submitted by
CINJA SEICK
FROM WINSEN (LUHE)

M. Sc.

Göttingen, 14. August 2022

Thesis Advisory Committee

Prof. Dr. Stefan Mathias,
AG Mathias, I. Physikalisches Institut

Dr. Henning Ulrichs,
Agilent Technologies, Waldbronn (former AG Ulrichs,
I. Physikalisches Institut, Universität Göttingen)

Prof. Dr. Stefan Kehrein,
AG Kehrein, Institut für Theoretische Physik

Members of the Examination Board

Reviewer:
Prof. Dr. Stefan Mathias,
AG Mathias, I. Physikalisches Institut

Second Reviewer:
Prof. Dr. Christian Jooß
AG Jooß, Institut für Materialphysik

Further Members of the Examination Board

Prof. Dr. Thomas Weitz,
AG Weitz, I. Physikalisches Institut

PD. Dr. Oliver Bünermann,
Physikalische Chemie I, Institut für Physikalische Chemie,

PD Dr. Martin Wenderoth,
AG Wenderoth, IV. Physikalisches Institut

Prof. Dr. Michael Seibt,
AG Seibt, IV. Physikalisches Institut

Date of oral examination: 28. September 2022

Abstract

$La_{0.7}Sr_{0.3}MnO_3$ (LSMO) and $(La_{0.6}Pr_{0.4})_{0.7}Ca_{0.3}MnO_3$ (LPCMO) are perovsikte manganites which both show a ferromagnetic-to-paramagnetic phase transition. Interestingly, the development of the new phase when crossing the phase transition occurs due to two different polaronic effects in both systems: correlated Jahn-Teller polarons in the case of LPCMO and large polarons in the case of LSMO.

In order to investigate the changes of energy dissipation which are caused by the two different phenomena, pump-probe experiments in the optical regime are performed to excite dynamics at the fs-timescale. The following dynamical evolution of both systems is studied up to 1.1 ns after the excitation by applying different external stimuli to both systems. With the help of the resulting temperature, fluence, and magnetic field dependencies, suggestions for the underlying processes of the four experimentally found dynamical steps are discussed. To obtain the electronic and a partially phononic response, as well as the contributions by the spin system, two different kinds of time-resolved techniques are used experimentally: transient reflectivity and time-resolved magneto-optical Kerr effect, both measured simultaneously.

Detailed static characterizations of the thin film samples as well as finite-difference time-domain simulations based on an one-dimensional 3 temperature model support the hypotheses which are deduced from the dynamical experiments. Thereby, the focus spots onto the excitation transitions where two different kind of excitation steps are suggested as well as onto the relaxation mechanisms back to the ground state where similar behavior are observed.

Acknowledgements

I would like to thank the members of my *Thesis Advisory Committee*, Professor Dr. Stefan Mathias, Dr. Henning Ulrichs, and Professor Dr. Stefan Kehrein, for their commitment to supervise my PhD studies, for their time spent on meetings about my thesis. In addition, I would like to thank Professor Dr. Stefan Mathias for accepting the position as my first referee. Many thanks go also to Professor Dr. Christian Jooß who agreed on becoming the second referee. I always appreciated his advises and scientific input through out my thesis.
Of course, I thank Professor Dr. Thomas Weitz, PD Dr. Oliver Bünermann, PD Dr. Martin Wenderoth, and Professor Dr. Michael Seibt for agreeing to join my examination board.

Special thanks go Dr. Daniel Steil and Dr. Henning Ulrichs for being the PIs of Project A06 and for being there to give an answer to all my questions, even the stupid ones.

I want to acknowledge all the collaborators within the CRC for the shared work and knowledge about all the fascinating techniques: Birte Kressdorf, Vitaly Bruchmann-Bamberg, Tim Titze, Dr. Ulrich Roß, Dr. Jörg Hoffmann, and Professor Dr. Vasily Moshnyaga.

I need to thank a lot of people from the I. Physikalisches Institut, guests, and former members but especially: Henrike Probst, Andy Weiser, Jonas Pöhls, Marten Düvel, Camillo Ballani, Sebastian Merten, Martin Lüttich, Leonard Schüler, Dr. Fryderyk Lyzwa, Dr. Yuansu Luo, Dr. Oleg Shapoval, and Professor Dr. Konrad Samwer.
To Marco Merboldt and Marius Keunecke, I want to say: thank you for the shared time in the office.

For the technical support and all the creative ideas for solutions on mechanical, technical, chemical, IT, electronic, vacuum, helium, and what-ever-appears-as-challenge problems, I

want to thank Uta Flippich, Carsten Mahn, Kai Dörner, Simon Stoldt, Katrin Gerke, Joachim Feist, Michael Tetzlaff, Alexander Herzberg, Bastian Beyland, and Hartmut Eichenberg. Furthermore, I thank Michaela Mecke and Finn Krummacker for all the help with administration and knowledge about forms, processes at the university and how-to-import-optical-crystals-from-China problems. Thank you all so much!

It was my pleasure and honor to be elected as equal opportunity and diversity manager of the I. Physikalisches Institut and the students' representative of the CRC1073 for several years. And in this context, I would like to thank the whole equal opportunity team of the faculty of physics for the team work. Alike, I acknowledge the collaboration with Kerstin Krüger, Regina Vinnen, Carmen Kaspar, Dr. Jörg Hoffmann and Professor Dr. Christian Jooß from the CRC.

I want to say thanks to Dr. Daniel Steil, Dr Henning Ulrichs, Vitaly Bruchmann-Bamberg and Karen Stroh for the suggestions for improvement and comments from the scientific point of view; as well as the corrections by Anki, Becky, Mufassra and Robin - thank you for your time and energy.

My dear family and friends, finally I would like to thank you from the bottom of my heart for being there for me, for giving mental support and believing in me.

Contents

List of Figures

Part 1

General Background

CHAPTER 1

Introduction and Motivation

Since a couple of years, the topic of *climate changes* has reached the broad societal mind and sensitized a part of the society to the topic of *sustainability*. Social movements like *Fridays for Future* are the result of a (slowly) changing mind set requesting the lasting consumption-based human lifestyle in many parts of the world. Already for the transition to the new millennium, the United Nations include the aim *"7 ensure environmental sustainability"* into their agenda of the *8 Millennium Development Goals* [1]. This worldwide political goal has been reinforced the issue of sustainability by five of the *17 Sustainable Development Goals (No. 7, 11, 13, 14, 15)* in the *Agenda 2030* [2] from 2015. In the recent months, German and European politicians are forced to find solutions for the issue of energy sustainability by the tragedy of the Ukrainian-Russian war and the resulting uncertainty for delivery of the fossil fuels, gas and oil.

Basic research on *transition metal oxides* is promising to provide a lot of technical solutions for the energy crises. Next to the Noble-Prize award-winning works on $LiCoO_3$ based batteries (John B. Goodenough, M. Stanley Whittingham, and Akira Yoshino, *Noble-Prize for Chemistry 2019*) [3], also other transition metal oxide classes are part of the research on new technical developments. Manganese based perovskites are suggested for solid oxide fuel cells [4]. Regarding the exponentially growing request for data storing and processing technology, the research interest on hole-doped Lanthanum-based perovskite manganites, such as $La_{0.7}Sr_{0.3}MnO_3$ (LSMO) and $(La_{0.6}Pr_{0.4})_{0.7}Ca_{0.3}MnO_3$ (LPCMO), increased significantly. The relatively high temperature ferromagnet/paramagnet phase transition of LSMO [5, 6, 7] and the high values of the colossal magnetoresistive which is reached in LPCMO [8, 9] make both materials suitable prototype candidates for later applications as digital devices for data storage and processing [10, 11, 12, 13].

Combining both, the need for a sustainable use of energy resources and the growing wish for digitization, two rather interesting question arises:

How do energy conversion processes in LSMO and LPCMO work?

And which possible controlling mechanisms can be developed to tune down the needed energy for writing and reading of digital data?

In order to make a tiny contribution to this gigantic challenge, the energy dissipation processes in $La_{0.7}Sr_{0.3}MnO_3$ and $(La_{0.6}Pr_{0.4})_{0.7}Ca_{0.3}MnO_3$ after an ultrashort optical excitation are studied crossing the ferromagnetic/paramagnetic phase transitions by the variation of the three external stimuli, temperature, applied magnetic field, and pump-fluence, within the scope of this thesis.

The present thesis is organized into four parts which are arranged as follows:

The first part introduces the reader to the topics of optical excitation and transitions (chapter 3), the special material class of correlated perovskite manganites and its electronic and magnetic properties (chapter 4) which is finalized with a literature overview on the static optical and ultrafast dynamical findings in manganites (section 4.5). The last chapter of this part gives a brief reminder of the basics of phase transitions and Ehrenfest's classification (chapter 5).

The second part addresses the investigations on a $(La_{0.6}Pr_{0.4})_{0.7}Ca_{0.3}MnO_3$ thin film grown on MgO substrate starting with the description of the experiments which are performed (chapter 6). Next to the time-resolved experiments (section 6.3), the results of static measurements (sections 6.1 and 6.2) are used as input parameters for the finite-difference time-domain (FDTD) simulations (chapter 7). In order to disentangle the complex signal analysis of the time-resolved data, the results of the transient reflectivity and time-resolved magneto-optical Kerr-effect measurements are presented separately (chapter 8), before finalizing the second

part with the merging of experimental findings and simulation results in the discussion chapter of LPCMO (chapter 9).

The experimental findings on $La_{0.7}Sr_{0.3}MnO_3$ thin films grown on STO substrates are presented (chapter 11) and discussed (chapter 12) in the third part. The introduction to this part is given by the description of the experiments and the sample system (chapter 10).

The final part consists of the summary of this thesis (chapter 13) accompanied by a critical reflection of the set up hypotheses in the outlook chapter (chapter 14).

CHAPTER 2

Word Definitions

This thesis is situated between two different fields of physics: the physics of transition metal oxides (TMO), especially perovskite manganites, and ultrafast dynamics (UD), especially optical transient reflectivity and the time-resolved magneto-optical Kerr effect. In both fields, special wordings are traditionally established, which might be misleading for researchers of the other field, since the phrases do have a different definition in the other field. Hence, in the following, a list of a couple of those phrases is given to clarify the definition, which is used in this thesis.

Core spins:
In the context of TMOs, a central question is, how the spins of occupied t_{2g} state belonging to the transition metal ion, e.g., Mn^{3+} or Mn^{4+}, are aligned with respect to the ones belonging to the neighboring transition metal ions. Since these t_{2g} electrons are localized rather close to the ion core - compared to the conduction electrons in the e_g states - these spins, which occupy the t_{2g} states, are called **core spins**.

Thermalization:
As it is going to be explained in section 3.4 in more detail, the excitation and parts of the following energy dissipation steps lead to a non-equilibrium between different (quasi-)particle groups of the sample. For example, at first, the energy might be stored in the electronic system on the low fs-timescale, whereas the phonons are much too slow to react on this timescale. The process which brings two different subsystems back into equilibrium with respect to each other is called x-y-thermalization, e.g., electron-electron thermalization or electron-phonon thermalization.

One special case needs to be mentioned in this context: if not discussed differently, the electron-electron thermalization is meant in the case of the usage of a standalone *thermalization*. This (electron-electron) thermalization process is outstanding, because, in this meaning, the thermalization process lead from a non-Fermi-Dirac distribution to a Fermi-Dirac distribution of the electronic system. Thus, since the stored energy can be attributed to a certain temperature by a Fermi-Dirac distribution, a temperature of the electron system can be defined the first time after the fs-laser pulse excites the sample.

Hot electrons:
Having established the (electron-electron) thermalization as the process leading to a definable electron temperature, the excited electrons are called **hot electrons** in the ultrashort time span between the excitation step and the thermalization step.

Non- and **quasi-equilibrium dynamics**:
Throughout the past decades, shorter and shorter timescales are reached by the further development of time-resolved experiments. Therefore, the usage of the terms **non-equilibrium dynamics** and **quasi-equilibrium dynamics** did change throughout the years. Thus, it shall be defined in the following, how these two phrases are used in the context of this thesis.
The term **non-equilibrium dynamics** includes the dynamics from the excitation until all three subsystems, electron, lattice, spin, are thermalized with respect to each other. In other words, the dynamics are meant which happen until the spin, the lattice, and the electron temperature are equalized. Examples are the photo-induced electron excitation or the electron-phonon interactions.
Everything that happens after the electron, phonon, and spin system reached the same temperature, but when the sample is still not yet relaxed back into the ground state, is called **quasi-equilibrium dynamics**. Examples for quasi-equilibrium dynamics are thermal diffusion or the remagnetization process.

Scattering:
Usually, scattering is classified into two types: elastic and inelastic scattering.

For the ultrafast dynamics, which are discussed here, a change of the energy distribution or a change of the total angular momentum, J, is needed in order to observe a change of the transient, optical signals. Elastic electron-electron scattering processes where no change of the absolute value of the single particle momenta (just a sign change) is achieved, such as back scattering caused by Coulomb repulsion or by repulsion due to Pauli-principle, do not change the statistic average of the occupation of the density of states and are, therefore, not resolvable in the experiments which are performed within this thesis.

Thus, when discussing scattering within the context of ultrafast dynamics in this thesis, scattering processes are meant which either change the energy or the absolute value of momentum or both of the scattered particles.

CHAPTER 3

Theory of Ultrafastly Driven (Electronic) Transitions

For this thesis, the transient, (magneto-) optical response in reflection of two perovskite manganites (LSMO and LPCMO) has been investigated experimentally on different timescales. The aim for this is a better understanding of the pathways of energy conversion and the mechanisms of the electron and spin dynamics after an fs-excitation. This chapter shall give an overview on different theoretical ideas and concepts which are established about the two questions:

Which processes happen on the ultrafast (few hundreds of fs up to about a picosecond)[1] *timescale?*

And which fundamental, physical laws are of great pertinence[2] *for a working hypothesis regarding this topic?*

Regarding the first question, the theory of quantum mechanics should be able to answer this in principle. Unfortunately, most real cases are not (yet) exactly solvable; at least not without great assumptions and approximations. Thus, extensive effort is needed to calculate some model systems using some more or less convenient assumptions.

Nevertheless, in any case and independent of the system, four conditions need to be fulfilled for every single process:

(1) energy conservation

(2) momentum conservation

[1] In general, tens of fs or even less are covered by the term *ultrafast dynamics* in literature, too. But as one will see in the experimental sections, the measurement signal of the two manganites surrounding time zero comprises a superposition of many different responses. Thus, it is already hard to determine where exactly time zero is, and even harder to properly disentangle the single signal stakes sparked of each step.

[2] Of course, every single physical law must be respected and fulfilled. What is meant here, is that some principles are not of notable order of magnitude in the treated regions.

(3) the possibility to make the transition

(4) conservation of the number of particles[3]

The demand (4) is such axiomatic in the field of solid state physics that this will not be discussed further. Of course, the other three requirements are obvious, too, but much easier to infringe in a conceptional idea. Therefore, it is helpful to have a closer look on them; as it is done in the sections 3.1, 3.2, and 3.3.
The last section, 3.4, gives a short introduction to different, established theoretical concepts and models suggesting the underlying processes of electron/spin dynamics and the interactions with other parts of a solid state material.

3.1 Energy Conservation

The idea of energy conversation, e.g., in a pump-probe experiment, is rather simple: The sum of all involved particles' energy changes needs to balance with the adsorbed (emitted) photon energies:

$$\sum E_{photon} + \sum_i \Delta E_i = 0. \tag{3.1}$$

In particular, the relevant photon energies in the pump-probe-experiments within this thesis are of about[4] $E_{pump} \approx 1.2 \pm \delta$ eV since the distribution of the pump-wavelengths is centered at around $\lambda_{c,pump} = 1030$ nm. Thus, optically excitated, electronic transitions with energy differences of E_{pump} and their integer multiples are resonant directly after the pump pulse only.

[3] Of course, quasi-particles are not included in this; since the concept of quasi-particles are just a simplified, mathematical treatment of two or more particles together as one due to a (specially and/or temporally limited) collective behavior which is (energetically) favoured under a certain condition.

[4] Note, that fs-light pulses are never monochromatic but a bunch of many different wavelengths distributed - often sech^2- or Gaussian-like - around a central wavelength, λ_c.

3.2 Momentum Conservation

When talking about electronic transitions, the spin angular momentum of the photon(s), $\pm n\hbar$, and the total angular momentum of the electron(s) **J** need to be considered as well as potentially involved quasi-particles, e.g., phonons, within momentum conservation. Thus, mechanisms for momentum transfer were under debate since ultrafast demagnetization processes have been discovered [14, 15, 16, 17, 18, 19, 20].

In general, three different pathways for momentum transfer are imaginable, when changing the total angular momentum of an already excited or within the process excited electron: (1) absorbing/emitting a photon; (2) scattering with an other electron; or (3) scattering with an quasi-particle, which carries an angular momentum of $\pm n\hbar$. Of course, the total angular momentum is not just given by the spin, but by the vector sum $\mathbf{J} = \mathbf{S} + \mathbf{L}$; but since the spin is of greater interest for the discussion of this thesis, it will be focused on the possible ways of "loosing" spin angular momentum.[5]

(1) Since a photon can carry a spin, **J** of the electron must change during an absorption[6] process. The question how **J** is changed is determined by the character of the multipole transition (see section 3.3); for example, a spin-flip is possible within a magnetic dipole transition.

A spin-flip which is introduced by **(2)**, electron-electron scattering, does not lead to a global demagnetization, since the total angular momentum of both electrons needs to be conserved. Both cases, (1) and (2), are rather unlikely compared to the transfer via electron-phonon scattering. Therefore, the electron-phonon scattering is going to be discussed in the following section 3.4 in more detail where the already existing theoretical models are introduced.

[5] Note, that so called *spin currents* are an important part of the discussion how UF demagnetization processes might occur, too. But here, the **J** of the considered electron does not change; the demagnetization is of a local character, caused by the transport of majority electrons away from the pumped and probed area. Therefore, spin currents do not lead to a globally change in M.

[6] To facilitate the reading of this text in the following, a possible emission process will be ignored. Nevertheless, in both cases (absorption and emission) the momentum transfer is equivalent but of opposite sign.

3.3 Selection Rules

When starting with the first process, the excitation of electrons by the interaction with the electromagnetic field of a photon, the first question which arises is which states might be the final states (of this excitation step). The most obvious conditions are the one of the energy and the momentum conservation (see sections above). But of course, the quantum mechanical selection rules need to be considered, too. A quite comprehensive derivation and discussion can be found in [21] or many other textbooks about quantum mechanics. Here, just a brief overview shall be given, which is strongly inspired by the book of Cohen-Tannoudji et al. in the following.

When talking about the excitation of an electron in an atom by the electromagnetic wave of a photon, in the low-intensity and plane-wave ($\lambda > a_0$) approximation, the Hamiltonian can be rewritten by replacing the exact vector potential of the exciting photon by a Taylor series. This rewriting is known as the multipole expansion in such a way, that the Taylor approximation of the first order is called the *electric dipole Hamiltonian* (ED), of the second order *magnetic dipole Hamiltonian* (MD), for the third order *electric quadrupole Hamiltonian* (EQ), etc. From these terms, selection rules can be found which specifies, which transitions are generally possible within the considered approximation. The selection rules for the first and second order approximations are:

$$\text{Electric dipole approximation} \begin{cases} \Delta l = \pm 1 & \text{(3.2a)} \\ \Delta J = 0, \pm 1 & \text{(3.2b)} \\ \Delta m_J = 0, \pm 1 & \text{(3.2c)} \end{cases}$$

and

$$\text{Magnetic dipole approximation} \begin{cases} \Delta l = 0 & \text{(3.3a)} \\ \Delta J = 0, \pm 1 & \text{(3.3b)} \\ \Delta m_J = 0, \pm 1 & \text{(3.3c)} \end{cases}$$

where $l,\ J,\ m_J$ refere to the quantum numbers of the azimuthal as well as the total angular momentum[7] and its projection.

Usually, electric dipole allowed transitions are considered for the interpretation of (ultrafast transient) optical response only. This is because, usually, the magnetic dipole transitions are considered to be 10^5 times weaker than the electric dipole transitions [22, 23, 24]. Nevertheless, magnetic dipole transitions exist and are experimentally corroborated in emission spectra [22] or in microwave absorption spectra [25]. In Eu^{3+}-doped fluoroborate glasses, a magnetic dipole transition is observed in transmission measurements in the visible range at an absorption wavelength of $\lambda \approx 525$ nm [26].

3.4 Energy Dissipation after an Ultrashort Excitation - the Three Temperature Model and Beyond

In the first sections, fundamental physical laws are discussed, which needed to be considered when discussing an ultrashort light excitation of material and the following induced dynamics. It is reminded that possible excitation processes need to fulfil the requirements of energy conservation (see sec. 3.1) and momentum conservation (see sec. 3.2) as well as the selection rules (see sec. 3.3), which are deduced from the multipole expansion of the photon vector potential. In this section, a more concrete picture of how the dynamics develop after an ultrashort excitation is given. The phenomenological *three temperature model (3TM)* is well established to picture the basic steps of energy conversion in a magnetically ordered system after an excitation by a fs-laser pulse. It is based on the two temperature model from 1974 [27]. Different version of this concept are developed since the first version of it was published in 1996 by Beaurepaire and co-workers [28]. But the basic concept of all approaches stays the same: the sample is divided into different subsystems which are described by different characteristics and, therefore, absorb different amounts of the pump pulse energy. This leads to an non-equilibrium situation and, furthermore, the subsystems react to this imbalance on

[7] Note, that the spin-orbit coupling cannot be neglected in perovskite manganites thus, $\boldsymbol{J} = \boldsymbol{L} + \boldsymbol{S}$ needs to be considered.

different timescales. A sketch of this concept is depicted in fig. 3.1.

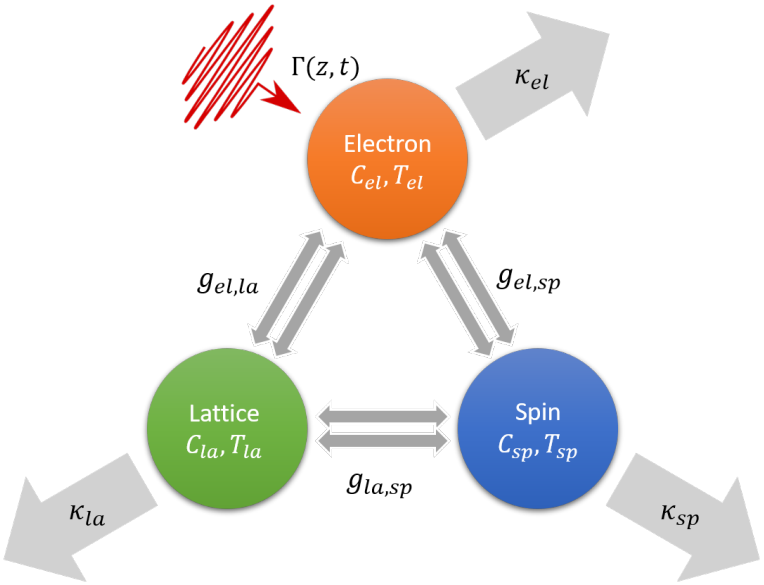

FIGURE 3.1: Sketch of the 3TM heat bath picture: Division of the sample system into three subsystems - electron, phonon, and spin, which are capable of exchanging energy and momentum. The assumption that the electronic subsystem is excited only by the initial pump-pulse in the visible/NIR range is included and indicated by the red arrow in the left corner. The final energy dissipation by thermal transport, κ_i, is visualized by the light grey arrows.

In the three temperature model from 1996 [28], the sample system is divided into different subsystems which are the electron (el), the lattice (la), and the spin (sp) subsystem. These subsystems function as heat baths since an individual specific heat, C_i, and a certain temperature, T_i, are attributed to each of them. Via coupling constants, $g_{i,j}$, an energy transfer between the different subsystem, i and j, is enabled. In the case, that the photon energy of the pump-pulse is in the visible (vis) or near infrared (NIR) range, it is assumed that the electronic subsystem is excited by the light pulse, only. A non-equilibrium situation is created: the electron subsystem is heated up while the other subsystems still remain at the base temperature. According to the coupling strength between the subsystems, which is considered by the constant $g_{i,j}$, the stored energy will be transferred from the electron subsystem into the others, hence, their temperatures will increase, too, until all subsystems are thermalized with respect to each other, $T_{el} = T_{la} = T_{sp} = T_{quasi}$. Usually, T_{quasi} is greater than the base

temperature, thus, this situation is called quasi-equilibrium. Quasi-equilibrium processes, such as thermal diffusion, transport the stored energy out of the probed area and therefore, relax the heated sample back into the ground state [16, 29].

The splitting of the sample system into different subsystems is justified for electron and lattice subsystems by the Born-Oppenheimer approximation. The advantage of dividing the sample into three heat baths and artificially separate the electronic and the spin system from each other is that the observed demagnetization of a ferromagnetic sample after a fs-excitation can be explained by an increase of the spin temperature and the resulting loss of magnetization. If T_{sp} reaches temporally the Curie temperature, T_C, the quenching of the spin subsystem approaches 100 %. During the demagnetization (and of course the remagnetization) the ration between majority and minority spins needs to change. This can be achieved by two mechanisms, the superdiffusive spin currents [19, 20, 30] and spin-flip process [14, 31]. Superdiffusive spin currents occur from an ultrafast transport of electrons, the lifetimes of which depend on the spin-polarization of the single electrons, which leads to a spin-polarization of the current. The ratio between majority and minority spins changes in time. If the lifetime of the majority electrons is longer than the one of the minority electrons, a demagnetization is observed since more majority electrons are transported away from the probed area. Note, that the momentum conservation of J is fulfilled for each electron. In contrast, spin-flip mechanisms require a counterpart which balances the momentum change of $\Delta S = \pm\hbar$ during the spin-flip. Koopmans et al. [14, 16, 31] suggested a Elliot-Yafet type of spin-flip process in order to ensure momentum conservation. Here, a scattering process flips the spin of the involved electron and creates (or annihilates) simultaneously a phonon which happens with a certain spin-flip scattering probability, α_{sf}. In many cases, an electron-electron scattering-type of spin-flip process is neglected, since an electron-electron scattering process rarely leads to a magnetization change due to momentum conservation. Hence, in assumption, only two coupling constants, $g_{el,la}$ and $g_{la,sp}$, are considered. Finally, a set of rate equations can be set up. As an example see the rate equation system 7.1 - 7.3 which is solved in the FDTD simulation in chapter 7.

The disadvantage of this purely phenomenological approach is that no detailed information of the electronic structure, e.g., the spin-resolved density of states, is taken into account. To overcome this issue, a new type of model, the μTM, is published by Müller and co-workers in [32, 33, 34], where the 3TM is combined with band structure information by utilizing the chemical potential of both spin channels, $\mu^{\uparrow}$ and $\mu^{\downarrow}$. By defining the two temperatures, $T^{\uparrow}$ and $T^{\downarrow}$, the dynamics of both the majority and minority spin channels can be traced by solving a spin-resolved Boltzmann equation.

In recent years, the time-dependent approach [35] of the density functional theory is developed further in order to trace the electron dynamics as well as the magnetization dynamics in solid state materials by ab-initio band structure calculations, e.g., for the electron-hole pair excitation in bulk silicon by Sato et al. [36]. Krieger and co-worker calculated the magnetization dynamics of the 3d ferromagnets (Fe, Ni, Co) by using the so called adiabatic local spin density approximation (ALSDA) in [37]. Later works by the group of S. Sharma and colaboraters investigated the energy-, time-, and spin-resolved dynamics of alloys and more complicated systems [38, 39, 40].

Following the framework of first-principles calculations, Rajpurohit and co-workers [41] combined a tight-binding model [42, 43, 44] with simulations using Ehrenfest dynamics [45, 46] in order to calculate temporal evolution of the electronic, atomic, and magnetic microstructure of $Pr_{0.5}Ca_{0.5}MnO_3$ after an ultrashort light pulse excitation. They predict two "hidden" phases to be introduced by the pump pulse.

CHAPTER 4

Sample Systems - Perovskite Manganites

The high research interests in perovskite manganites is based on the large variety of different effects, which are potentially interesting for technical applications. The unique characteristic of perovskite manganites is the lattice structure, see fig. 4.1 [47], which can be viewed as being constructed by a central manganese cation, which is surrounded by an octahedron of oxygen anions, and the corners of the unit cell are marked by the so called A-site cation. Thus, $AMnO_3$ results as a general, chemical formula of this material class. Even though the pseudo cubic lattice structure of manganese-based perovskites is relatively simple, one can switch from a antiferromagnetic insulator (e.g., $LaMnO_3$ [49, 50, 51], $SrMnO_3$ [52], $CaMnO_3$ [44, 49, 53], and $PrMnO_3$ [44, 54]) to an multiferroic compound (e.g., $TbMnO_3$ [55] , and $DyMnO_3$ [56]) simply by exchanging the A-site cation. The spectrum of different effects becomes even larger, if (i) the valency of the manganese cation is tuned or (ii) if ratio of the

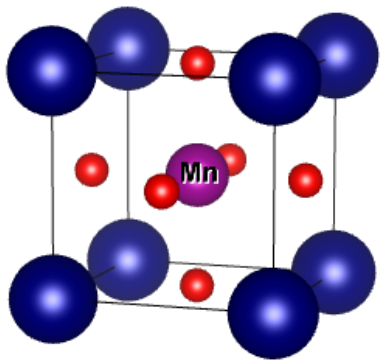

FIGURE 4.1: Manganite as an example for a perovskite structure: purple - manganese cation, red - oxygen anions, blue A-site cation. Drawn with the help of VESTA [48].

cation radii inside the lattice is changed by a A-site doping.[1] The physical effects, which result from these two variations, are introduced in sec. 4.1 for (i) the charge carrier doping, and (ii) the lattice doping in sec. 4.2.

4.1 Magnetic Order and Electron Mobility - Jahn-Teller Polaron

An example for the case (i) is the substitution of La^{3+} by Sr^{2+}, where the manganese ion are forced to increase the oxidation state from Mn^{3+} to Mn^{4+}. As a results, a rich phase diagram occurs which includes a variety of different magnetic, electronic, and structural ground states, see fig. 4.2.

As visible in fig. 4.2, the physical properties of the antiferromagnetic (AFM), insulating $LaMnO_3$ becomes a metal for a Sr-doping of 0.3, which is still ferromagnetically ordered well above room temperature. This property makes $La_{0.7}Sr_{0.3}MnO_3$ (LSMO) an interesting material for basic research [58]. The reasons for this drastic property change is a competition between two effects: the trapping of electrons due to a so called Jahn-Teller distortion which supports the antiferromagnetic superexchange coupling of the manganese ions on the one side and the hole-doping which raise the mobility of the electrons and forces the manganese ions to order ferromagnetically via the so called double-exchange. These mechanisms are explained in the following in more detail.

[1] A third option to tune the properties of a transition metal oxide is the pointed insertion of oxygen vacancies. But, since the thin films, which are investigated here, are grown by the vacuum-free preparation technique *metalorganic aerosol deposition (MAD)* under an oxygen partial pressure of $p_{O_2} \approx 0.2$ bar, an oxygen situation of nearly 100 % is expected [57]. Only, a statistical vacancy doping caused by entropic reasons is assumed to appear. Therefore, a discussion of this third variation option is skipped here.

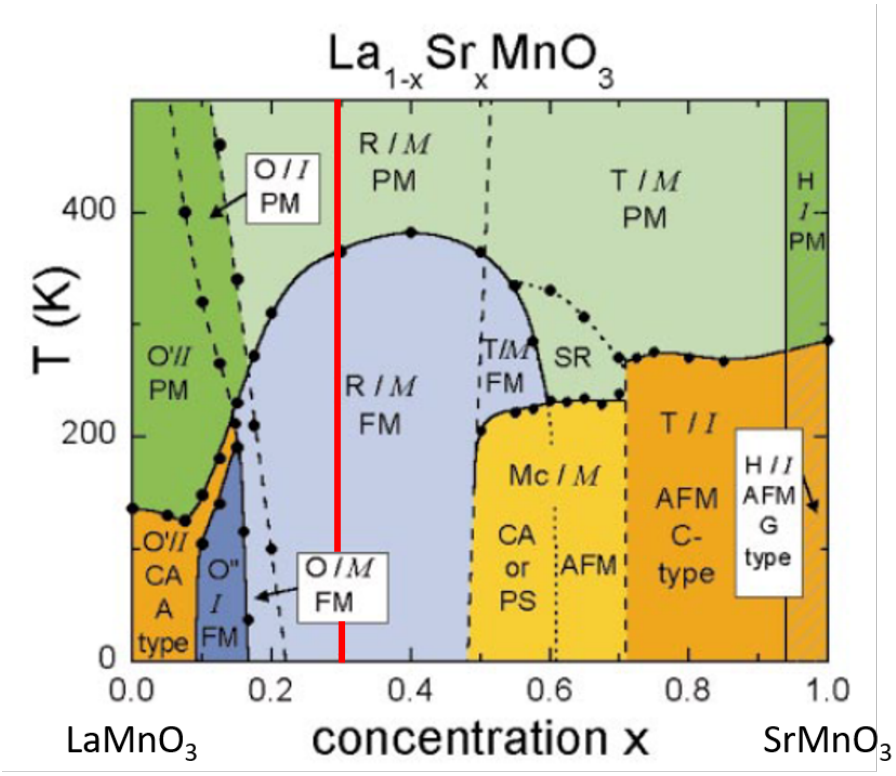

FIGURE 4.2: Phase diagram of Sr-doped $LaMnO_3$. Each phase is encoded by a color and an abbreviation, which references the *lattice structure* / *conduction state* and the *magnetic ground state*; for the case of $x = 0.3$, this is means: a rhombohedral (R) metal (M), which is ferromagnetic (FM) in below $T_C \approx 350$ K and paramagnetic (PM) above the Curie temperature. Edited and reprinted figure with permission from [51]. Copyright (2002) by the American Physical Society.

4.1.1 Jahn-Teller Polaron

As described above, the perovskite manganites consist of a lattices which is based on oxygen octahedra the center of which is a Mn^{3+} or Mn^{4+} ion. Here, the binding electrons are quite localized, thus the tight-binding model and therefore, molecular orbitals are a good approximation. To simplify the picture at first, a Mn^{4+} ion will be considered as central ion. The electron configuration of such a Mn^{4+} ion is $[Ar]3d^3$. And the crystal field leads to a splitting of the 3d orbitals into energetically lower $t_{2,g}$ orbitals (d_{xy}, d_{xz}, and d_{yz}) and energetically higher e_g orbitals ($d_{x^2-y^2}$ and d_{z^2}) [47]. The sketch in fig. 4.3 depict this model. Due to Hund's rule, the three electrons in the 3d shell prefer a parallel alignment of the spin, thus, all three $t_{2,g}$ orbitals are occupied by one electron each. The $t_{2,g}$ orbitals hybridize

with the 2p orbitals of the oxygen to form the bounds and, therefore, are viewed as always localized [47]. And the e_g orbitals are shifted above the Fermi energy for the case of Mn^{4+} e.g., $SrMnO_3$.

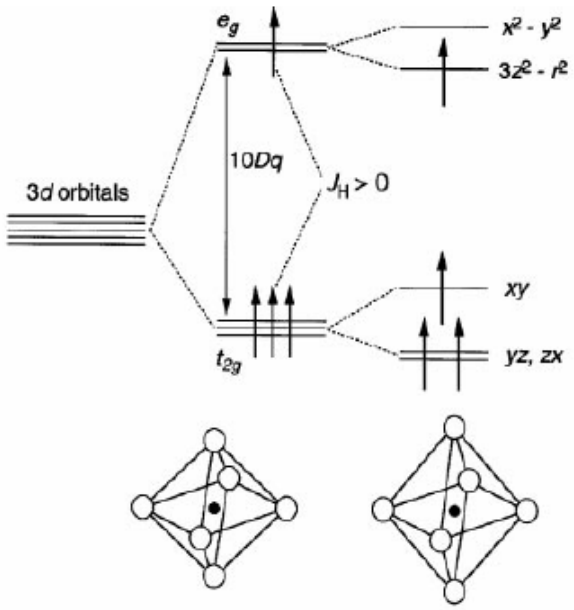

FIGURE 4.3: Sketch of the 3d states of Mn^{3+}: (left hand) degenerated for a free-standing ion; (middle) considering the crystal field splitting introduced by a cubic lattice; (right hand) considering the splitting of the e_g states due to a Jahn-Teller distortion of the oxygen octahedron. Reprinted from [47], Copyright (1999), with permission from Elsevier.

If an additional electron is added, in order to build a Mn^{3+} ion, additional energy is needed due to Coulomb repulsion. Caused by the bigger radius of the Mn^{3+} ion, the oxygen octahedron is distorted, which leads to a second splitting of the 3d energy levels, the so called *Jahn-Teller splitting* [47, 59]. Now, the $e_{g,1}$ orbital is shifted below the Fermi energy and the $e_{g,2}$ is shifted further above, e.g., in $LaMnO_3$. Again, all electron spins are aligned parallel to follow the second Hund's rule. Both systems, purely built by Mn^{4+} ions and purely built by Mn^{3+} ions, are insulators, since the Fermi level lies in between a gap, either the one between $t_{2,g}$ and e_g states or the gap of the Jahn-Teller splitting, as depicted right hand in fig. 4.3.

If both systems are combined by an A-site doping with varied valance of the cations, the resulting manganite becomes conducting [47, 50, 51]. In fig. 4.2 the case of LMO which is

hole-doped by Sr^{2+} ion is shown. The mobility of the e_g is increased by the raised number of Mn^{4+}, which provide unoccupied e_g states. Under certain conditions, which are explained later in section 4.1.3, an e_g electron can hop from an former Mn^{3+} site onto a Mn^{4+} site. But, since the occupation of an e_g state requires a distortion, a so called *breathing*, of the oxygen octahedron, the octahedron which surrounds the previously occupied Mn^{3+} ion needs to relax. Since, the distortion of the lattice, which is caused by the Jahn-Teller splitting, is coupled to the motion of electron, a *Jahn-Teller polaron* (JTP) is defined as quasiparticle. If an electron hopes from one manganese site to an other, the Jahn-Teller distortion "follows".

Through out the years, it is shown that different kind of JTP exist, which are classified by its sizes [60]: large and small polarons. Small polarons exhibits a radius of about one unit cell and are theoretically described by the Holstein model [61, 62] in the framework of a short-range electron-phonon interaction. The result of this electron-phonon interaction, a thermal activation is needed for electron hopping [60]. In contrast, large polarons are treated in an approach of a long-range electron-phonon interaction which is suggested in the theory by Fröhlich and co-workers [63, 64]. Here, the mobility is viewed as a free carrier mobility [60].

An example material which shows small polarons is $La_{0.7}Ca_{0.3}MnO_3$ [65, 66]. $La_{0.7}Sr_{0.3}MnO_3$, which is studied in this thesis, is demonstrated to exhibit large polarons [65, 66]. Due to the approximated free carrier mobility in case of large polarons, the mobility is decreased by increasing the temperature [60], as experimentally observed for instance in [6, 67, 68] and many more.

By neutron scattering [69, 70] and by x-ray diffraction [71, 72] a short range correlation of the polarons close to the phase transition is demonstrated in $La_{0.7}Ca_{0.3}MnO_3$, $Nd_{0.7}Sr_{0.3}MnO_3$ and different dopings of PCMO. It is shown in doping-dependent measurements [69] that these correlated polarons mediate the ferromagnetic/paramagnetic phase transition in the CMR[2] material LCMO. The studies on NSMO [71], a CMR-material, found a destruction of the polaronic nanoclusters inside a magnetic field. In a later study, Moshnyaga and co-workers [8] investigated the CMR effect of LPCMO thin films grown on MgO[3] under the aspect of

[2] A description of the CMR effect, colossal magnetoresistance effect, is given in section 4.4.

[3] Those films are comparable to the thin film which is discussed in chapter 9.

correlated Jahn-Teller polarons. An insulating polaronic state is suggested to mediate the phase transition from the ferromagnetic metallic phase into the paramagnetic insulating phase due to the occurrence of a network of correlated polarons in the domain walls which lead to an antiferromagnetic coupling of ferromagnetic nanodomains. For more details see also section 4.4. In contrast to the CMR materials, LCMO, PCMO, and LPCMO, no correlation of the polarons is found in LSMO [73].

Based on the lattice structure (see fig. 4.1), the overlap between the orbitals of two neighboring Mn ions is quite small, hence, a direct transition from a Mn^{3+} ion into a Mn^{4+} ion is negligible for the electronic transport. Instead, a hopping process takes place via the O2p states. As mentioned above, Mn^{3+} or Mn^{4+} ions prefer a high spin configuration caused by Hund's rule. Thus, two cases are possible when considering two neighboring manganese ions: a ferromagnetic (parallel) coupling of both high spin ions or an antiferromagnetic (antiparallel) coupling of both spin systems. As the reader will see in the following, both arrangements lead to different electronic states. In section 4.1.3, the ferromagnetic case is discussed, where the so called *double-exchange* empowers the ferromagnetic coupling. In contrast, the *superexchange* induces an antiferromagnetic coupling of two neighboring Mn ions, see section 4.1.2. The central property is the localization of the electrons. If the electron is localized, this means that the hopping interaction, t, is smaller than the potential energy, U, which is needed to occupy an orbital in neighboring Mn ion, the superexchange leads to an antiferromagnetic coupling. How this occurs is going to be discussed in the following section.

4.1.2 Superexchange

As described above, the highest occupied states in a Mn^{3+} ion-based perovskite are the $e_{g,1}$ states. In order to discuss conductivity and electron mobility, it is necessary to consider the mobility of electrons sitting in these states. For a transition between two orbitals, the magnitude of overlap between the considered orbitals is important. Since the overlap between two $e_{g,1}$ states of two neighboring Mn^{3+} ions is vanishing, the probability of a direct transition vanishes, too. The interaction of both neighboring Mn^{3+} ion is mediated by the oxygen. In

this section, the case $t << U$, a localization of the $e_{g,1}$ electron is discussed, and hence, the impact of the surrounding O2p states on the $e_{g,1}$ electron. In order to do so, a simplified model of the e_g states of two Mn^{3+} ion and a mediating O2p orbital is depicted in fig. 4.4 and is considered in the following. A quantum mechanical theory of the superexchange interaction is published by Anderson in the year 1950 [74].

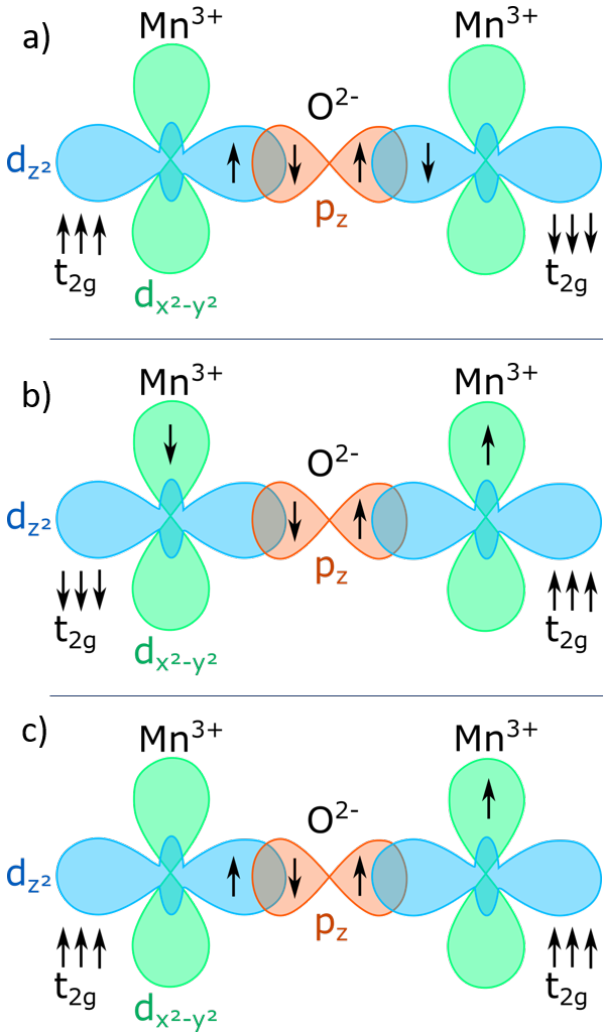

FIGURE 4.4: Sketch of the e_g states of two Mn^{3+} ions which are mediated by an oxygen p_z state. (**a**) antiferromagnetic coupling of the Mn^{3+} ions which is compatible with the spin arrangement of the oxygen ion for delocalization. (**b**) antiferromagnetic coupling of the Mn^{3+} ions which is incompatible with the spin arrangement of the oxygen ion for delocalization. (**c**) ferromagnetic coupling of the Mn^{3+} ions which is incompatible with the spin arrangement of the oxygen ion for delocalization.

If two Mn^{3+} ions with localized electrons are neighboring, a slight delocalization is achieved if both e_g electrons are coupled antiparallel with respect to each other. In the case which is depicted in fig. 4.4 (a), the electrons in the O2p orbital are allowed (Pauli-principle) to hop into the Mn3d orbitals. Furthermore, if one electron which previously occupied an O2p state has hopped onto a Mn site, the electron from the opposite Mn ion is able to hop into the free oxygen state. Due to this delocalization, the energy of the system can be minimized [74]. It is the energetically favored configuration.
For the second antiferromagnetic arrangement, see fig. 4.4 (b), the hopping, and therefore the delocalization, is forbidden due to Pauli-principle. A similar argument appears for the case of the parallel alignment, a ferromagnetic coupling, of both e_g spins, see fig. 4.4 (c).
Note, that the electrons which occupy the $t_{2,g}$ states, the core-spins, prefer a parallel alignment with respect to the e_g spins, as discussed above. Therefore, in the case of a dominating superexchange, the magnetic ground state of the manganite is an antiferromagnet.

4.1.3 Double-Exchange

In the previous section, an explanation model, the superexchange, for the antiferromagnetic and insulating behavior of materials such as $LaMnO_3$ or $PrMnO_3$, which exhibit only one type of is given. But, in 1950, Jonker and van Santen published a study [75] about the magnetism of A-site-doped manganites, such as $La_{0.9}Sr_{0.1}MnO_3$ and $La_{0.7}Sr_{0.3}MnO_3$. They observed a ferromagnetic behavior for a lot of doped compounds. In order to explain the ferromagnetism of this mixed-valance manganites, Zener [76] suggested the concept of a double-exchange. Anderson and Hasegawa [77] as well as de Gennes [78] expand the double-exchange model by calculating the exchange integral, J, of general spin, S.

The clue of this model is that the e_g of a mixed-valance manganite can delocalize, and therefore, minimize their energy, if neighboring e_g spins are aligned parallel with respect to each other, as depicted in fig. 4.5 (a). In the superexchange model discussed previously, the electrons are able to delocalize over orbitals but limited to the space of the surrounding unit cell. But if the spins are ferromagnetically aligned and Mn^{3+} or Mn^{4+} ions are mixed within

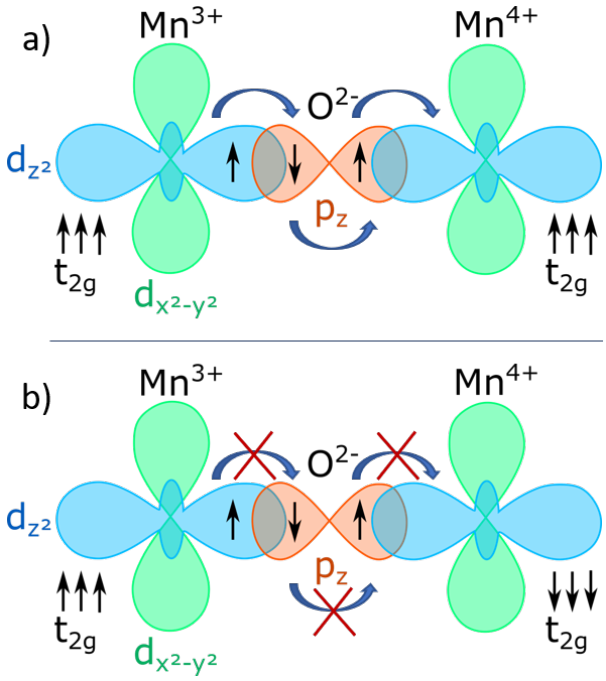

FIGURE 4.5: Sketch of the e_g states of a Mn^{3+} ion and a Mn^{4+} ion which are mediated by an oxygen p_z state. (**a**) ferromagnetic coupling of the Mn ions enables electron hopping. (**b**) antiferromagnetic coupling of the Mn^{3+} ions suppresses electron hopping.

the material, a hopping across the boarders of the unit cell becomes possible. To visualized this idea, again, a simplified model of two Mn ions the coupling of which are mediated by O2p orbital is depicted in fig. 4.5. But this time, one of the Mn^{3+} ion is replaced by an Mn^{4+} ion; the model system is hole-doped. Due to the doping, holes in some $e_{g,1}$ states are provided. Therefore, an electron from the O2p state enabled to occupy this state by thermal activation. The released Op2 state can, now, be occupied by the $e_{g,1}$ electron of the other Mn ion. The latter step is possible if the $e_{g,1}$ electron and the empty O2p state exhibit the same spin alignment due to Pauli-principle. This requires a ferromagnetic alignment of the core-spins, the $t_{2,g}$ spins, of the Mn^{4+} ion with respect to the Mn^{3+}. Otherwise (see fig. 4.5 (b)), the electron which hops from the O2p site to the Mn^{4+} would need to provide additional energy for Hund's coupling.

The consequence of this model is that the electron mobility is coupled to the degree of saturation magnetization of the mixed-valance manganite compound. Above the Curie temperature, the hopping is restricted to random alignment of neighboring core-spins, thus the

valance electrons are more or less trapped; whereas, the conductivity rises if the compound is cooled down. By increasing the saturation magnetization the carrier mobility approaches more and more the free carrier mobility.

4.2 Influence of the Ionradii on the Electron-Phonon Coupling

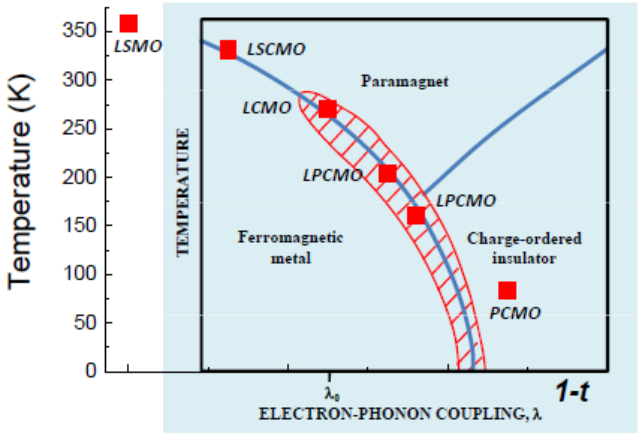

FIGURE 4.6: Generic phase diagram with data from [79]. The transition temperature for manganites with different tolerance factors. The picture is reprinted from [80]: *Electron-lattice correlations and phase transitions in CMR manganites*, 523 by V. Moshnyaga and K. Samwer. Copyright 2011 by John Wiley and Sons. Reproduced with permission of John Wiley and Sons via Copyright Clearance Center.

The secondly named opportunity to manipulate the properties of manganites is to substitute the A-site cation by a cation with a different ion radius. In this case, the oxidation state of the manganese ions might stay the same, but the electron system is changed due to changes in the lattice structure. In case of a perfect cubic perovskite, the distance between the A-site cation and the neighboring oxygen anion, d_{A-O} would be equal to $\sqrt{2}d_{Mn-O}$, where d_{Mn-O} correspond to the manganese-oxygen bond length. For most of the compounds, this is not given, hence a Goldschmidt tolerance factor is defined by the ratio of both, $f = d_{A-O}/(\sqrt{2}d_{Mn-O})$, in order to classify the deviation from the ideal, cubic case. As an example, $f_{LSMO} \approx 0.996$ [81] for the rhombohedral, crystalline $La_{0.7}Sr_{0.3}MnO_3$.

When the lattice is distorted, the electron-phonon coupling changes. The distortion of the lattice lead to a change of the overlap of orbitals belonging to neighboring atoms. Hence, e.g., the transition probability between the orbitals or the hybridization of orbitals is changed. The lattice distortion impacts directly the electronic states of the compound.
A higher electron-phonon coupling leads to a stronger trapping of the electron in the Jahn-Teller distortion. As seen in the section 4.1.2, a higher localization of the electrons lead to a breakdown of the ferromagnetic coupling. This argumentation explains the generic phase diagram, which is reprinted in fig. 4.6 from [80] and [79]. As visible in that phase diagram, the different properties of LSMO and LPCMO are based on the different electron phonon coupling of both systems. Since this two systems are investigated in this theses, the properties of both systems, which are of importance for the understanding of the findings, are going to be summarized the following two sections: sec. 4.3 for LSMO and sec. 4.4.

4.3 Properties of LSMO

Strontium-doped Lanthanum-manganite, $La_{1-\chi}Sr_{\chi}MnO_3$ (LSMO), is of rhombohedral lattice structure roughly in the doping range $0.2 \lesssim \chi \lesssim 0.45$ [51]. Due to the hole-doping, it becomes an ferromagnetic conducting material below its Curie temperature which is determined for an optimal doping ($\sim 1/3$) to about $T_C \approx 370$ K in case of a bulk crystal [5]. For thin films of LSMO transition temperatures of about $T_C \approx 350$ - 360 K are reported [6, 7]. Huijben and co-workers demonstrated in [7] that T_C is dependent on the thin film thickness. Furthermore, it depends on the substrate material caused by the lattice mismatch between substrate and LSMO which leads to induced strain effects at the interface.
A $SrTiO_3$ substrate in (100) orientation, as used for this thesis, causes an peudocubic lattice structure, $a_c = 3.866$ Å, of LSMO grown in an (100) orientation [82]. With the cubic lattice constant of $a_{STO} = 3.9045$ Å[83], a relatively low mismatch of ~ 1 % [82] is achieved what just slightly impacts the magnetic and electric properties of the thin film by tensile strain.

Large polarons (see section 4.1) impinge on the electronic structure of $La_{0.7}Sr_{0.3}MnO_3$ [65, 66] and stabilize the ferromagnetic coupling, therefore, support the relatively high Curie

temperature [60, 76, 77, 78]. When crossing the phase transition, LSMO exhibits an insulating paramagnetic ground state [5, 84], see $R(T)$ data in appendix C1.2. Compared to LPCMO, the second compound which is investigated in this thesis, LSMO exhibits a relatively low electron-phonon coupling (see fig. 4.6).

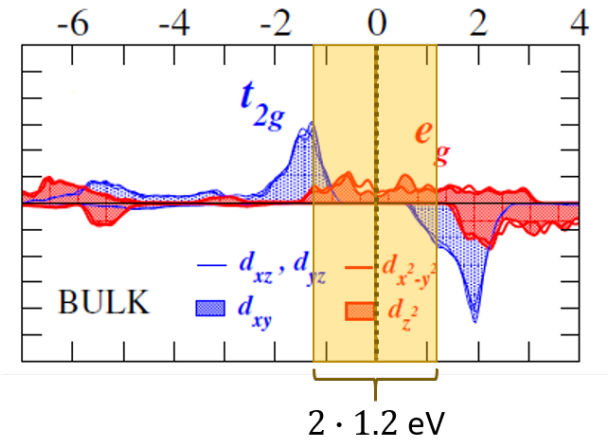

FIGURE 4.7: Spin-resolved density of states for the Mn3d orbitals of bulk LSMO calculated by DFT. The figure is edited by marking the accessible states by an 1.2 eV pump pulse in yellow. The picture is reprinted with permission from [85]. Copyright 2007 by the American Physical Society.

Pruneda et al. [85] calculated the spin- and orbital-projected density of states for the Mn3d states of bulk LSMO in the framework of density functional theory, which is reprinted with permission in fig. 4.7. The figure is edited by adding the potential excitation window for the pump-pulse which is used in the pump-probe experiments (see chapter 10).

4.4 Properties of LPCMO

Pr-doped $La_{0.7}Ca_{0.3}MnO_3$ is a bandwidth-controlled perovskite manganite which shows the so called *colossal magnetoresistance* (CMR) effect [8, 9, 86]. The (colossal) magnetoresistance effects [87] is defined as:

$$CMR = \frac{R_0 - R_H}{R_H}, \tag{4.1}$$

the reduction of resistivity by an external magnetic field. In the case of thin film of $(La_{0.6}Pr_{0.4})_{0.7}Ca_{0.3}MnO_3$ (LPCMO), colossal magnetoresistance effect reaches values of $CMR(1\ \mathrm{T}) \approx 2000\ \%$ [9] at moderate fields already what leads to the term *colossal* magnetoresistance effect. These colossal changes of the resistance appear close to the phase transition from the ferromagnetic metallic phase into the insulating paramagnetic phase. Thereby, the external magnetic field stabilizes the internal ferromagnetic coupling close to the Cure temperature and, in the model of double-exchange (see section 4.1.3), this empowers electron hopping and, therefore, reduces the resistivity. The Curie temperature of $(La_{0.6}Pr_{0.4})_{0.7}Ca_{0.3}MnO_3$ is at about $T_C \approx 200$ K [8, 9, 88].

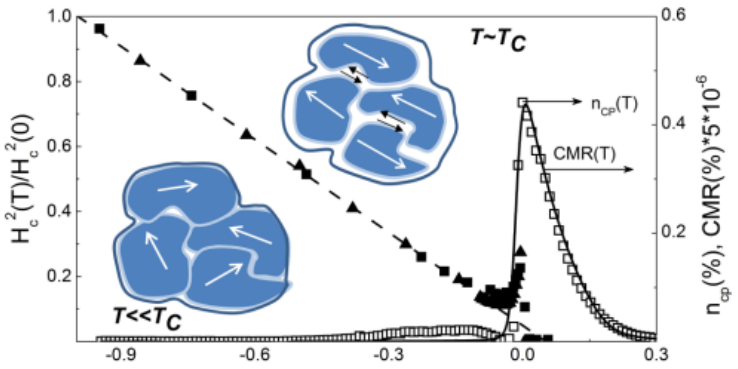

FIGURE 4.8: The filled symbols represent the normalized coercive field, h_c^2, on the left scale as a function of the normalized temperature for LPCMO films. The relative amount of correlated polarons, n_{CP}, (open squares) on the right scale depending on the normalized temperature. The picture (c) is reprinted with permission from [8]. Copyright 2014 by the American Physical Society.

As seen above, the magnetic structure in the region around the phase transition in LPCMO is of interest in order to understand the appearance of this CMR effect. Hence, a microscopic picture of the magnetic structure is given in the following. Uehara et al. performed a doping-dependent study on $La_{5/8-y}Pr_yCa_{3/8}MnO_3$ regarding static magnetic and electric properties. In order to explain their findings, they suggested a phase separation model of sub-micrometer-scaled domains, ferromagnetic and charge-ordering domains coexist in the phase transition region. This picture is elaborated by Moshnyaga and co-workers [8] for the case of strain-free [89, 90] LPCMO thin films grown on MgO substrate. As depicted in the left one of the

two blue sketches in fig. 4.8, different ferromagnetic domains persist next to each other below T_C. In the phase separation regime, the single ferromagnetic domains are surrounded by a network of correlated Jahn-Teller polarons, a charged ordered insulating phase. This insulating phase lead to an antiferromagnetic coupling of the ferromagnetic domains, which exhibit a diameter of about ~ 6 - 8 nm and which are separated from each other. As a result, the macroscopic conductivity is restrained by the insulating charge-ordering phase. Increasing the temperature, the ferromagnetic domains decreases until a fully paramagnetic insulating phase is established.
In contrast to LPCMO, LSMO does not show a *colossal* magneto resistance effect since the electron-phonon coupling is much weaker compared to LPCMO [57].

4.5 Optical Properties of Perovskite Manganites

4.5.1 Static Optical Properties

In the past, different groups investigated and interpreted the response of perovskite manganites to different kinds of spectral measurements. When looking at different manganites, some feature in the spectra recur with small modifications (small energy shifts, intensity variations, line-widths, etc.) others will not be comparable, enforced by the individual characteristics of the electronic structure of each component. An overview of the most common hypotheses interpreting these spectra will be given here. Nevertheless, this section is going to focus on studies done on similar or related systems as investigated here. This means in particular thin film systems, grown at STO-substrate, of optimally doped $La_{0.7}Sr_{0.3}MnO_3$ compound, $(La_{0.6}Pr_{0.4})_{0.7}Ca_{0.3}MnO_3$ thin films grown at MgO, or related systems, in that sense that only one proviso is changed at best. Next to that, the literature overview is restricted to phenomena observed (and discussed) at photon energies around ~ 1.2 eV.

When talking about the (optical) conductivity properties of perovskite manganites in the requested frequency range, all literature seems to agree in the point that an electron is transferred to a final 3d state of one of the Mn-ions. But the discussed ideas of initial state (the

initial ion type) as well as of the specific, final spin and electronic configuration do differ on a paper-by-paper basis.

Yamaguchi et al. [91] measured and interpreted the polar MOKE, optical conductivity, and off-diagonal elements of the dielectric tensor in the perovskite bulk TMOs $La_{1-\chi}Sr_{\chi}MnO_3$ and $La_{1-\chi}Sr_{\chi}CoO_3$ for hole-doping of $\chi = 0,\ 0.1,\ 0.2,\ 0.3$ within a shown spectral range of $\hbar\omega$ up to 5.3 eV.

Focusing on the 0.3-hole doping of LSMO, the authors mainly discuss two optical features at $\omega_0 = 1.2$ and 3.5 eV. With the troika of experiments in combination with literature, they determine the transitions at both frequencies to be a charge transfer transition each and specify them as type I transition, where the off-diagonal elements show dissipation-type behavior in the real part and a dispersion-type in the imaginary part of the dielectric tensor. In the end they conclude that the 1.2 eV feature belongs to a charge transfer transition between O2p states and the unoccupied e_g-spin-up state of a Mn^{3+} ion, which then turns into a +II-oxidation state. The higher energy transition at $\omega_0 = 3.5$ eV is suggested to be a charge transfer transition from an O2p state into an spin-down $t_{2,\,g}$ state of a Mn^{3+} ion.

In another study from **1998 by Quijada and co-workers** [67], the optical conductivity of thin films of $La_{0.7}Sr_{0.3}MnO_3$, $La_{0.7}Ca_{0.3}MnO_3$, and $Nd_{0.7}Sr_{0.3}MnO_3$ grown on LAO was assessed under the aspect of the thermal crossing of the insulator-to-metal transition. Within their spectral range (5 meV up to 5 eV), they identified three main peaks which exist in all three materials: at about 1 eV, 3 eV[4] , and 4 eV.

These three features are associated (starting from the lowest energy) with a charge transfer transition from one JT-distorted Mn-ion to either an other Mn^{3+} into the upper $e_{g,\uparrow}$ level or into a - till then - unoccupied $e_{g,\uparrow}$ states of a Mn^{4+} ion. The feature of the middle energy range

[4]Speculating comment: In the related figure (Fig. 2 in that paper), I cannot see any peak at ~ 3 eV. How I see the data in the area of about 3 eV is as follows. At around 4 eV (as the authors wrote), there is a peak with an high intensity and a wide extent; and the 3 eV is one of the first parts of the increasing flank, which starts right away from a local minimum (~ 2.8 eV). Decreasing the photon energy further, a local maximum/peak arises at roughly $\sim 2 - 2.2$ eV right infront of the minimum at 2.8 eV. This 2.2 eV-peak is not discussed in the paper. Therefore, my speculation is that the authors intended to discuss the 2.2 eV-maxima (in LSMO, LCMO, and NSMO) instate of 3 eV.
Two other possibilities are, that the authors mend the minimum at ~ 2.8 eV and called accidentally it "peak", or mend Fig. 5 instated of Fig. 2.

is connected to similar inter-atomic transfer by the authors but with anti-parallel spins. And a charge transfer from the oxygen 2p states into the e_g of a Mn^{3+} or Mn^{4+} is attributed to the 4 eV signature.

When focusing on the energy range close to the pump energy of this thesis, in 1-eV-feature is associated with a spin-parallel charge transfer either from Mn^{3+} to another Mn^{3+} (afterwards Mn^{2+}) or from a Mn^{3+} to an Mn^{4+}, which than turns into a Mn^{3+} JT-distorted ion. Even though the authors do not explicitly write that, it will be presumed in the following that they intended a direct transition from one to another Mn-ion and not a two- or more-step process. This needs to be pointed out since the aim of this thesis is to investigate the temporal-development of the dynamics; but one-, two-, or more-step processes would show different imprints on the transient spectroscopy signals. For example, the idea of the spontaneous transition from one Mn ion to another is theoretically described in the concept of electron hopping, where an electron hops from an O2p state to an Mn^{4+} ion and the O2p-hole is then free to be occupied by a second electron coming from an other Mn^{3+} ion. See section 4.1 for a more detailed description of the hopping process. This assumed authors' intention of the single step transition is derived from the fact that they assigned the charge transfer transition from O2p to e_g state of Mn^{4+}, which is necessary for the classical hopping idea, to the much higher energy of 4 eV.

Furthermore, Quijada et al. interpreted the temperature dependence of the optical conductivity at around 1 eV as follows. In the ferromagnetic phase, the 1 eV peak is found to shift to lower energies and at the same time the peak intensity increases, hence, the authors assigned this to a turning into a Drude-like behavior. When increasing the temperature and approaching the phase transition at T_C, the optical conductivity with a value of $\sigma \approx 700\ \Omega^{-1}\ c^{-1}$ gets closer to the Mott conductivity [67].

Rauer, Rübbhausen, and Dörr report on the optical conductivity and magneto-optical response of thin films LSMO and LCMO and suggest another interpretation of thermal-development of the optical conductivity data in 2006 [92]. In their optical conductivity study, they identified five spectral features changing with the temperature within the range from 0.5 - 5.5 eV for both materials. In contrast to Quijada et al. [67] they associate the interatomic

transition from the lower e_g state of one Mn^{3+} into the lower e_g state of a Mn^{4+} to the energy range of the Drude-like peak at $\hbar\omega \lesssim 1$ eV. In comparison to Yamaguchi et al. [91], the authors attributed the other Mn-interside transition, $d_i^4(e_g^1)d_j^4(e_g^1) \rightarrow d_i^3(e_g^0)d_j^5(e_g^2)$ to ~ 1.3 eV. In addition the off-diagonal elements ϵ_{xy} are measured for both materials. Unfortunately the data cut-off is around the here used pump-energy. Thus, a comparison of the findings in [92] and in [91] is not possible regarding the expected excitation transition for the experiments in the chapters 10 and 6. They assign a charge transfer transition (O2p to $e_{g,1}$) to the feature at 2.2 eV, which is not visible in [91] at all. The transition at 3.1 eV is suggested to be a low-spin state intersite transition from t_{2g} to t_{2g}.

In general, it is notable that the thin film spectra differ strongly from bulk data. However, the authors do not command on this. Possible reasons could be substrate-induced strain, a loss of oxygen or an enhancement of the surface and interface effects for thin films, but without the special expertise about these kind of thin films, it seems to be more speculation than faithful science.

Independent on the different assignments of the transitions to certain energies, the paper agree in the temperature dependent transfer of spectral weight when crossing the magnetic phase transition [67, 92, 93, 94]. As described in section 4.1.3, some hole-doped manganites, e.g., LSMO or LCMO, not just become a ferromagnet but also turn into a conducting state when decreasing the temperature below the critical temperature. The metal-like state evolves by closing the previous band gap. To achieve this, electronic states are shifted from above the former band gap close to the Fermi energy. In optical spectra, this behavior is observed as *spectral weight transfer (SWT)*.

In conclusion, three different studies on LSMO had been introduced in this section whereas three different types of transitions are suggested to be excited by photon energies around ~ 1.2 eV. The first one is a charge transfer transition (CTT) from an O2p state to an $e_{g,2}$ of an Mn^{3+} ion in the majority channel [91]. The second suggestion is, what is going to be called a photo-induced hopping (PIH) in the following, a direct transition from one $e_{g,1}$ of an Mn^{3+} into a neighboring e_g of an Mn^{4+} (turning into a Mn^{3+}) [67]. And the third idea named

literature is an intersite transition (IST) from a $e_{g,1}$ of an Mn^{3+} (turning into a Mn^{3+}) into a $e_{g,2}$ of a Mn^{3+} (turning into a Mn^{2+}) [67, 92].

4.5.2 Literature Overview of Dynamical Studies on Manganites

First studies of the ultrafast dynamical of manganites, especially LSMO, LCMO and PCMO, have been published at the beginning of the new millennium.[5]

In contrast elementary transition metal ferromagnets where no direct imprint of the magnetization dynamics in transient reflectivity data is expected [95, 96, 97], magnetism-related dynamics in manganites, e.g., spin-lattice relaxation, can be observed and investigated by measuring the transient reflectivity signal. This can be explained by the phenomenon of the *dynamical spectral weight transfer (DSWT)*. If a manganite is excited by an ultrashort laser pulse close to an ferromagnetic metallic to paramagnetic insulating phase transition, electrons near the Fermi energy are excited to states which lies above the Fermi level by approximately the amount of the pump energy [98, 99].
This DSWT is investigated by Fiebig and co-workers [99] and Lobad and co-workers [98, 100, 101] for PCMO and LCMO, respectively. For the charge-ordered, insulating antiferromagnet PCMO (0.3 - 0.5 doping) a melting of the charge ordering is found below 1 ps [99]. A light-induced insulator-to-metal transition is suggest in analogy to the known magnetic field-induced insulator-to-metal transition.
Lobad et al. quantified the DSWT in LCMO [98]. In following works [100, 101], the spin-lattice relaxation time, $\tau_{sp,la}$, of LCMO and LSMO is studied across the phase transition. A strong increase in $\tau_{sp,la}$ is observed when approaching $T \sim 0.95 \cdot T_C$. A connection of this phenomenon to the spin specific heat, C_{sp} is suggested [100, 101], where the spin specific heat in the mean field approach is proportional to $C_{sp} \propto -\partial M^2/\partial T$ [100]. Ogasawara et al. [102] demonstrated in LSMO that a similar critical slowing down is observable in the magneto-optical responds, too, where the demagnetization time increases when approaching

[5] Note, that, in many cases, the temporal pulse durations at that time were lager than the one reached in this setup. Since the measurement signal is always a folding of the dynamical responds of the sample system and the laser pulse shape, this might result in different measurement signal, particularly at the first hundreds of fs.

$T \sim 0.9 \cdot T_C$.

A connection between the dynamical spectral weight transfer and the formation and percolation of correlated Jahn-Teller polarons is suggested for LCMO by Ren and co-workers in [103] as well as a relaxation of electrons via long-living meta-stable states in the minority spin channel [104].

A contradicting explaniation for the slowing down close to the phase transition is suggested by Bielecki et a. [105]. The authors investigated LMO and LCMO thin films and analyzed the transient reflectivity data by a fit consisting four exponential functions for the dynamics in the ps to ns regime. Next to the electron-lattice interaction and the spin-lattice interaction, two of the four time constants are suggested to be assigned to thermal diffusion. In addition Bielecki et al. studied the ultrafast dynamics of both systems, LCMO and LMO, and found the insulating LMO to show much slower electron-electron interaction than metallic LCMO.

CHAPTER 5

Phase Transitions

From a material scientific point of view, phase transitions are quite interesting phenomena: more or less suddenly, a drastic change in the physical properties (regarding a certain phenomenon) occurs by continuously varying a control parameter and thereby passing through an discontinuity of the thermodynamically ground state.[1] Thereby, the continuously changed control paramaeter can be of an external nature, e.g., the environmental temperature[2], applied magnetic or electric fields, pressure etc., or it can be an internal factor such as doping.

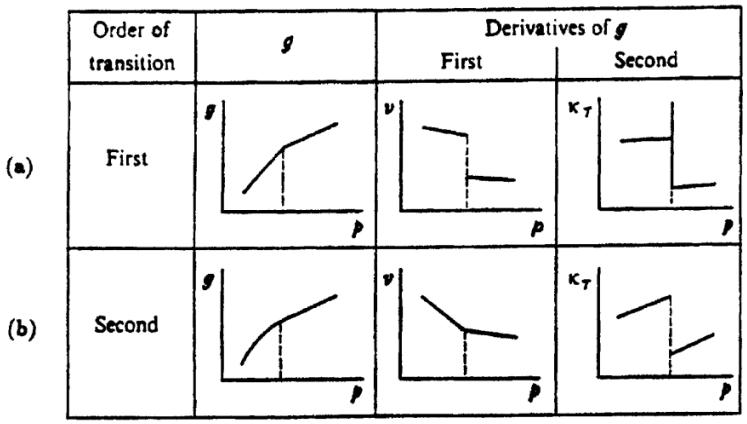

FIGURE 5.1: Scheme of Ehrenfest's classification of phase transitions by the discontinuity of derivatives of the Gibbs free energy, g, with respect to the control parameter, p. Reprinted figure with permission from [107]. Copyright (1998) by Springer-Verlag Berlin Heidelberg.

The fist classification of phase transitions (PT) is suggested by Paul Ehrenfest in 1933 [107]. This classification differentiates different kind of transitions by the question in which order

[1] The special case of a topological [15, 106] insulator is no part of the discussion in this chapter.

[2] Later in this thesis, this temperature is often called *base temperature* in the experimental chapters.

of the derivative of the Gibbs free energy with respect to the control parameter does a discontinuity appear at the phase transition. The two most common ones are depicted in fig. 5.1: (a) first-order transition and (b) second-order transition. An example for a first-order phase transition in manganites is the ferromagnetic phase transition in $La_{2/3}Ca_{1/3}MnO_3$ [108] and bulk LPCMO [8, 79]; whereas, a second-order phase transition is found for the magnetic transition in bulk LSMO [109, 110, 111].

The thermodynamically stable state is that phase which exhibits the smaller Gibbs free energy under the given environmental conditions. In the framework of classical thermodynamics, the Gibbs free energy is defined as:[3]

$$G = U + pV - TS - V\mathbf{M} \cdot \mathbf{B}_{ext} \tag{5.1}$$

which gives a total differential of without externally applied fields:

$$\mathrm{d}G = V\mathrm{d}p - S\mathrm{d}T + \sum_i \mu_i \mathrm{d}N - V\mathbf{M} \cdot \mathrm{d}\mathbf{B}_{ext}. \tag{5.2}$$

Therefore, a first-order phase transition which is introduced by a temperature change is classified by a discontinuity in the entropy, S, and a second-order PT by a discontinuity in the specific heat, C_p.

A second-order phase transitions occurs via a region of phase separation. Here, both phases exists in separated domains next to each other. In contrast, a first-order transition requires latent heat to overcome the energy barrier for entering the more disordered phase.

Investigations of relaxation times near a phase transition point found a so called *critical slowing down* [114, 115] where the relaxation times diverge when approaching the phase transition. Also in optical pump-probe experiments, such a slowing down close to the critical point is observed [102, 116]. In the framework of the Ising model, this divergence of the relaxation time is connected to a diverging specific heat.

During an ultrafast pump-probe-experiments, phase transitions might be crossed. For example the ferromagnetic/paramagnetic phase transitions is studied for different manganites [98, 102,

[3] The following relations can be found in textbooks or lecture scripts about thermodynamic, e.g., [112, 113].

104]. A structural transition [117, 118] is studied by using femtosecond electron diffraction. And also, charge- or orbital-ordering phase transitions are investigated [99, 119, 120]. All these experiments have two things in common: (i) a critical slowing down of the relaxation times are observed close to the static phase transition temperature, and (ii) that the phases, which is introduced by the excitation of an optical pump pulse, are thermodynamically stable and can be reached in static measurements as well. Since ultrafast excited dynamics are non-equilibrium dynamics, also meta-stable states can be promoted [41, 121, 122, 123]. These phase transitions are called *hidden phases* since they cannot be observed in a static measurement.

Independent on the (meta-)stability of the transient state, the phenomenological model to explain transient phase transition is that the energy difference between the Gibbs free energies of both thermodynamic states is provided by the stored energy of the pump pulse.

Part 2

Non-Equilibrium and Quasi-Equilibrium Dynamics of $\left(\mathbf{La}_{0.6}\mathbf{Pr}_{0.4}\right)_{0.7}\mathbf{Ca}_{0.3}\mathbf{MnO}_3$

CHAPTER 6

Experiments on $(\mathbf{La}_{0.6}\mathbf{Pr}_{0.4})_{0.7}\mathbf{Ca}_{0.3}\mathbf{MnO}_3$

The experiments on the LPCMO system were performed in a collaborative work. Therefore, I would like to especially thank Karen Stroh, Vitaly Bruchmann-Bamberg, Andreas Weisser, Tim Titze, and Dr. Daniel Steil for providing the measured data for this thesis.
Karen Stroh has grown the used LPCMO thin film by metalorganic aerosol deposition (MAD) including a structural analysis. She did parts of the SQUID and the CMR measurements as well as the static optical spectroscopy on the film.
The thermal conductivity was determined by Vitaly Bruchmann-Bamberg using the 3ω technique [124].
The time-resolved MOKE and transient reflectivity measurements of the data set, which are shown in this thesis, were performed by Dr. Daniel Steil, Tim Titze, and Andreas Weisser.

6.1 Growth and Static Characterization

For this part, a sample of 40% Pr-substituted $La_{0.7}Ca_{0.3}MnO_3$ was grown on a (100)-MgO substrate by MAD [57, 125]. The $(La_{0.6}Pr_{0.4})_{0.7}Ca_{0.3}MnO_3$ thin film with a thickness of $d_{psTR} = 56$ nm was divided into two parts; one was left as grown for the picosecond transient reflectivity and time-resolved magneto-optical Kerr effect measurements and the substrate of the second part was cleaved in such way that the film was suitable for measuring the static optical properties, such as transmission and reflectance.

Static characterization of the electric and magnetic properties of the sample was made by using a rf-SQUID magnetometer [126, 127] and a Physical Property Measurement System

(PPMS), both by the company *Quantum Design*.[1] Table 6.1 summarizes the basic static characteristics of the sample.

TABLE 6.1: Static characteristics of the LPCMO thin film:

Property	Sample value
Curie temperature	
@ 100 Oe	194 K
@ 1180 Oe	195 K
@ 7770 Oe	200 K
MIT temperature	
@ rest field	185 K
@ 1180 Oe	187 K
@ 7770 Oe	189 K
CMR-effect approx.	
@ 1 T	2000 %
Film thickness	56 nm

6.1.1 Static Optical Spectroscopy

The static, optical characterization is done by Karen Stroh, as well as its analysis. Nevertheless, a brief introduction to the measurements shall be given, since the data are of importance as input parameter for the FDTD simulation (see chapter 7) and for the understanding of the transient reflectivity change (see chapter 9).

For the data which are shown in this work (see fig. 9.13), the transmittance, $\mathcal{T}$, and the reflectance, $\mathcal{R}$, of the cleaved part of the sample (see above sec. 6.1) are measured in the spectral range of 200 nm - 2100 nm and are corrected by normalizing to the reference spectrum of the empty setup in order to calculate $\mathcal{A} = 1 - \mathcal{T}$. To determine the temperature dependence of the transmittance and reflectance, the sample is measured between $T = 300$ K and 100 K by using a liquid helium continuous-flow cryostat.

In addition, the absorption coefficient, $\alpha(\lambda)$, as well as the complex and real part of the

[1] The SQUID- and PPMS-measurements are performed with the non-cleaved part due to stability reasons.

reflective index $N = n + ik$ are calculated following the approaches of [128, 129, 130, 131]:

$$\alpha(\lambda) = \frac{1}{d} \cdot \ln\left(\frac{(1-\mathcal{R})^2}{2\mathcal{R}} + \sqrt{\frac{(1-\mathcal{R})^4}{4\mathcal{T}^2} + \mathcal{R}^2}\right)$$

$$n(\lambda) = \frac{1+\mathcal{R}_{as}}{1-\mathcal{R}_{as}} + \sqrt{\frac{4\mathcal{R}_{as}}{(1-\mathcal{R}_{as})^2} - k^2}$$

$$k(\lambda) = \frac{\lambda}{4\pi d} \cdot \ln\left(\frac{\mathcal{R}\cdot\mathcal{T}}{\mathcal{R}-\mathcal{R}_{as}}\right).$$

$\mathcal{R}_{as}$ corresponds to the surface reflectance of a single interface of the sample composed of plane-parallel faces. See also [9] for more details.

6.2 Thermal Conductivity by 3ω-Technique

As the reader is will see in chapter 7, the thermal conductivity of the sample is needed as T-dependent input parameter for the FDTD simulation. Therefore, Vitaly Bruchmann-Bamberg measured the thermal conductivity of the sample and determined the contribution of single parts of the sample (thin film, interface, and substrate).

Since the thin film (56 nm) is much thinner than the substrate (~ 0.5 mm), a special technique is needed to determine the thermal conductivity of the LPCMO layer. The 3ω method is based on the measurement of the third harmonics of ω in the voltage across a strip line structured on the sample [124]. The strip line, which consists of a thin metal pattern, e.g., made of gold, is utilized as heater and thermometer at the same time by simply choosing a four-point measurement geometry: An oscillating current (ω) is sent through the line which results in a Joule heating of the frequency 2ω. A part of the heat energy dissipates by the thermal transport through the sample. The consequence is a thermal conductivity-dependent temperature oscillation, $\Delta T(\omega, D_{sub}, \kappa_{sub}, \kappa_{film})$, which is proportional to the voltage measured at 3ω.

In the case of a conducting thin films, e.g., LPCMO below T_{MI}, the measurement technique needs to be extended by an insulating interlayer between the metallic strip line and the conducting sample. In the current case, an interlayer of 80 nm amorphous Al_2O_3 is grown between the LPCMO thin film and the (200 nm)Au-(5 nm)Cr strip line of 10 µm width. In

order to filter out the contribution by this interlayer, an amorphous Al_2O_3 layer on a substrate is measured individually and is subtracted from the measurement of the LPCMO film with the same insulating capping.

6.3 Ultrafast Optical Spectroscopy

The transient reflectivity at the timescale ranging from several fs till ~ 1.1 ns (psTR) as well as the time-resolved magneto-optical Kerr effect (TRMOKE) have been investigated using the setup which is sketched in fig. A.1. It is an optical pump-probe experiment with a fs-pulsed fiber amplifier by *Active Fiber Systems*, which is operated at a repetition rate of f =50 kHz. The fundamental beam with a central wavelength of $\lambda_{pump} = 1030$ nm (1.2 eV) is used as pump and the probe beam provides a central wavelength of $\lambda_{pump} = 515$ nm (2.4 eV), which corresponds to the second harmonic. The setup is explained in the appendix A1 in more detail. This section focuses on the measurement geometry.

In contrast to the common MOKE-geometries (longitudinal, polar, transverse), the easy-axis of the sample is oriented here with a 45°-angle with respect to both the external magnetic field and the incoming light; neither parallel nor perpendicular. This geometry idea has two reasons: First, according to the tilt with respect to the externally applied magnetic field, it should be possible to excite and see magnons in general. Of course, whether it is possible in a particular case, depends on many different factors, e.g., whether the scattering and boundary conditions are full-filled, a sufficient fluence and far more. Secondly, in this geometry, a narrower gap of the electromagnet compared to the longitudinal case yields a higher magnetic field; up to almost 800 mT.

The temperature has been scanned between $T = 100 - 300$ K by a ^{4}He cryostat in between the gap to measure the dynamical changes close to the phase transition. Three different warming cycles are measured, where three different external magnetic field are applied: $B_1 \approx 120$ mT, $B_2 \approx 780$ mT and a zero field warming (ZFW) cycle. During the cooling in between the single series, no magnetic field is applied. Furthermore, two magnetic field-dependent

series are performed at $T_1 = 195$ K and $T_2 = 200$ K. For all five series, the incident light has a fluence of $F \approx 5.9$ mJ/cm^2. Finally, the pump-fluence is varied at fixed $T = 200$ K and $B = 780$ mT. This series is measured last in order to prevent damage of the sample. Unfortunately, it seems that a cryostat window was burned during the fluence series; most likely the damage happened at $F \approx 7$ mJ/cm^2.

CHAPTER 7

FDTD-Simulation

As the reader sees in chapter 8 among other things, a strong slowing down of the relaxation process is found in the ferromagnetic phase in comparison to the intermediate AFM and insulating PM phase of LPCMO. One can imagine three different scenarios, which might lead to this effect:

(1) A phenomenon, which is part of every relaxation process after an ultrashort excitation, is the thermal diffusion, where the energy, which is deposited in the thin film during the pump-process, diffuses out of the probed area via thermal transport. The process of the thermal diffusion is strongly dependent on the thermal conductivity of the different parts of the sample system as well as on the interfacial thermal resistance, the so-called *Kapitza resistance* . Thus, a phase transition inside one part of the sample, e.g., the thin film, might lead to a strong change in the thermal transport of the whole sample system. And therefore, might lead to a slowing down if the thermal transport is decreased across the PT. Bielecki and co-workers [105] discuss for LMO and LCMO that the thermal diffusion is a part of the long term relaxation time and investigated it under the viewpoint of different probe-energies deep in the magnetic phases: antiferromagnetic (LMO) and ferromagnetic (LCMO).

(2) It is known [8, 57] that the ferromagnetic-paramagnetic phase transition in manganites are often mediated by the appearance of polarons. In the case of LPCMO thin films, it has been shown that the FMM phase transforms into the high-temperature paramagnetic phase by passing though an intermediate phase separation state where FMM domains are coupled antiferromagnetically by an insulating quasi-particle matrix of correlated Jahn-Teller polarons [8, 57]. Therefore, a second scenario might be that the long-time dynamic is somehow connected to a transient disappearance (and later recovery) or a photo-induced creation (and later disappearance) of these quasi-particles, the correlated JT polarons.

(3) A third possible explanation might be a phenomenon, which is quite well known in the context of phase transitions: the *critical slowing down (CSD)*. Many known phase transitions, e.g., magnetic or structural transitions, are connected to a change in the ordering of the system, e.g., the spin order or the arrangement of the atoms. When thinking of a system, which is cooled down, the change in the order is strong when approaching the phase transition. For example, when crossing from the non-ordered state of a PM into the highly ordered state of a FM, the spin system needs to undergo strong ordering even for only small temperature changes. A FM-to-PM phase transition might be introduced by the energy of a pump-pulse in a pump-probe experiment. When the pump-pulse hits the sample close to the phase transition, but still in the FM phase, a part of the stored energy dissipates into the spin system and might lead to a total demagnetization of the sample; than the sample is in a PM state during a "short" period of time within the experiment. To relax back into the FM ground state, the destroyed spin order needs to be rearranged during the remagnetization process. The restoring potential for this step is the lower the closer the base temperature is to the phase transition temperature, thus, the remagnetization process becomes quite slow when the base temperature approaches the phase transition. The phenomenon of a critical slowing down[114, 115] is observed.

Of course, the question is now, which of the three options are observed in the LPCMO thin films (see sec. 9.5). Thus, a model to estimate possible contributions is needed. Regarding the first option, a strong change in the thermal diffusion caused by the PT, an estimating model is set up by implementing a finite-difference time-domain (FDTD) simulation [9, 120, 132]. After the temperature change of the phonon system is calculate by using the simulation, the transient reflectivity is calculated and finally, the relaxation time of the modeled reflectivity signal is fitted by a single exponential function. In a second step, the same model is slightly modified by taking the temperature change of the spin system into account in order to assess the impact of the remagnetization process on the relaxation time.

The FDTD simulation was implemented and performed by Dr. Henning Ulrichs and Tim Titze. It simulates the energy dissipation paths in one dimension based on a modified 3 temperature model (3TM) [9], which considers the experimental results of temperature dependent absorption coefficients and thermal conductivity as well as an estimated specific

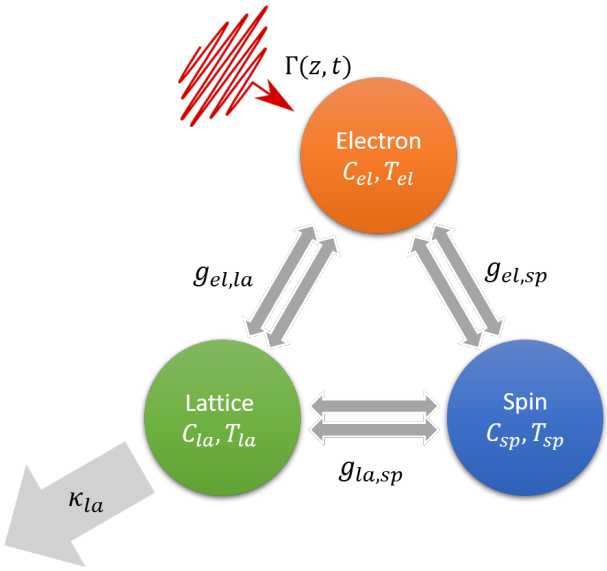

FIGURE 7.1: Sketch of the 3TM used in the FDTD simulation for LPCMO: Devition of the sample system into three subsystems - electron, phonon, and spin, which are capable of exchanging energy and momentum. The assumption that the electronic subsystem is excited only by the initial pump-pulse in the visible/NIR range is included and indicated by the red arrow in the left corner. The final energy dissipation by thermal conductivity of the lattice, κ_{la}, is visualized by the light grey arrow.

heat of LPCMO and MgO based on literature. The latter is going to be explained in more detail later. But, let's start with the three temperature model which is sketched in fig. 7.1 for LPCMO. Following the idea of [27, 28], the material system is divided into three heat baths, electron (el), lattice (la), and spin (sp). An individual specific heat, C_i, is assigned to each of them. These three subsystems are coupled to each other by individual coupling constants, $g_{i,j}$, which allows an energy transfer between the individual subsystems. Since energy is equivalent to a certain temperature in the case of equilibrium, it is assumed that an individual temperature can be assigned to each of the subsystems, which are equal to each other in the equilibrium case. If energy is transferred in one subsystem only, as it can be assumed for ultrashort excitations in the optical regime, as it is done in the experimental part of this thesis, where in a good approximation the energy is absorbed by the electrons only, then a non-equilibrium situation between these three subsystems is created. By the implementation of the subsystem temperatures, T_{el}, T_{la}, and T_{sp}, a differential equation system for one spatial dimension, z is perpendicular to the sample surface, can be set up to calculate the temporal

evolution of the single subsystem temperatures:

$$\rho C_{el}\frac{\partial T_{el}}{\partial t} = \kappa_{el}\frac{\partial^2 T_{el}}{\partial z^2} - g_{el,la}(T_{el} - T_{la}) - g_{el,sp}(T_{el} - T_{sp}) + \Gamma(z,t), \tag{7.1}$$

$$\rho C_{la}\frac{\partial T_{la}}{\partial t} = \kappa_{la}\frac{\partial^2 T_{la}}{\partial z^2} + g_{el,la}(T_{el} - T_{la}) - g_{la,sp}(T_{la} - T_{sp}), \tag{7.2}$$

$$\rho C_{sp}\frac{\partial T_{sp}}{\partial t} = \kappa_{sp}\frac{\partial^2 T_{sp}}{\partial z^2} + g_{el,sp}(T_{el} - T_{sp}) + g_{la,sp}(T_{la} - T_{sp}). \tag{7.3}$$

A summarizing legend of the formula symbols is given in table 7.1.

TABLE 7.1: Legend of the 3TM-parameters:

Symbol	Physical property
ρ	mass density
$C_i(T)$	specific heat of the subsystem i
$T_i(t,z)$	current temperature of the subsystem i
t	delay time
$\kappa_i(T)$	thermal conductivity of the subsystem i
z	spacial dimension perpendicular to the sample surface
$g_{i,j}$	coupling constant between the subsystems i and j
$\Gamma(z,t)$	laser absorption

The thermal transport of each subsystem can be taken into account by the individual thermal conductivity values, κ_i. But, within the performed FDTD-simulations, $\kappa_{sp} = \kappa_{el} = 0$ is assumed. Instead, the experimental values of κ, which are measured by Vitaly Bruchmann-Bamberg using a 3ω-technique [9, 124], are used as a temperature-dependent input parameter for κ_{la}. The values of the thermal conductivity for MgO are taken from [133]. Since, the thermal transport is influenced by the symmetry break at the interface between LPCMO and Mgo, a finite Kapitza interfacial conductance of $G = 2 \cdot 10^{10}$ W/m^{2}K is considered. This jump is numerically implemented following the method in [134]. As mass density, the values of $\rho_{\text{LPCMO}} = 6.198$ g/cm^3 for the LPCMO film and $\rho_{\text{MgO}} = 3.58$ g/cm^3 [83] for the MgO substrate are used. In the study [135], a spin-lattice coupling constant of $La_{0.7}Ca_{0.3}MnO_3$ $g_{la,sp} = 2.5 \cdot 10^{15}$ W/m^{3}K is found. This value as well as $g_{el,la} = 1.5 \cdot 10^{18}$ W/m^{3}K is assumed in the FDTD model for the LPCMO thin film. It is not expected that these values do perfectly match the actual LPCMO values, since the Pr-doping obviously changes the lattice and therefore the properties which are connected to the lattice. But, the value of $La_{0.7}Sr_{0.3}MnO_3$ is found to be of the same order with $g_{la,sp;LSMO} = 5 \cdot 10^{15}$ W/m^{3}K [135], thus, it seems to

be a suitable assumption. The model parameters, ρ and $g_{i,j}$, are assumed to be constant in temperature.

In contrast, the specific heat cannot be considered as independent of the temperature. Especially, close to the Curie temperature, significant changes are expected in C_{sp}. But also, the specific heats of the electron and phonon systems change with the temperature even in simplified models: $C_{el} \propto \gamma T$ (Sommerfeld theory) and $C_{la} \propto \left(\frac{T}{\theta}\right)^3$ (Debye low temperature approximation). Unfortunately, no experimental data are available for the spin specific heat of the LPCMO thin film, which is measured here. But, it is possible to utilize the FDTD simulation for calculations, which are based on two differently estimated model of the spin specific heat, in order to assess the changes of the relaxation time, which depend on the spin specific heat changes: (i) the values of bulk LPCMO [136, 137]; and (ii) the literature values of LCMO [138], which are shifted by the difference between the Curie temperatures of the LCMO and the one of LPCMO. Both used data sets are depicted in fig. 7.2 (d) and (e), respectively. The T-dependence of specific heat of MgO, as shown in fig. 7.2 (b) is build from the data of [133] and [139].

In order to take the penetration depth as well as multiple internal reflection at the interface and surface of the LPCMO film into account for the laser absorption, $\Gamma(z,t)$, the optical parameter of the LPCMO, MgO, and vacuum are considered by the usage of an optical transfer matrix formalism [140]. The needed reflective index of the used LPCMO film is calculated from the static, optical spectroscopy measurements by Karen Stroh. The reflective index of MgO is taken from [141].

After the temporal evolutions of the subsystem temperatures, especially T_{la}, are calculated by the previously mentioned model, the time-dependent longitudinal strain is simulated by solving a one-dimensional elastic wave equation. A stress-free surface and the assumption of no back-reflection at the backside of the sample, $z = d_{LPCMO} + d_{MgO}$, determine the boundary conditions.

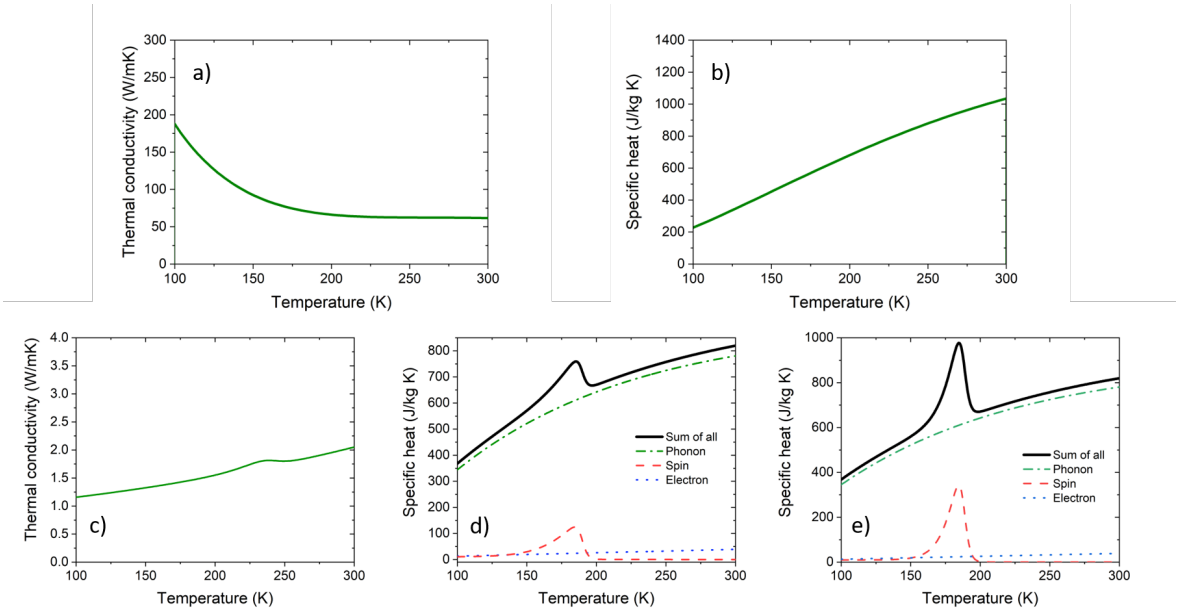

FIGURE 7.2: Teperature-dependent input parameters of the FDTD simulations: The upper row represents the parameters for MgO - (**a**) thermal conductivity and (**b**) specific heat. The lower row shows the parameters for LPCMO - (**c**) thermal conductivity and the two options for the specific heat (**d**) values of the buld LPCMO [136, 137], and (**e**) the values of LCMO [138], which are shifted in temperature to the LPCMO transition temperature.

CHAPTER 8

Results - $(La_{0.6}Pr_{0.4})_{0.7}Ca_{0.3}MnO_3$

8.1 Transient Reflectivity of $(La_{0.6}Pr_{0.4})_{0.7}Ca_{0.3}MnO_3$

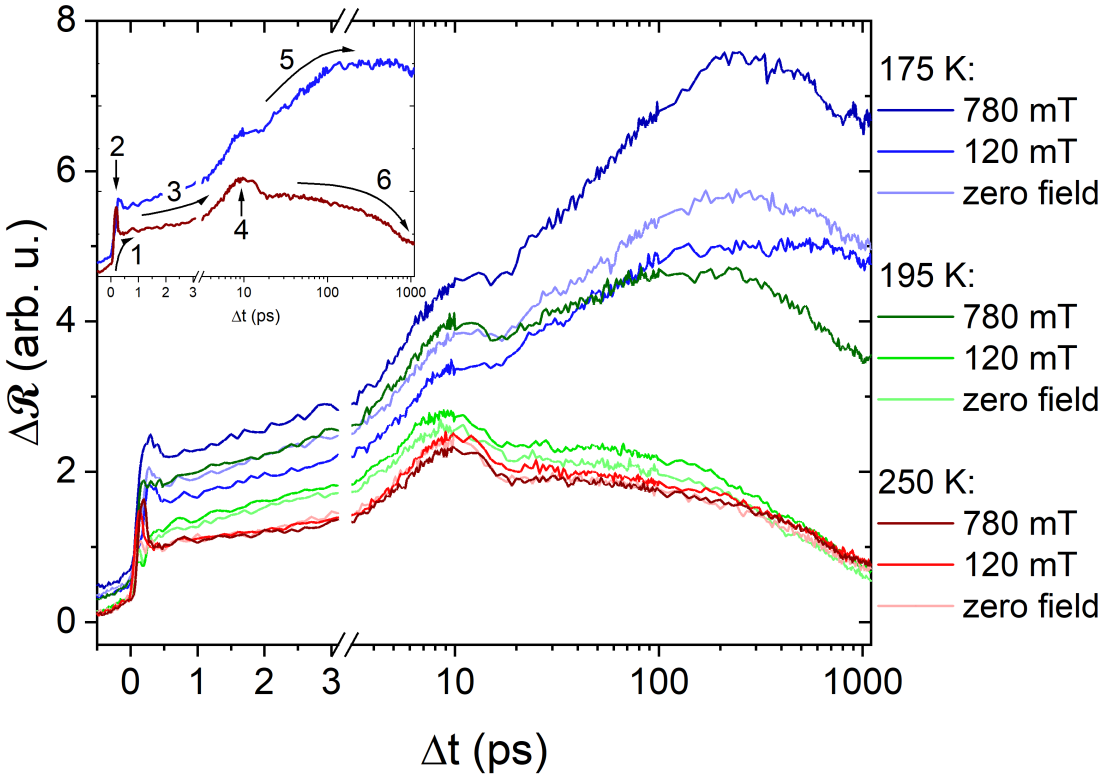

FIGURE 8.1: Exemplary traces of the psTR signal for three temperatures: 175 K (blue), 195 K (green), and 250 K (red). The data are part of three warming cycles measured at the externally applied fields: 780 mT (shades), 120 mT (hues), and zero field (tints). In the inset, the features are marked, which are discussed in the text below. All data are measured at an incident fluence of $F \approx 5.9$ mJ/cm^2.

As described in chapter 6, three different measurement series has been performed: T-, F-, and B-dependent while the other two parameters were kept constant. The figure 8.1 shows a selected set of psTR data measured on a LPCMO thin film[1]. To give an example of the overall emerging features, which are introduced in this section, data traces for the ferromagnetic phase (blue), close to the phase transition (green), and for the PM phase (red) have been chosen from the temperature dependent series in the inset of figure 8.1. All temperatures are studied under three different magnetic field conditions $B_1 \approx 0$ mT, $B_2 \approx 120$ mT, and $B_3 \approx 780$ mT within three warming cycles. The incident fluence for all measurements of these cycles was kept at $F \approx 5.9$ mJ/cm^2.

Two curves are selected for the inset of fig. 8.1 to show the overall representative behavior well above and well below T_C. Here, 6 features in the psTR data are identified, which are going to be introduced in this chapter, and will be discussed in the chapter 9:

(1) initial increase due to the fs-laser excitation
(2) oscillations at the first hundreds of femtoseconds
(3) further increase of the reflectivity change on a-few-ps-timescale
(4) peak-like structure at $\Delta t \approx 8.5$ ps
(5) third increase in the reflectivity change at the timescale of a couple of tens pico-seconds
(6) decrease of the signal.

A phenomenological fit has been developed to describe five of these six features and shall be presented in the following:

$$\Delta\Re = G \cdot exp(-(t - t_P)^2/2 \cdot \omega) - \sum_{i=1}^{4} A_i \cdot exp(-\Delta t/\tau_i). \tag{8.1}$$

The parts marked by the numbers **1, 3, 5** and **6** in the inset of 8.1 are represented by the sum of the four exponential functions. Since **1, 3, 5** always show a positive slope and **6** always represents a relaxing behavior, the amplitudes are constrained to $A_{1,2,3} \geq 0$ and $A_4 < 0$. Furthermore, the relaxation process has been limited to $\tau_4 < 2 \cdot 10^7$ ps, since the

[1]The entire set of data are shown in appendix B1.

laser repetition rate has been kept at 50 kHz and no hints for a non-recovery behavior within that time has been found in the data. The results will be outlined in section 8.1.1 for the two lower timescales, in section 8.1.3 for the feature No. 5, and section 8.1.4 describe the results of the relaxing process, τ_4.

The Gaussian peak function is chosen to describe the local maximum, feature No. 4. In the section 8.1.2.1, it will be shown that - most likely - this feature is not a single peak but a strongly damped oscillation. Hints for an oscillating behavior might be visible in some data, e.g., at $T = 175$ K and $B = 780$ mT, where it seems that a sparse oscillation might be visible after the initial peak. In case that this is true, a damped, sinusoidal function would be a more appropriate description. Unfortunately, due to that extremely fast vanishing of the oscillation, it was not possible to fit an equation like 8.1, where the Gaussian peak is replaced by a damped, sinusoidal function. Notwithstanding, the results of the Gaussian peak fit are discussed in section 9.3.

As starting point, we will begin with the sub-ps and low-ps timescale, which are marked by the numbers 1 and 3 in the inset of fig. 8.1; within the equation 8.1 they are represented by the first and second exponential functions with the free fit parameters of the amplitudes A_1 and A_2 as well as the time constants τ_1 and τ_2.

8.1.1 Initial and Secondary Increase in Reflectivity Change

In this subsection, the fitting results of the first two exponential functions of equation 8.1 and the dependence of the fit parameters on temperature (fig. 8.2), magnet field (fig. 8.3) and fluence (fig. 8.4) will be presented.

8.1.1.1 Temperature Dependence of A_1, A_2, τ_1, and τ_2

Starting with the evolution with the increasing base temperature, within all parameters and each here externally applied magnetic fields, a more or less dramatic change close to the Curie temperature is visible in figures 8.2 a - d.

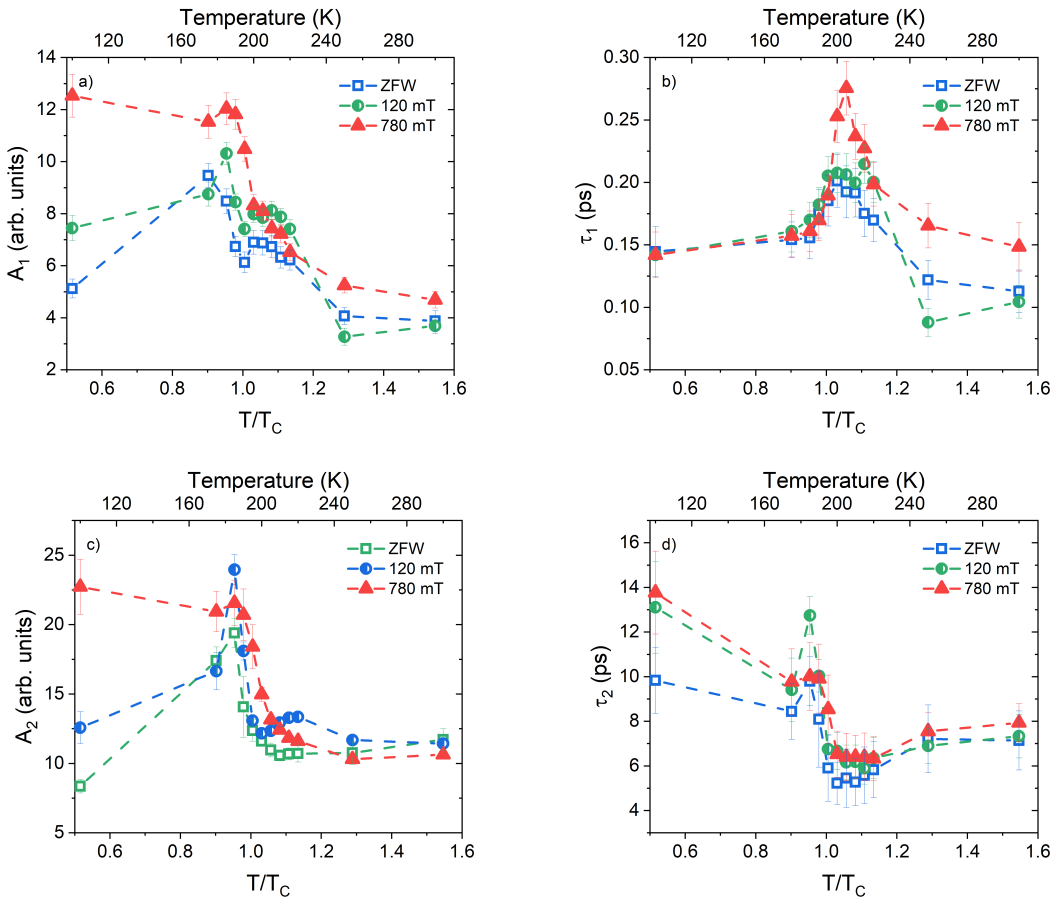

FIGURE 8.2: Fit results of the first and the second increase in $\Delta\mathcal{R}$ for three different warming cycles: blue, open squares - Zero field; green, half-filled circles - $B = 120$ mT; red, filled triangles - $B = 780$ mT. The amplitude, A_1, and the time constant, τ_1, plotted in (**a**) and (**b**); the second amplitude and timeconstand, A_2 and τ_2, in (**c**) and (**d**). The errors are calculated from the fit. The color-matched dotted lines as guide to the eye.

Both amplitudes (A_1 in fig. 8.2 (a) and A_2 in fig. 8.2 (c)) drop at the PT for all fields turning from the FMM into the PMI phase. This drop seems to shift with increasing magnetic field by $\Delta T \approx 10$ K. For the high-temperature range, the amplitudes for the different external fields seems to converge to at least a similar value. The low-temperature behavior remains predominantly unclear since there is only one measurement point (at $T = 100$ K) available for each field. Nevertheless, an increase of both amplitudes with the field in the low temperature regime appears to be notable and would be consistent with field-dependent measurements at $T = 195$ K, see fig. 8.3 (a) and 8.3 (c).

The time constant, τ_1, which is plotted in 8.2 (b), exhibits three different regions within the measured temperature range (when increasing the temperature): (i) a slight increase or almost constant value for the ferromagnetic metallic phase; (ii) a peak structure across the PT which decreases in the AFM insulatiing state; and finally (iii) a slight decreasing behavior for the PM insulating phase. It is remarkable that in the FMM phase, no differences are found for different external magnetic field values; whereas, at the PT and above, the τ_1 process is slower for higher magnetic fields. This behavior includes an asymmetric broadening of the peak structure across the PT. also the peak height is raised by the magnetic field.
The overall temperature-dependent trend of τ_2 in fig. 8.2 (d) is decreasing. In detail, a decreasing behavior for the FM phase, a small peak right before the PT, and a minimum right after the PT, as well as a more or less constant response in the PM are found when increasing the base temperature. The dependence on the external magnetic fields is quite small, but still, a slight upward shift is present by applying a field.

8.1.1.2 Magnetic Field Dependence of A_1, A_2, τ_1, and τ_2

The external magnetic field dependence of the psTR was measured for two different temperatures, $T_1 = 195$ K and $T_2 = 200$ K. The results for the first and second exponential functions of the fit 8.1 are plotted in the figures 8.3 (a) - (d).
Prima facie, A_1 shows inverse behavior for the single temperatures: at T_1, A_1 increases almost perfectly linearly with the field, whereas the behavior at T_2 suggests a over-all downward-trend. But looking into the details of the second trace, a more complex, curved shape might be a possible interpretation, where a decrease for lower fields is found and, after a turning point at about ~ 600 mT, A_1 starts to rise again. As a result, the variation of A_1-values at T_2 is relatively weak, whereas A_1 doubles its intensity at $T_1 = 195$ K meanwhile.
In contrast, A_2 grows, more or less linearly, with the applied field and show a comparable slope for both temperatures. The greatest difference between both curves seems to be the amplitude off-set for no external field.

Turning to the description of the B-field dependence of the time constants, τ_1 and τ_2, similar

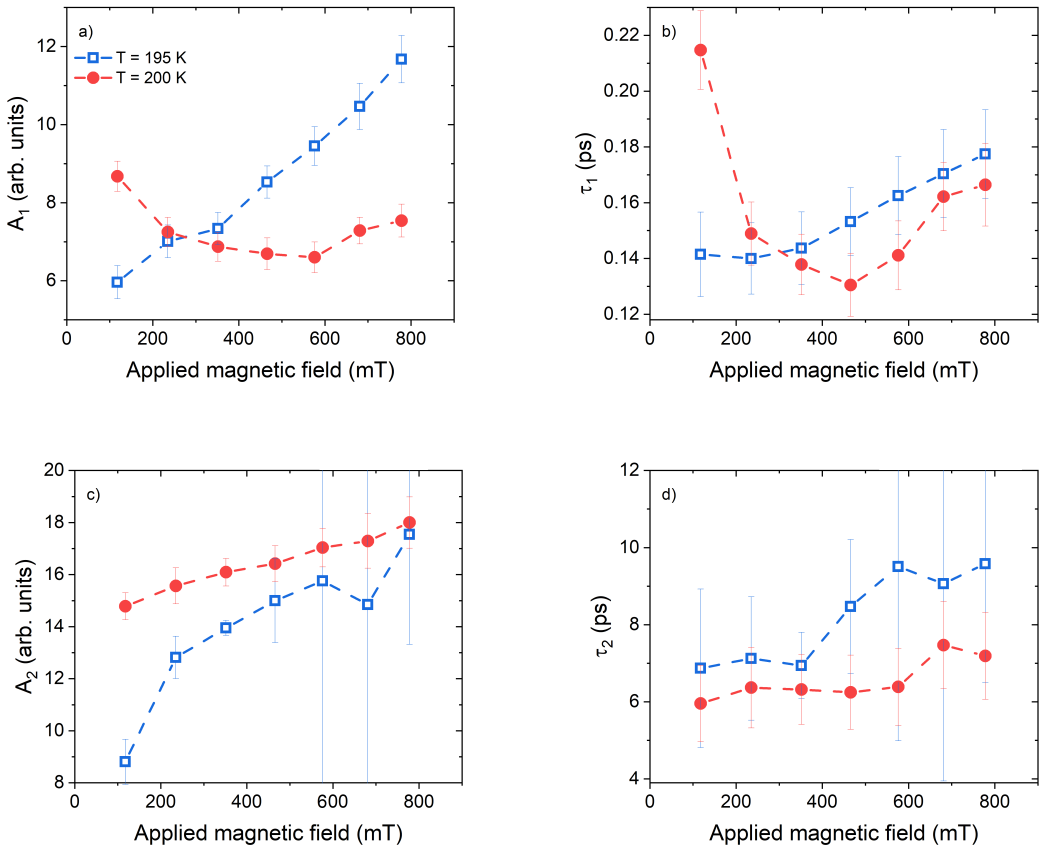

FIGURE 8.3: Fit results of the first and the second increase in $\Delta\mathcal{R}$ depending on the externally applied magnetic field for two temperatures close to the Curie temperature: blue, filled squares - $T = 195$ K; red, open circles - $T = 200$ K. The amplitude, A_1 and the time constant τ_1 plotted in (**a**) and (**b**); the second amplitude and timeconstand, A_2 and τ_2 in (**c**) and (**d**). The color-matched dotted lines as guide to the eye. Note that the from the fit calculated errors for the amplitudes are not plotted since the they are orders of magnitudes higher than the fitted values. The errors for the time constants are calculated from the fit.

but not the same behavior is found. τ_1 at T_1 shows a linear trend for higher fields to slow down, but a deviation from this trend for lower fields. For T_2, the curvature is more pronounced and the turning point is shifted downwards to ~ 450 mT, compared to the A_1-behavior.
Within the error bars, the τ_2-process slows down linearly at both temperatures, but with an higher offset for $T_1 = 195$ K. Unfortunately, the relative error, especially for $T_1 = 195$ K, is quite high. Hence, these curve shapes should be viewed with caution.

8.1.1.3 Fluence Dependence of A_1, A_2, τ_1, and τ_2

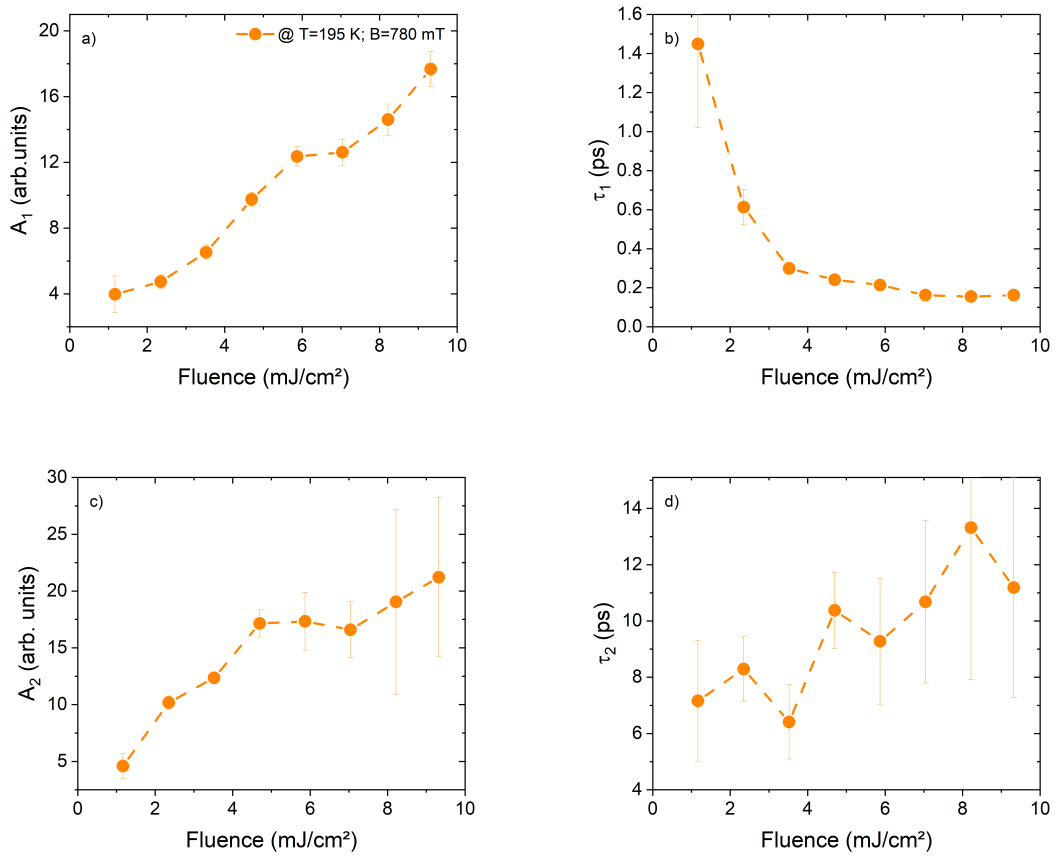

FIGURE 8.4: Fit results of the first and the second increase in $\Delta\mathcal{R}$ depending on the incident pump fluence at $T = 195$ K $\approx T_C$ and $B = 780$ mT. The amplitude, A_1 and the time constant τ_1 plotted in (**a**) and (**b**); the second amplitude and time constant, A_2 and τ_2 in (**c**) and (**d**). Dotted lines as guide to the eye. Note that the errors calculated from the fit for the amplitudes are not plotted since the they are orders of magnitudes higher than the fitted values. The errors for the time constants are calculated from the fit.

The fit results of A_1, A_2 and τ_1, τ_2 for the fluence-dependent measurement series are plotted in fig. 8.4 (a) - (d).

When having a look at fig. 8.4 (a), the first amplitude, A_1, increases by raising the fluence. It is unfortunately possible that the cryostat window was damaged during the high-fluence measurement. This might be seen in the data, where a dip is observed at $F \approx 7$ mJ/cm^2.[2] Unfortunately, due to this dip, it is not possible to say whether the overall behavior tends to

[2]This dip recurs in A_2 (fig. 8.4 (c)) and A_4 (8.13 (b)).

be a linear increase or a parabola.
The first process speeds up for higher fluence and seems to approach a value of about $\tau_{1,\text{off-set}} \approx 0.15$ ps, as shown in 8.4 (b). Decreasing the fluence, a drastic slowing down is found.

Turning to the second exponential increase, an upwards trend for A_2 is visible in fig. 8.4 (c) by a stronger pump of the system. Again, a dip at $F \approx 7$ mJ/cm^2 is visible.
The time constant, τ_2, rises linearly within the error bars in fig. 8.4 (d). The range of τ_2 is of about 6 to 14 ps within the measurement range.

8.1.2 Peak-Like Structure at $\Delta t \approx 8.5$ ps

Before starting the presentation of the fit results of the peak-like-structure at $\Delta T \approx 8.5$ ps for different external stimuli, an additional analyses step will be explained in the following:
Later, in chapter 9, the peak-like structure is assigned to Brillouin scattering, also known as coherent acoustic phonon excitation, inside the LPCMO layer. When thinking about the changes of energy dissipation channels, which is the topic of this thesis, the relative intensity of the lattice dynamics with respect to the electron dynamics is of interest; because, this gives a hint how much energy is transferred into the shock wave, which is imposed to the system by the sudden heating up due to the ultrashort laser pulse. Thus, next to the fitted intensity, G, of the peak-like structure, the relative height of this feature is plotted in the following sections, too. Thereby, the relative intensity is calculated by $G_{rel} = G/A_4$, which is a measure of the total height of the psTR data trace since the fourth exponential function is the only relaxing function in the fit eq. 8.1.

8.1.2.1 Temperature Dependence of the Peak-Like Structure

In fig. 8.5 (a), the position of the described peak maximum is found to slightly increase for higher temperatures. But, within the spreading of the data points, no clear shape is identifiable. The appearance time of this feature ranges from ~ 8 ps to ~ 9.7 ps.

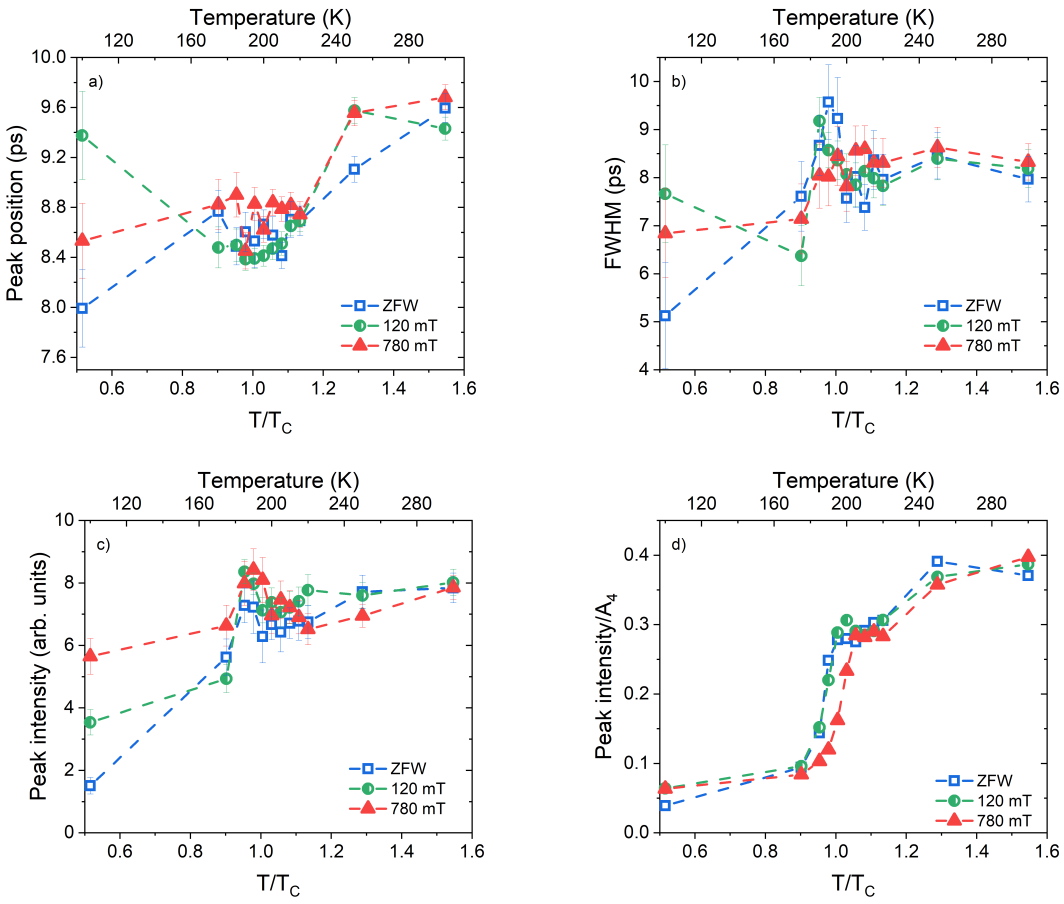

FIGURE 8.5: Fit results of the peak-like structure in $\Delta\mathcal{R}$ for three different warming cycles: blue, open squares - Zero field; green, half-filled circles - $B = 120$ mT; red, filled triangles - $B = 780$ mT. The peak position is plotted in (**a**) and the full width at half maximum in (**b**) and the intensity in (**c**). The errors are calculated from the fit. The relative peak height with respect to the fourth amplitude, G/A_4, is plotted in (**d**). The color-matched dotted lines as guide to the eye.

The full width at half maximum (FWHM) is plotted in fig. 8.5 (b), where a temperature-dependent shift is observed towards longer times as an overall trend. At low temperature, the points for the three different magnetic fields spread quite strongly, whereas the data point deep in the PM phase almost overlap. At the phase transition, a peak appears in the ZFW measurement, which seems to be reduced by applying an magnetic field.

The peak height, which is plotted in fig. 8.5 (c), shows a rising behavior when the temperature is increased. Again, a peak at the phase transition is found. But this time, it grows in height when applying a magnetic field in addition to a shift towards higher temperatures. Deep in

the PM phase, the magnetic field dependence seems to disappear and all three curves seems to approach the same value for the same base temperature.

Finally, the relative height, G/A_4, is presented in fig. 8.5 (d). For all three warming cycles, a tripartite behavior is found, what seems to correlate with the three different magnetic ground states of the LPCMO: (i) a very low - almost vanishing - percentage with respect to the total transient reflectivity signal in the ferromagnetic metallic phase is observed. This is followed by a drastic increase of the relative signal importance at the PT and (ii) a plateau within the intermediate AFM phase. And finally, a last step, (iii), is reached within the paramagnetic insulating phase, where the peak-like structure reaches almost 40 % of the total psTR signal height. Within each state [(i) - (iii)], the values of the percentage are independent on the magnetic field, but the steps from one into another step shift toward higher temperature when increasing the magnetic field, like the magnetic states do, too.

8.1.2.2 Magnetic Field Dependence of the Peak-Like Structure

Turning to the magnetic field dependence at $T_1 = 195$ K and $T_2 = 200$ K, both the peak position (see fig. 8.6 (a)) and the FWHM (see fig. 8.6 (b)) are found to be independent on the field with in the SNR.

The peak intensity, G, as well as the relative height, G/A_4, show only a sight field dependence at $T_2 = 200$ K. Whereas the reactions of the amplitude and relative height become more pronounced for the lower temperature $T_1 = 195$ K. The importance of the peak-like structure is reduced when the system is forced into the ferromagnetic metallic phase by the external magnetic field.

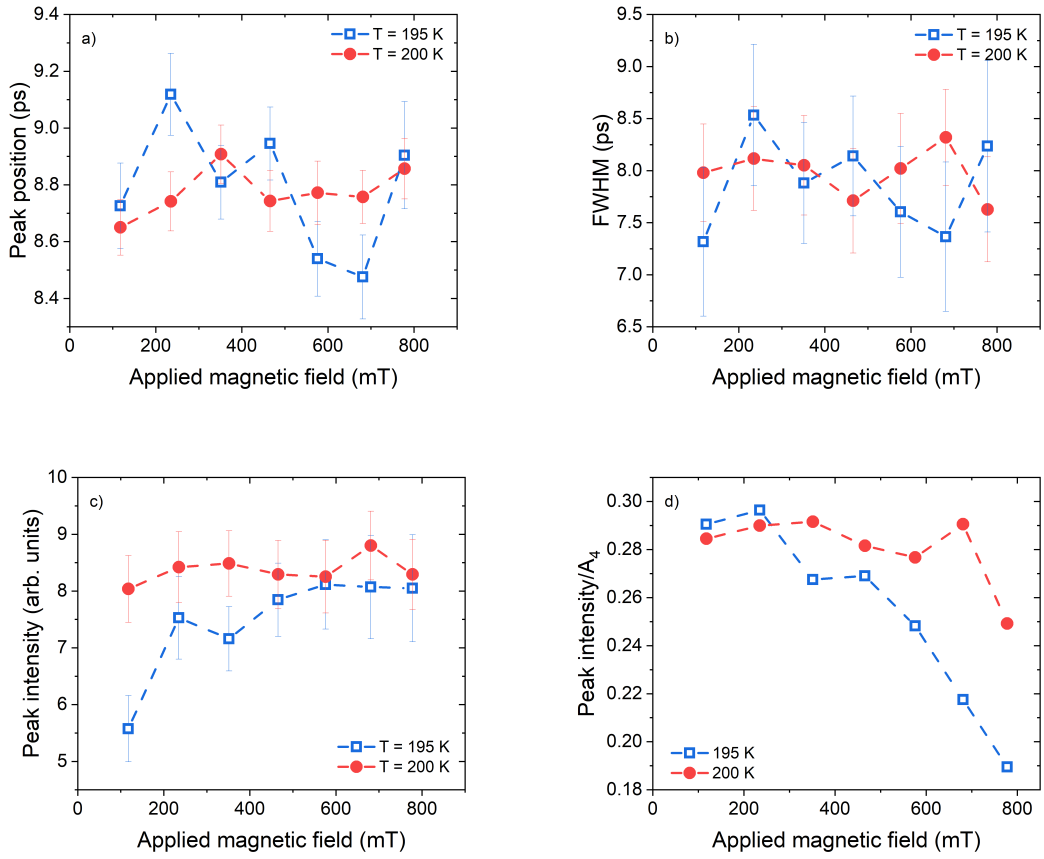

FIGURE 8.6: Fit results of the peak-like structure in $\Delta\mathcal{R}$ depending on the externally applied magnetic field for two temperatures close to the Curie temperature: blue, filled squares - $T = 195$ K; red, open circles - $T = 200$ K. The peak position is plotted in (**a**) and the full width at half maximum in (**b**) and the intensity in (**c**). The errors are calculated from the fit. The relative peak height with respect to the fourth amplitude, G/A_4, is plotted in (**d**). The color-matched dotted lines as guide to the eye.

8.1.2.3 Fluence Dependence of the Peak-Like Structure

The dependency of the peak-like structure on the incident fluence is depicted in fig. 8.7 (a) -(d). The central peak position (fig. 8.7 (a)) as well as the FWHM (fig. 8.7 (b)) shift to smaller times when increasing the pump fluence.[3]

The peak intensity, G, increases linearly by the incident fluence in fig. 8.7 (c). Again, a dip might appears at $F \approx 7$ mJ/cm^2, which is believed to be an imprint of a cryostat window

[3]Note, that the data point for the lowest fluence is believed to be underestimated due to the low intensity at this fluence.

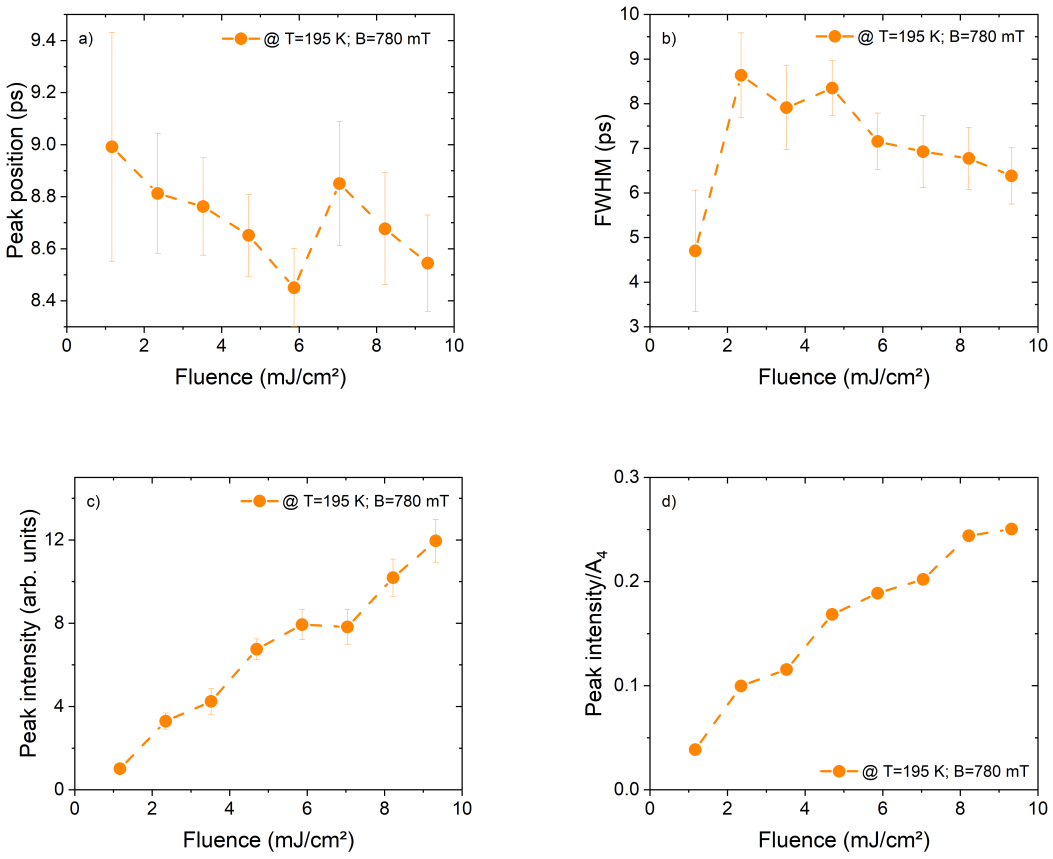

FIGURE 8.7: Fit results of the first and the second increase in $\Delta\mathcal{R}$ depending on the incident pump fluence at $T = 195$ K $\approx T_C$ and $B = 780$ mT. The peak position is plotted in (**a**) and the full width at half maximum in (**b**) and the intensity in (**c**). The errors are calculated from the fit. The relative peak height with respect to the fourth amplitude, G/A_4, is plotted in (**d**). The color-matched dotted lines as guide to the eye.

damage.

Interestingly, the importance of the feature with respect to the whole psTR signal increases when the incident fluence is raised, see fig. 8.7 (d). This finding suggest an origin of this feature which is connected to the heating of the electronic system by the pump process and less influenced by other energy dissipation channels.

8.1.3 Third Increase in Reflectivity Change

8.1.3.1 Temperature Dependence of A_3 and τ_3

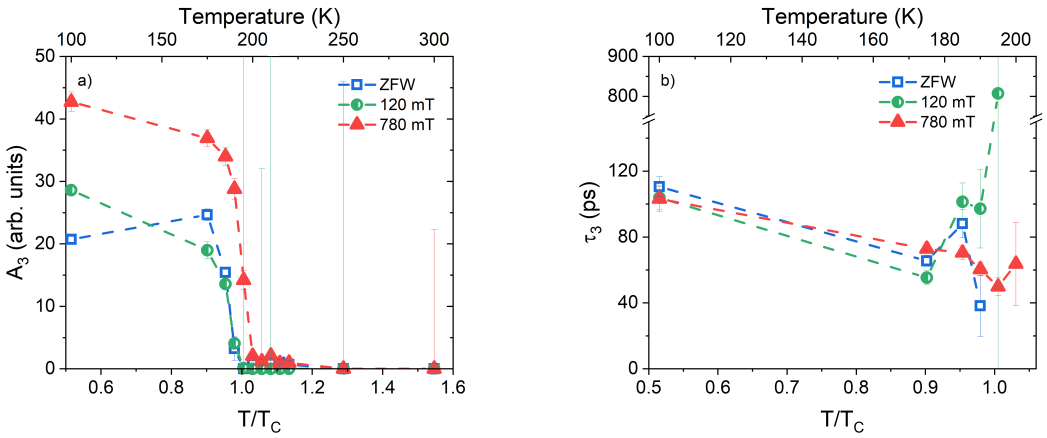

FIGURE 8.8: Fit results of the third increase in $\Delta\mathcal{R}$ for three different warming cycles: blue, open squares - Zero field; green, half-filled circles - $B = 120$ mT; red, filled triangles - $B = 780$ mT. (**a**) the amplitude, A_3 and (**b**) the time constant τ_3. The errors are calculated from the fit. The color-matched dotted lines as guide to the eye.

The temperature dependence of the third increase is plotted in the fig. 8.8. Note, that the fit results for the time constant, τ_3, are plotted in fig. 8.8 (b) only for non-vanishing values of A_3. The greatest change in A_3 happens across the magnetic phase transition, as one sees in fig. 8.8 (a). In the ferromagnetic phase below T_C, the amplitude, A_3, exists, whereas A_3 vanishes for high temperatures. Furthermore, it is remarkable to see the point of the greatest slope shifting to higher temperatures with increasing magnetic field. Generally speaking, the amplitude close to the PT is increased by an external field.

Turning to the trends of the time constant, τ_3, in fig. 8.8 (b), it seems that the process speeds up when approaching T_C. This is the case at least for the zero field and the 780 mT measurement; the fit results for $B = 120$ mT show an opposite trend. Considering this figure only, it remains unclear whether this is a real effect in LPCMO or some kind of artefact, e.g., of the fit. In the following section, results of field dependent measurements are presented. According to the magnetic field-dependent results in fig. 8.9 (a), no process A_3 exist for $T = 195$ K and $B = 120$ mT. This is the reason, why the deviating behavior of the data point at $T = 195$ K

and $B = 120$ mT in the temperature-dependent measurements of fig. 8.8 (b) is believed to be an artefact by the fit due to the low ratio of A_3 compared to $A_{1,2,4}$ close to the PT. Nevertheless, it can be said, that τ_3 is quite independent on the applied magnetic field compared to the reduction of τ_3 by an increase of the temperature.

8.1.3.2 Magnetic Field Dependence of A_3 and τ_3

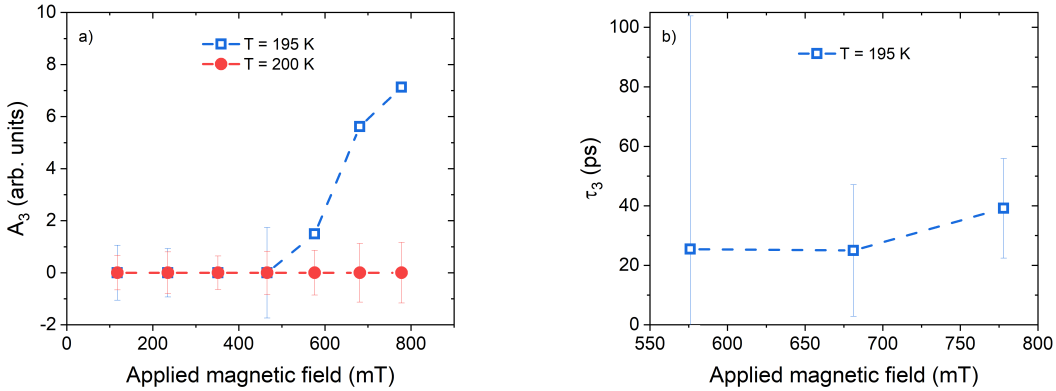

FIGURE 8.9: The magnetic field-dependent fit results of the third increase in $\Delta\mathcal{R}$ measured at $F = 5.9$ mJ/cm^2 and $T_1 = 195$ K (blue, open squares) and $T_2 = 200$ K (red, filled circles) (**a**) the amplitude, A_3 and (**b**) the time constant τ_3. The errors are calculated from the fit. The color-matched dotted lines as guide to the eye.

The figures 8.9 (a) and (b) present the magnetic field dependence at two temperatures, $T_1 = 195$ K and $T_2 = 200$ K, of A_3 and τ_3, respectively. It is clearly visible, that A_3 completely vanishes for 200 K. Thus, no data points for $T_2 = 200$ K are plotted in fig. 8.9. For $T_1 = 195$ K and low fields, the behavior of A_3 is similar. It changes for fields above 500 mT where the amplitude starts to rise. Note, that the error bars for the three non-vanishing data points are not shown, they are bigger than the actual value by a factor of approximately 5. The corresponding values of τ_3 seems to be rather independent on the external field within the error bars.

8.1.3.3 Fluence Dependence of A_3 and τ_3

A_3 as well as the corresponding time constant, τ_3, consequently decrease by raising the fluence until A_3 vanishes at the highest fluence as depicted in fig. 8.10. A_3 show a rather linear behavior, whereas τ_3 increases quite drastically for low fluences. In other words, τ_3 seems to level-off for high fluences.

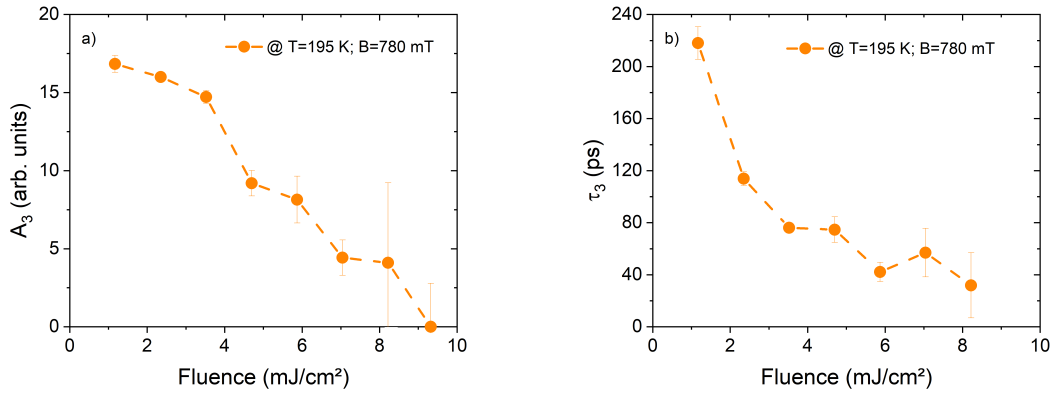

FIGURE 8.10: The fluence-dependent fit results of the third increase in $\Delta\mathcal{R}$ measured at $B = 780$ mT and $T = 200$ K (**a**) the amplitude, A_3 and (**b**) the time constant τ_3. The errors are calculated from the fit. The color-matched dotted lines as guide to the eye.

8.1.4 Relaxation Back to the Ground State

8.1.4.1 Temperature Dependence of A_4 and τ_4

The behavior change of the relaxation process, τ_4, dependent on the temperature is shown in fig. 8.11. In fig. 8.11 (a), A_4 shows a two level behavior depending on the magnetic phase: Coming from the ferromagnetic metallic phase, A_4 drops down at the phase transition, e.g., for the highest applied field by a factor of roughly 4. Being in the PM phase, the amplitude seems to be rather independent on the external magnetic field, whereas for the low temperature FM region, A_4 is raised by applying a magnetic field. Similar to A_3, the drop of the fourth amplitude is shifted to higher temperatures by applying higher fields.

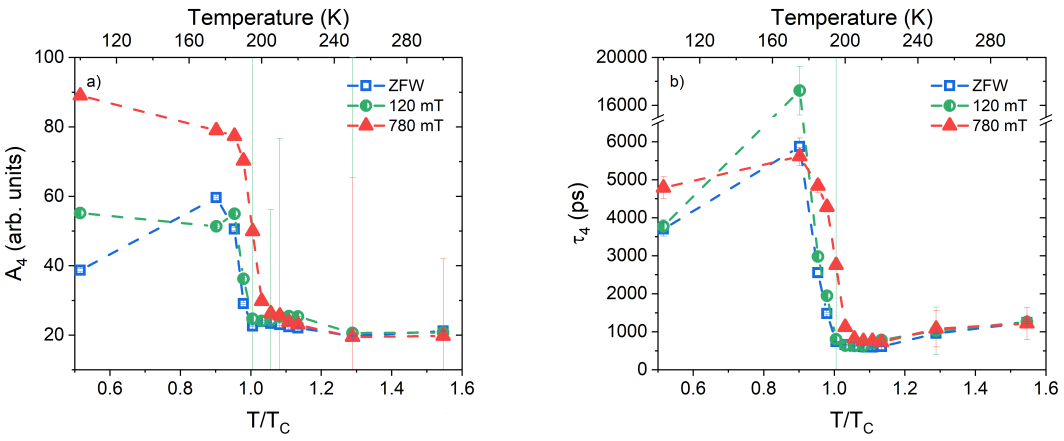

FIGURE 8.11: Fit results of the tertiary increase in $\Delta\mathcal{R}$ for three different warming cycles: blue, open squares - Zero field; green, half-filled circles - $B = 120$ mT; red, filled triangles - $B = 780$ mT. (**a**) the amplitude, A_4 and (**b**) the time constant, τ_4. The errors are calculated from the fit. The color-matched dotted lines as guide to the eye.

Turning to the corresponding time constant in fig. 8.11 (b), τ_4 seems to be rather independent on the magnetic field again for the PM phase. It seems to stay at a level of $\tau_{4,PM} \approx 1000$ ps. When approaching the transition temperature from above, a large increase of τ_4 happens which is again shifted towards higher temperatures if an magnetic field is applied. Depending on the external stimuli, this slowing down of the fourth process is massive: at the peak, a value of almost 18 ns is reached for $T = 175$ K and an applied field of $B = 120$ mT.[4] Well within the FM phase, the time constant decreases again for low temperatures, but seem to stay well above the value of the PM phase.

8.1.4.2 Magnetic Field Dependence of A_4 and τ_4

The magnetic field-dependent fit results of the fourth process are depicted in fig. 8.12. The amplitude, A_4, exhibits two different behaviors depending on the base temperature of the sample. At $T_1 = 195$ K, a more or less linear increase with the external field is found. In contrast, almost no change is visible at $T_2 = 200$ K by ranging the external magnetic field.

[4] Note, that it might be possible to find even longer relaxation times for lower magnetic fields and lower temperature. But in these experiments those external stimuli values are not tested.

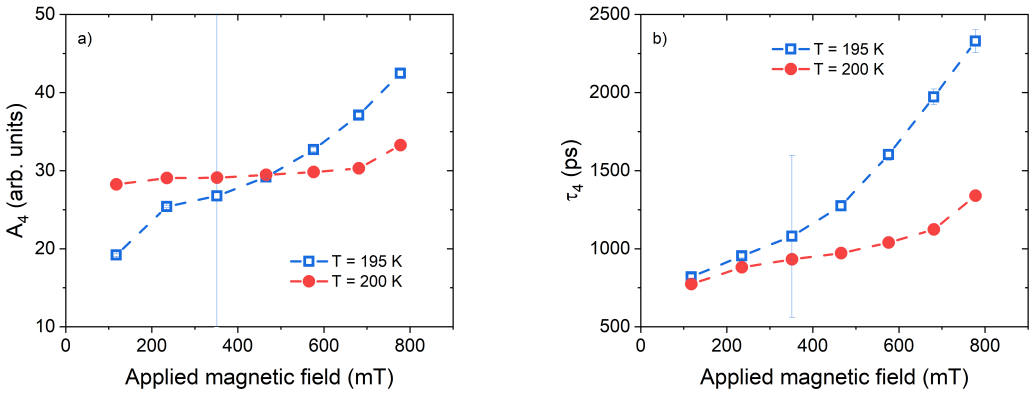

FIGURE 8.12: The magnetic field-dependent fit results of the tertiary increase in $\Delta\mathcal{R}$ measured at $F = 5.9$ mJ/cm^2 and $T_1 = 195$ K (blue, open squares) and $T_2 = 200$ K (red, filled circles) (**a**) the amplitude, A_4 and (**b**) the time constant, τ_4. The errors are calculated from the fit. The color-matched dotted lines as guide to the eye.

In comparison, the time constant, τ_4, is found to show a steeper, non-linear raise at $T_1 = 195$ K and just a slight increase at $T_2 = 200$ K.

8.1.4.3 Fluence Dependence of A_4 and τ_4

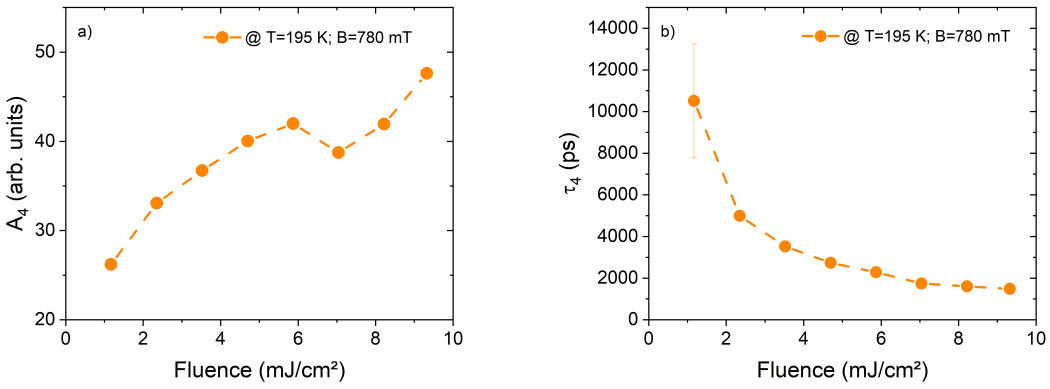

FIGURE 8.13: The fluence-dependent fit results of the tertiary increase in $\Delta\mathcal{R}$ measured at $B = 780$ mT and $T = 195$ K (**a**) the amplitude, A_4 and (**b**) the time constant, τ_4. The errors are calculated from the fit. The color-matched dotted lines as guide to the eye.

The fit results of the fluence-dependent measurements at $T = 195$ K and an applied magnetic field of $B = 780$ mT for the τ_4-process are presented in fig. 8.13. The amplitude, A_4, increases almost continuously by increasing the fluence, see fig. 8.13 (a). Only one dip is found at $F \approx 7$ mJ/cm^2. At exactly this fluence, a kink is found in the amplitude of the first rise, A_1, see fig. 8.2 (b). Again, this dip is assigned to the consequences of a damage in the cryostat window by the high fluence.

The fit results of the belonging time constant, τ_4, is plotted in fig. 8.13 (b). For low fluences, the time constant τ_4 diverges at $T = 195$ K$\approx T_C$. By increasing the fluence, τ_4 decreases in such way that it seems to level off to a value of roughly 1000 ps.

8.2 Time-Resolved Magneto-Optical Kerr Effect of $(La_{0.6}Pr_{0.4})_{0.7}Ca_{0.3}MnO_3$

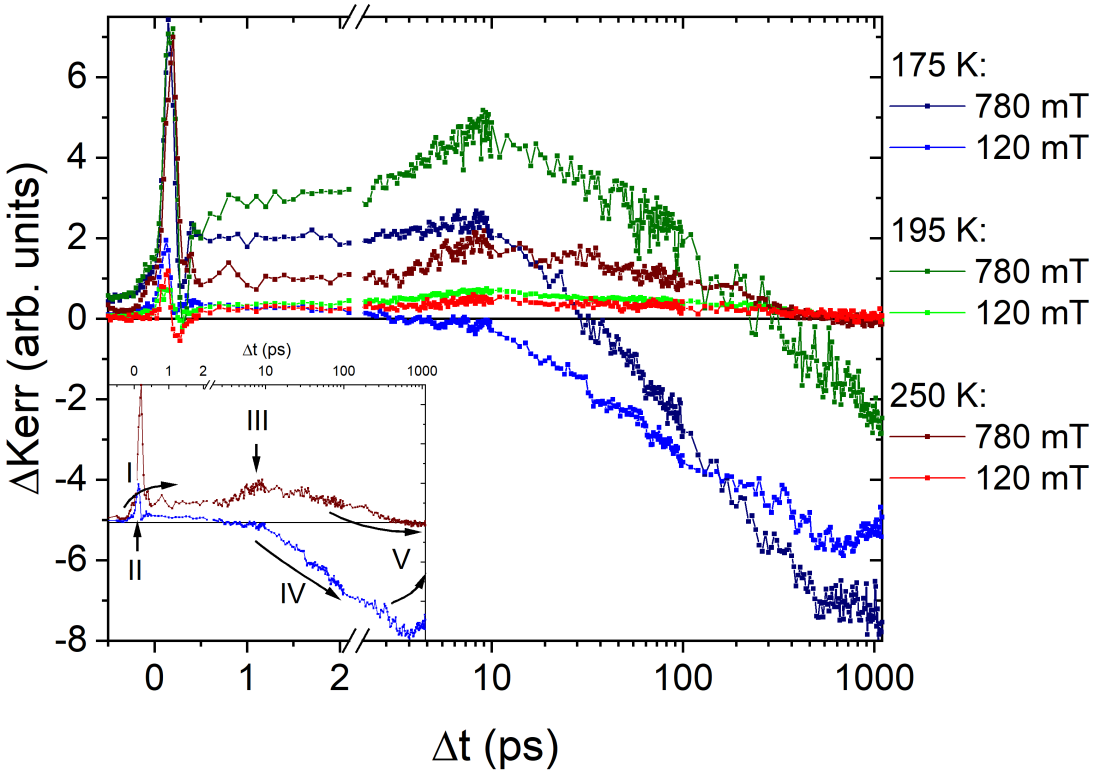

FIGURE 8.14: Exemplary traces of the TRMOKE signal of LPCMO for three temperatures: 175 K (blue), 195 K (green), and 250 K (red). The data are part of three warming cycles measured at the externally applied fields: 780 mT (shades) and 120 mT (hues). In the inset, the features are marked, which are discussed in the text below. All data are measured at an incident fluence of $F \approx 5.9$ mJ/cm^2.

Simultaneously to the transient reflectivity, the magneto-optical response is measured. The TRMOKE traces corresponding to the traces in fig. 8.1[5] are presented in fig. 8.14. One recognizes that the behavior varies quite strongly depending on the external field and the temperature. Nevertheless, up to five features were identified, as depicted in the inset of fig. 8.14:

[5]Note, that there are no TRMOKE measurements available for the ZFW case, since an externally applied field is necessary a magnetization state-based measurement technique like TRMOKE.

I. an initial increase of the Kerr signal due to the fs-laser pulse
II. oscillations (almost a Lorentz-peak-like behavior) at the first hundreds of femtoseconds, which is strongly pronounced
III. peak-like structure at $\Delta t \approx 8.5$ ps
IV. only in case of $T \leq T_C$, a decrease of the signal, which crosses the zero-line; thus this is a demagnetization of the sample.
V. relaxation back to the zero-line[6].

Again, a splitting of the behavior at T_C is found in the TRMOKE data, too. Previously, a third increase of about 100 ps appeared in the transient reflectivity signal when entering the ferromagnetic phase. Now, a demagnetization with respect to the ground state magnetization is found as feature IV, when crossing the PT into the ferromagnetic phase.
In contrast to the transient reflectivity results where up to three increases are found, the feature I is the only increase before the appearing of the relaxation in the TRMOKE response. Hence, up to three slope changes are observed in the TRMOKE data, only (neglecting the two peak-like structures, II and III).

Even though, similar features are found in the psTR as in the TRMOKE data, the TRMOKE data will not be fitted by eq. 8.1. The feature II, the Lorentzian peak-like structure, is quite dominant at the sub-ps timescale; in some cases, it rises up to twice the height of the remaining signal. This in combination with the fact that the relaxation is still not reached for some cases within the delay time $\Delta t \leq 1.1$ ns leads to the point that a hypothetical τ_I would be underestimated, and, in those cases where no relaxation is visible, the hypothetical τ_{IV} would be overestimated by a fit of three exponential functions. Thus, a quantitative analysis is not possible here. Nevertheless, a qualitative description of the changes which are introduced by varying the external stimuli, $T,\ B,\ F$, is going to be presented in the following. Note, the two peak-like features II and III will not be discussed here. The other three features are presented in the chronological order of the dynamics.

[6]Note, that no recovery is visible for some of the traces below T_C, since the delay-line range is too short.

8.2.1 The Initial Increase in the TRMOKE Signal

The feature I, an initial increase of the TRMOKE signal, is remarkable. Usually, a decrease, which corresponds to a demagnetization, is expected in a ferromagnet after an ultrashort excitation [16, 96, 97, 142] since the stored energy heats up the spin system. For a paramagnet, no magnetization change is expected at all, besides the special case of a light-induced transient ferromagnet phase. But as visible in fig. 8.15, in almost every measured TRMOKE trace, the initial increase exists and persists on the first few ps through out all measured temperatures.

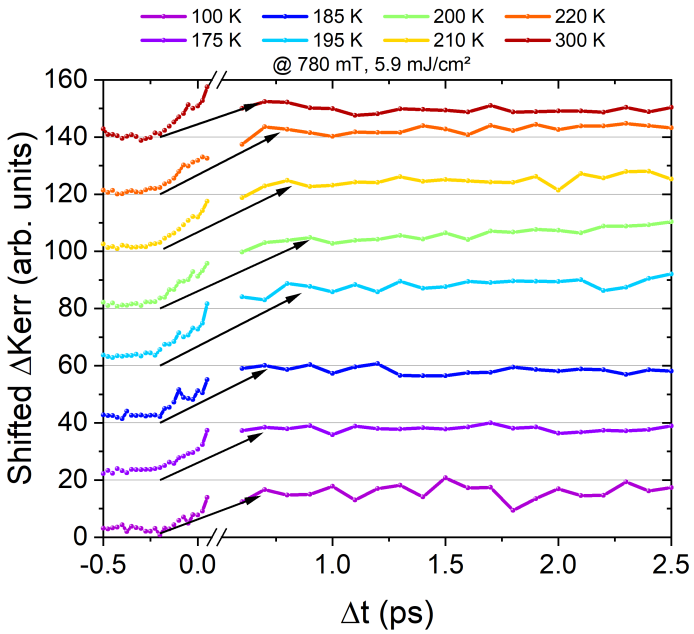

FIGURE 8.15: Selection of the T-dependent TRMOKE data measured at $B = 780$ mT and $F = 5.9$ mJ/cm^2 for delay times up to $\Delta t \leq 2.5$ ps; shifted in y-direction. The black arrows as guide to the eye for the change in the initial increase with the temperature. The Lorentzian peak-like feature (II) is hidden.

As visible in fig. 8.15, the initial increase of the TRMOKE data varies in the amplitude and in the time constant dependent on the temperature as indicated by the black arrows. When approaching the phase transition, the amplitude becomes bigger and the needed time increases.

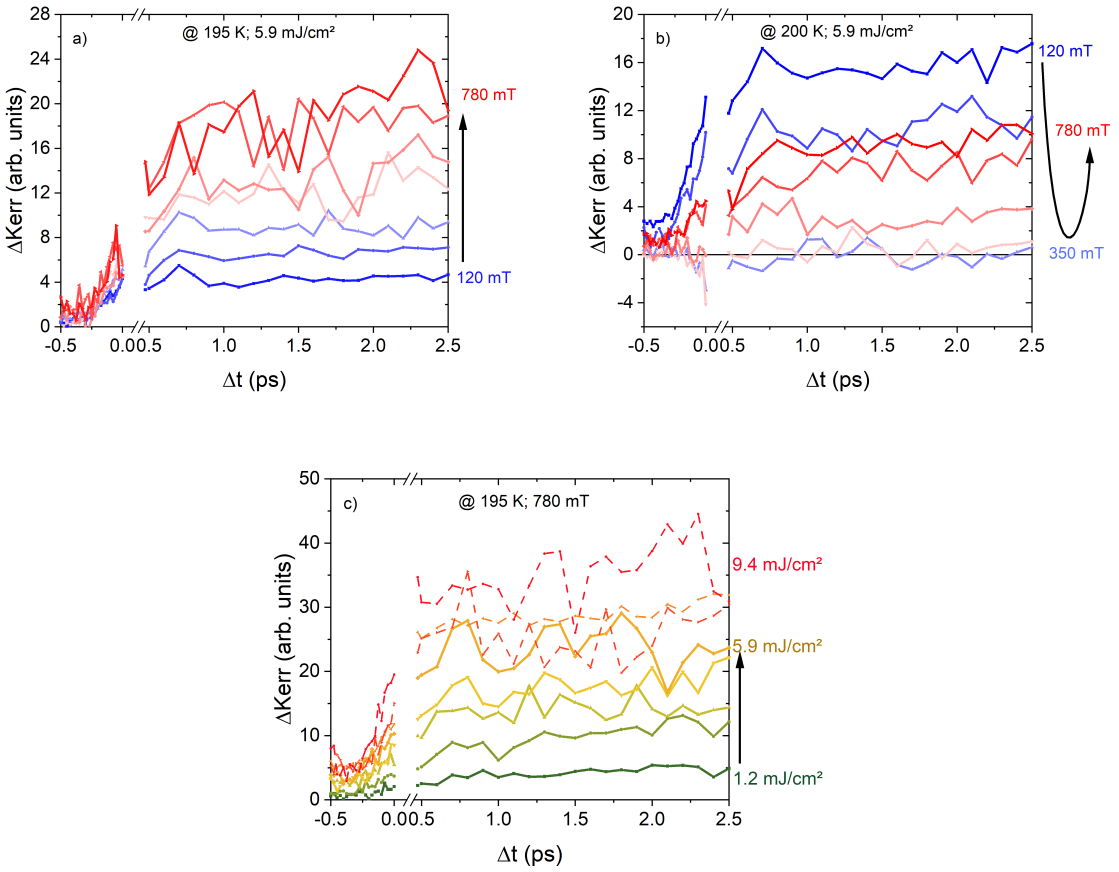

FIGURE 8.16: (**a**) B-dependent TRMOKE data measured at $T = 195$ K and $F = 5.9$ mJ/cm^2, (**b**) B-dependent TRMOKE data measured at $T = 200$ K and $F = 5.9$ mJ/cm^2, and (**c**) F-dependent TRMOKE data measured at $T = 195$ K and $B = 780$ mT for delay times up to $\Delta t \leq 2.5$ ps; shifted in y-direction. The black arrows as guide to the eye for the change in the initial increase. The Lorentzian peak-like feature (II) is hidden.

The magnetic field dependence of the initial increase exhibits two different behaviors for the two measured temperatures, $T_1 = 195$ K and $T_2 = 200$ K (see fig. 8.16 (a) and (b), respectively). In the case of the lower temperature, the amplitude simply increases by applying an higher field. For $T_2 = 200$ K, the amplitude first decreases until a field of $B \approx 350$ mT is applied and, for fields higher than $B \geq 460$ mT, the amplitude of the initial step increases again. Note, that these two measurements are the only two, where this initial feature is completely suppressed.

In fig. 8.16 (c), an increase of this feature is observed for an increasing fluence. Note, that

those three measurements which are performed with a damaged cryostat window at fluences higher than $F \geq 7$ mJ/cm^2 are indicated by the dashed lines.

8.2.2 The Demagnetization

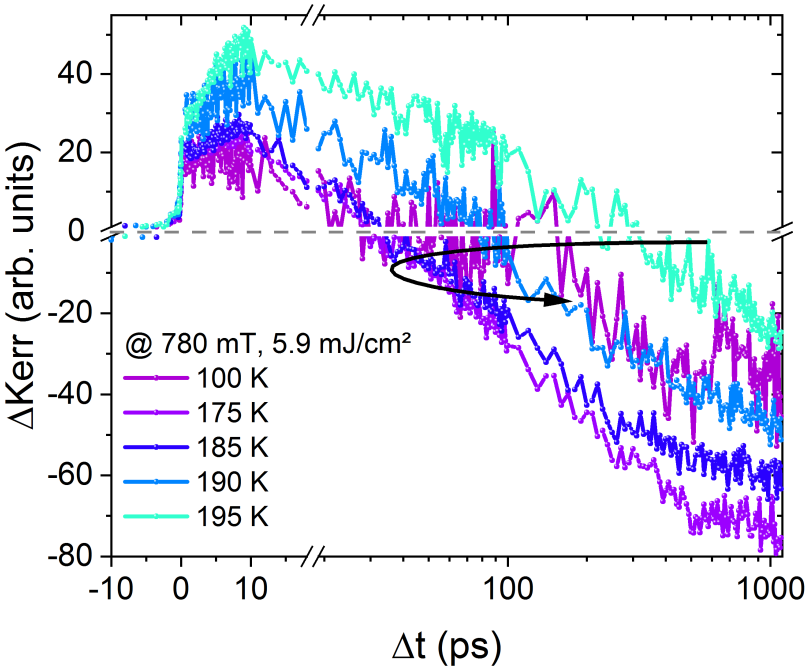

FIGURE 8.17: Selection of the T-dependent TRMOKE data measured at $B = 780$ mT and $F = 5.9$ mJ/cm^2 which exhibit a demagnetization. The black arrows as guide to the eye for the change in the demagnetization with the temperature. The Lorentzian peak-like feature (II) is hidden.

Fig. 8.17 shows an example of the temperature dependence of the demagnetization process. It is visible that the process becomes slower and slower when approaching the phase transition. The black arrow indicates the decreasing of the demagnetization when turning from high to lower temperatures. For the lowest value of T, 100 K, the needed time for demagnetization increases again.

The two magnetic field-dependent series, $T_1 = 195$ K and $T_2 = 200$ K, show an opposite trend for the demagnetization process when applying an higher magnetic field in fig. 8.18

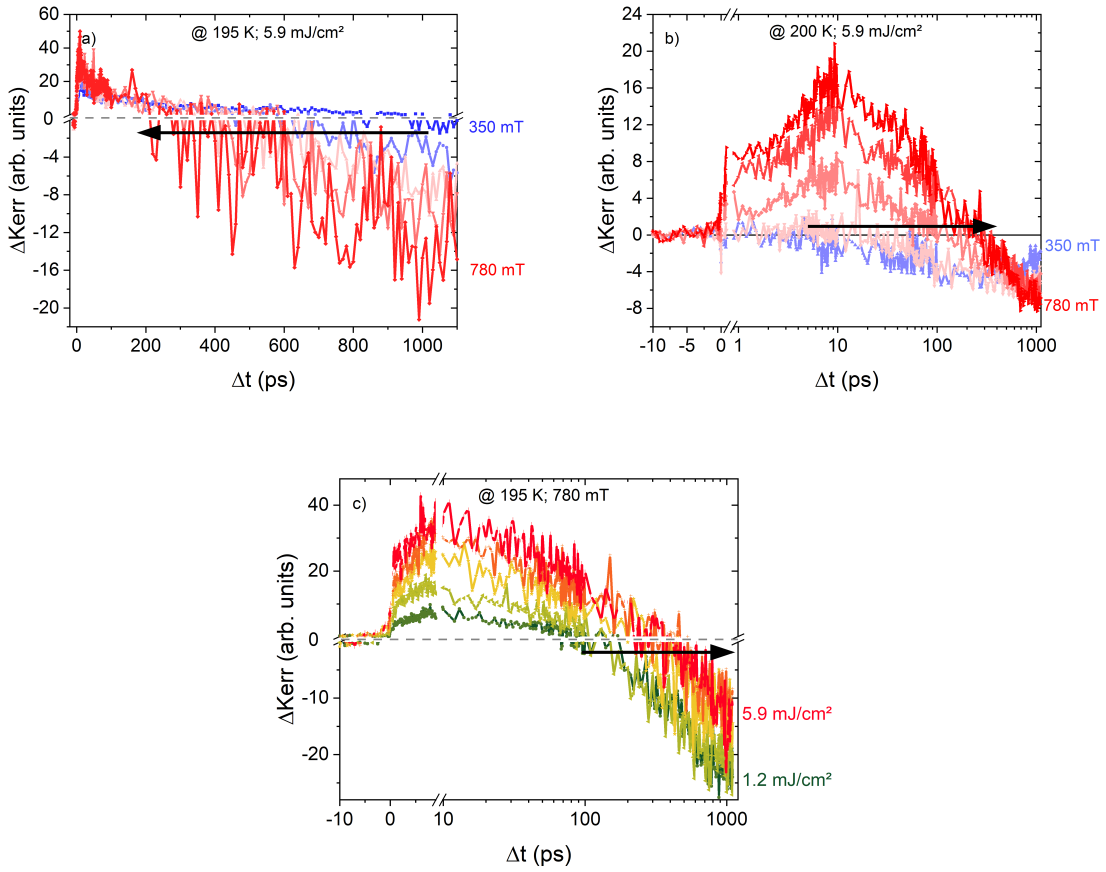

FIGURE 8.18: (Selection of TRMOKE data which exhibit a demagnetization for **a**) B-dependent data measured at $T = 195$ K and $F = 5.9$ mJ/cm^2, (**b**) B-dependent data measured at $T = 200$ K and $F = 5.9$ mJ/cm^2, and (**c**) F-dependent data measured at $T = 195$ K and $B = 780$ mT. The black arrows as guide to the eye for the change in the demagnetization. The Lorentzian peak-like feature (II) is hidden.

(a) and (b), respectively: for $T_1 = 195$ K, the demagnetization process speeds up and for $T_2 = 200$ K, the demagnetization process slows down when increasing the external magnetic field.

When increasing the pump fluence at $T = 195$ K and $B = 780$ mT, the demagnetization process slows down as shown in fig. 8.18 (c).

8.2.3 The Relaxation Process in the TRMOKE Signal

For most measurements below T_C, no remagnetization process is observed, most likely because of a too short delay-line. Three of the few traces, which show a relaxation behavior below T_C, are plotted in the fig. 8.19. Next to it, the inset shows the fitted relaxation times, τ_4, of the transient reflectivity measurements. For both TRMOKE and psTR, a similar trend is observed: when decreasing the temperature close but below to the phase transition, the relaxation back to the ground state slows down.

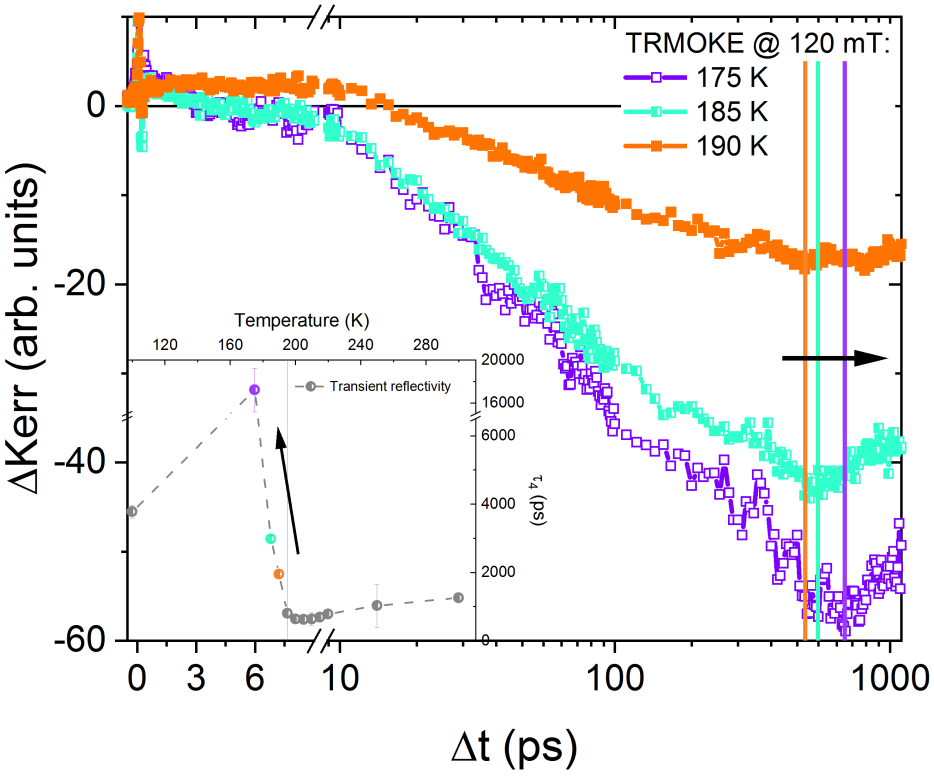

FIGURE 8.19: **Main graph**: three examples of TRMOKE traces in which a remagnetization process becomes clearly visible. The data are part of the T-dependent series, which is measured at $B = 120$ mT and $F = 5.9$ mJ/cm^2. The color-matched vertical lines mark the turning point of the traces, where the remagnetization process becomes dominant. The **inset** shows the fit results for τ_4 of the transient reflectivity traces. The data points, which correspond to the TRMOKE traces in the main graph, are color-matched.

CHAPTER 9

Discussion - $(\mathbf{La}_{0.6}\mathbf{Pr}_{0.4})_{0.7}\mathbf{Ca}_{0.3}\mathbf{MnO}_3$

The results in chapter 8 has been evaluated by fitting a superposition of four exponential functions and one Gaussian peak (s. equation 8.1). In the first instance, this fit is purely phenomenological. However, every emerging feature represents one or more physical processes, which mark the energy dissipation pathway after the ultrashort excitation. By careful analysis of the reactions of these processes to changes of the external stimuli, suggestions of the underlying interactions can be developed.

In this chapter, these processes are discussed by combining the static properties (sec. 6.1 and appendix C), the time-resolved results (psTR sec. 8.1; TRMOKE sec. 8.2), and the calculations done by FDTD simulation (chapter 7). Thus, a sketch of the energy dissipation pathway from the excitation and the non-equilibrium dynamics to the quasi-equilibrium dynamics, which finally lead to the relaxation of the system, is given, as well as how this path is influenced by external control parameters, namely, externally applied magnetic field B, pump fluence F, and base temperature T.

In such a manner, the fit parameters A_i needs to be reflected upon. The amplitudes of the exponential functions reflects both, the probability of the related process(es) to happen as well as the impact of a single process on the change of the measurement signal. Note, the here investigated processes assemble more fundamental, physical processes. Thus, besides others, the number of occupied initial states and available final states, the probability to absorb a needed quasi-particle, e.g., for momentum conservation, the wave functions overlap between the initial and final state, the degree of resonance as well as the strength of the spectral weight transfer contribute to the amplitude A_i.

In contrast, τ_i merges the single, averaged times of the more foundational processes. For instance, if the wave functions' overlap of initial and final states is enhanced when a special

phonon mode is excited and if this mode exhibits a (strong) environmentally dependent frequency shift, τ_i is most likely supposed to slow down or speed up, respectively.

But, since the electron, lattice, and spin subsystems are highly correlated in a transition metal oxide like LPCMO, the complex net of interaction effects between them requires the consideration of an interdependence of a manifold of energetic contributions. How complex this network is, is outlined in the chapter 4 where the most basic interactions between the subsystems in manganites are summarized. The simulations published by Rajpurohit and co-workers in [41] are an example of how challenging the theoretical description of ultrafast dynamics in manganites is. To build up a model, Rajpurohit and co-workers combine a variety of different approaches in order to predict, among other things, the development of the spin subsystem in $Pr_{0.5}Ca_{0.5}MnO3$ after a fs-laser excitation of the electronic system. Therefore, quantitative estimations are unfeasible within the scope of this thesis. Nevertheless, a qualitative model picture of the dynamical processes shall be given here.

The structure of this chapter is in line with the temporal evolution of the transient reflectivity signal, see fig. 9.1:

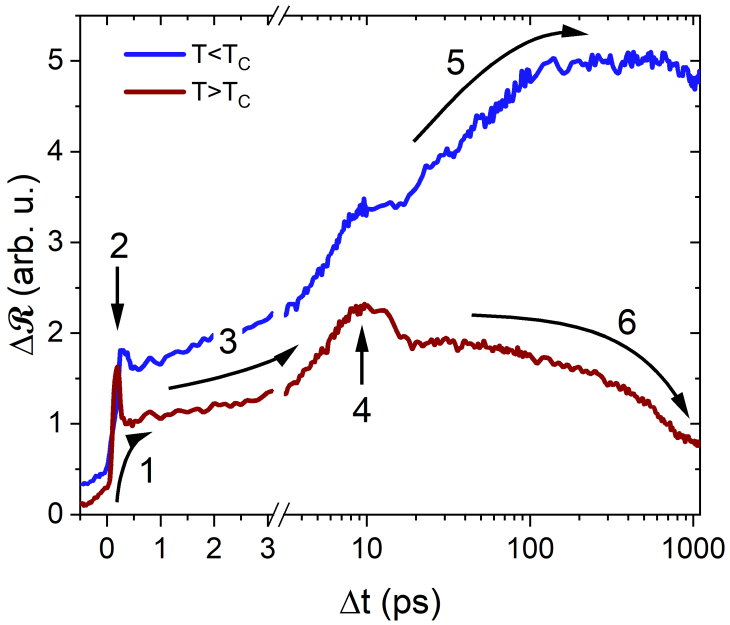

FIGURE 9.1: Two exemplary traces of the psTR signal for a temperature below the Curie temperature (blue), and a temperature above T_C (red). The arrows mark the features, which are discussed in this chapter.

The excitation process, features No. 1 and 2, is discussed as a starting point in sec. 9.1. The suggested assignment of a second electron-phonon interaction to the feature No. 3 (sec. 9.3) is followed by the analysis of the peak-like structure, feature No. 4, under the viewpoint of Brillouin scattering. As the last remaining increasing function, the feature No. 5 is suggested to represent the spin-lattice interaction in sec. 9.4. Finally, in sec. 9.5, the feature No. 6 will be shown to consists of at least two different relaxation processes.

9.1 Feature No. 1 - Excitation and Thermalization of the Electronic System

It has been shown in section 8.1.1 that the initial increase of the signal, labeled as feature No. 1 and described by A_1 and τ_1, varies between $\tau_1 \geq 75$ fs and ≤ 300 fs. For the extraordinary case of low fluence close to the PT, τ_1 seems to reach values above one ps, see fig. 9.2 (b). These values are comparable to the thermalization times published in literature for perovskite manganites [98, 99, 104, 105, 143, 144, 145]. Consequently, τ_1 will be labeled as *thermalization time* in the following as it is done in those papers.

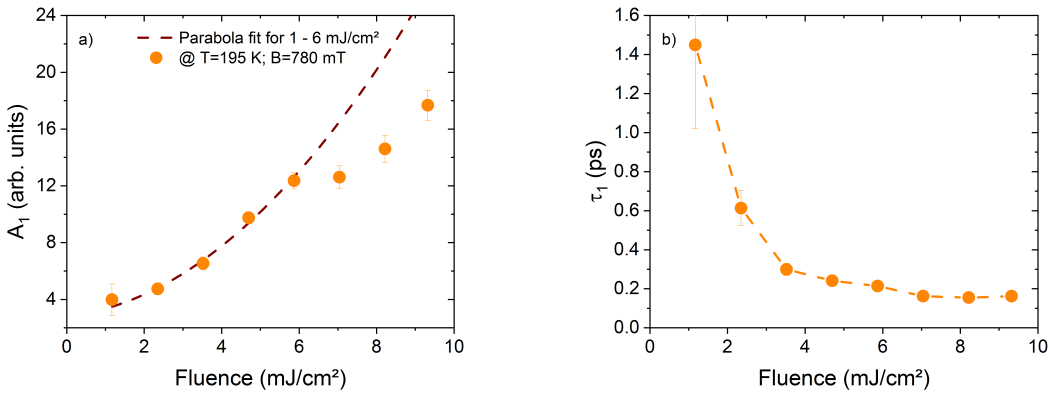

FIGURE 9.2: The fit results of $\Delta\mathcal{R}$ for the initial increase (**a**) the amplitude, A_1, with a parabola fit as guide to the eye and (**b**) the time constant, τ_1, dependent on the fluence measured at $T = 195$ K and in an external magnetic field of $B = 780$ mT.

As already discussed in the sections 6.3 and 8.1.1.3, the cryostat window was most likely damaged during the measurements of the high fluences above $F \geq 7$ mJ/cm^2. Nevertheless, a non-linear behavior of A_1 is found for lower fluences as visible in fig. 9.2 (a). A parabolic fit of the low fluence range is plotted as guide to the eye to underline this non-linear behavior of the amplitude.

In a strongly simplified picture, inter alia, the absence of a phase transition or a non-consideration of unusual characteristics of the band structure, this non-linearity is quite surprising for low fluences. Usually, a linear dependence of the amplitude, A_1, on the fluence would be expected due to the assumption of a linear dependence of the number of excited electrons on the number of incoming photons. A break of this linearity between excited electrons and number of incoming photons points toward a non-trivial responds of the electronic structure to photonic excitation by the chosen photon energy of the experiment. Two exemplary hypotheses, which might explain the observed data (see fig. 9.2), will be discussed in the following.

The first ansatz, which shall be discussed here, is that the electronic band structure is changed by the electron excitation in such a (strong) way that the variation of the optical indices which is caused by the excitation becomes non-linear. This might be caused by circumstance that the experiment is performed close to the static, electronic phase transition at $T = 195$ K. This would mean in other words: the excitation of already a low number of electrons[1] drives an electronic phase transition temporary. Note, that experimentally no signs of irreversibility within the repetition rate was observed. Hence, this light-introduced or light-assisted phase transition would be meta-stable and would relax back into the unexcited ground-state during the time span of $\Delta t < 1/50$ kHz $= 20$ µs after the excitation. A photo-induced phase, which is dependent on the fluence, with a meta-stability which persists longer than 20 µs is excluded since no drift of the data was observed during the measurement series.

The second ansatz considers a less drastic impact of the electronic excitation on the band structure: it might be the case that an excitation by a two-photon process is resonant under the conditions of the fluence-dependent measurement series. In this case, the parabolic fit in fig. 9.2 (a) would not merely be a simple guide-to-the-eye-line but would represent the

[1] The absorbed number of photons per unit cell is estimated to be in the low %-regime (see appendix A3).

quadratic fluence dependence of the amplitude A_1 caused by the two-photon process (2PP), too. This second hypothesis of a 2PP would entail a main excitation energy of about $\hbar\omega \approx 2.4$ eV (equal to the probe energy).

9.1.1 Hypothesis I - Extraordinarily Strong Band Structure Change by the Ultrafast Excitation

For the first hypothesis, the excitation-induced, temporary phase transition, it is important to understand that there are potentially 2 different kind of phase transitions possible within the scope of this hypothesis: (I) a light-assisted version of the transition from the FM-phase into the PM-phase which is statically already known (see section 4.4); (II) a transient transition into a light-induced, hidden phase, e.g., such as describe for $Pr_{0.5}Ca_{0.5}MnO_3$ in [41]. (See also chapter 5 for more information regarding phase transitions.) But, note, that only one case can be appropriately discussed here: the case (I) of the light-assisted FM-to-PM transition. The second case (II) is also possible, but, due to the large number of generally known electronic phases in perovskite manganites, it is not expedient to start a discussion about this bunch of options without supporting theoretical calculations. Therefore, the following argumentation focuses on case (I), the light-assisted ferromagnetic-metallic to paramagnetic-insulating phase transition. To underline that the case (I) is meant in the following, the term "temporary phase transition" is going to be used frequently in contrast to the term "transient phase transition" which refers to a light-induced transition into a hidden phase.

For the discussion of the temporary phase transition, 2 things should be considered. First, the general idea behind the hypothesis of the temporary phase transition is that energy is transferred into the system by the absorption of photons during the ultrafast excitation; due to this additional energy, the volume ratio between the two electrical phases, here, the ferromagnetic metallic and the paramagnetic insulating phase, is shifted towards the higher temperature phase, here, the paramagnetic insulating phase. In terms of the fluence-dependent measurement series, the consequence of this would be that the higher the fluence, the higher the change of the volume ratio between FM and PM phase during the experiment. Therefore, the tendency of the system's response would be expected to be similar for both external stimuli,

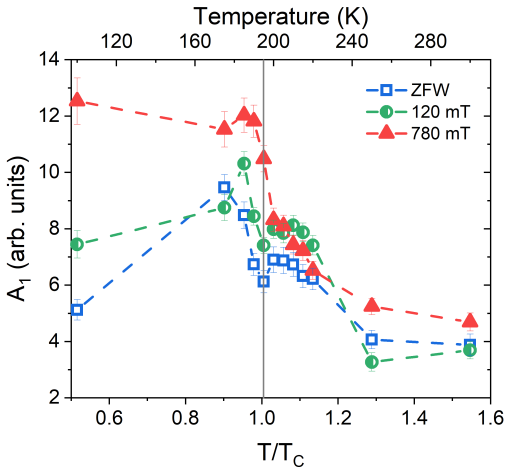

FIGURE 9.3: Temperature dependence of the amplitude, A_1, for three different applied magnetic fields in a warming cycle. The gray, vertical line marks the temperature, $T = 195$ K, which was set during the fluence-dependent measurement series (see fig. 9.2).

fluence or temperature. Thus, the temperature-dependent warming cycle measurement series at $B = 780$ mT (see fig. 9.3, red, filled triangles) should be taken into account, too.

In fig. 9.3, a clear decreasing trend is visible when turning from the low temperature phase (FM) into the high temperature phase (PM) while increasing the set temperature of the cryostat; the amplitude, A_1, decreases what represents a decreasing reflectivity change during the ultrafast excitation. The gray vertical line at $T = 195$ K marks the cryostat temperature which was set during the fluence-dependent measurement series.

Note, that the increase of the electron temperature after the pump pulse ($F = 5.9$ mJ/cm^2) is calculated within the framework of the simplified FDTD simulation model (see chapter 7) to a value of about $\Delta T_{el} \sim 40$ K. Hence, the increase of the heating of the electronic subsystem by the change of the pump fluence, fig. 9.2, as well as by the change of the cryostat temperature, fig. 9.3, are assumed to be approximately of a similar order. Thus, within the hypothesis of the temporary phase transition, the change in the amplitude, A_1, is expected to show a similar trend for both experimental series, temperature- and fluence-dependent. But in contrast, two contrary dependencies of amplitude, A_1, on the two different external stimuli, fluence and temperature, are found within the resolution of the chosen temperature or fluence steps in fig. 9.3 or fig. 9.2 (a), respectively.

The second thing which should be considered in this discussion is the hysteretic nature of phase transitions. Due to this hysteretic response, it is conceivable that the results in fig. 9.2

and in fig. 9.3 are not comparable, since two different parameters have been varied from one data point to the next one. To overcome this issue, additional measurement series are recommended to be done which persist of a couple of temperature-dependent warming cycles at a constant magnetic field of $B = 780$ mT, but each warming cycle would be measured at a different fluence.

In conclusion, the two contrasting responses of A_1 on the increase of the temperature and of the fluence hint at the voidness of the hypothesis that the fluence dependency of A_1 is explained by a drastic change of the electronic structure caused by a temporary phase transition due to the pump pulse excitation. Nevertheless, additional measurements are needed to exclude a hysteretic effect as reason for the deviation between fig. 9.2 (a) and fig. 9.3. Furthermore, the hypothesis of a transient phase transition into a hidden phase might explain the data, but is not discussible without supporting theoretical calculations, such as by TDDFT.

9.1.2 Hypothesis II - Two Photon Process

Following the idea of a two photon process (2PP), a charge transfer process is suggested by [67, 91, 92, 98] (summarized in section 4.5.1) as explanation for the absorption peak around the required energy range of about ~ 2.4 eV. All papers [67, 91, 92, 98] assign a charge transfer transition from an oxygen 2p states to a Mn-ion to the energy range between 2 and ~ 3 eV independent of the discrepancy in the interpretation of the optical conductivity data below 2 eV. Admittedly, a single fluence-dependent directly measured at the PT is not best suited as a proof for the whole thermal range which is addressed in this thesis. Therefore, the hypothesis of a charge transfer transition (CTT) will be taken up repeatedly in the following to check the consistency of this theory.

Turning to the F-dependence of the related time constant, τ_1, a decrease with increasing fluence is observed see fig. 9.2 (b). τ_1 is supposed to be mediated by the thermalization of the electrons, which is related to the scattering probability of the hot electrons. If electrons are excited into conduction states, the mobility of the (hot) electrons is increased and a scattering

event becomes more likely, compared to the case of a trapped, immobile electron. The more electrons are excited the higher the chance of such an electron-electron scattering, which leads to thermalization of the electronic system. Note, that in the case of an charge transfer transition from the O2p into the Mn3d states, the mobility of the electrons close to the Fermi level is raised by two effects: (i) the electron is excited into conduction states above the Fermi energy, and (ii) the excitation of a CTT creates a hole in the O2p states. The latter enhances the hopping of electrons, since the O2p states are an integral part of the hopping process. Also in the framework of the theoretical model of a Fermi-liquid, an decreasing behavior is predicted [33, 95] $\tau_{el-el} \propto T_{el}^{-2}$ justified by a lager phase space for electron-electron scattering.

Now, having established the idea of a CTT from a O2p state to an Mn-ion, it enables to explain the remarkable temperature dependence of τ_1 now. Fig. 9.4 (b) shows a peak-like behavior for the temperature region close to and a little above the Curie-temperature, i.e., an increase in amplitude between $0.95 \cdot T_C < T < 1.2 \cdot T_C$ of a factor of ~ 2. Moshnyaga et al. [8] demonstrates that this temperature range corresponds to the intermediate antiferromagnetic, insulating phase which is dominated by correlated Jahn-Teller polarons see fig. 9.4 (c). Remembering the concept of correlated JT polarons from chapter 4.1.1, a close network of distorted oxygen octahedra which surround Mn^{3+}-ions is formed in this region and forcing the nano-scaled FM domains into an antiparallel coupling with respect to each other. A sketch of this phase separation behavior is drawn in fig. 9.4 (c) shortly above the centre.
Now, thinking of a CTT from an oxygen site to an Mn-site, this polaronic formation needs to be modified in order to create enough space for an additional, occupied 3d-orbital independent of whether the electron is transferred to a Mn^{3+}-ion, turning into a Mn^{2+}, or to a Mn^{4+}-ion, turning into a Mn^{3+}-ion. In order to stabilize the new occupation of a 3d-orbital, at least a few atomic cores need to readjust their positions. This additional requirement slows down the whole charge transfer process within the AFM intermediate phase region.

The observations of the magnetic field-dependent series are in line with this finding of a peak in the intermediate state as visible in fig. 9.4 (b). Apart from the two lowest fields at 200 K, an increase of the time constant is observed in this region when increasing the applied

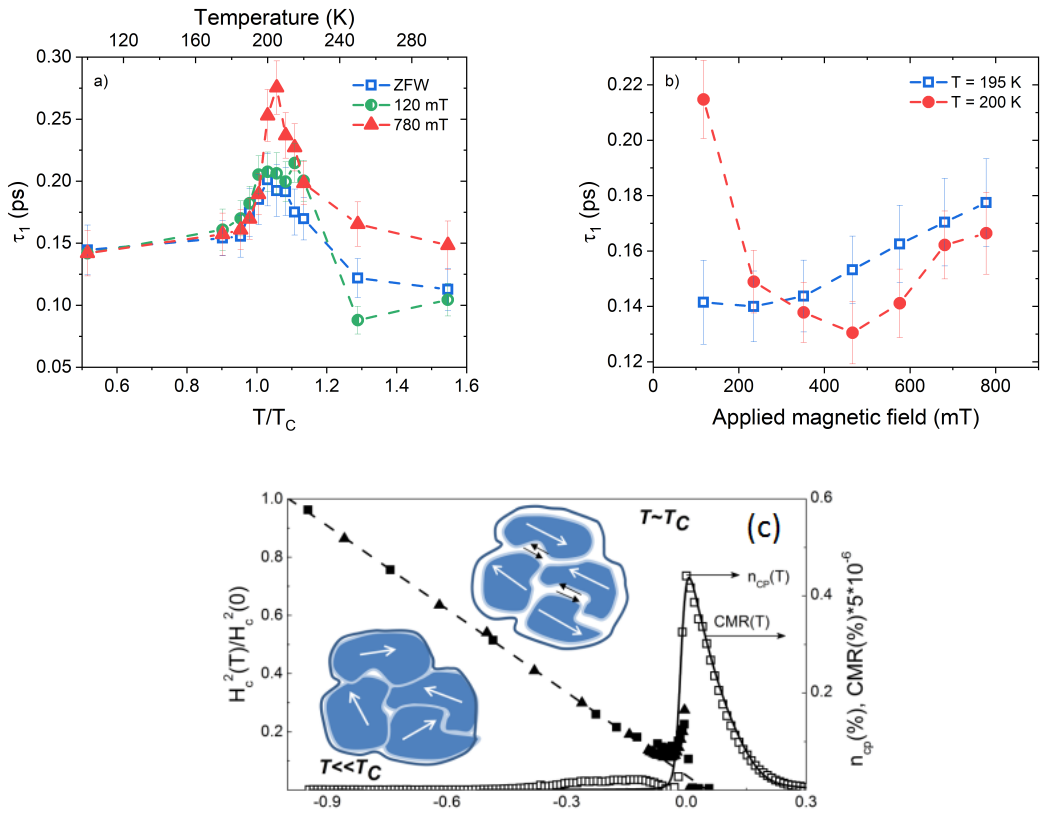

FIGURE 9.4: The fit results of $\Delta\mathcal{R}$ for the initial increase, τ_1, for (**a**) the temperature dependence measured at $B_1 = 0$ mT (open blue squares) and $B_2 = 120$ mT (half-filled green circles) and $B_3 = 780$ mT (filled red triangles) and a fluence of $F = 5.9$ mJ/cm^2; and (**b**) the magnetic field dependence measured at $T_1 = 195$ K (open blue squares) and $T_2 = 200$ K (filled red circles). (**c**) The filled symbols represent the normalized coercive field, h_c^2, on the left scale as a function of the normalized temperature for LPCMO films. The relative amount of correlated polarons, n_{CP}, (open squares) on the right scale depending on the normalized temperature. The picture (c) is reprinted with permission from [8]. Copyright 2014 by the American Physical Society.

magnetic field. This suggests a connection to the colossal magnetoresistance, see fig. 9.4 (c), open squares.

In conclusion, the F-dependent measurement series point towards a charge transfer transition from an O2p state into a Mn3d state which is enabled by a two photon process. The dependences of τ_1 on the temperature and the external magnetic field show reasonable results regarding this hypothesis. In the following, the discussion will be extended to the response of

the Kerr signal therefore.

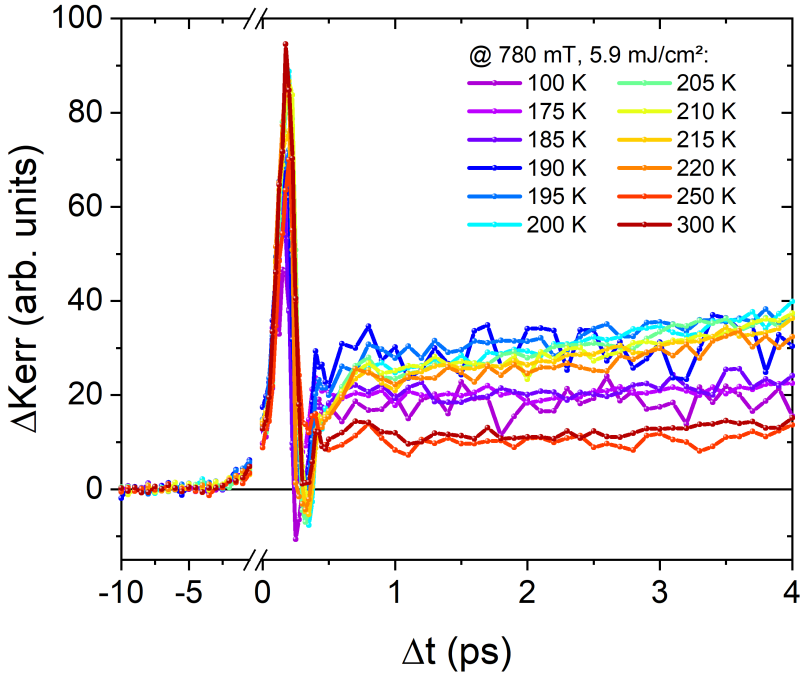

FIGURE 9.5: Increasing behavior of the feature No. I in the time-resolved magneto-optical Kerr signal measured in an external field of $B = 780$ mT with a fluence of $F = 5.9$ mJ/cm^2. The out-standing oscillation with in the first ps is labeled as feature No. II.

In fig. 9.5 a selection of representative TRMOKE signals are plotted. For almost all parameter of the external stimuli which are chosen for the measurements, the TRMOKE signal rises at the fist hundreds of fs and stay above the zero line (neglecting the oscillations of feature No. II). This behavior is persistent for all three magnetic states of the sample (FM, AFM-coupled, PM). Since the Kerr response is proportional to the magnetization of the sample, this behavior is surprising especially for the FM phase, where the stored energy of the pump pulse usually leads to a demagnetization of the sample. But the comparison with the static Kerr signal of LSMO [91] shows that a CTT can lead to an increase of the Kerr rotation. It is presumed that this is connected to the increase of the total angular momentum, $\mathbf{J} = \mathbf{S} + \mathbf{L}$, which is introduced by the transfer from a $L = 2$ (O2p) into a $L = 3$ (Mn3d). Due to the spin-orbit

coupling, the change in J is visible in the Kerr signal.

To summarize the discussion of the second hypothesis, the fluence-dependent measurements point towards a two photon process. Thus, the excitation energy of (a part of) the pump process is raised to $\hbar\omega \approx 2.4$ eV. Literature, which measured static optical spectra of manganites [67, 91, 92, 146, 147, 148], assigns a charge transfer transition from an O2p state into a Mn3d state to this excitation energy. The temperature-dependent and external magnetic field-dependent results are explainable by this hypothesis as well as the remarkable initial increase in the time-resolved MOKE data. Therefore, it is suggested that at least a part of the excited electrons undergo a charge transfer transition by the absorption of two pump photons.

9.2 Feature No. 2 - Coherent Optical Phonons

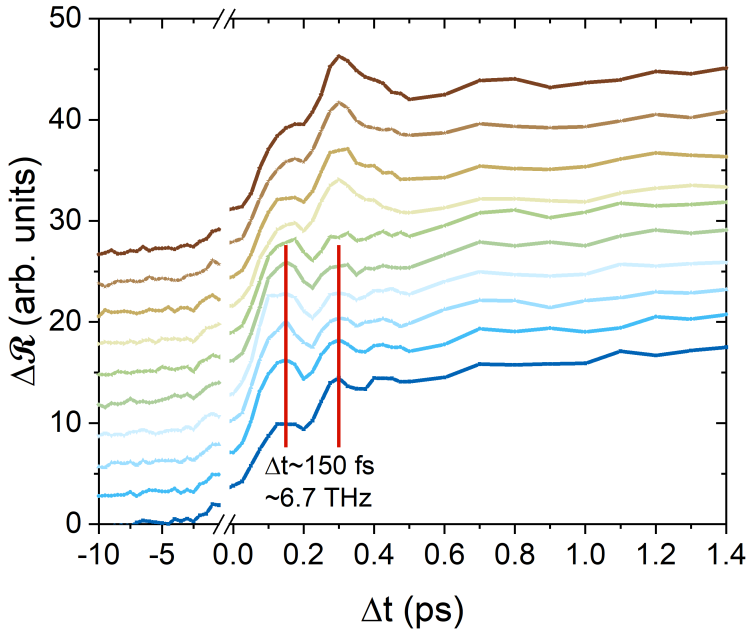

FIGURE 9.6: Zoom-in of a selection (no certain series) of typical $\Delta\mathcal{R}$ traces to visualize the oscillations of feature No. 2. Shift in y-direction.

The feature No. 2, oscillations at the first hundreds of femtoseconds, will not be discussed in detail since the temporal resolution in combination with the data quality is not sufficient

enough to further evaluate the oscillation at the fs-timescale, e.g., analysing a fast Fourier transformation (FFT). Nevertheless, the ultrafast oscillations, which are depicted in fig. 9.6, exhibit oscillation frequencies in the THz regime. A easily visible frequency is picked as an example and is indicated by the two vertical red lines. This is the frequency range of optical phonons, which are investigated for similar LPCMO films by static Raman spectroscopy in [8, 149, 150].

As discussed in the previous section 9.1, to excite an electron into an e_g state of a manganese ion, a rearrangement of the surrounding oxygen octahedron [118] is necessary in order to reduce the Coulomb energy of the Mn states. This strongly suggests a coherent optical phonon excitation enforced by the excitation of the electrons by the pump pulse. This hypothesis is in line with findings in literature [99, 105, 118, 151].

In conclusion, the feature No. 2 is assigned to the coherent optical phonon excitation.

9.3 Feature No. 3 and No. 4 - Second Electron-Lattice Interaction and Brillouin Scattering

The first two features suggested an excitation and thermalization process of electrons which lead to a disturbance of the JT distortions, which are established in the ground state, caused by the occupancy of a Mn3d state above the Fermi-energy. Here, the strong electron-phonon coupling of the manganite empowered the first step, τ_1, by enabling the transferability of the excited electron into an additional Mn3d state via the excitation of coherent optical phonons and, thereby, the activation of the surrounding oxygen octahedron. In other words, the absorbed energy is now stored in occupation of the higher energy level and in the disturbance of the JT distortions, which existed before the pump-pulse. Note, that the activation of the oxygen octahedron is not necessarily equivalent to the thermalization of the electrons with the entire lattice. Thus, the follow-up question is, how does the stored energy dissipates after the excitation and thermalization of the electrons - the first step - is established?

It will be argued in the following, that the second exponential increase, feature No. 3, is very likely caused by a second electron-lattice interaction. But before that, the feature No. 4, the

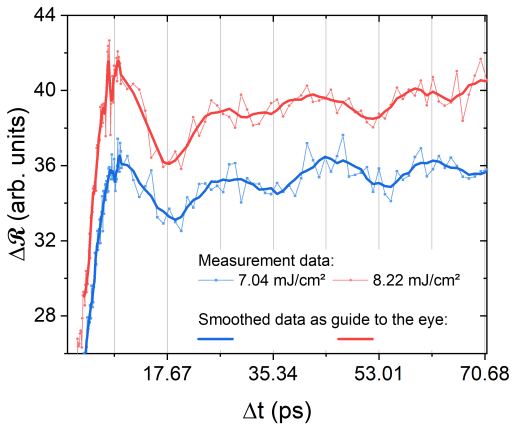

FIGURE 9.7: Exemplary psTR data which show distinct Brillouin scattering. Two different fluenceses of the same measurement series at $T = 195$ K and $B = 780$ mT are plotted: (blue) $F_1 \approx 7$ mJ/cm^2 and (red) $F_2 \approx 8.2$ mJ/cm^2. The color-matched, smoothed data as guide to the eye.

peak-like structure, is going to be assigned to Brillouin scattering (BS) inside the LPCMO film. In the framework of the FDTD simulations, the appearance of the Brillouin scattering is suggested to be connected to the energy transfer from the electrons into the excitation of coherent acoustical phonons. Note, that other hypothesis might explain the development of the coherent acoustic phonons, too, e.g., a phonon-phonon scattering process of the previously excited coherent optical phonons. But a phonon-phonon type of scattering process is not included in the FDTD model as a possible energy dissipation channel. Hence, a weighing of the hypotheses based on the simulation model is not possible.

In contrast to the initial peak at about $\Delta t \approx 8.5$ ps of feature No. 4, the attached oscillations are barely visible in most of the LPCMO time-resolved data. In order to highlight these oscillation, two exemplary measurement data are plotted together with their smoothed traces in fig. 9.7. In both cases, an oscillation with a frequency of roughly $f \approx 55 - 60$ GHz is apparent. The gridlines in the graph underline the periodicity of these oscillations. Due to the missing intensity of this feature, it is only possible to fit the first maximum but not the damped oscillations, as it is done by the Gaussian peak in eq. 8.1.

As a first hint for Brillouin scattering, a brief estimation of the arrival time of the first maximum is calculated in the following. When $d = 56$ nm is the film thickness and $v \approx 6600$ m/s the sound velocity of the LPCMO[2], then the first maximum of the Brillouin scattering should

[2]See [137] at p. **57**, figure *4.8 (a)*: the bulk values of the longitudinal sound velocity are plotted in dependence on T. The figure shows a range between $v_{50\ K} \approx 6600$ m/s and $v_{300\ K} \approx 6150$ m/s for no field.

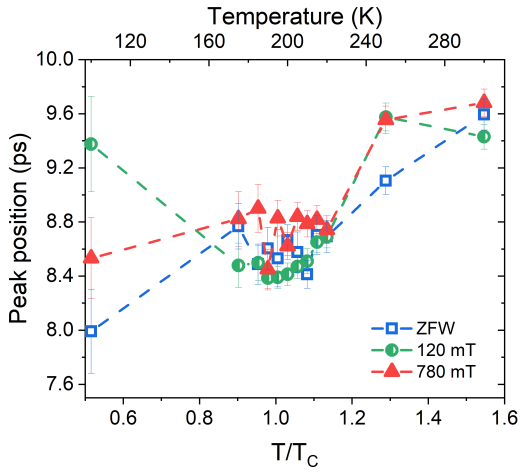

FIGURE 9.8: Temperature-dependent evolution of the fitted Gaussian peak position for three different applied magnetic fields: (blue open squares) zero field; (green half-filled circles) $B = 120$ mT; and (red triangles) $B = 780$ mT. The color-matched dashed lines as guide to the eye.

be visible at:

$$t_{Brillouin} = \frac{d}{v}. \tag{9.1}$$

Hence, predicted values for the temperature range, which is covered in the experiments, are:

$$t_{100\ K} \approx 8.5 \text{ ps} \quad \text{and} \quad t_{300\ K} \approx 9.1 \text{ ps}.$$

Taking the error bars into account, the estimated values match to the results from the fit eq. 8.1, see fig. 9.8, which shows the center position, t_p, of the fitted Gaussian peak.

In addition to this estimate, the temporal evolution of the heat-induced strain can be calculated by FDTD simulations. In fig. 9.9 (b), the simulated strain inside the film as well as in parts of the MgO-substrate is mapped as a function of depth and pump-probe delay. As visible in the fig. 9.9 (b), three different strain waves are generated after the simulated excitation, propagating through the sample, and interfere with each other during the temporal evolution: (i) a strain wave starting at the surface of the LPCMO and propagating through the film, into the direction to the substrate; (ii) a strain wave which is formed at the interface between the substrate and the LPCMO layer and propagates into the substrate, away from the LPCMO layer; and (iii) a compression wave, as a counterpart of the strain wave (ii), which is initiated at the interface between the LPCMO layer and the substrate and propagates into the LPCMO layer, towards the direction to the thin film surface.

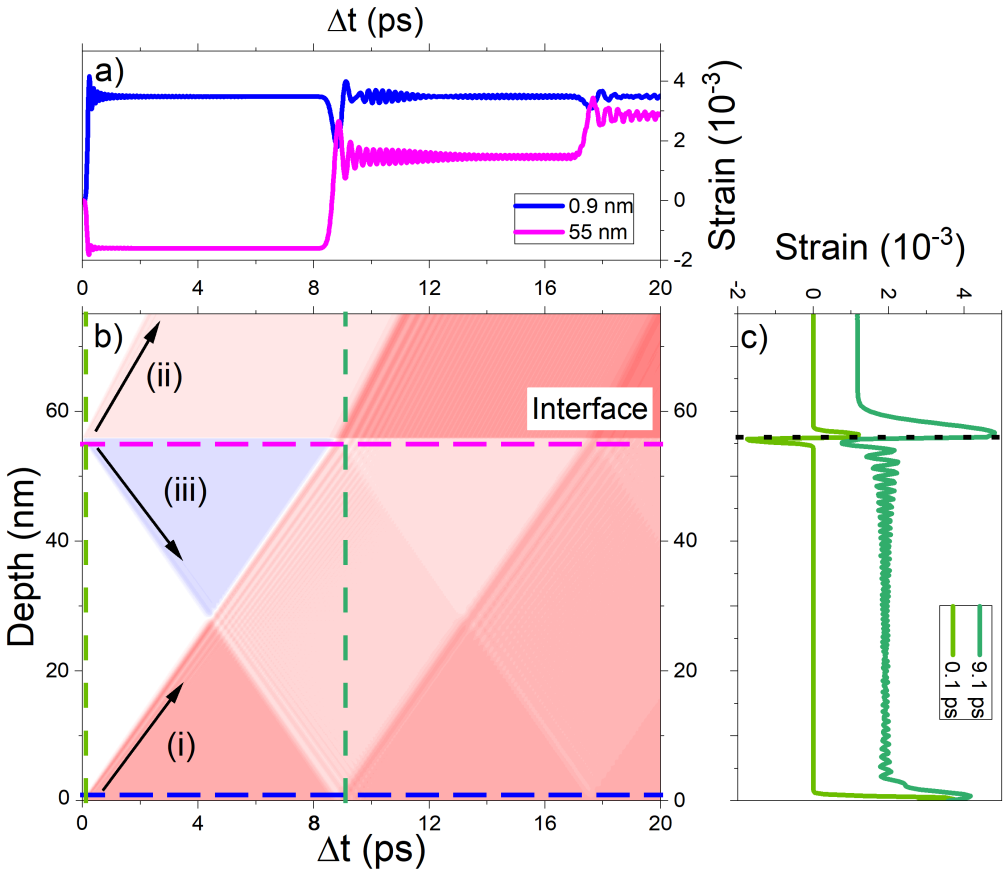

FIGURE 9.9: (**a**) time traces of the strain for two different depths. (**b**) map of the simulated strain, which is introduced to the sample for the first 20 ps after the excitation, by FDTD calculations. The color code refers to the sign of the strain: bluish colors - compression of the lattice; white - unchanged; reddish colors - expansion of the lattice. The black arrows point into the propagation direction of the three induced strain waves. (**c**) strain profile in dependence on the depth. The dotted, grey line marks the interface between LPCMO and MgO.

The fig. 9.9 (a) and (c) show strain profiles along the temporal axis and the depth of the sample, respectively. These simulation results underscore the hypothesis of BS. For instance, the blue curve in 9.9 (a), which represents the temporal evolution of the strain close to the sample surface, exhibits a strong variation in the strain at about $\Delta t \approx 9$ ps. This value is rather close to both the fitted Gauss position of the experimental data and to the value for $T = 300$ K of the rough estimation calculated with bulk values for the sound velocity.

In total, this leads to the conclusion, that feature No. 4, the peak-like structure, is most

likely the fist maximum of Brillouin scattering in the film.

The answer to the question, what causes the second increase in the psTR traces, the feature No. 3, which is described by τ_2, is not that obvious. Here, different possible explanations exist in literature. In elder papers [98, 100, 101, 135], one increasing function is part of the fitting routine for describing the ps-timescale in question. In all these publications, this temporal step is assigned to the spin-lattice relaxation. The reader will see later on that this hypothesis of the spin-lattice interaction is not a suitable explanation for the increase, which is found here in LPCMO.
In contrast to that hypothesis, the authors of [105] observed an increase of the transient reflectivity signal in LCMO and LMO at a timescale of $\sim$ 10 ps and assigned it to the electron-lattice interaction. Since, the feature No. 2 was assigned to the excitation of coherent optical phonons which are caused by the electronic excitation in sec. 9.2, the assignment of feature No. 3 to an electron-lattice interaction on the timescale of $\sim$ 10 ps would mean that two separate electron-lattice interactions persist in LPCMO.
Nevertheless, hints for a second electron-lattice interaction in a manganite compound can be found in literature where Li and co-workers [118] observed two timescale for lattice dynamics in $La_{0.84}Sr_{0.16}MnO_3$ using femtosecond electron diffraction (FED): they observed a first dynamical step in the order of about one picosecond and another lattice dynamics in the order of tens of picoseconds. Hence, their first and second process of lattice dynamics take place on similar timescale than the coherent optical and acoustical phonon excitation which are observed in this thesis.

To clarify which of both hypothesis, spin-lattice relaxation or second electron-lattice interaction, could explain the present case, one should have a closer look on the measurement data of LPCMO in fig. 9.10. In the upper panel (see fig. 9.10 (a)), exemplary traces of the reflectivity response are plotted for the timescale in question and the surrounding time steps. After the initial increase and the corresponding THz oscillations which are discussed in sec. 9.1 and 9.2, all traces turn into a second, slower increase which is comparable for each temperature. An appreciable difference between the different temperatures becomes notable on longer timescales ($\Delta t \gtrsim 10$ ps), where the behavior is split into two groups: a long-term relaxation

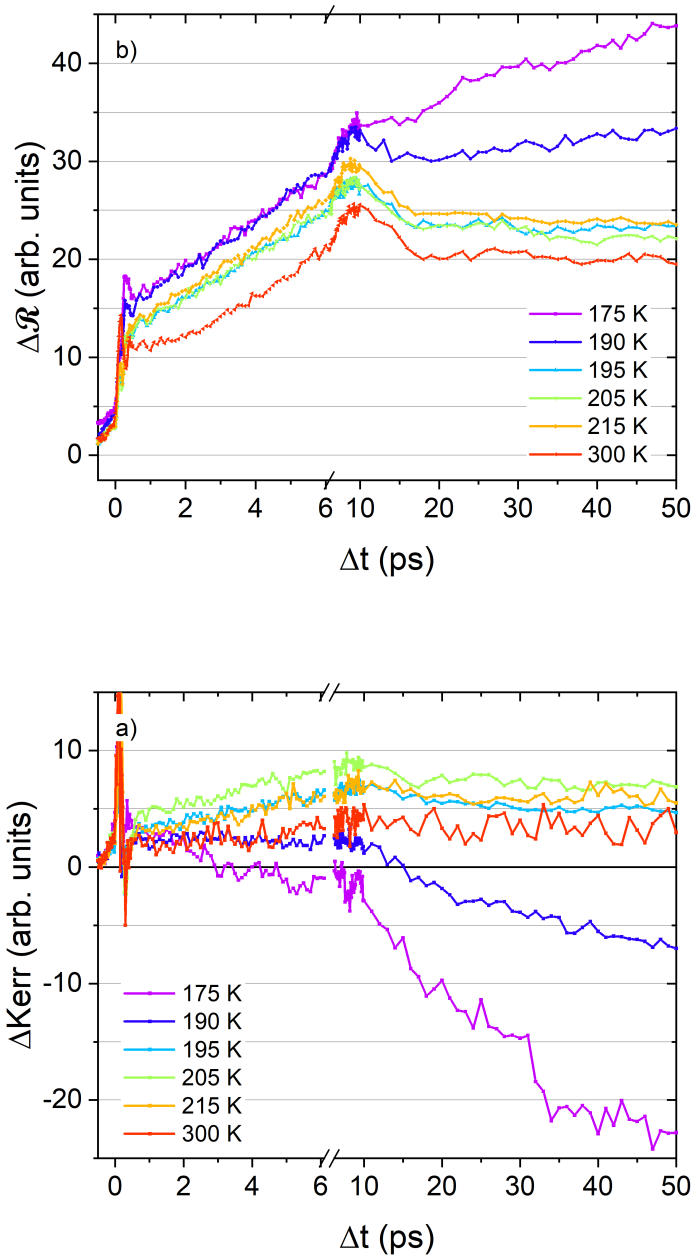

FIGURE 9.10: Comparison of the two signals (**a**) transient reflectivity and (**b**) time-resolved MOKE for an external magnetic field of $B = 120$ mT on the ps-timescale until 50 ps.

for $T < T_C$ and a third increase for $T > T_C$.[3]

The corresponding magneto-optical responses are plotted in the lower panel (see fig. 9.10 (b))

[3]The discussion of the third increase can be found in the following section 9.4.

for the same time window. The observed TRMOKE signal looks differently compared to the reflectivity, but, note that every feature which is visible in the psTR traces has a counterpart in the TRMOKE traces; every feature but one: there is no dynamics going on at the timescale of the second increase. Besides some side effects of the surrounding features, especially feature No. 4 and 5, the TRMOKE trace show a plateau between $\Delta t \sim 2 - 6$ ps. Due to only weak side effects, this plateau is most unambiguously visible in the cases of $T = 300$ K and $T = 190$ K. This finding excludes a magnetic dynamic as reason for the appearance of feature No. 3.

Since the magnetic structure of the sample stays unchanged (for all magnetic ground states of the sample), an energy relaxation between the spin and the lattice subsystem is rather unlikely. In conclusion, it is strongly suggested that the feature No. 3 of the reflectivity signal, the second increase, is caused by a second electron-lattice interaction.
As a final command, please note that it is not specified in this thesis, which kind of electron-lattice interaction drives the dynamics here. The measurement data of psTR or TRMOKE in the optical range do not provide any insights to the character of lattice effects, e.g., whether it is a localized (polaron) or a delocalized (acoustic phonon) lattice effect. To investigate this question, lattice-sensitive technique is suggested, such as FED or time-resolved x-ray diffraction.

9.4 Feature No. 5 - Spin-Lattice Relaxation

In this section the feature No. 5 which is mostly influenced by the phase transition will be discussed: the third exponential increase, described by A_3 and τ_3. The most remarkable property of this feature is the vanishing of it above the phase transition. This behavior is accessible by the two investigated external stimuli, temperature and magnetic field, as visible in fig. 9.11 (a) and (b). To underscore this phenomenon, the static SQUID-measurements, measured at the same applied magnetic fields in a cooling cycle, are plotted beside the T-dependent fit results of A_3 in fig. 9.11 (a). Note, that the statically measured SQUID-data are scaled individually in the y-direction in order to match the height of the amplitude of

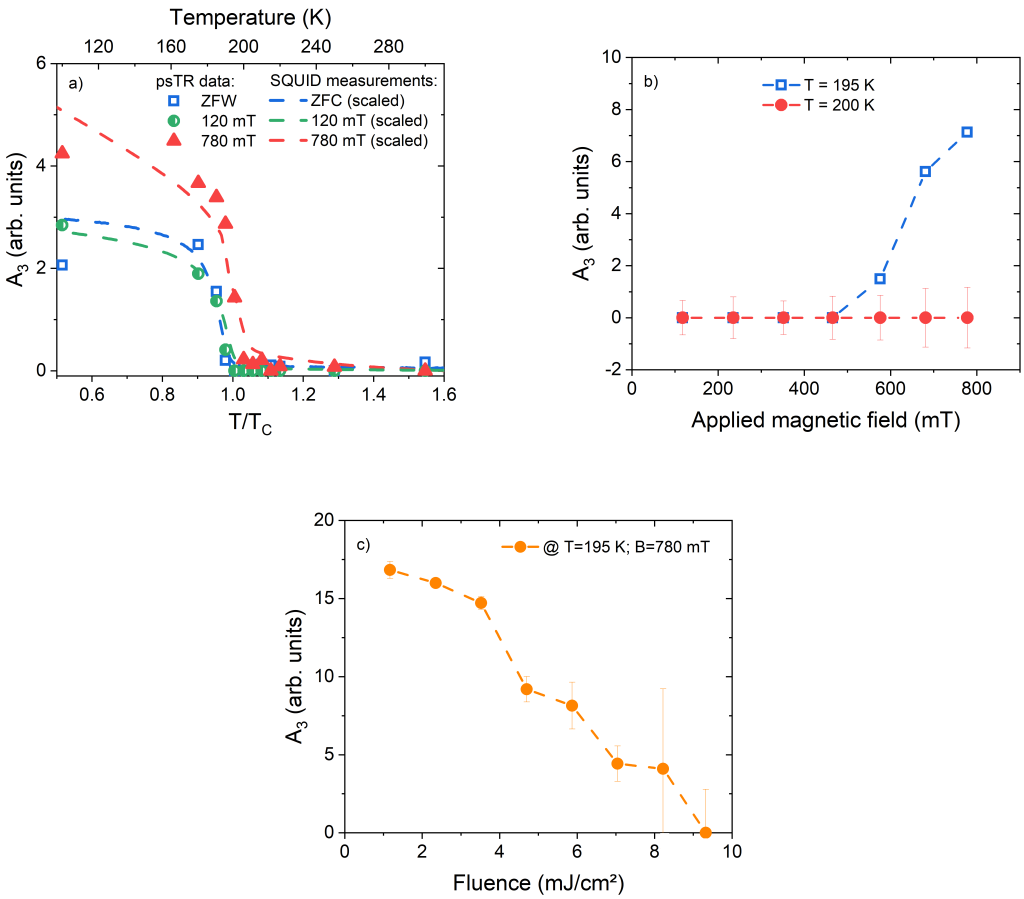

FIGURE 9.11: The fit results of the third exponential amplitude, A_3 of $\Delta\mathcal{R}$ in dependence on the three external stimuli: (**a**) temperature including the static SQUID measurements as color-matched, dashed lines, which are individually scaled in height; (**b**) external magnetic field and (**c**) the pump fluence.

the time-resolved measurements, A_3. The appearance of the ferromagnetic phase in the magnetization measurements and the appearance of the third exponential function match perfectly.

The two magnetic field-dependent series show two different behavior in fig. 9.11 (b). At a base temperature of $T_2 = 200$ K, non of the applied fields suffices to establish a sufficient ferromagnetic state to allow for a fit of A_3. For $T_1 = 195$ K, close to the statically measured T_C, a non-vanishing value of A_3 can be fitted for moderate fields, $B \gtrsim 500$ mT.

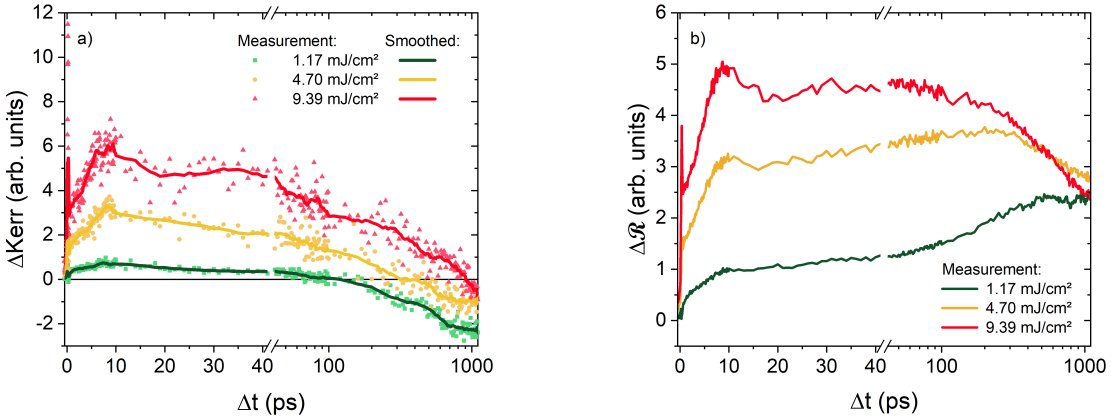

FIGURE 9.12: Measurement data of (**a**) the Kerr signal change and (**b**) $\Delta\mathcal{R}$ for three selected pump fluences. In (a), the smoothed data are meant as guide to the eye.

Note, that A_3 is equal to 0 for the case of the highest fluence in fig. 9.11 (c), too. But this might be misleading since the demagnetization time is strongly enlarged for high fluences hence it is overlapped by the thermal diffusion (see 9.5) already. As example for this trend, three TRMOKE traces, with different pump fluences, are plotted in fig. 9.12 (a) and the corresponding psTR traces in fig. 9.12 (b). It is visible that the slowing down of the demagnetization time leads to the result that the overlap between the τ_3 and the relaxation back into the ground state, τ_4, becomes such high that the amplitude, A_3, is not visible in the reflectivity measurements anymore. Hence, it is not resolvable for the fit.

The vanishing of A_3, when leaving the ferromagnetic metallic phase, is already quite a strong hint that the τ_3-process is connected to the spin order of the system. Nevertheless, for a normal ferromagnet it would not be expected to find a direct imprint of the magnetization dynamics in transient reflectivity data. Studies on elementary 3d transition metal ferromagnets [95, 96, 97] which investigated the transient reflectivity assume a two-tier or tripartite - depending whether they include the long term heat transport in the model or not - dynamic without considering spin-lattice relaxation as a signal part: electron-electron scattering, electron-phonon scattering, and thermal diffusion. In a first approximation, this reduction of the phenomenological fit to three time constants, electron-electron scattering,

electron-phonon scattering, and thermal diffusion, is plausible when analyzing the measurement procedure which is used here. Since, the MOKE signal is detected simultaneously, each plotted data point consists of an integer number of 2 points which are measured during individual measurement runs: at least, two runs are performed, for both polarity, $+B$ or $-B$, each. This is needed to extract the magnetic-field-induced asymmetry of the light polarization for the MOKE signal. But, since the psTR are calculated by the averaged sum of the measured intensity change, any magnetic-field-induced asymmetry effect, if existing in the intensity change of the sample, should cancel out in a good approximation.

But it is shown in literature [67, 92, 93, 94, 152] that the appearance of a ferromagnetic metallic phase coincides with a transfer of spectral weight in the case of (some) manganites, such as LSMO [67, 92, 94], charged ordered LSMO [93], LCMO [67, 92, 152], and NSMO [67]. Consequently, the transition into the FMM phase is connected not only to a polarization change of the reflected light, but also to an intensity change in a large range of visible and infrared wavelengths which is caused by a redistribution of the electron density of states when turning from an insulating gap to conducting states at the Fermi-energy. Time-resolved studies on manganites [98, 99, 100, 101, 102, 104, 151, 153, 154] demonstrated that it is possible to introduce dynamically a transient version of the spectral weight transfer (SWT) phenomenon (see also section 4.5.2). The so-called dynamical spectral weight transfer (DSWT) is already observed in PCMO [99, 153], LCMO [98, 100, 101, 104, 151, 154], LSMO [100, 102] as well as LMO [104]. Now, since energy is transferred into the system by the pump-pulse, the spectral weight transfer happens the other way around, as it is summarized by Lobad et al. [100].

For the here measured sample, a SWT is observed in the static optical spectroscopy measurements, see fig. 9.13. The results are comparable to the spectra of optimally doped LCMO which are published in [98]. For high temperatures, a peak of $1 - \mathcal{T}$ is found at around $\hbar\omega_0 \approx 1.2$ eV which starts to red-shifts when crossing T_C. This behavior demonstrates the band-gap closing when turning from the insulating into the metal-like state. The SWT from higher photon energies towards energies close to the Fermi-energy is underlined by the two grey curves in fig. 9.13 (c): a strong increase is found for $\hbar\omega_0 \approx 0.6$ eV (light grey) at about

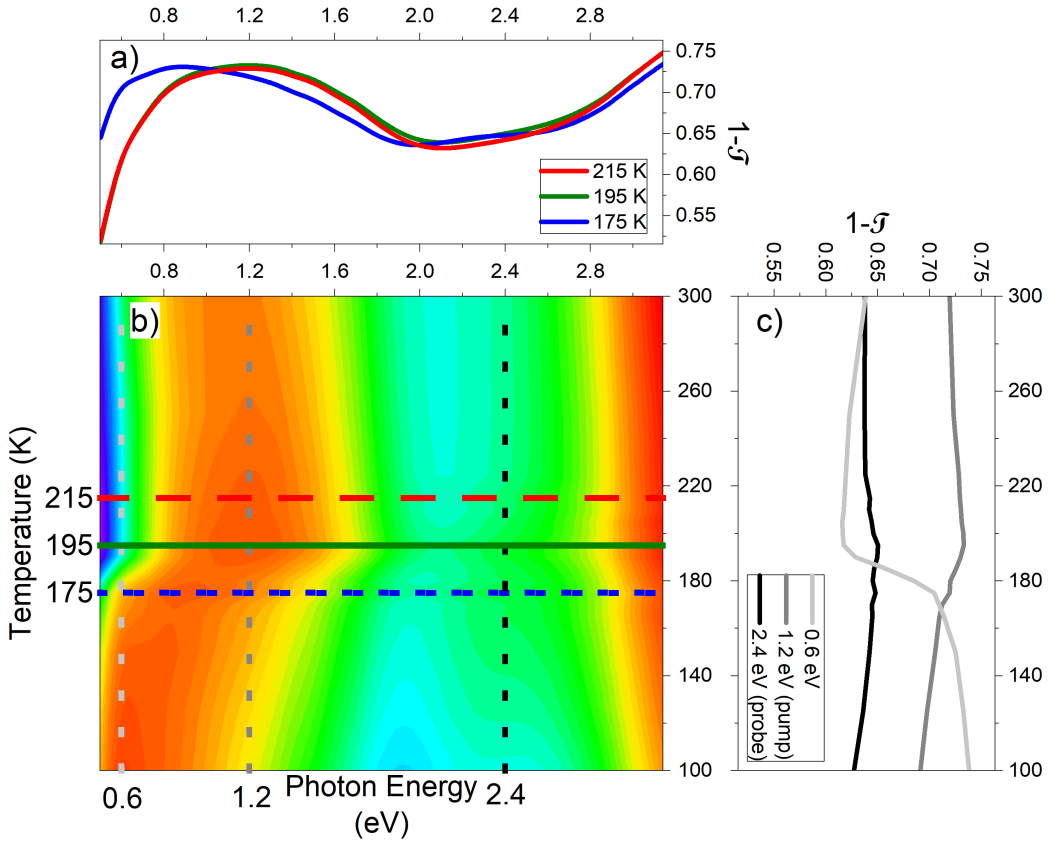

FIGURE 9.13: (**a**) $1 - \mathcal{T}$ in dependence of the photon energy for three temperatures across the phase transition. (**b**) Intensity map of $1 - \mathcal{T}$ dependent on the two parameter temperature and photon energy. The dashed and solid, horizontal and vertical line mark the profile position of the cuts in (a) and (c). (**c**) $1 - \mathcal{T}$ profile for three different photon energies: black - 2.4 eV (probe pulse); grey - 1.2 eV (pump pulse); light grey - 0.6 eV.

$T \approx 185$ K, whereas the photon energy of $\hbar\omega_0 \approx 1.2$ eV which corresponds to the pump energy in the time-resolved measurements looses spectral weight.

A similar phenomenon is believed to be observed in the transient reflectivity traces. Caused by the pump-excitation, the electron system is heated, followed by a shift of the spectral weight towards higher energies. When the spin-lattice relaxation sets in and the demagnetization starts, more and more electrons are flipped from the majority into the minority states, what leads to a larger SWT. The sign of the DSWT is independent on the direction of the applied magnetic field. In other words, the reflectivity changes continuously during the temporal evolution of the (spin-lattice) relaxation process, no matter in which direction the applied

B-field is pointing to; the signal change which is induced by the spin-lattice relaxation process is not canceled out by the average.

Therefore, an assignment of the third exponential process to the spin-lattice relaxation is plausible.

9.5 Feature No. 6 - Relaxation Back into the Ground State

The feature No. 6, which is described by the fourth exponential function, A_4 and τ_4, is the only decreasing element, which is found within the scope of the experiments. Therefore, it is assumed to be the long-term relaxation back to the ground state, after all subsystems, electron, phonon, and spin, are excited and thermalized with respect to each other to a quasi-equilibrium temperature which is nevertheless higher than the base temperature before the initial excitation. This quasi-equilibrium temperature, now slowly decreases by macroscopic relaxation processes, such as thermal diffusion, remagnetization, radiative recombination where applicable, and relaxation of induced quasi-particles.

In the temperature-dependent measurements, a strong increase of the relaxation time, τ_4, is observed, see the black data points in fig. 9.14, when the base temperature falls below T_C. As described in chapter 7, three phenomena might possibly cause this slowing down, which is approximately of an order of magnitude: (i) a strong change of the thermal transport properties might lead to an slowing down of the thermal diffusion; (ii) a critical slowing down might be induced by the fact that the re-ordering process of the spin system took more time while the restoring potential becomes smaller when approaching the Curie-temperature; or (iii) a melting/excitation of JT polaronic quasi-particle might need to be reversed.
In order to estimate the contribution of the thermal diffusion versus the contribution of the spin subsystem to this critical phenomenon, a finite-difference time-domain (FDTD)

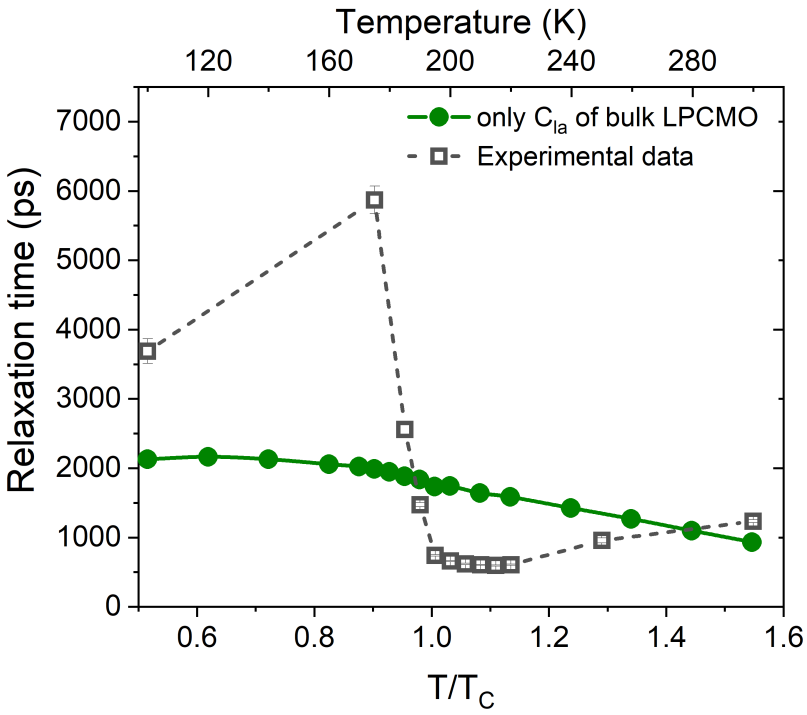

FIGURE 9.14: The fitted relaxation times of the measured transient reflectivity (black, open squares) and of the reflectivity, which is calculated by the simulated temperature change of the phonon system only (green, filled circles).

simulation [9, 120, 132] is performed by Tim Titze and Dr. Henning Ulrichs and is studied under two different kind of analyses. As a brief reminder, the model is based on a one-dimensional 3 temperature model, where the specific heat, optical parameters as well as thermal conductivity of both material systems, LPCMO and MgO, are fed as temperature-dependent input parameter next to the mass density, electron-lattice as well as spin-lattice coupling constant, and the Kapitza interfacial conductance, which are kept constant at all temperatures. For more information regarding the FDTD simulation model, see chapter 7.
In the case of the investigations on the contribution of the thermal diffusion, the model is computed as described in chapter 7 and, afterwards, the calculation of the resulting reflectivity signal are done by taking into account the response of the phonon system only. In other words, it is estimated that no contribution of the spin subsystem, e.g., the remagnetization, is visible in the transient reflectivity signal. Of course, this assumption is demonstrated to be wrong, as discussed in the previous section 9.4, but the assumption is necessary in order to determine the thermal diffusion contribution only. After, the reflectivity signal is simulated, the relaxation

back to the ground state is fitted by an exponential function. The results are plotted in fig. 9.14 next to the experimental data points for τ_4 from the zero field measurement.

As visible in fig. 9.14, the increase of τ_4 in the measurement data, when going from the PM into the FM phase, cannot be reproduced by this model. In general, the simulated temperature dependence of the relaxation time shows only slight changes, hence neither the experimental data points in the FM phase nor the data points in the intermediate phase are describable by this model, which is dominated by thermal diffusion. Experimental data and simulation results only show comparable values for high temperatures deep within the PM phase. Therefore, the outcome of this simulation model, which includes the thermal diffusion only, does not explain the found behavior of τ_4. Another model is needed.

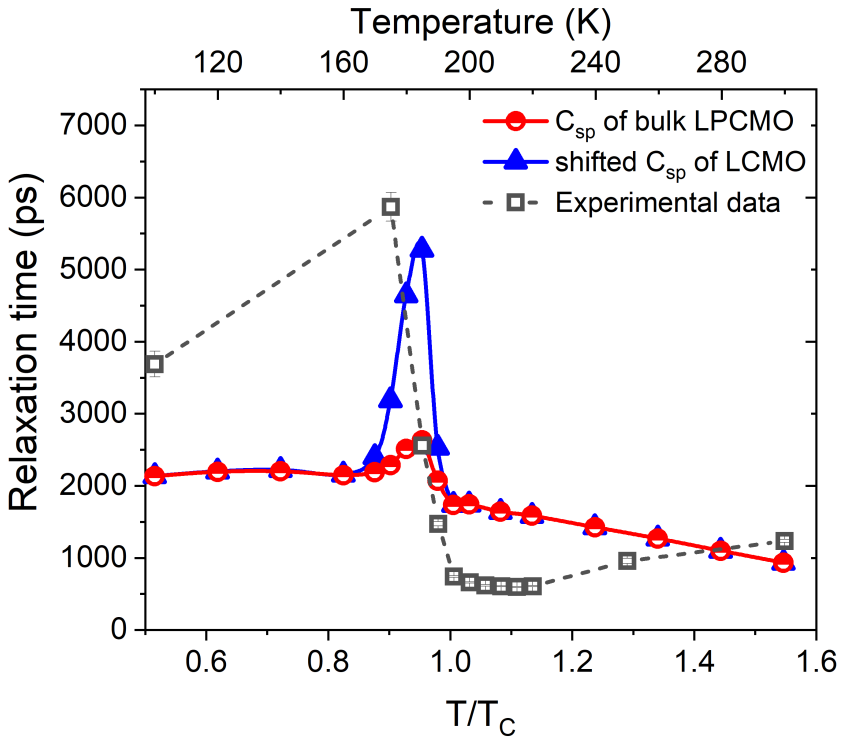

FIGURE 9.15: The fitted relaxation times of the measured transient reflectivity (black, open squares) and of the FDTD simulation, where the reflectivity is calculated by considering both the phonon and the spin subsystem, which is calculated for two different approaches: (red, half-filled circles) C_{sp} is equal to the values of bulk LPCMO [136, 137]; and (blue, filled triangles) C_{sp} is equal to the T-shifted values of LCMO [138].

An assuming model for the second hypothesis, where the rearrangement of the spin order after excitation needs more time when the restoring potential becomes smaller close to the phase transition temperature, can be set up by taking the findings of the previous section 9.4 and their consequences into account. In the former section, it is demonstrated that the spins-lattice relaxation contributes to the reflectivity signal. As a logical consequence of this, it is expected that the remagnetization process should be visible in the transient reflectivity signal, too. Thus now, the expected reflectivity signal, which results from the FDTD simulations, is calculated by the temperature change of the phonon as well as the one of the spin subsystem. It is assumed that both subsystems contribute to equal parts. The results are plotted in fig. 9.15, again next to the experimental results.

Since no measured heat capacity data of the used LPCMO thin film are available, two approaches are calculated. As a fist assumption, the bulk values of LPCMO [136, 137] are used. In the second estimation, the values of a related material, LCMO [138], are taken and shifted by the difference between LCMO and LPCMO transition temperature. In contrast to bulk LPCMO, a first-order-like phase transition is found for LCMO in literature [108]. Hence, the imprint of the LCMO PT occurs as a more δ-peak like behavior in the specific heat than for bulk LPCMO. In this way, an upper limit of the LPCMO thin film specific heat is modeled and tested in a FDTD simulation.

This second approach leads to results, which simulate the found experimental results much better (see fig. 9.15), but still do not completely reproduce the measurement data. Nevertheless, in these two cases, an increasing behavior is found at the Curie temperature. The resulting increase for the assumed C_{sp} of bulk LPCMO is quite small compared to the measured data, what originates from the second order character of the bulk LPCMO phase transition. The imprint of the transition in the specific heat is relatively smooth. In contrast, LCMO shows a first order transition [108], thus a more spike-like imprint is found at T_C.

Therefore, the interim conclusion of the τ_4-process is that thermal diffusion receives a share in the relaxation process; for the high-temperature paramagnetic phase, thermal diffusion might even account for the highest percentage of the τ_4-process. But, it cannot explain the massive increase of τ_4 when crossing the transition into the ferromagnetic phase. Instead, the additional energy dissipation channel, which appears for the ferromagnetic phase, empowers

the temporal storage of a part of the energy by the introduction of disorder to the spin system, i.e. the demagnetization. The reverse process of this disorder, the remagnetization, becomes lengthy close to the phase transition, which is known as the critical slowing down phenomenon. Due to this critical slowing down, the energy, which is stored in the disorder of the spin system, needs more time to convert into other energy dissipation channels, e.g., the thermal diffusion, which transports the pump energy away from the probed area. Hence, the relaxation process slows down, too.

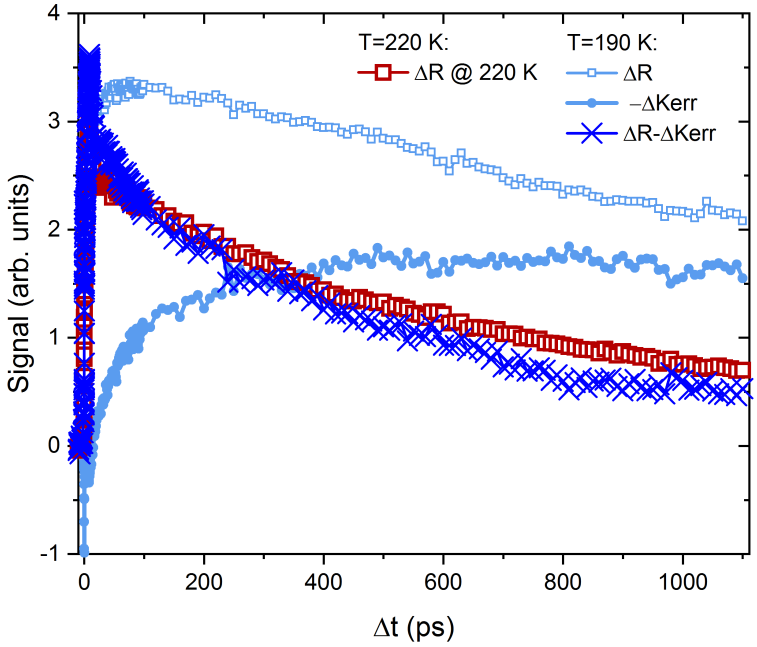

FIGURE 9.16: Experimental data for $F = 5.9$ mJ/cm^2 and $B = 120$ mT: The red, open squares correspond to the psTR at $T = 220$ K$> T_C$; the blue data points belong to $T = 190$ K$< T_C$, where the open squares represent the psTR data, the filled circles represent the negative TRMOKE and the big crosses correspond to the difference between psTR and TRMOKE.

In order to underline the critical slowing down of the spin subsystem as the reason for the strong increase of τ_4, another data proceeding step is suggested: the subtraction of the magneto-optical signal from the psTR signal. This step should give a second hint, if the

increase of τ_4 is explained by the critical slowing down. If a slowing down of the magnetization dynamics close to the phase transition causes the increase in τ_4 of the psTR data in the ferromagnetic phase, then the subtraction of the TRMOKE data should lead to an relaxation time, which is comparable to the relaxation time of the unchanged psTR data above T_C. As an example, the data set measured at $T = 190$ K, $F = 5.9$ mJ/cm^2 and $B = 120$ mT is plotted in fig. 9.16; for comparison the psTR data, which are measured at a base temperature of $T = 220$ K, is shown, too. Comparing both data sets, the unchanged set above T_C (red squares) and the difference set for $T < T_C$ (blue crosses), a similar behavior is found, including relaxation times of the same order. Note, that in this evaluation step two assumptions are done, which should be further examined. First, two different kind of measurement signals, an intensity change and a polarization change, are compared to each other. If the dynamical spectral weight transfer is proportional to the induced demagnetization, this would be an appropriate assumption. The second assumption is that the magnetic change of the reflectivity signal is considered to contribute equally to the total reflectivity change than the rest. This second assumption is misleading if the ratio between the electron-lattice and spin-lattice coupling constant is temperature dependent.

This second type of FDTD model, where the DSWT is taken into account by considering the change of the spin temperature as a part of the transient reflectivity signal, strongly suggest an assignment of the strong increase in τ_4 to the critical slowing down of the spin subsystem close to the FM/PM phase transition.

Still, the FDTD simulation is not capable to reproduce two parts of the results. The experimental results for the intermediate, antiferromagnetically coupled phase (approximately $T_C \lesssim T \lesssim 1.2 \cdot T_C$) are over estimated by a factor of about ~ 2. And the relaxation time deep in the ferromagnetic phase is underestimated[4]. These mismatches might be caused by the fact that the FDTD model is based on a simple one-dimensional 3 temperature model. For instance, one assumption of the 3TM is that the coupling constants $g_{i,j}$ are independent on the temperature. This approximation might be sufficient deep inside an single phase, e.g., the paramagnetic phase. But obviously, the spin-lattice interaction changes dramatically for

[4]Note, that here one measured data point exist only. See $T = 100$ K.

example in the phase-separated region. It is shown in [8] that the ferromagnetic-metal to paramagnetic-insulator transition occurs via a phase separation region, where nano-scaled ferromagnetic domains are antiferromagnetically coupled with respect to each other which is mediated by a insulating matrix of correlated Jahn-Teller polarons. This behavior suggests that the interaction between the electrons and the lattice changes throughout the whole region [80]. In addition, the presumption that the system can be modeled by three subsystem, which interact via two coupling constants, $g_{el,la}$ and $g_{la,sp}$, might be wrong: the suggestion of the second exponential increase, τ_2, being assigned to a second electron-phonon coupling requires a model with a second electron-phonon coupling constant, which enables this additional energy transfer. Finally, quasiparticles, such as correlated Jahn-Teller polarons, which either might be destroyed by the laser pulse and therefore need to be arranged or might be induce by the light as long living quasiparticles which would need to relax again are also not considered in the 3 temperature model.

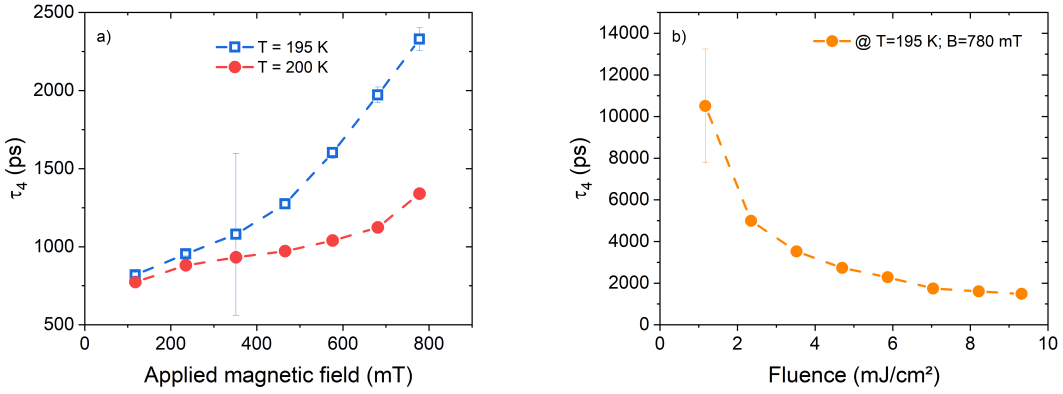

FIGURE 9.17: Fit results for the fourth time constant, τ_4, depending (**a**) on the external magnetic field, which are measured at $T_1 = 195$ K (blue, open squares) and $T_2 = 200$ K (red, filled circles) both at $F = 5.9$ mJ/cm^2; and (**b**) on the fluence at $T = 195$ K and $B = 780$ mT. The error bars are calculated from the fit. The color-matched dashed lines as guide to the eye.

Nevertheless, with the assignment of the strong increase, when turning into the FM phase, to the critical slowing down of the spin subsystem, the B-field-dependent and fluence-dependent results of τ_4 (see fig. 9.17) can be understood as a shift of the transition temperature, which is

controlled by the external simuli $B,\ F$.

In fig. 9.17 (a), an increase in the relaxation time τ_4 with the external magnetic field is found for both base temperature, whereby the increase is stronger for $T = 195$ K. By applying an external magnetic field, the ferromagnetic phase is stabilized and the static transition temperature is shifted towards higher values. For the magnetic fields, which are applied during the measurements, the static transition temperatures are determined to range between $T_{C,1} = 194$ K ($B = 0.1$ mT) and $T_{C,2} = 200$ K ($B = 780$ mT) by SQUID magnetometry. In case of the psTR series at $T = 200$ K, the base temperature is above the field-dependent T_C with the exception of the highest field; the ground state of the sample is already the intermediate, phase separated state. When pumping energy into the system by the fs-pump pulse, the phase does not change and no phase transition is crossed. Instead, the remaining alignment of the spin subsystem to the external field, which still exist in the phase separated state, becomes randomized. The resulting τ_4, the relaxation time back to the ground state, is slightly increased with respect to the purely paramagnetic phase, since the small amount of spin alignment, which is left at the ground state, needs to be rearranged. But it is still faster than for a ground state shortly below the Curie temperature. Now, if the external magnetic field is increased, more spins are aligned within the field in the ground state, since the transition temperature is closer to the base temperature. As a result, the recovery of the spin system after the excitation requires more time; τ_4 increases.

If the sample is cooled to $T = 195$ K, already moderate fields force the spin system into the ferromagnetic ground state. When these moderate fields are applied and the system is excited by a pump pulse, the system reacts with a transient change of the magnetic phase; for a short amount of time, the excited LPCMO crosses the Curie temperature into the intermediate, AFM state. To relax back into the ferromagnetic ground state, the sample needs to remagnetize. As discussed above, this required more time.

An opposite effect is observed, if the fluence in increased close to the Curie temperature: the relaxation time, τ_4, decreases. In fig. 9.17 (b), the results of such a measurement series is plotted. Here, the sample is kept under the conditions $T = 195$ K and $B = 780$ mT, thus the ground state of the sample is ferromagnetic, but close to the transition temperature. In the limit of low fluences, the heating of the subsystems by the pump pulse is low. Nevertheless,

the demagnetization is close to 100 %, since the base temperature is already close to the phase transition. Since a small transient temperature change is induced by low fluences only, the restoring potential is also low. As a result, the re-ordering of the spin system during the relaxation process slows down. In contrast, if the value of the fluence is increased, the transient temperature change is higher. As a consequence, the restoring potential is higher and the remagnetization process becomes faster.

As a last step of this discussion, the relaxing dynamics of the time-resolved magneto-optical response is going to be analyzed. Unfortunately, in most of the TRMOKE traces, which are measured within the T-, B-, and F-dependent series, no remagnetization behavior is visible within the maximum pump-probe delay of $\Delta t = 1.1$ ns. In principle, this might be a hidden corroboration of the critical slowing down hypothesis. In the previous section 9.4, it is shown, that the DSWT causes a visibility of the magnetization dynamics in the transient reflectivity traces. Hence, the relaxation process, τ_4, is merged from different contributions, such as remagnetization, thermal diffusion, or the collapse of potentially excited, long-living quasi-particles, respectively the recovery of potentially destroyed quasiparticles. But, in contrast to the TRMOKE traces, a relaxing behavior is visible in almost every transient reflectivity trace; see appendix B1, fig. B.2, and B.2. Since, most remagnetization processes are not visible in the TRMOKE data, the other possible relaxation processes need to be faster in average than the remagnetization. Otherwise, the τ_4 timescale would not have be found in the the scope of the experiments.

Nevertheless, a clearly visible remagnetization is observed in the three TRMOKE traces which are plotted in fig. 9.18. To visualize the slowing down trend of the magnetization dynamics, the turning points where the remagnetization process starts to dominate the single traces are marked by the color-matched vertical lines. The slowing down in the MOKE data follows the trend for the τ_4 fit results of the reflectivity data, see inset.
Two arguments are found in the TRMOKE data. First, next to the remagnetization process, another, faster process needs to contribute to the reflectivity signal, in order to explain the visibility of a relaxing behavior in almost all psTR data. Second, as far as the remagnetization

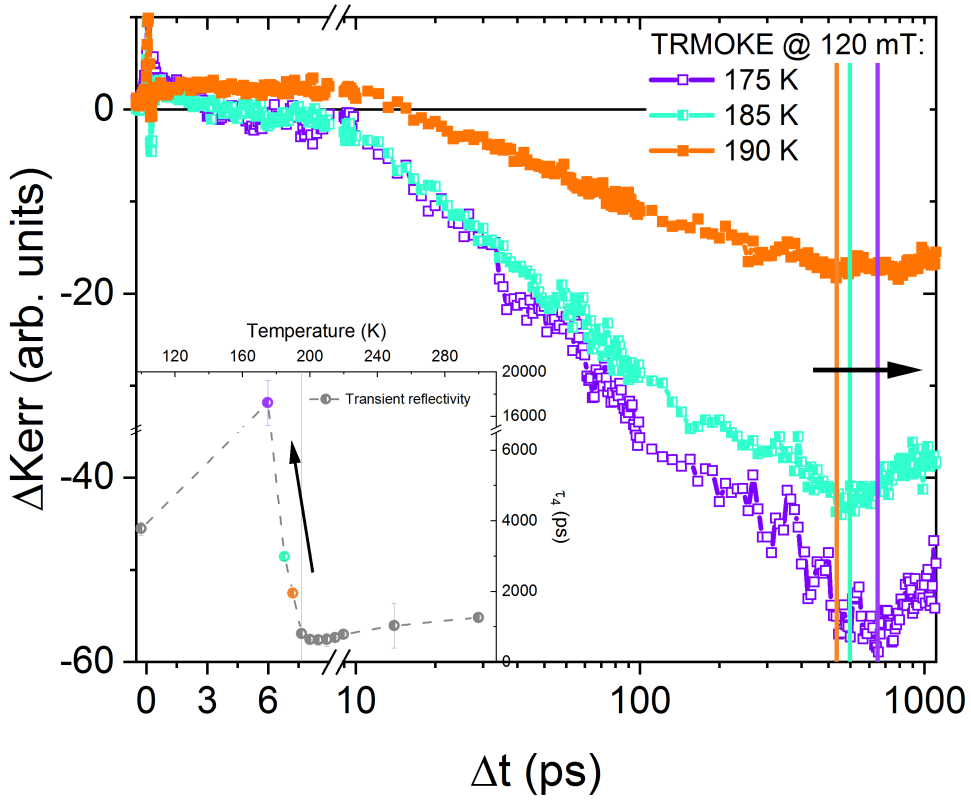

FIGURE 9.18: **Main graph**: three examples of TRMOKE traces in which a remagnetization process becomes clearly visible. The data are part of the T-dependent series, which is measured at $B = 120$ mT and $F = 5.9$ mJ/cm^2. The color-matched vertical lines mark the turning point of the traces, where the remagnetization process becomes dominant. The **inset** shows the fit results for τ_4 of the transient reflectivity traces. The data points, which correspond to the TRMOKE traces in the main graph, are color-matched.

behavior of the TRMOKE signals can be evaluated, the needed time for the re-ordering of the spin system becomes longer with a trend which is comparable to the slowing down trend for τ_4. Both arguments underline the assignment of the strong increase in τ_4 to the critical slowing down of the magnetization dynamics when approaching the phase transition.

In conclusion, at least two contributions to the relaxation step back into the ground state, which is described by the fourth time constant, τ_4, of the fit, eq. 8.1, are found which dominate the function on different thermal regions. By the comparison of the experimentally determined

τ_4 and the results of the FDTD simulations, thermal diffusion is found to be the predominant energy dissipation path at high temperature within the paramagnetic phase, e.g., at room temperature. The combination of the TRMOKE signal and a FDTD simulation model, which contains the contributions of the spin dynamics to the reflectivity signal, strongly suggests the critical slowing down of the magnetization dynamics close to the FM/PM phase transition as reason for the strong increase of τ_4 in that temperature region.

Most likely, next to the thermal diffusion and the magnetization dynamics, a third processes contributes to the relaxation step. Hints for this are found in the mismatch between the experimentally determined τ_4 and the simulated relaxation time, especially in the region of the intermediate polaronic state. This leads to the idea that this third process might be connected to the excitation or the melting of (polaronic) quasiparticles, which need to relax on the long-timescale. Neither the scope of the experiments nor the FDTD models are sufficient to review this hypothesis. In order to access the lattice dynamics in a more appropriate approach, experiments, such as femtosecond electron diffraction [117, 118, 155], are recommended to investigate the long-term dynamics of the lattice after a fs-excitation of the electron system.

9.6 Discussion Summary of the Dynamics in LPCMO

In conclusion, a thin film of LPCMO is investigated by two different time-resolved optical spectroscopy techniques: transient reflectivity, in order to be sensitive to the changes in the electron distribution, and the transient magneto-optical Kerr effect, in order to probe the magnetic contributions to the dynamics.

In both data sets, up to six dynamical features are found which are assigned to: (1) initial excitation and thermalization of the hot electrons; (2) imprint of coherent optical phonon excitation; (3) a second electron-phonon interaction; (4) Brillouin scattering inside the LPCMO layer; (5) spin-lattice relaxation (within the ferromagnetic phase only); (6) long term relaxation back to the ground state, e.g., by remagnetization process, thermal diffusion or else.

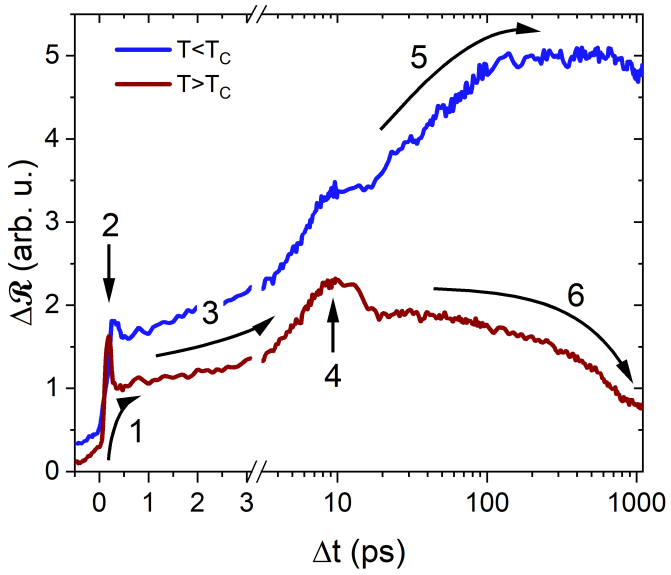

FIGURE 9.19: Two exemplary traces of the psTR signal for a temperature below the Curie temperature (blue), and a temperature above T_C (red). The arrows mark the features which are discussed in this chapter.

The TRMOKE signal which is found above T_C is remarkable, not just because it exists even 100 K above the magnetic transition temperature, but also due to the fact that an increasing behavior is found, which occurs at the lower ps-timescale within the ferromagnetic phase before the spin-lattice relaxation starts, too.

The greatest changes in the psTR data, which are found while crossing the PT, are the emergence of an additional energy dissipation step, A_3 and the slowing down of the relaxation time, τ_4. The emerging A_3-process is shown to represent the spin-lattice relaxation, which becomes detectable by transient reflectivity due to the dynamical spectral weight transfer. The slowing down of τ_4 is directly connected to the necessary reordering of the spin system with in the ferromagnetic phase. It peaks at the PT in the so called critical slowing down, where the relaxation time expand up to more than 16 ns by a factor of more than 20.

By the combination of both techniques, the initial excitation is suggested to mainly be a charge transfer process, where an electron from an O2p state is transferred to a state of a Mn

ion, e.g., most likely the empty e_g, 1 of a Mn^{4+}. Hints for this hypothesis are first the initial increase in the MOKE data, which seems to be more dependent on the external magnetic field than on the magnetic ground state of the sample. This increase might be explained by the change of J, which would is coupled to such a CTT. Furthermore, the dependence on the fluence might underline a two-photon excitation. The so reached excitation energy of 2.4 eV would correspond to literature values [67, 91, 92, 146, 147, 148] which are assigned to this transition type.

Nevertheless, another hypothesis which considers a strong excitation-dependent change of the band structure, e.g., a light-introduced transition into a hidden phase, cannot be discussed here due to the absence of supporting theoretical calculations. Therefore, it is explicitly not excluded as an explanation for the observations. In addition to the theoretical calculations, it is recommended to augment the experimental data portfolio by measuring additional temperature-dependent series for different fluences while keeping the magnetic field constant, e.g., at $B = 780$ mT.

Overall, it was shown that the energy dissipation pathway can easily be controlled by the manipulation of the phase transition by external stimuli in thin films of the CMR material $(La_{0.6}Pr_{0.4})_{0.7}Ca_{0.3}MnO_3$.

Part 3

Non-Equilibrium and Quasi-Equilibrium Dynamics of $La_{0.7}Sr_{0.3}MnO_3$

CHAPTER 10

Experiments on $La_{0.7}Sr_{0.3}MnO_3$

10.1 Sample System - $La_{0.7}Sr_{0.3}MnO_3$

Three optimally doped $La_{0.7}Sr_{0.3}MnO_3$ (LSMO) films are grown on a Ti-terminated (100)-$SrTiO_3$-substrate by metalorganic aerosol deposition (MAD). The static magnetic, structual, and electronic properties of thin LSMO films grown at STO are well known. Static properties of LSMO thin films at STO(100) are published in [6, 156]. The exact properties of the here used samples are summarized in table 10.1. The transition temperatures for the second and third sample were again determined by SQUID magnetometry [126, 127]. Since, the substrate for the main sample is too big to install it into the SQUID, a different method was used to measure T_C. Utilizing the cryostat, the electromagnet and the fs-probe of the time-resolved setup, static hysteresis loops are recorded by exploiting the static magneto-optical Kerr effect. The difference between the saturation magnetization for $\pm B$ are plotted in dependence on the temperature in fig.

The thicknesses of all films are determined by measuring the XRR which is analized by the software

TABLE 10.1: Static characteristics of the LSMO thin films:

	Main sample	Second sample	Third sample
Substrate	10×10 mm^2	5×10 mm^2	5×10 mm^2
Curie temperature @ 100 Oe	353 K	350 K	357 K
Film thickness	56 nm	76 nm	30 nm

10.2 Ultrafast Optical Spectroscopy Setup

The impact of external stimuli on the dynamics close to the FM/PM-PT was measured with an optical pump-probe spectroscopy setup, at which sub-40 fs laser pulses were used (s. fig. A.2). This laser pulses are provided by an fiber amplifier system by *Active Fiber Systems* with an of 50 kHz repetition rate. Again, the fundamental IR-laser beam ($\lambda_c = 1030$ nm) is used to pump the system, whereas the second harmonic ($\lambda_{probe} = 515$ nm) is used as probe to detect the induced changes in the transient reflectivity and simultaneously TRMOKE.
Similar as before for LPCMO, the ^{4}He-cryostat with the sample is placed in between the poles of a variable-gap electromagnet. But in contrast LPCMO, the LSMO sample is arranged parallel to the magnetic field and the angle of the incident light is about 45°. Hence, the LSMO systems are measured in an usual longitudinal TRMOKE geometry. After the interaction with the sample, the beams are reflected onto dielectric mirrors, which are designed to be highly reflective for the probe beam and highly transparent for the pump beam. A non-polarizing beamsplitter is used to measure the time-resolved magneto-optical Kerr effect (TRMOKE) and the transient reflectivity (psTR) simultaneously with the help of two detectors. The reflectivity detector is a single Si-photo diode with an integrated, tunable amplification by *Thorlabs*. On the other hand, a balanced-bridge detector is applied to measure the MOKE-signal.
A temporal delay between both the pump and the probe pulse is created by sending the pump-beam though a piezo-controlled stage before the beam hits the sample. The positioning of the delay stage enables a scanning range of more than 1.1 ns.

Finally, the environmental control is achieved by a variable-gap electromagnet and a ^{4}He cryostat in between the gap, both by *Lake Shore*. For the measurements on LSMO, the samples are positioned in such way that the in-plane component of the thin film magnetization lies parallel to the magnetic field lines of the electromagnet. The laser light is reflected in a 45°-angle. In this way, environmental conditions of $T = 150 - 380$ K and $B = 0 \sim 600$ mT as well as $F \approx 0.4 - 2$ mJ/cm^2 were applied to the samples.

CHAPTER 11

Results - $La_{0.7}Sr_{0.3}MnO_3$

11.1 Ultrafast Reflectivity of Thin LSMO Films

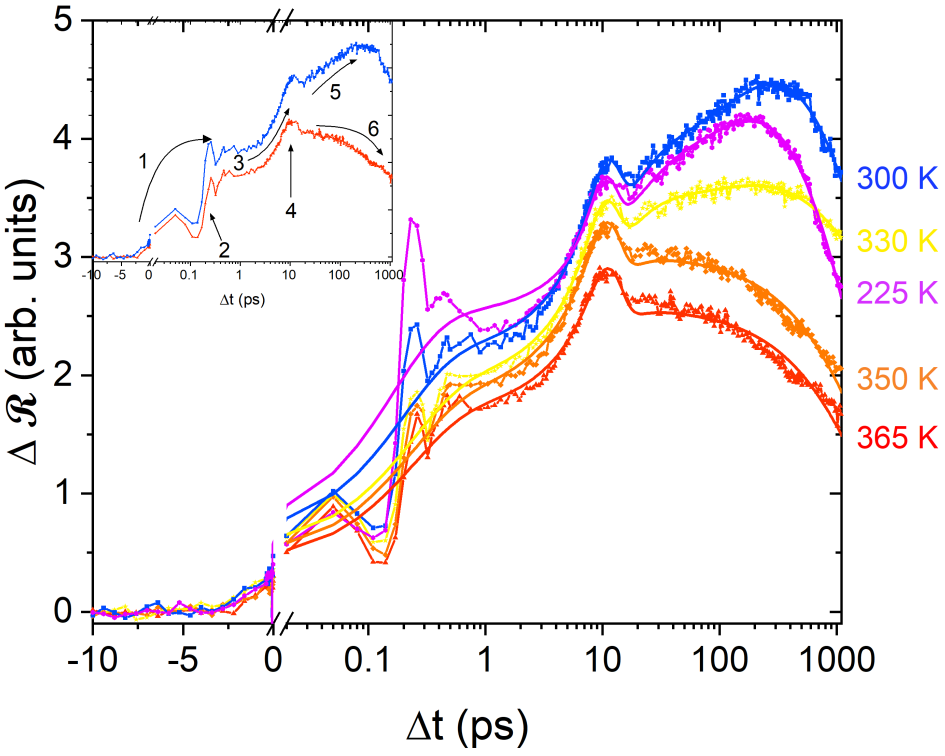

FIGURE 11.1: Exemplary traces of the time-resolved reflectivity change for five temperatures (as labeled in the graph) measured on LSMO ($T_C = 353$ K). The color-equivalent, solid lines represent the associated fits (see eq. 8.1).

As described in chapter 10, a variety of different time-resolved measurements with a pump energy of about 1.2 eV and a probe of about 2.4 eV has been performed. Two different kind of detectors were used to access the magneto-optical responds as well as the transient

reflectivity simultaneously. Typical measurement traces are plotted in fig. 11.2 (psTR) and 11.14 (TRMOKE).[1] As visible when comparing fig. 8.1 and 11.1, similar features in the psTR-data appear for both materials, LPCMO and LSMO; the features 1-6, see chapter 8, can be identified in LSMO, too:

(1) initial increase due to the fs-laser excitation
(2) oscillations at the first hundreds of femtoseconds
(3) further increase of the reflectivity change on a-few-ps-timescale
(4) peak-like structure at $\Delta t \approx 10$ ps
(5) third increase in the reflectivity change at the timescale of a couple of tens pico-seconds
(6) decrease of the signal.

Therefore, the reflectivity data are evaluated in the same way than the LPCMO data. For extracting the time constants, τ_1 till τ_4 the equation 8.1 is fitted here, too:

$$\Delta\mathcal{R} = G \cdot exp(-(t - t_P)^2/2 \cdot \omega) - \sum_{i=1}^{4} A_i \cdot exp(-\Delta t/\tau_i).$$

The fit results for the psTR measurements depending on different external stimuli, $T,\ B,\ F$, will be presented in the following sections, 11.2.1 - 11.2.3.

In the second part of this chapter (11.2), the behavior of the TRMOKE signal of LSMO (see fig. 11.14) will be found to be quite different from the TRMOKE traces of LPCMO (compare fig. 8.14). Unfortunately, due to the high noise level and the disadvantageous long dynamics - compared to the delay range of the experiment (1.1 ns) - a fit of the TRMOKE traces by eq. 8.1 does not lead to clear and credible trends since the fit results spread quite strong around possible trends. Therefore, only a qualitative evaluation is presented.

Note, that in the following, almost no amplitudes, A_i, are presented. The reason for this

[1] Note, logarithmic x-scaling in both cases provides the recognizability for all timescales. Moreover, this type of scaling might enable readers to comprehend the later used model (see equation 8.1) more easily.

is that the different series are not measured within one run, but almost a year of time span with partly several weeks of break in between two series. Due to that, a full adjustment and signal optimization procedure was done for every single measurement series. That included a signal-to-noise-ratio-optimization by tuning the probe intensity. Since the signal amplitudes depend rather drastically on the incident probe intensity, the amplitudes vary quite strongly between two series compared to the field- or pump-fluence-induced effects. Furthermore, the reflectivity change, ΔR, cannot be normalized since only differential changes are measurable by the setup. Therefore, a comparison of amplitudes form different series might be deluding. In compensation, two additional series are performed on two additional samples in order to determine the change in the amplitudes of the first and second process by varying the external magnetic field and the pump fluence at least for $T = 200$ K.

11.1.1 Temperature-Dependent Reflectivity Dynamics of LSMO

Since the parameters of LSMO develop differently compared to LPCMO throughout the temperature range, typical evolution traces of the time constants, τ_1 - τ_4, for LSMO are presented in fig. 11.10 (a) - (d). The full set of measurements belonging to this series is shown in the appendix B.4.

Starting with the earliest timescale, τ_1, see fig. 11.2 (a), a non-linearly increasing behavior for the FM phase is found which turns into a slight decay for the PM phase. As a result, a maximum in τ_1 appears slightly beneath the static transition temperature. Taking into account all presented data (see, e.g., fig. 11.6 (a) and 11.10 (a), too), τ_1 varies between ≈ 80 fs and ≈ 250 fs depending on the external stimuli.
τ_2 shows an opposite behavior in fig. 11.2 (b). Approaching T_C from below, τ_2 speeds up. For the PM phase, it seems to level off to a value of roughly ≈ 6 ps which seems to be more or less independent of the external stimuli. Altogether (see, e.g., fig. 11.6 (b) and 11.10 (b), too), the second time constant varies between 6 ps$\lesssim \tau_2 \lesssim 20$ ps.
In fig. 11.2 (c), the values of τ_3 are plotted for those cases which full-fill the condition $A_3 > 0$. For low temperatures, τ_3 slightly decreases reaching a turning point at about ~ 90 % of

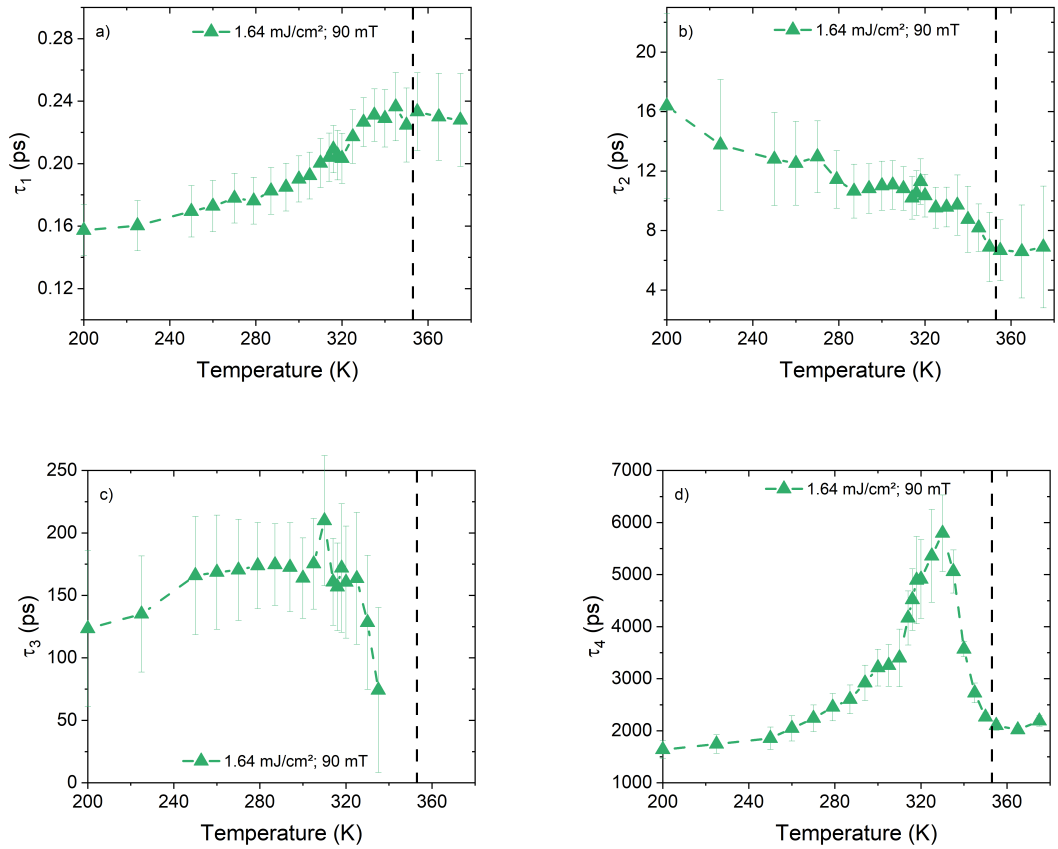

FIGURE 11.2: Exemplary, temperature-dependent fit results for $\Delta\mathcal{R}$ of the four time constants of the exponential functions from eq. 8.1: (**a**) τ_1, (**b**) τ_2, (**c**) τ_3, and (**d**) τ_4. All data are measured at an applied magnetic field of $B = 90$ mT and a fluence of $F \approx 1.6$ mJ/cm^2. The errors are calculated from the fit. The color-matched lines as guide to the eye. The vertical, dashed, black line marks the statically determined $T_C = 353$ K of the LSMO sample.

T_C and finally drops down till it disappears. Within the measured range, τ_3 reaches values between ~ 25 ps and ~ 300 ps (see, e.g., fig. 11.6 (c) and 11.10 (c), too).

For temperatures (far) away from the transition, τ_4 exhibits quite similar levels of 1000 ps - 2000 ps in both the FM and the PM phase, see fig. 11.2 (d). But at about $T \approx 0.95 \cdot T_C$, a strong peak is found which shows a long grade coming from low temperatures, whereas a fast decay is observed when turning into the PM phase. Depending on the conditions, τ_4 rises up to values well above 10 ns at this spike.

In the following sections, it will be shown that the height of this peak as well as the center

position changes for different external stimuli. Since, a reliable way of evaluating these quantities is needed, different peak functions are tested as fitting routine. Next to Gaussian and Lorentzian functions which failed due to, e.g., the symmetric flanks in both functions, the in the context of phase transitions well-known asymmetric double sigmoidal function (Asym2Sig) is tested. The latter type of fitting turned out to be the most credible as visible in fig. 11.3. Here, the results for the different fit functions are plotted. It is clearly visible that the symmetry of Gaussian and Lorentzian functions lead to an underestimation of the peak position as well as the peak height. Thus, the asymmetric double sigmoidal fit will be used in the following to evaluate the τ_4 behavior further.

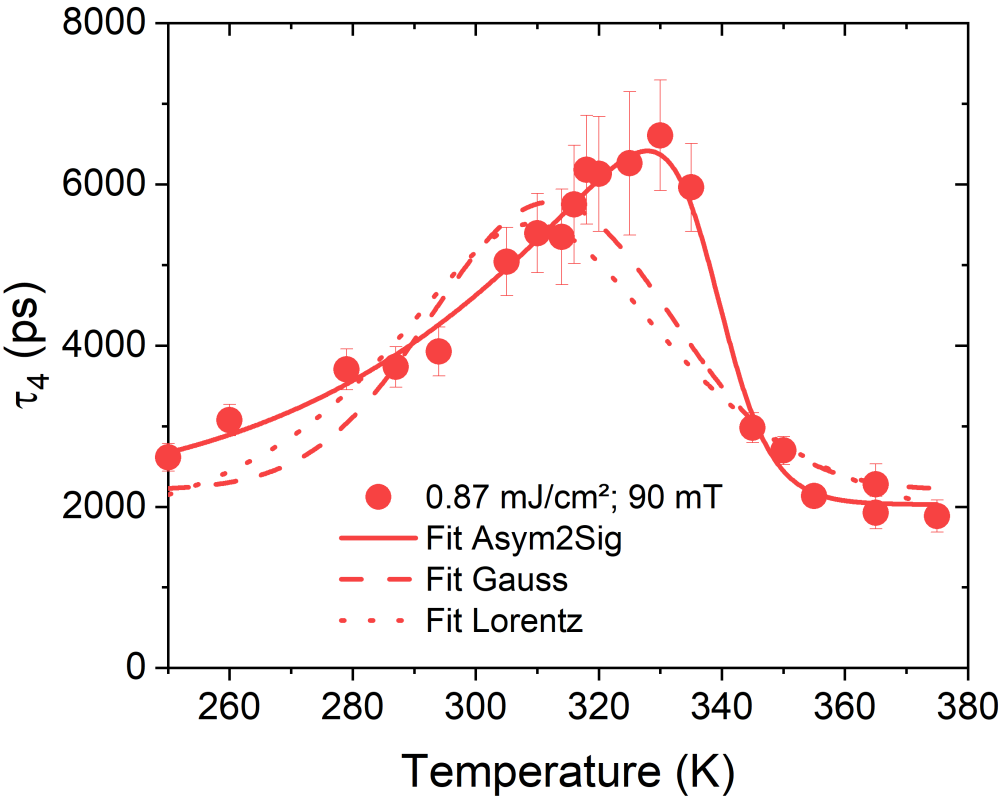

FIGURE 11.3: Exemplary temperature-dependent τ_4 series (red data points) and three different fit models: solid line - an asymmetric double sigmoidal function, dashed line - Gaussian peak function, and dotted line - Lorentzian peak function. The error bars of the data point are calculated from the fit of eq. 8.1.

Turning to the overall temperature dependence of the amplitudes, an almost linear decrease is observed for A_1 in fig. 11.4 (a). Beside this decrease, a small kink possibly shows up at about $T \approx 320$ K. But within the noise level (also in other series), it is not clear whether the slope changes at this temperature or it is just randomly appearing.

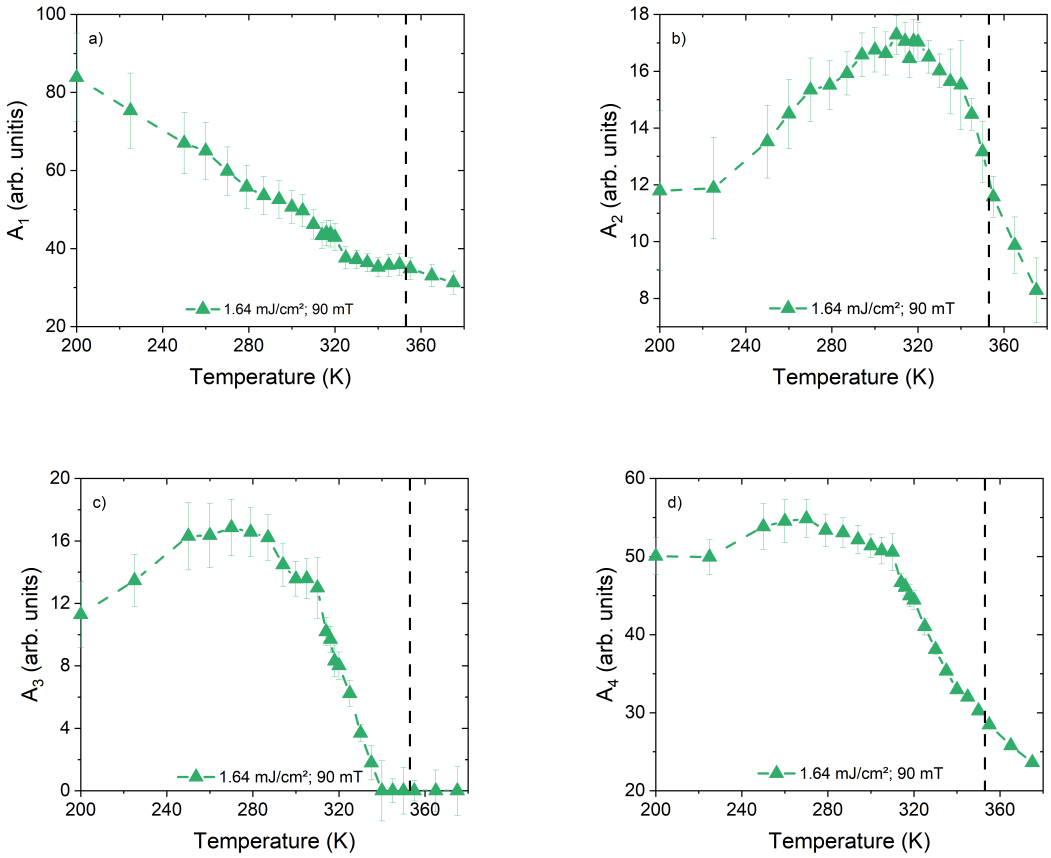

FIGURE 11.4: Exemplary, temperature-dependent fit results for $\Delta\mathcal{R}$ of the four amplitudes of the exponential functions from eq. 8.1: (**a**) A_1; (**b**) A_2; (**c**) A_3; and (**d**) A_4. All data are measured at an applied magnetic field of $B = 90$ mT and a fluence of $F \approx 1.6$ mJ/cm^2. The errors are calculated from the fit. The color-matched lines as guide to the eye. The vertical, dashed, black line marks the statically determined T_C.

The hypothesis, that the kink in A_1 reflects a physical phenomenon, might be underscored by the fact, that the other amplitudes exhibit a change in the behavior at that region, too. In the case of the second amplitude, see fig. 11.4 (b), A_2 turns into a decreasing behavior above $T \sim 0.9 \cdot T_C$. In contrast, the amplitude rises with the temperature deep in the FM phase.

In comparison to the peak-like behavior in A_2, the relaxation amplitude, A_4, exhibits a kink at that temperature, see fig. 11.4 (d). But, its decrease with the temperature starts earlier, thus for low temperatures only, a rise of A_4 is found. It seems that the maximum of A_4 is more comparable to the one of A_3 than to the one of A_2.

Finally, in A_3, see fig. 11.4 (c), no behavior change can be found at $T \approx 0.9 \cdot T_C$ within the SNR. Nevertheless, an increase for low temperatures is shown comparable to the one in A_4 as well as a decrease after a similar turning point in the middle range. The third amplitude vanishes for the PM phase; similar to how it is observed for LPCMO see fig. 8.8 (a).

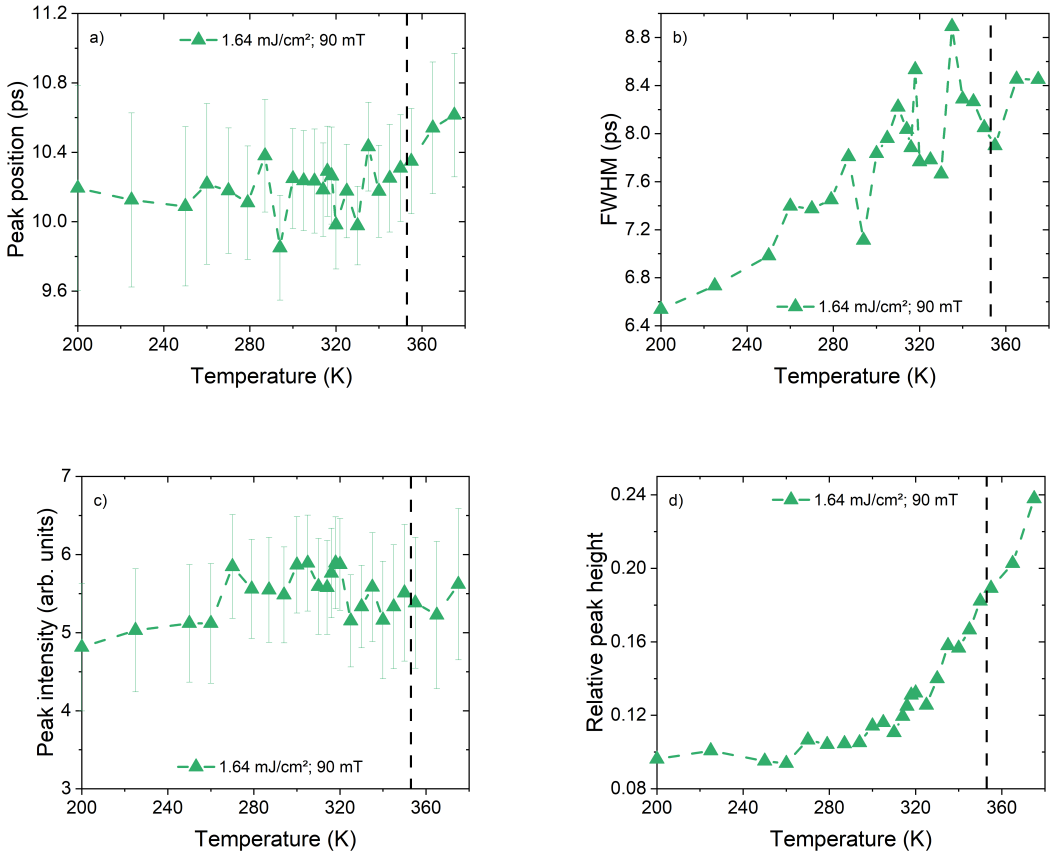

FIGURE 11.5: Exemplary, temperature-dependent fit results for the Gaussian peak in eq. 8.1, which describes the peak-like structure at $\Delta t \approx 10$ ps: (**a**) t_P; (**b**) the full width at half maximum; (**c**) G; and (**d**) G/A_4. All data are measured at $B = 90$ mT and $F \approx 1.6$ mJ/cm^2. The errors are calculated from the fit. The color-matched lines as guide to the eye. The vertical, dashed, black line marks the statically determined T_C.

Lastly, the temperature dependence of the Gaussian peak fit at around $\Delta t \sim 10$ ps, see eq. 8.1, is presented starting with the center position in fig. 11.5 (a). The first maximum of the oscillation is centered around $\Delta t \approx 10.2$ ps in the average. This center stays rather independent of the temperature taking the SNR into account. Perhaps, a slight increase of $\sim 5\ \%$ is visible for higher temperatures.

In fig. 11.5 (b), the full width at half maximum is plotted. In average, the width amounts roughly 7.5 ps. It rises by about 2 ps over the whole temperature range. A significant change in the behavior at or close to the PT is not found within the SNR.

The peak intensity G, see fig. 11.5 (c), seems to stay rather constant, which might be deluding, since the height of the underlying exponential functions changes with the temperature. Thus, a relative height is depicted in fig. 11.5 (d). Here, the peak intensity, G, is scaled to A_4, which is a measure of the total height of the psTR data trace since it is the only relaxing function in the fit eq. 8.1. The relative height, now, shows a drastic change of the importance of the feature No. 4 with respect to the total signal. Beneath $T < 0.9 \cdot T_C$, it stays rather constant at about 10 %; in contrast, it rapidly increases for higher temperatures up to one fourth of the signal for that shown fluence.

The following two sections, 11.1.2 and 11.1.3 will present how the general, here discussed behavior changes while varying the pump fluence, F, and the external magnetic field, B, respectively.

11.1.2 Fluence-Dependent Dynamics of LSMO

Starting with the first time constant in fig. 11.6 (a), a slight but clear slowing down trend is observed when increasing the fluence. This trend seems to persist along the whole thermal range within the SNR, but the data suggests that this trend is temperature-dependent. While the time constant almost doubles at $T = 200$ K, the change of τ_1 is of about 10-20 % close to the PT.

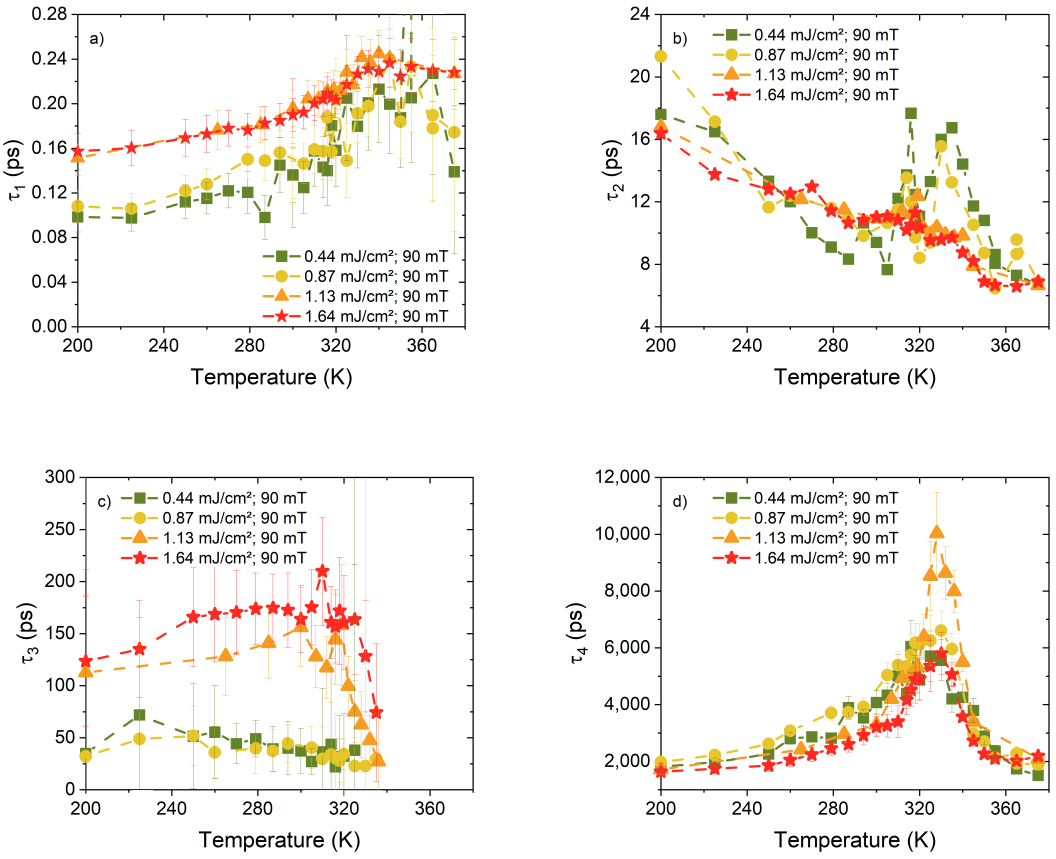

FIGURE 11.6: Fit results for $\Delta\mathcal{R}$ of the four time constants of the exponential functions: (**a**) τ_1; (**b**) τ_2; (**c**) τ_3; and (**d**) τ_4. Each panel includes results for four different fluences measured all with an applied, magnetic field of $B = 90$ mT. The errors in (a), (c) and (d) are calculated from the fit. The color-matched lines as guide to the eye.

The slowing down of τ_1 is remarkable, since the thermalization is expected to become shorter if more electrons are excited above the Fermi-energy (see also section 8.1.1 and 12.1). Due to this reason, a second sample[2] is measured in a fluence-dependent series, see fig. 11.7, where the temperature and magnetic field were kept constant at $T = 200$ K and $B = 90$ mT, respectively. Note, that the actual values of τ_1 for both samples do slightly differ. Nevertheless, a similar behavior is found for the second sample. For low fluences up to $F \approx 2$ mJ/cm^2, τ_1 increases and it seems to level-off for even higher fluence values.

[2]Thanks to Leonard Schüler who provided the thin film sample of $d_{S09} = 76$ nm LSMO grown at STO. For this film, a Curie temperature of $T_C = 350 \pm 2$ K was measured by SQUID magnetometry at $B = 100$ Oe.

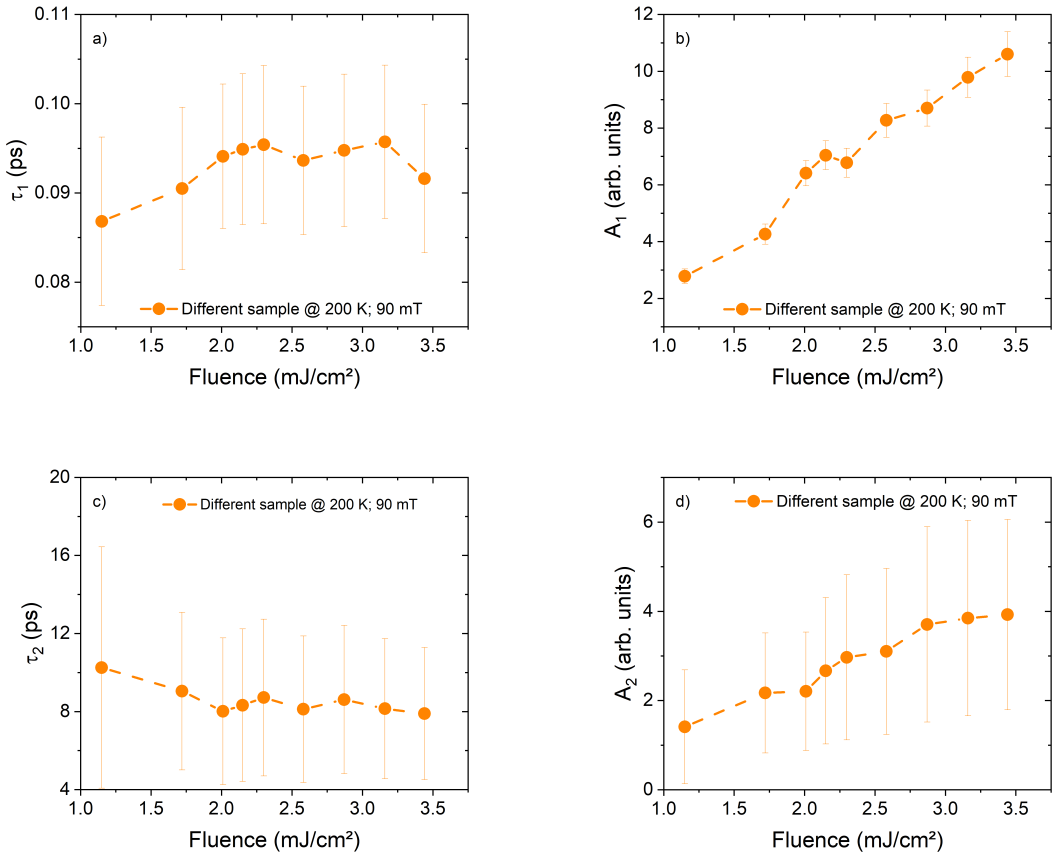

FIGURE 11.7: Fit results for a fluence-dependent series of $\Delta\mathcal{R}$ of the initial time constant (**a**) τ_1, (**b**) A_1, (**c**) τ_2, and (**d**) A_2 measured at $T = 200$ K and $B = 90$ mT. The errors are calculated from the fit. The color-matched lines as guide to the eye.

Turning to the second time constant, τ_2, in fig. 11.6 (b), a peak close to the PT appears when decreasing the pump fluence. It seems that this peak is shifted towards lower temperature by increasing the pump fluence. The development of the peak might be another indication for the described kink from above (see fig. 11.2 (b)). For low temperatures, the second process becomes faster for higher fluences. Again, this is reproducible by measuring the second sample as visible in fig. 11.7 (c) and (d). Note, that no error bars in 11.6 (b) are shown to enable a better overview. The data for τ_2 including the error bars are shown in the appendix, chapter C1.2.

Fig. 11.6 (c) shows, that the third increase, τ_3, increases quite strongly with the fluence. The time constant is increased by a factor of roughly 3. The higher fluence data suggest, that the sudden drop, when approaching the PT, shifts to higher temperatures when increasing the pump fluence.

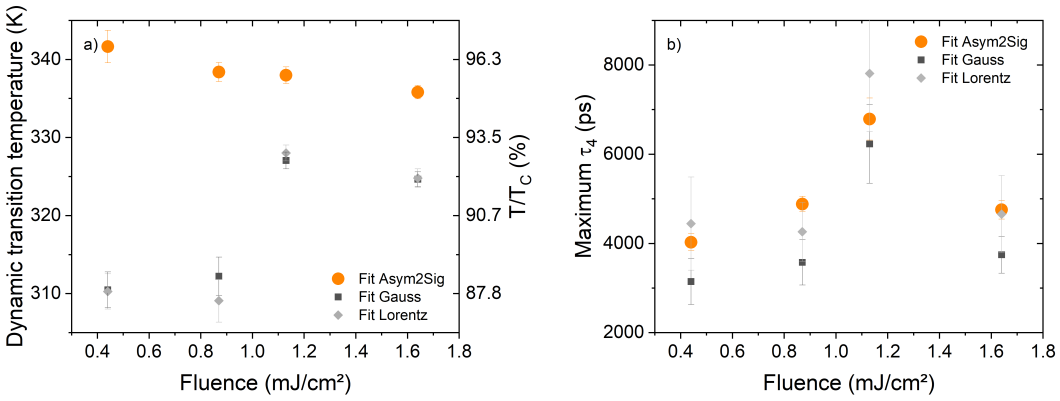

FIGURE 11.8: Fit results for a fluence-dependent series of τ_4 for (**a**) temperature of the peak maximum and (**b**) the corresponding maximum of τ_4. The errors are calculated from the fit.

As already remarked in sec. 11.1.1, the most pronounced change of τ_4 is a (strong) variation of the peak due to the external stimuli. How the fluence impacts the peak position and the peak height is depicted in fig. 11.8 (a) and (b), respectively.

Following the Asym2Sig fit, the peak shifts towards lower temperatures when increasing the pump fluence. For fluences up till $F \sim 1.2$ mJ/cm^2, the maximum value of τ_4 rises; for the highest fluence, it drops down again.

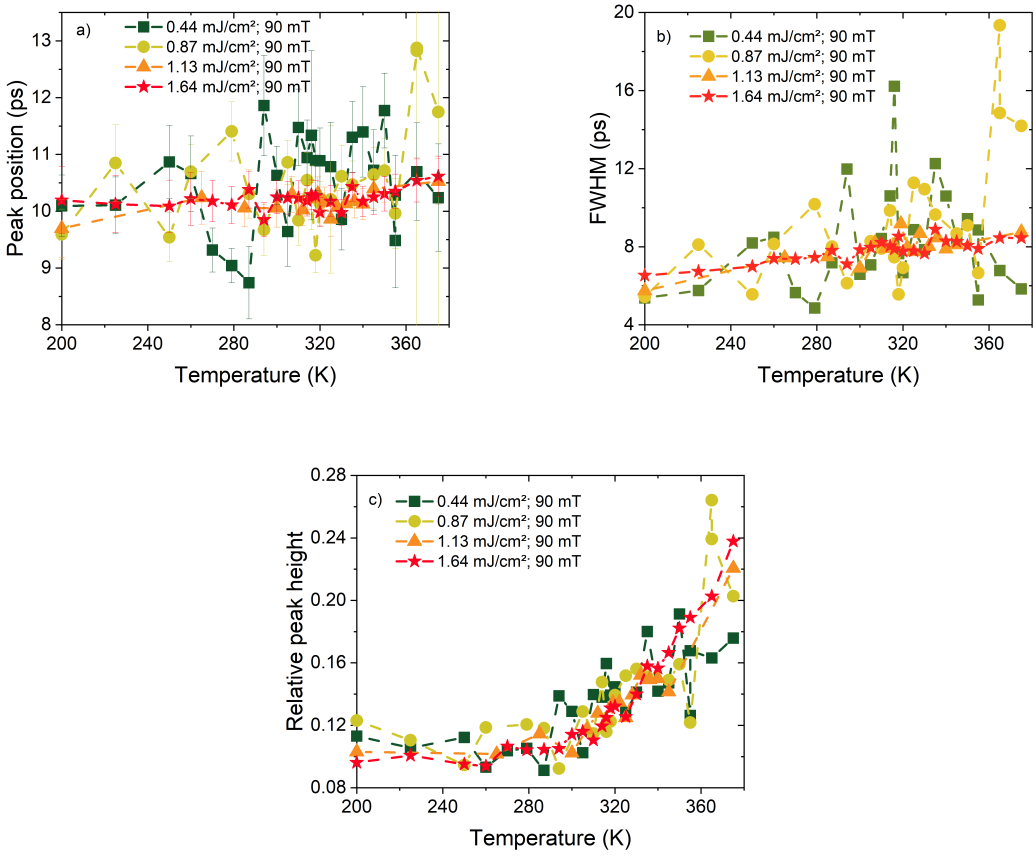

FIGURE 11.9: Fluence-dependent fit results for the Gaussian peak in eq. 8.1, which describes the peak-like structure at $\Delta t \approx 10$ ps: (**a**) t_P; (**b**) the full width at half maximum; and (**c**) G/A_4. All data are measured at $B = 90$ mT. The errors are calculated from the fit. The color-matched lines as guide to the eye.

The results for the Gaussian fits of the peak-like structure are presented in fig. 11.9 (a) - (c). No fluence-induced changes of the fitting parameter can be reported within the SNR. Nevertheless, the trends, named above in the description of fig. 11.5, are underscored by these fluence dependent data.

11.1.3 Magnetic Field-Dependent Dynamics of LSMO

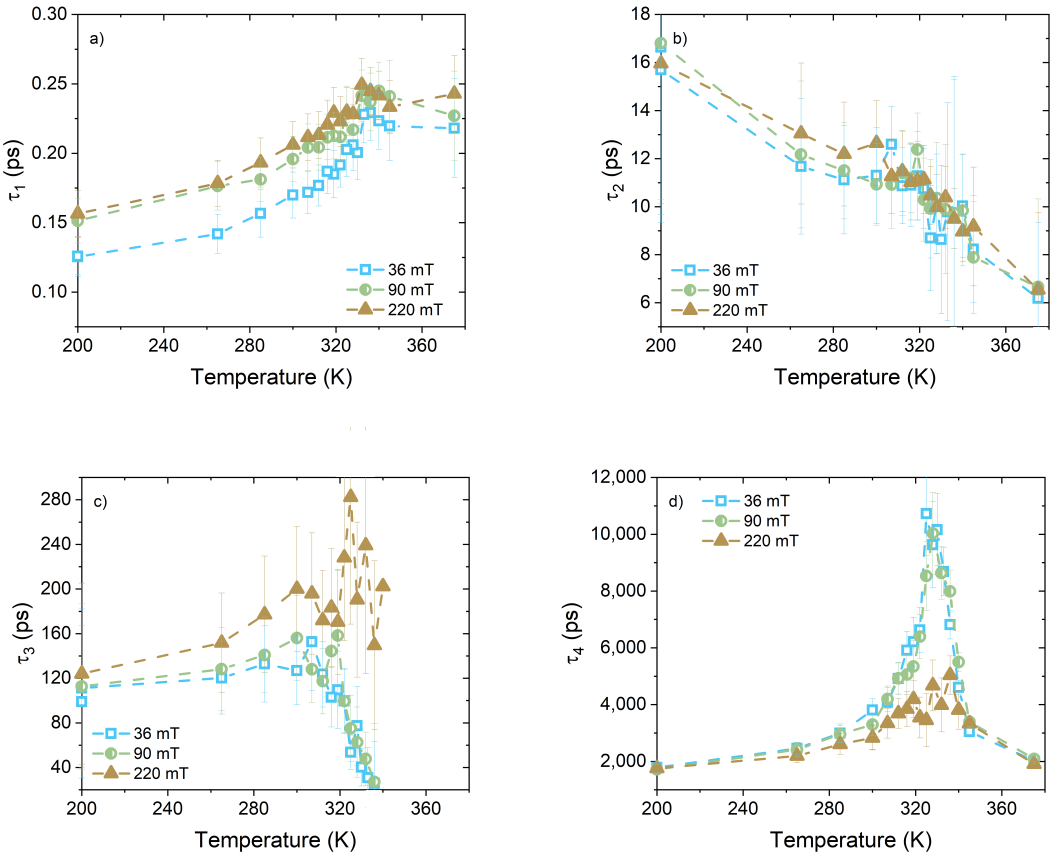

FIGURE 11.10: Fit results for $\Delta\mathcal{R}$ of the four time constants of the exponential functions: (**a**) τ_1; (**b**) τ_2; (**c**) τ_3; and (**d**) τ_4. Each panel includes results for three different applied magnetic fields measured all with a fluence of $F = 1.13$ mJ/cm^2. The errors are calculated from the fit. The color-matched lines as guide to the eye.

Addressing the magnetic field dependence of the dynamics in fig. 11.10, the time constants of all three rising exponential functions increase by raising the external field. In contrast, the peak in τ_4 decreases drastically by applying a moderate magnetic field of $B = 220$ mT.

The magnetic field-dependent trends of the first and second process for $T = 200$ K in fig. 11.10 (a) and (b) are validated by measuring a third LSMO sample[3] as visible in fig. 11.11

[3]This third LSMO thin film exhibits a static Curie-temperature of $T_C = 357$ K measured at $B = 100$ Oe and a thickness of $d_{A0643} = 30$ nm.

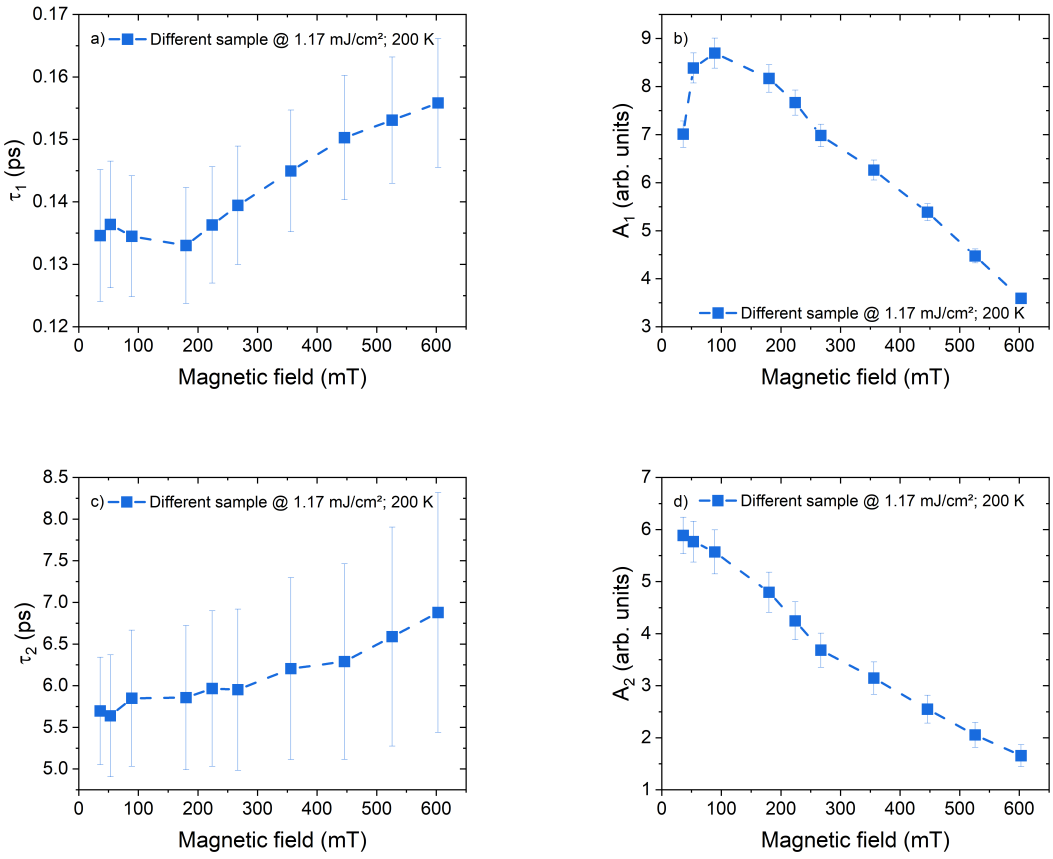

FIGURE 11.11: Fit results for a magnetic field-dependent series of $\Delta\mathcal{R}$ of the initial time constant (**a**) τ_1, (**b**) A_1, as well as the second increase (**c**) τ_2, and (**d**) A_2 measured at $T = 200$ K and $F = 1.17$ mJ/cm^2. The errors are calculated from the fit. The color-matched lines as guide to the eye.

(a) - (d). Both time constants, τ_1 and τ_2, increase when applying an higher magnetic field. In contrast, both amplitudes, A_1 and A_2, show a decreasing behavior with rising field, see fig. 11.11 (b) and (d).

The further evaluation of the peak in τ_4 by a Asym2Sig fit points out a positive shift of the peak position, fig. 11.12 (a), and outlines a decrease of the maximal relaxation time, see fig. 11.12 (b). The shift of the peak coincides with a migration of the vanishing point of A_3 towards higher temperatures, visualized by the termination of the shown τ_3 values in fig. 11.10 (c).

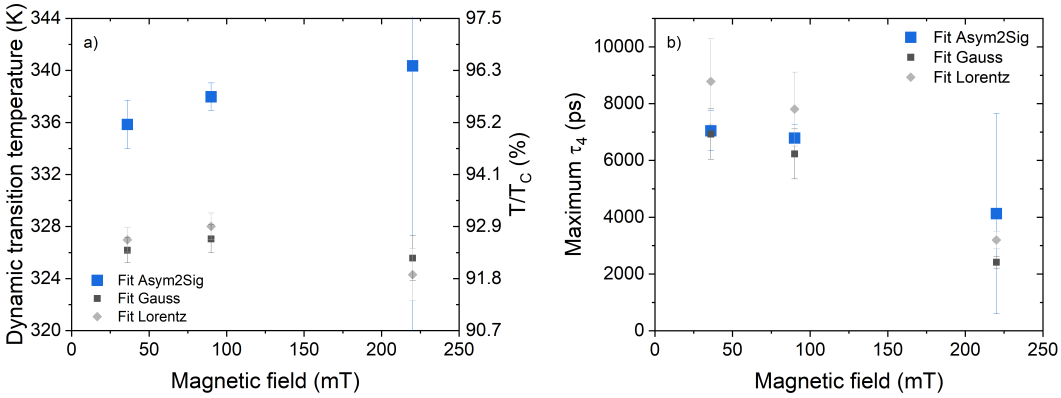

FIGURE 11.12: Fit results for a magnetic field-dependent series of τ_4 for (**a**) temperature of the peak maximum and (**b**) belonging maximum of τ_4. The errors are calculated from the fit.

The results for the Gaussian fits of the peak-like structure are presented in fig. 11.13 (a) - (c). No magnetic field-dependent changes of the fitting parameter are found within the SNR. But again, the field-dependent data corroborate the trends, suspected above in the description of fig. 11.5.

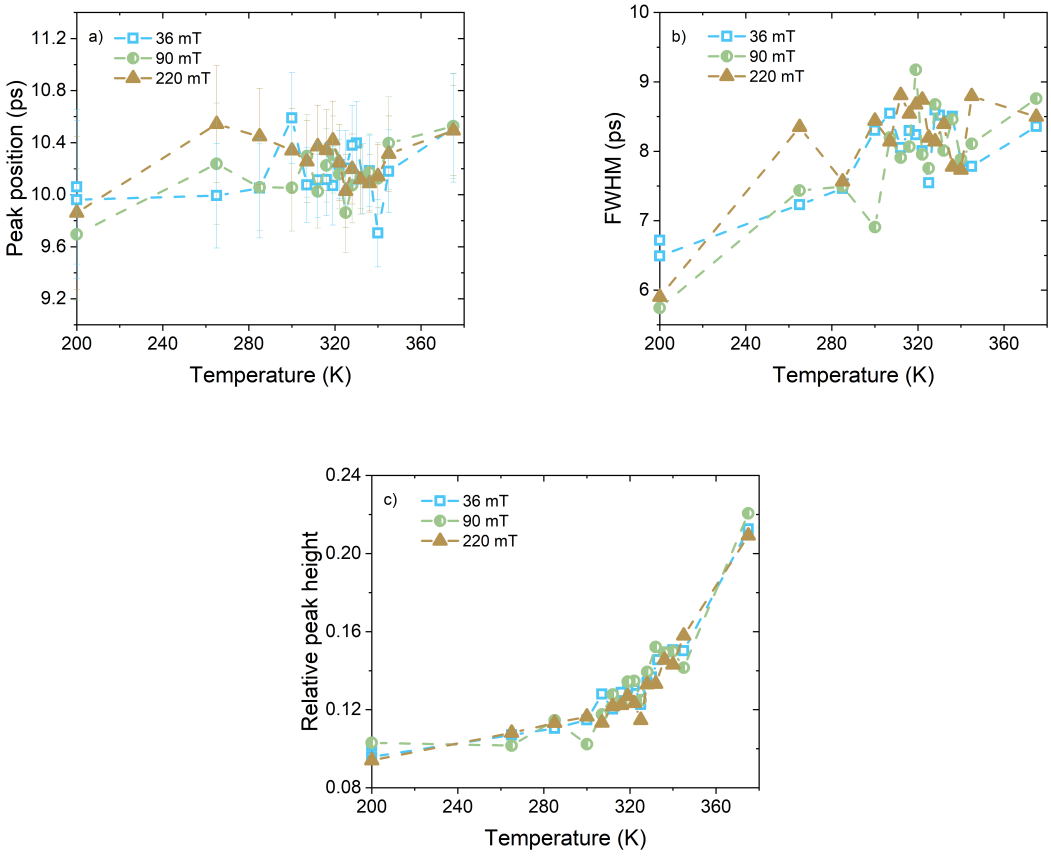

FIGURE 11.13: Fluence-dependent fit results for the Gaussian peak in eq. 8.1, which describes the peak-like structure at $\Delta t \approx 10$ ps: (**a**) t_P; (**b**) the full width at half maximum; and (**c**) G/A_4. All data are measured at $B = 90$ mT. The errors are calculated from the fit. The color-matched lines as guide to the eye.

11.2 Time-Resolved Magneto-Optical Kerr Effect of $La_{0.7}Sr_{0.3}MnO_3$

Fig. 11.14 shows the selection of time-resolved magneto-optical Kerr effects measurements which correspond to those measurements which are chosen for fig. 11.1, the examples of the transient reflectivity. As expected for the magneto-optical response, no dynamics appears for measurements done at a base temperature above T_C, e.g., the red curve. The measurements below T_C exhibit up to four visible features which arise when cooling down the sample. Note

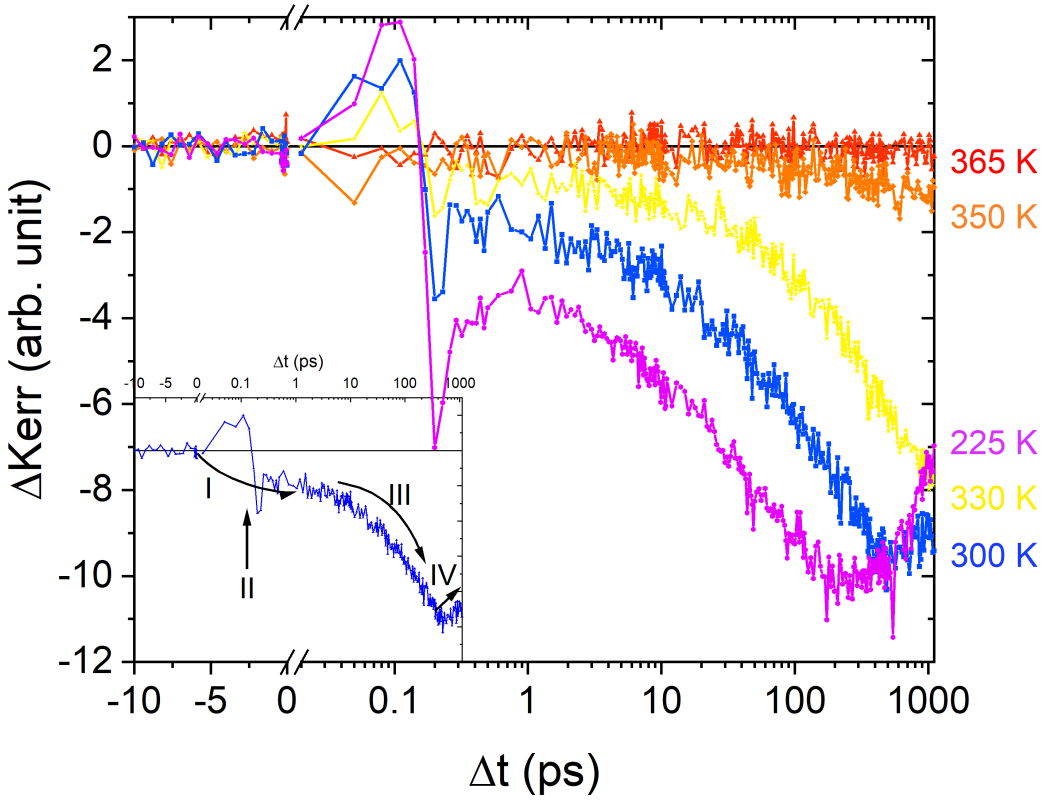

FIGURE 11.14: Exemplary traces of the change of the TRMOKE for five temperatures (as labeled in the graph), $T_C = 353$ K. In the inset, the features are marked, which are discussed in the text below.

the logarithmic x-scaling. In the inset of fig. 11.14, the four features are marked by the black arrows:

I. initial decrease
II. oscillations (almost a Lorentz-peak-like behavior) at the first hundreds of femtoseconds, which is strongly pronounced
III. second decrease on the ps timescale
IV. remagnetization

Similar to the case of LPCMO, no fit results of equation 8.1 will be presented. The dominate Lorentzian peak-like structure, feature II, the invisibility of the relaxation process on the

measured timescales as well a the low signal to noise ratio lead to a high uncertainty. Hence, a qualitative description of the TRMOKE data of LSMO is given in the following sections.

11.2.1 The Initial Decrease in the TRMOKE Signal

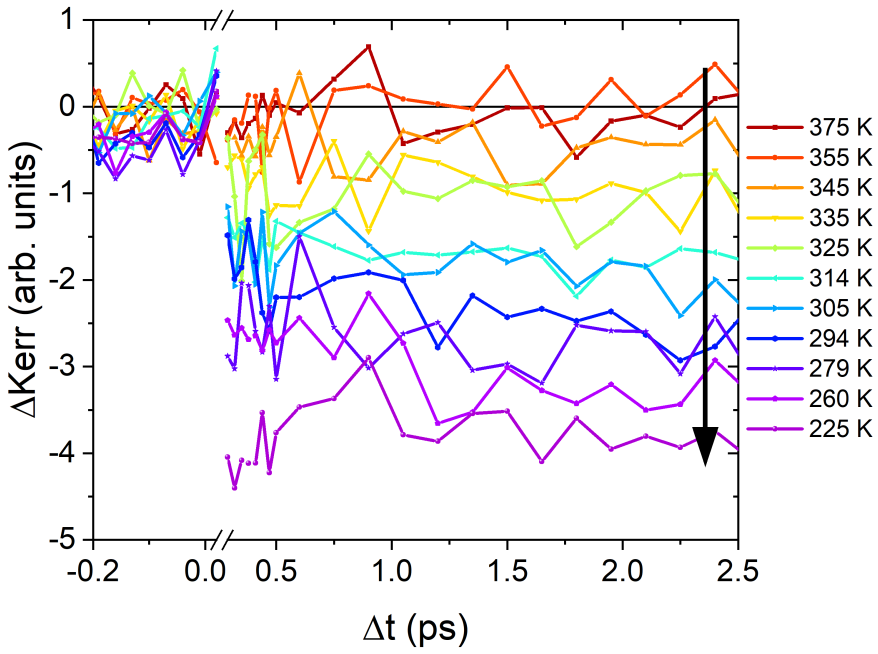

FIGURE 11.15: Exemplary traces for the change of the TRMOKE at $\Delta T \leq 2$ ps with the temperature. The black arrow marks the trend in the amplitude of the initial decrease with decreasing temperature. The Curie temperature of the sample is $T_C = 353$ K. The feature II, the Lorentzian peak-like structure, is hidden.

The fig. 11.15 visualizes the trend of the initial decrease, feature I, within the TRMOKE signal which is measured depending on the base temperature in an applied magnetic field of $B = 90$ mT. The initial decrease of the TRMOKE signal increases by decreasing the base temperature as indicated by the black arrow. Above T_C, no such dynamic is observed.

In fig.11.16 (a), a magnetic field-dependent series measured at $T = 200$ K is presented. When the magnetic field is increased, the absolute value of the amplitude of the initial decrease

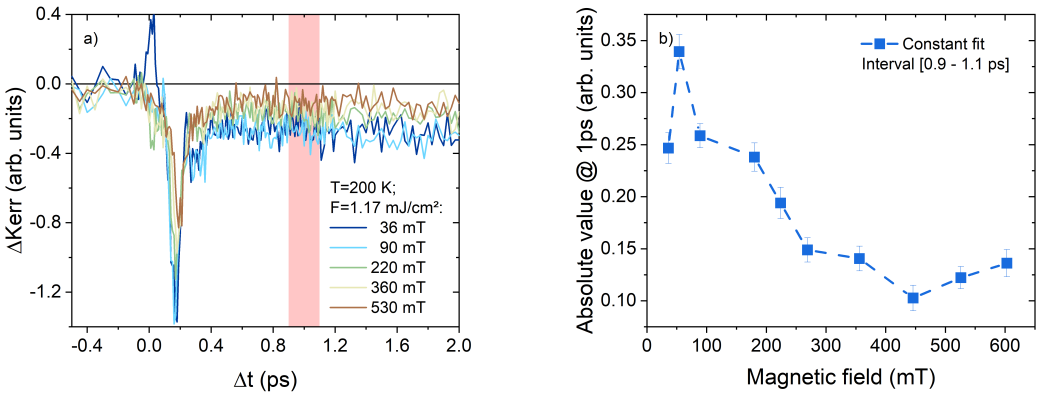

FIGURE 11.16: (**a**) Exemplary traces for the change of the TRMOKE at $\Delta T \leq 2$ ps with an applied magnetic field. The reddish area marks the fit interval for a fit of a constant.(**b**) fitted constant as a function of the applied magnetic field.

decreases. This trend is craved out by a fit, $f(\Delta t) = c$, of a constant parameter in an interval around 1 ps, which is plotted in fig. 11.16 (b).

11.2.2 The Second Decrease in the TRMOKE Signal

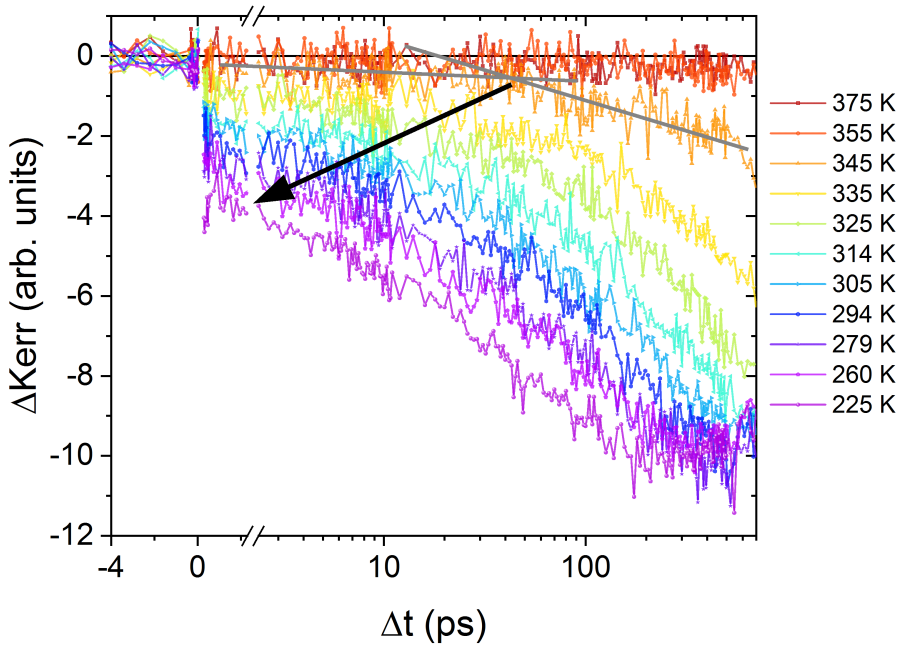

FIGURE 11.17: Exemplary traces for the change of the TRMOKE on the intermediate ps-timescale with the temperature. The black arrow marks the trend in the appearance of demagnetization with decreasing temperature. The Curie temperature of the sample is $T_C = 353$ K. The feature II, the Lorentzian peak-like structure, is hidden.

Turning to the decrease of the signal on the tens till hundreds of picoseconds, the demagnetization process (see fig. 11.17) becomes faster when the base temperature is decreased more and more. Therefore, the demagnetization becomes dominant at earlier timescales already for low temperatures.

Even without a fit, it can be supposed from the TRMOKE traces close to T_C, that the demagnetization time increases up to hundreds of picoseconds when approaching the PT from below. The yellow-orange curve in fig. 11.17 is an example for this behavior: even though the demagnetization becomes the dominant process at $\Delta t \sim 50$ ps, no indication of a turning-point from demagnetization into remagnetization can be found up to 1.1 ns[4]

[4]The x-axis is cut at $\Delta t = 700$ ps, but the yellow-orange trace is plotted in 11.18 till 1.1 ns.

11.2.3 The Remagnetization

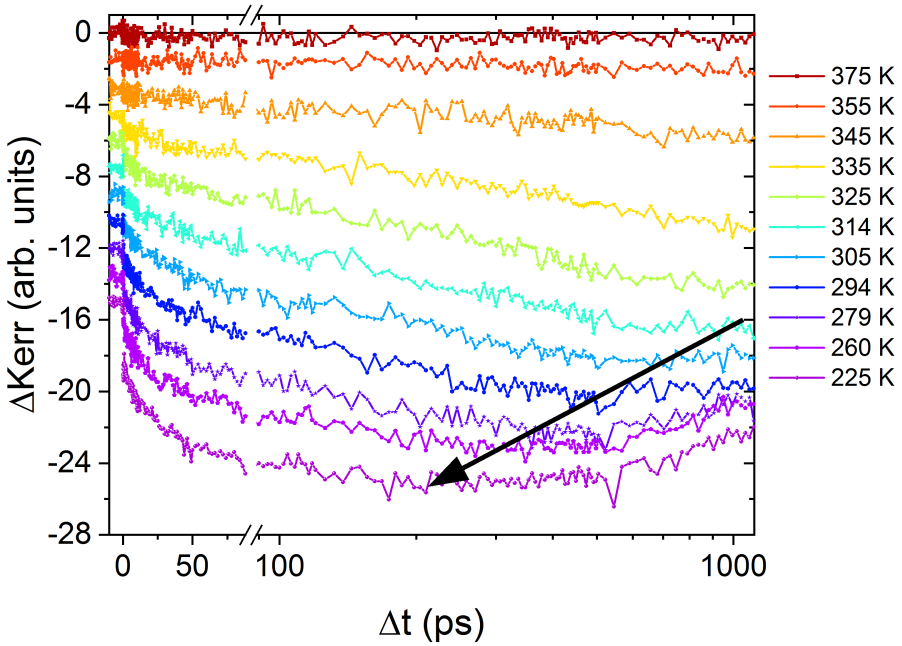

FIGURE 11.18: Exemplary traces for the change of the TRMOKE on the high ps- till ns-timescale with the temperature. The black arrow marks the trend in the appearance of remagnetization with decreasing temperature.The Curie temperature of the sample is $T_C = 353$ K. The feature II, the Lorentzian peak-like structure, is hidden.

In fig.11.18 the trend of the relaxation process is visualized. A remagnetization process is not visible by eye in some TRMOKE traces since the scope of the delay-line is too short for measuring parts of the relaxation process, see yellow to red curves in fig. 11.18. Nevertheless, an increase in the signal, back to the ground state, is observed for base temperatures $T \lesssim 320$ K. When further decreasing the temperature, the remagnetization becomes dominant already at earlier timescales.

CHAPTER 12

Discussion of $La_{0.7}Sr_{0.3}MnO_3$

The results, which are presented in the preceding chapter 11, suggest a similar assignment of the timescales to the types of macroscopic dissipation process steps for LSMO as for LPCMO, e.g., the third process is strongly suggested to be connected to the spin-lattice interaction (see section 12.4) as it was discussed in the case of LPCMO already (see section 9.4). Nevertheless, the individual manifestations differ between both materials which give a hint towards different, underlying, atomistic processes. Therefore, the results of the dynamic measurements of LSMO are going to be discussed in the following.

The order of the features in the discussion will follow the chronological order of the dynamics, starting with the lowest timescale. The discussion of every single timescale will be started with the consideration of the T-dependent development. This data give a general idea of how the system behaves when becoming more metal-like/ ferromagnetic or how the system reacts when the mobility of the electrons is shrunk down due to trapping in Jahn-Teller distortion. Thereby, the interpretations of the transient reflectivity response on the external stimuli change are underlined by the findings in the magneto-optical response.

In fig. 12.2, exemplary psTR traces and an exemplary TRMOKE trace is plotted in order to remind the discussed features. Note the logarithmic scaling of the time axis.

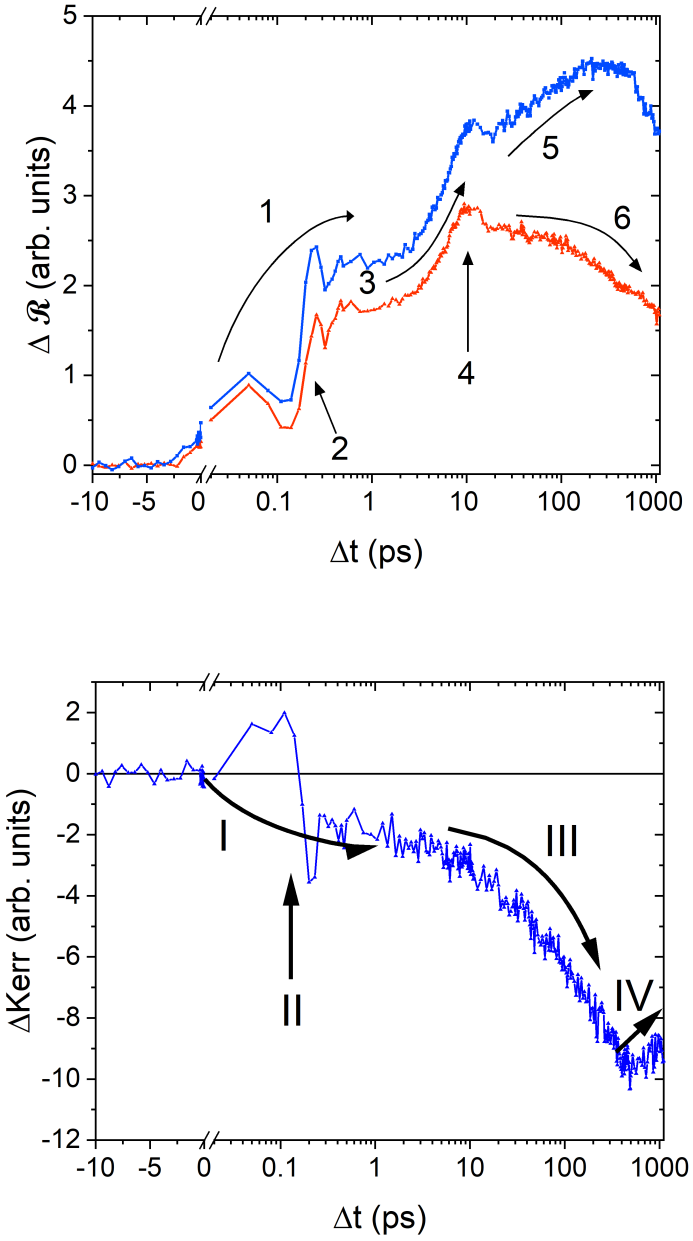

FIGURE 12.1: **Upper panel**: labeling of the 6 features, which are observed in the transient reflectivity signal; **lower panel**: labeling of the 4 features, which are found in the TRMOKE data.

12.1 Feature No. 1 - Excitation and Thermalization of the Electronic System

In accordance with the literature [99, 104, 105, 143], the first process is suggested to represent the excitation by the fs-laser pulse and thermalization of the electronic system. An interesting question in this context is of course, which kind of transition(s) provide(s) the major part of the excitation process. Very probably, not only one distinct excitation happens since LSMO, as a half-metal [6, 47, 85, 86, 157, 158], should provide continuously (free) electronic states across the Fermi-energy, at least to some extend. Nevertheless, literature [67, 91, 92, 147] shows that there is an absorption edge which is resonant for energies close to the here-used pump energy (1.2 eV), thus the corresponding transition(s) is(are) expected to dominate the initial dynamics. But, as discussed in section 4.5, different transition types are suggested in literature. The hypotheses range from a charge transfer type (from O2p to an e_g state of a Mn ion) [91], an intersite transition (from an $e_{g,1}$ state of a Mn^{3+} ion into the higher $e_{g,2}$ state of another Mn ion) [67, 92], to a photo-induced hopping process is enabled by those energies (from an $e_{g,1}$ state of another Mn^{3+} ion into the unoccupied $e_{g,1}$ state of a Mn^{4+} ion) [67]. Furthermore, hypothetically, a spin-flip transition (SFT) should not be excluded without proper theoretical support. A spin-flip transition is electric dipole forbidden, as argued in [67, 91, 92, 147] and others, but a magnetic dipole transition might be still available since the splitting between spin-up and spin-down states are in the optical region [85, 159, 160], see also the projected DOS calculated by DFT in fig. 4.7. [1]

To summarize this short reminder, four different kinds of transitions are proposed as possible transitions in a pump-process in LSMO (charge transfer, intersite, photo-induced hopping, and spin-flip), whereby all options lead to an occupation of a manganese 3d-state above the Fermi-energy.

It is also important to remind, that the polaronic trapping of $\mathbf{e_g}$ electrons is caused by electrostatic potential [63, 64, 74], Pauli-principle and/or Hund's coupling [74, 76, 77] (see section

[1] Note, since spin-orbit coupling in manganites is not negligible, the spin, S, is not a good quantum number anymore, but the total angular momentum, J. Nevertheless, the term "spin-flip" is still going to be used in the following to emphasise the changes in the magnetic order by a concordant transition.

4.1). Even though, this trapping is caused by electron-electron interaction among others, these interactions cannot be understood as inelastic scattering processes. (Otherwise, the e_g electrons would gain (or lose) constantly energy.) Since these interactions do not change the distribution of states, these scattering processes will be neglected when talking about scattering in following.

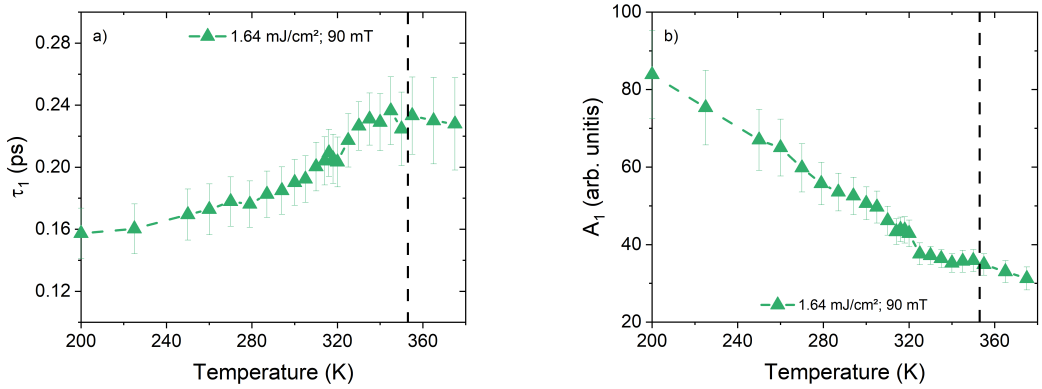

FIGURE 12.2: Fit results of the first process dependent on the temperature: (**a**) τ_1; (**b**) A_1. All measurements are performed in an external magnetic field of $B = 90$ mT and $F = 1.64$ mJ/cm^2. The errors are calculated from the fit. The color-matched lines as guide to the eye.

In general, two things change in LSMO throughout the temperature range which might change the transition probability of the excitation process: first the magnetic ordering of the system, which is accompanied by a reduction of the electron mobility, and second the number of excited phonon modes. The latter, is especially important for all interatomic transitions (excluding an intra-atomic spin-flip), because they require an ultrafast rearrangement of the oxygen octahedron caused by the distortion which is induced by an additional electron at the final state Mn ion, as discussed for the LPCMO case already, see sections 9.1 and 9.2. Regarding the firstly named change, i.e, the increase of the conductivity in line with the change of the macroscopic magnetic state, a clear trend of τ_1 towards faster timescales is found when becoming more metal-like. As a short reminder, the fig. 11.2 (a) and 11.4 (a) are replotted in 12.2. This is inline with the observations by Bielecki et al. [105], where the authors demonstrated in manganites a slowing down of the electron-electron scattering

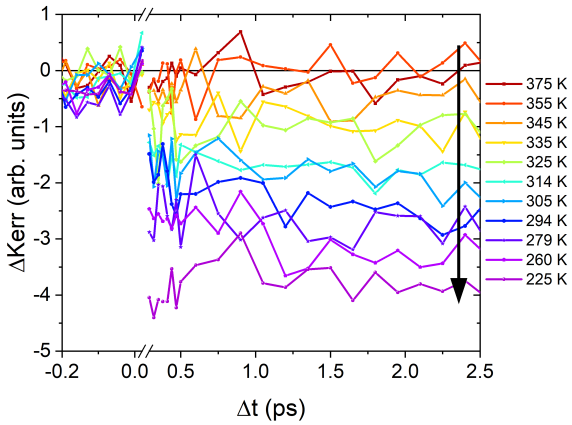

FIGURE 12.3: Exemplary traces for the change of TRMOKE at $\Delta t \leq 2$ ps with the temperature. The black arrow marks the trend in the amplitude of the initial decrease with decreasing temperature. The Curie temperature of the sample is $T_C = 353$ K. The feature II, the Lorentzian peak-like structure, is hidden.

when turning into an insulating state. In the paper [105], they explained this behavior with the accumulating polaronic trapping of the electrons and the resulting increasing immobility of the charge carriers.

Next to the findings in the transient reflectivity signal, an ultrafast response of the LSMO is observed in the TRMOKE signal as well, see fig. 12.3. The dependence of this ultrafast decrease on changes of the external stimuli provide important information of the type of electron excitation. In a system, where the spin-orbit coupling is not negligible, a change in the total angular momentum, J, is needed to change the off-diagonal matrix elements of the dielectric tensor and therefore, to lead to a change of the TRMOKE signal.

As visible in section 11.1 and in the following, the τ_1 data points are shifted more or less constantly when comparing two different measurement series if the external magnetic field or the fluence was varied in-between. In other words, the variation of these two external stimuli have similar effects, referencing on the sign of change, on the excitation and thermalization processes independent on the initial phase of the sample. Note that the absolute value of the shift difference is nevertheless dependent on the temperature.

The following subsection will discuss the question which transition type might be the main contribution to the excitation process. It is important to understand that this discussion is based on an assumption which is derived from these findings. Since, the direction of the shift

stays the same, it is assumed that the main excitation process stays the same for both ground states, independent whether the initial state is ferromagnetic or paramagnetic. This assumption helps to set up an hypothesis of the main excitation step in that way that it opens up the possibility to discuss the excitation in the ionic-picture which is well-known in the context of manganites perovskites. The advantage of the ionic picture is that the considered electrons are more or less localized at a specific site. Once again, it is emphasized that theoretical calculation such as TDDFT should be performed in order to support (or to falsify) this hypothesis.

Within this framework, each of the following subsection are going to discuss one of the four transition types; starting with the intersite transition.

12.1.1 Intersite Transition

One suggestion in literature [67, 92] is an intersite transition from an $e_{g,1}$ of one Mn^{3+} into a $e_{g,2}$ state of an other Mn^{3+}, turning into a Mn^{2+} ion, as depicted in fig. 12.4 upper panel. Since the probability of this transition depends on the core spin alignment of the two involved ions, a strong, positive dependence of A_1 on the magnetic ordering is expected. Furthermore, the thermalization time is expected to decrease within an increasing magnetic field. As visible in the comparison of the middle and the lower panel in fig. 12.4, the electrons of the Mn^{2+} are trapped by an antiparallel alignment of the core spins. Due to the localization of the hot electron, the phase space for electron-electron scattering is quite reduced: The Mn^{2+} ion itself provides spin down states only. Hence, energy for Hund's coupling is required in order to occupy one of the spin down states. Furthermore, the surrounding O2p states are fully occupied, too, unless, an electron undergoes a transition from an O2p state to the other Mn ion (here the Mn^{4+}). Since this Mn ion exhibits antiparallel core spins, the remaining O2p hole cannot be occupied by the electrons of the Mn^{2+} ion. Consequently, the time until the hot electron can relax by electron-electron scattering increases in this case. For the temperature dependence of the time constant, τ_1, this would result in an increasing behavior when increasing the base temperature and reducing more and more the ferromagnetic alignment of the Mn ions. As shown in fig. 12.3, the expectations regarding a temperature

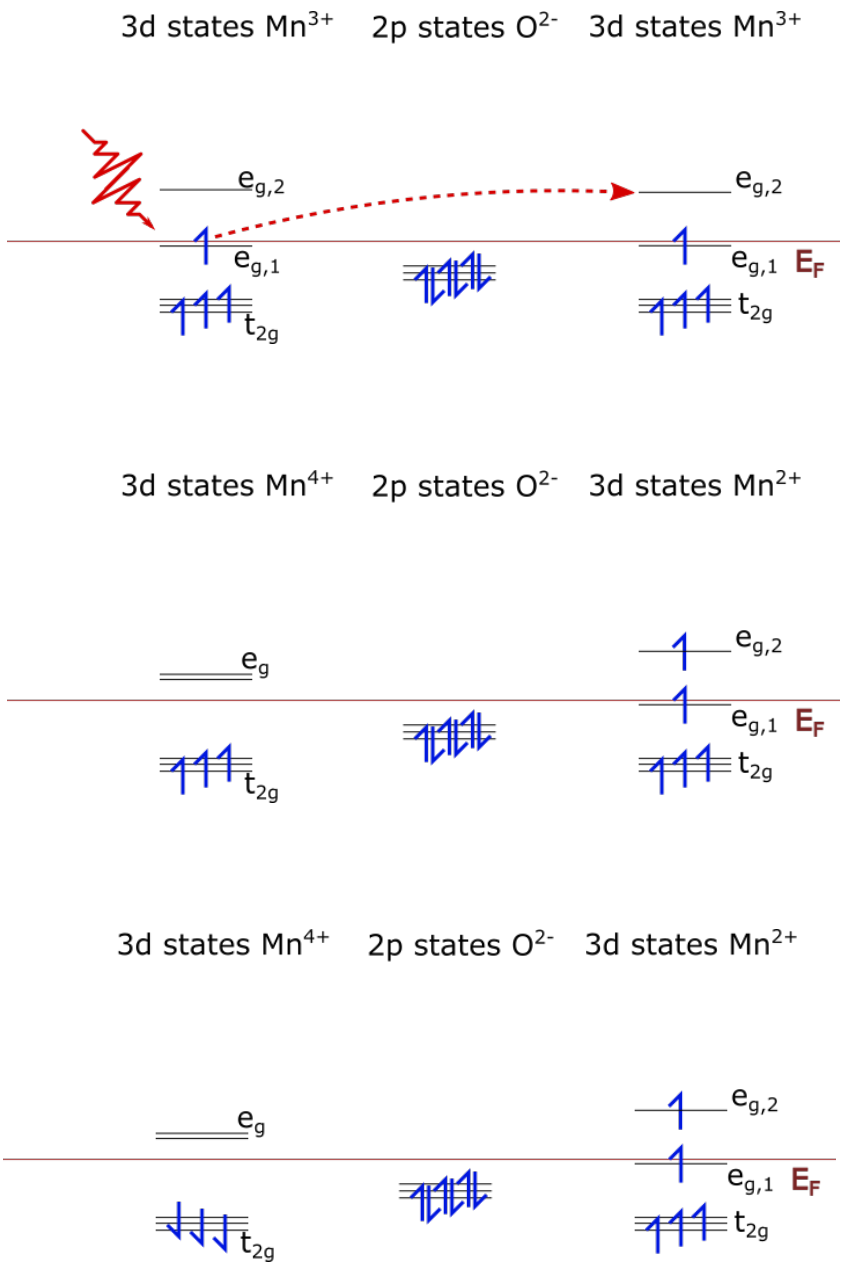

FIGURE 12.4: Intersite transtion: **Upper panel**: Excitation from a $e_{g,1}$ state of a Mn^{3+} into an Mn $e_{g,2}$ state of a neighboring Mn^{3+}. **Middle panel**: Excited configuration with parallel alignment of the neighboring core spins. **Lower panel** Excited configuration with antiparallel alignment of the neighboring core spins.

change are inline with the results from the transient reflectivity measurements.

Following the hypothesis of a reduction of the phase space for electron-electron scattering by antiparallel spin alignment, the dependence on the external magnetic field is analogue. If

a magnetic field is applied, the ferromagnetic ordering is supported. Thus, the mobility of the hot electrons is enhanced and the phase space is increased. Therefore, the time constant, τ_1, is expected to decrease inside an applied magnetic field. Furthermore, the amplitude, A_1, is expected to increase by increasing the magnetic field. Inside a magnetic field, the probability to find two neighboring Mn^{3+} ions is higher; an intersite transition in the high-spin configuration is more likely.

Turning to the fluence dependence, one would expect an increase of the amplitude, A_1, since more electrons should be excited when pumping with more photons. With the intersite transition, electrons are excited from an energy level close to the Fermi energy into a state above the Fermi energy, and creating a hole below the Fermi level. Therefore, the conductivity of the manganite is increased by exciting this transition. In analogy of the behavior of a Fermi liquid [33, 95], a speeding-up of the thermalization, and therefore of τ_1, is expected for a higher pump fluence. At least for low temperature, where the conductivity becomes better and better, there is no reason, why the thermalization time should increase when a system turns from a more insulator-like to a more metal-like state, while more hot electrons are excited. And exactly, this is what is observed in the temperature-dependent series: When turning from the more insulating state (higher temperature) into a state of higher electron mobility (lower temperature), the process τ_1 becomes faster (see fig. 12.2). Therefore, if more electrons are pumped into conduction states above the Fermi-energy by an increased fluence, while conserving the majority spin, the system is expected to show a more metal-like behavior. Thus, a speeding-up of this process should be observed while increasing the pump fluence.

A summary of the previous discussion of the expectations of the intersite transition reaction on external stimuli are given in table 12.1. A comparison of the expectations with the measurement results will be given in the following.[2]

As visible in fig. 12.5 (a) and (b), the upward trend of τ_1 at higher fluence is contrary to the expectations. Next to the fluence dependence, the magnetic field reaction, see fig. 12.6, does not refer to an intersite transition, too. Based on these plain disagreements of the experimental

[2]For the sake of overview, the contrasting results only will be plotted in this section again. If the reader is interested in the other findings, too, please have a look in section 11.1.1.

TABLE 12.1: Expected reactions of a intersite transition:

	τ_1	A_1
temperature	increase ✓	slight decrease ✓
caused by	generally decreasing mobility	the thermal expansion and less parallel alignment between neighboring Mn ions
fluence	decrease χ	increase ✓
caused by	larger number of hot electrons	more photons
magnetic field	slight decrease χ	increase χ
caused by	generally increasing mobility larger number of hot electrons	more neighboring Mn ions are parallel aligned

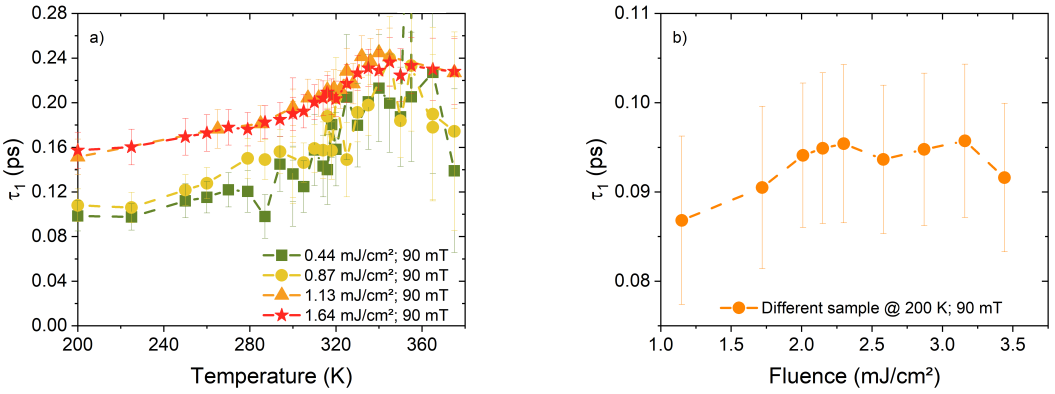

FIGURE 12.5: Fit results of τ_1 in dependency of the fluence: (**a**) temperature-dependent series measured at different fluences; (**b**) a fluence-dependent series measured on another sample at $T = 200$ K. All measurements are performed in an external magnetic field of $B = 90$ mT. The errors are calculated from the fit. The color-matched lines as guide to the eye.

results in contrast to the theoretical expectations, an intersite transition is doubted to be the major excitation process. Especially, the results in fig. 12.6 recommend a type of transition, which is more sensitive to the macroscopic magnetic state of the sample, e.g., as the decrease in A_1 suggests in fig. 12.6 (b).

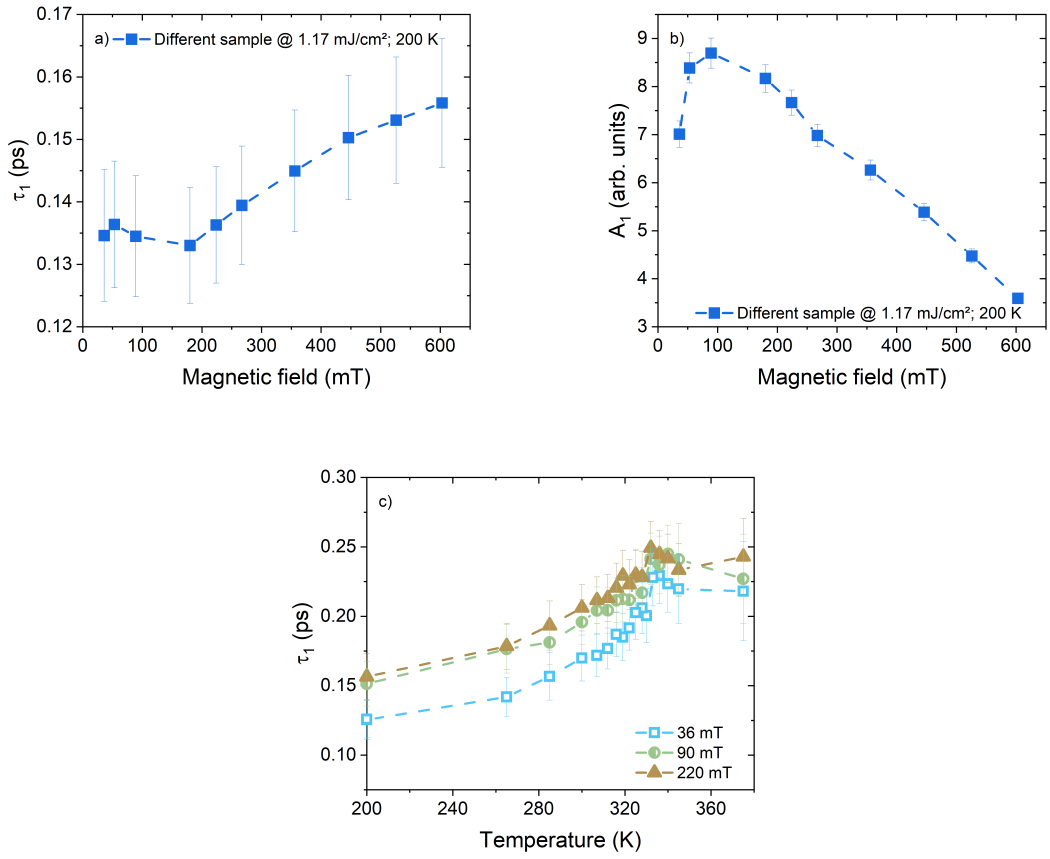

FIGURE 12.6: Fit results of τ_1 in dependency of the applied magnetic field: (**a**) τ_1 and (**b**) A_1 from a field-dependent series measured on another sample at $T = 200$ K; (**c**) temperature-dependent series measured on the main sample at different fields. The errors are calculated from the fit. The color-matched lines as guide to the eye.

12.1.2 Charge Transfer Transition

The discussion will be continued with the expected changes of the parameters A_1, τ_1 with varying T, F, B in case of a charge transfer transfer (CTT) scenario (electron from O2p to Mn e_g state). A sketch of this transition is drawn in fig. 12.7.

The amplitude, A_1, is expected to be rather T-independent relative to the other transitions, since the O2p states are fully occupied in the ground state, so that an electron can be provided for a spin-conserving transition independent of the macroscopic magnetization state. Furthermore, due to the hybridization of the O2p states with the Mn3d states [159, 161, 162], the

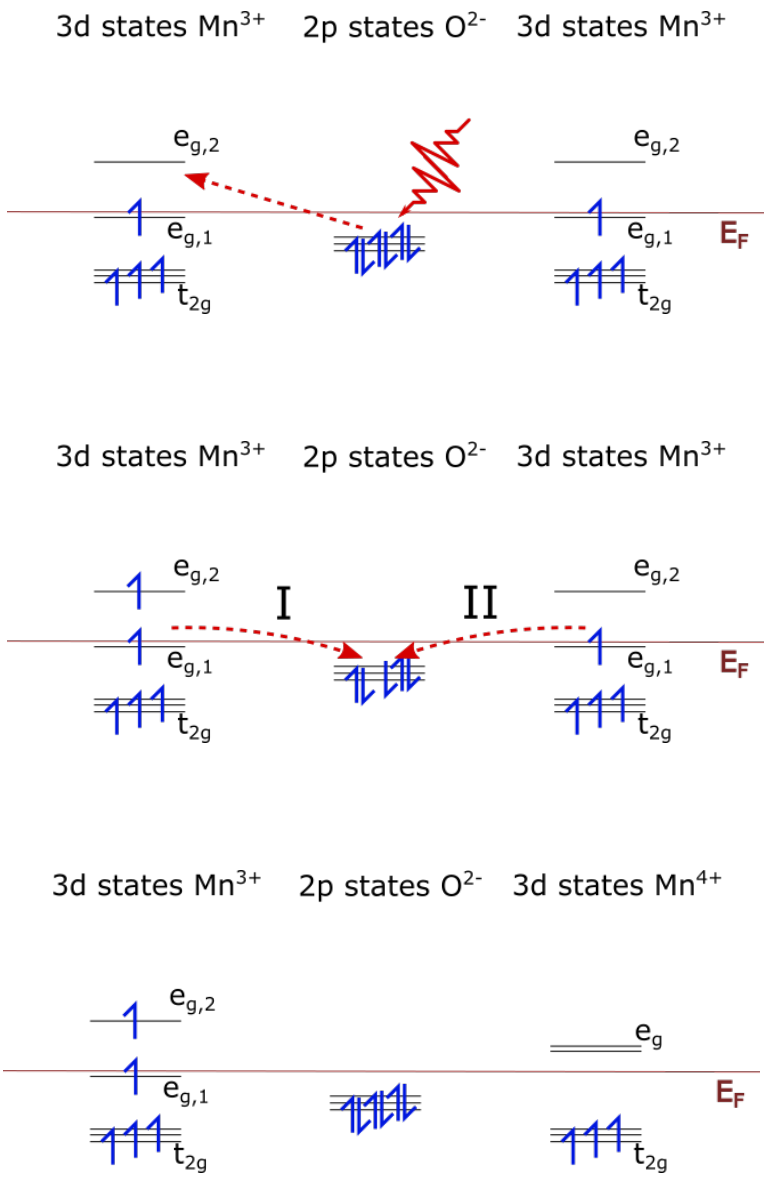

FIGURE 12.7: Charge transfer transition: **Upper panel**: Excitation from an O2p state into an Mn $e_{g,2}$ state. **Middle panel**: Possible hopping from Mn $e_{g,1}$ states into the empty O2p state. **Lower panel** The hopping process II (in the middle panel) leads to a situation which is similar to the excited state of an intersite transition (see middle panel of fig. 12.4).

thermal reduction of the spin splitting of the O2p states, when increasing the temperature, is expected to be proportional to the reduction of the Mn spin splitting; at least in a first approximation. Therefore, the energy difference between the occupied O2p and unoccupied e_g states of a Mn ion is expected to stay roughly the same. Hence in a rough approximation,

the transition probability of a charge transfer transition from O2p to e_g states is expected to be more or less independent of the macroscopic, magnetic ground state. Nevertheless, the transition probability might be influenced by optical phonon modes which include motions of the oxygen ions with respect to the central Mn ion. But to the best of my knowledge, no publication exists, where the transition probability of a charge transfer transition was calculated in dependency of the population number of these phonon modes. Thus, an estimation is needed here: Since, the transition probability is dependent on the overlap of the initial and final state throughout the transition itself, it is assumed that A_1 decreases caused by the reduction of the overlap due to the thermal expansion. Only in the case, that very specific phonon modes, which positively influence the overlap, are excited predominantly, an enhancement of A_1 is expected. Regarding the fluence dependence of a charge transfer transition, the probability, and therefore A_1 should increase when more photons are provided.

Since, no suddenly developing bottleneck is expected for a O to Mn ion transition (see above), no sudden or drastic change in τ_1 should exist for a charge transfer transition. But, since the thermalization time of the hot electrons is included into τ_1, it should slow down in case of a decrease in the mobility of the electrons at the base temperature[3] caused by a (polaronic) trapping of the (hot) electrons, which leads to a reduction of the electron-electron scattering and, hence, to an enhancement of the hot electron lifetime. As argued in the previous section 12.1.1, the mobility of the electrons in general is expected to be increased by the charge transfer transition: here, an hole is excited in the O2p states and the electron is transferred into a conduction state above the Fermi level. The O2p holes which are part of the hopping conduction model in manganites (section 4.1.3), and contribute therefore to the conductivity. An argumentation like that, demands a decrease of the thermalization time when increasing the fluence due to the more metallic like state, as argued before (sec. 12.1.1). The table 12.2 summaries the aforementioned expectations of the reaction of a charge transfer transition caused by changes in $T,\ F,\ B$.

[3]The set temperature value for the cryostat is meant by "base temperature", thus the environmental temperature of the sample system.

TABLE 12.2: Expectated reactions of a charge transfer transition:

	τ_1	A_1
temperature caused by	slight increase (✓) the generally decreasing mobility	slight decrease ✓ the thermal expansion
fluence caused by	decrease χ increase of mobility by excitation	increase ✓ more photons
magnetic field caused by	unchanged or slight decrease χ the generally increasing mobility	roughly unchanged χ

As before, the expected magnetic field dependence of this transition type, does not match with the experimental data. In combination with the fluence dependence, which is opposite as well, the transition type of a majority charge transfer from an O2p state to a Mn $e_{g,2}$ state can be excluded as reason for the experimental findings.

12.1.3 Photo-Induced Hopping

A third transition which is suggested in literature [67] is from an occupied Mn $e_{g,1}$ state into an unoccupied $e_{g,1}$ state of another Mn ion. The resulting occupation of this transition is equivalent to the occupation which is achieved by a thermal hopping (see section 4.1.3). Here, the intermediate step via the O2p states during a thermally driven hopping is skipped. Due to this reason, the transition is called *photo-induced hopping*. From a static point of view, the initial and final state are equivalent. Thus, Quijada and co-workers [67] suggested in their hypothesis, that the energy of the ~ 1.2 eV transition is needed as breathing distortion energy, E_B, which needs to be introduced as a JTD to the octahedron surrounding the previously unoccupied Mn ion. This transition type is, therefore, special in that sense, that this transition does not change the electron-k- space-distribution after it is fully executed in a good approximation. From the electron, as an indistinguishable Fermion, point of view, there is no energy difference whether it sits in the initial state corresponding to one Mn^{3+} ion or in the final state, which belongs to another identical Mn^{3+} ion. Hence, the Fermi-Dirac distribution of the electron system is not changed after the transition.[4] A visualizing sketch is depicted in fig. 12.8; as visible when comparing the upper and the lower panel, the occupied

[4]Note, that this statement estimates a fully completed activation of the oxygen octahedron, which surrounds the final state Mn ion, as well as a fully completed relaxation of the JTD surrounding the initial state Mn ion.

density of states stays unchanged from an energetic point of view, in the approximation of an ideal crystal.

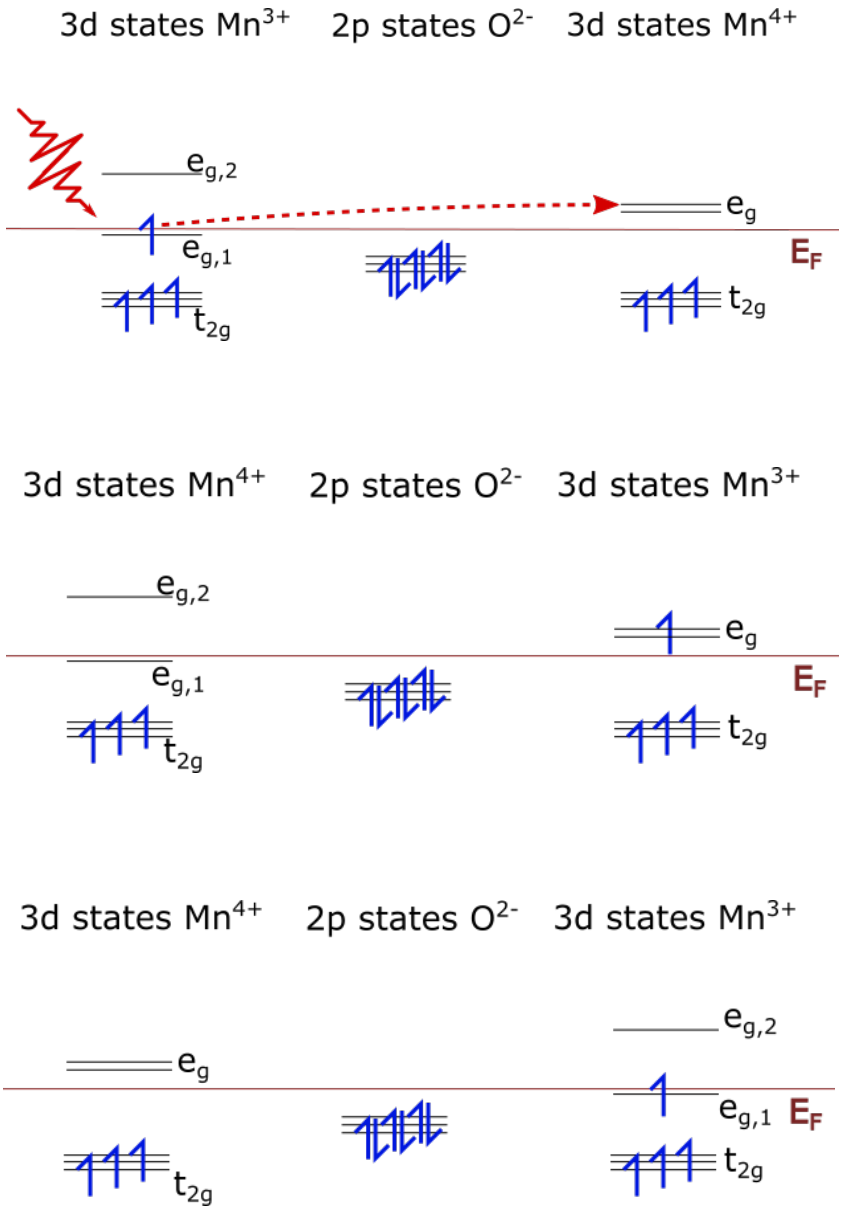

FIGURE 12.8: Photo-induced hopping process: **Upper panel**: System before a hopping process is photo-induced. **Middle panel**: Electron is transferred before the surrounding oxygen octahedra are rearranged. **Lower panel** Established transition with a relaxed octahedron at the initial site and an JT distorted octahedron at the final site.

Since, the transient magneto-optical response is measured, too, a brief estimation of the change in the total angular momentum, J, caused by a photo-induced hopping is going to

be discussed in the following. A significant change of macroscopic average of J during a pump-probe experiment can be excluded for geometrical reasons: The overlap the wave functions, which have different values of J and belong to different Mn ions, is insignificantly low. Hence, the probability for a photo-induced hopping transition, which changes J, is vanishing Therefore, no transient change in the Kerr signal is expected.

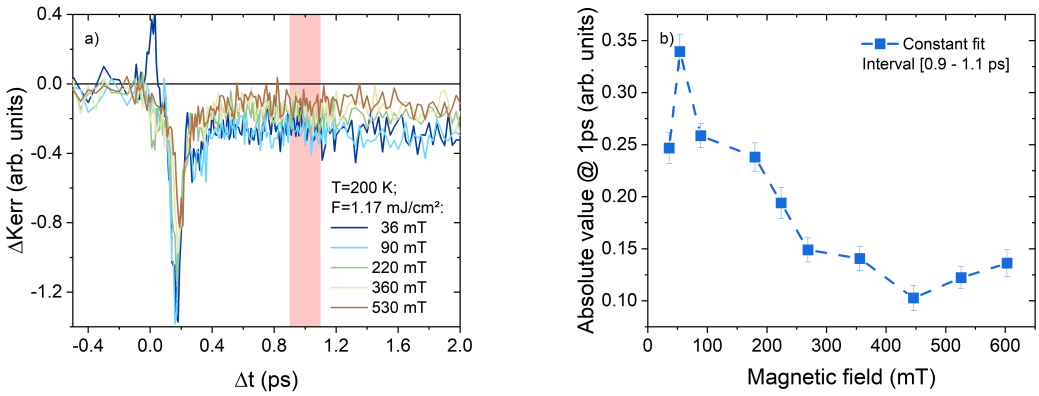

FIGURE 12.9: (**a**) TRMOKE signal shortly after the excitation for different magnetic fields. All measurements done at $T = 200$ K and $F = 1.17$ mJ/cm^2. The reddish marked area correspond to the fit interval for $f(\Delta t) = c$. (**b**) the field-dependent fit results. The errors are calculated from the fit. The color-matched lines as guide to the eye.

As shown in fig. 12.9 (a), there is a transient change in the Kerr signal at the sub-ps timescale already. Following the findings in the MOKE results, a transition, which leaves the J unchanged in the macroscopic average, does not explain the data. Moreover, fig. 12.9 (b) shows an inverse magnetic field dependency of the absolute value of the signal amplitude, averaged in the interval $[0.9 - 1.1]$ ps, which is absolutely counterintuitive for a hopping process, since a stronger alignment of the Mn core spins would encourage hopping. Therefore, a photo-induced hopping transition is most likely excluded.

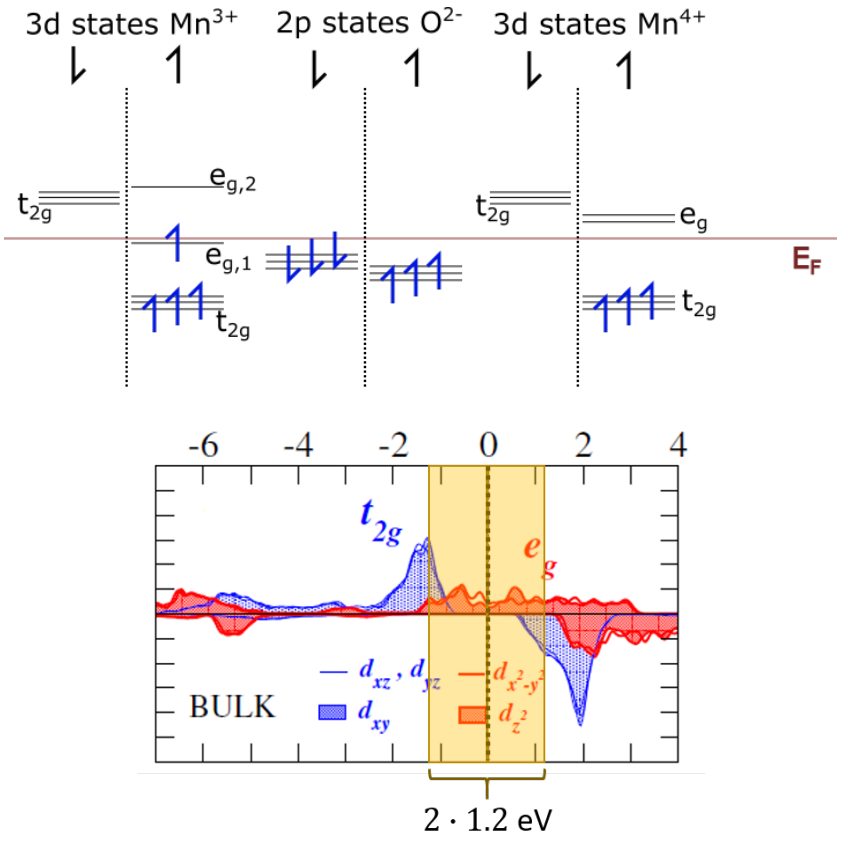

FIGURE 12.10: **Upper panel:** Sketch of the energy levels of different states close to the Fermi-energy, E_F, in a hole-doped manganite, e.g., LSMO. In order to demonstrate the energy splitting of the spin states, the majority and minority channels are depicted separately for each ion. The orbitals corresponding to a Mn ion are named in the sketch. **Lower panel**: Spin-resolved density of states for the Mn3d orbitals of bulk LSMO calculated by DFT. The figure is edited by marking the accessible states by an 1.2 eV pump pulse in yellow. The picture is reprinted with permission from [85]. Copyright 2007 by the American Physical Society.

12.1.4 Photo-Induced Spin-Flip Transition

It was shown in section 12.1.1 - 12.1.3, that non of the transition, which is proposed in literature, is able to explain the observed behavior of the initial increase of the transient reflectivity signal. The issues to explain the magnetic and fluence-dependent behavior persist throughout all propositions. Especially, the response to an externally applied field does not fit to a electron-spin-conserving transition. When applying a (higher) field within the PM phase,

a more metallic like behavior is expected, because the electron mobility is promoted by double exchange at least close to the PT. In contrast, the results for different fields in fig. 12.6 (c) seem to be shifted towards longer timescales but the overall temperature dependence does not change its shape by varying the magnetic field. This leads to the idea that a non-electron-spin-conserving excitation might be a solution. Thus, finally, a newly suggested hypothesis shall be discussed here: a light-induced spin-flip transition (SFT), e.g., by assuming a magnetic dipole transition.

In order to discuss the expectations of the reactions of a spin-flip transition with respect to external stimuli, a new type of sketch for the energy levels, which are included in possible (hopping) transitions, is needed to be established. The usual way of sketching the energy levels ignoring the spin splitting covers the fact that much more energy is needed to initiate an anti-parallel spin hopping than a parallel spin hopping. Thus, if more energy is needed for the initial step, this type of hopping is much less probable and therefore, the thermalization process, which depend on hopping, takes longer. For this purpose, the type of sketch which is shown in fig. 12.10 is introduced. This kind of picture is inspired by the figure 1 (a) of the paper [163]. In fig. 12.10, the energy levels which contribute to a potential hopping process of the three ions, which are included in such a process, are depicted. As referenced in the picture, for all three ions, both spin channels (minority and majority) are shown separated by the vertical dashed lines. As an example picture, the unexcited ground state was chosen.
Of course, these sketches do not represent the complete physical picture, e.g. states in manganites do not exhibit only a molecular orbital-like character but also a band-like character. But still, the sketches shall help the reader to comprehend the hypothesis, which is set up in this section. Having said all that, let's turn to the hypothesis itself.

In contrast to electron-spin-conserving transitions, a spin-flip transition reduces the mobility of the excited electron due to its antiparallel alignment with respect to the average core spins of the surrounding Mn ions within the FM phase. As sketched in fig. 12.11 middle panel, a hopping of an majority O2p electron into an majority $e_{g,1}$ state is energetically favored and, hence, more likely. But as visible in the middle panel of fig. 12.11, in this case, the O^{1-} ion

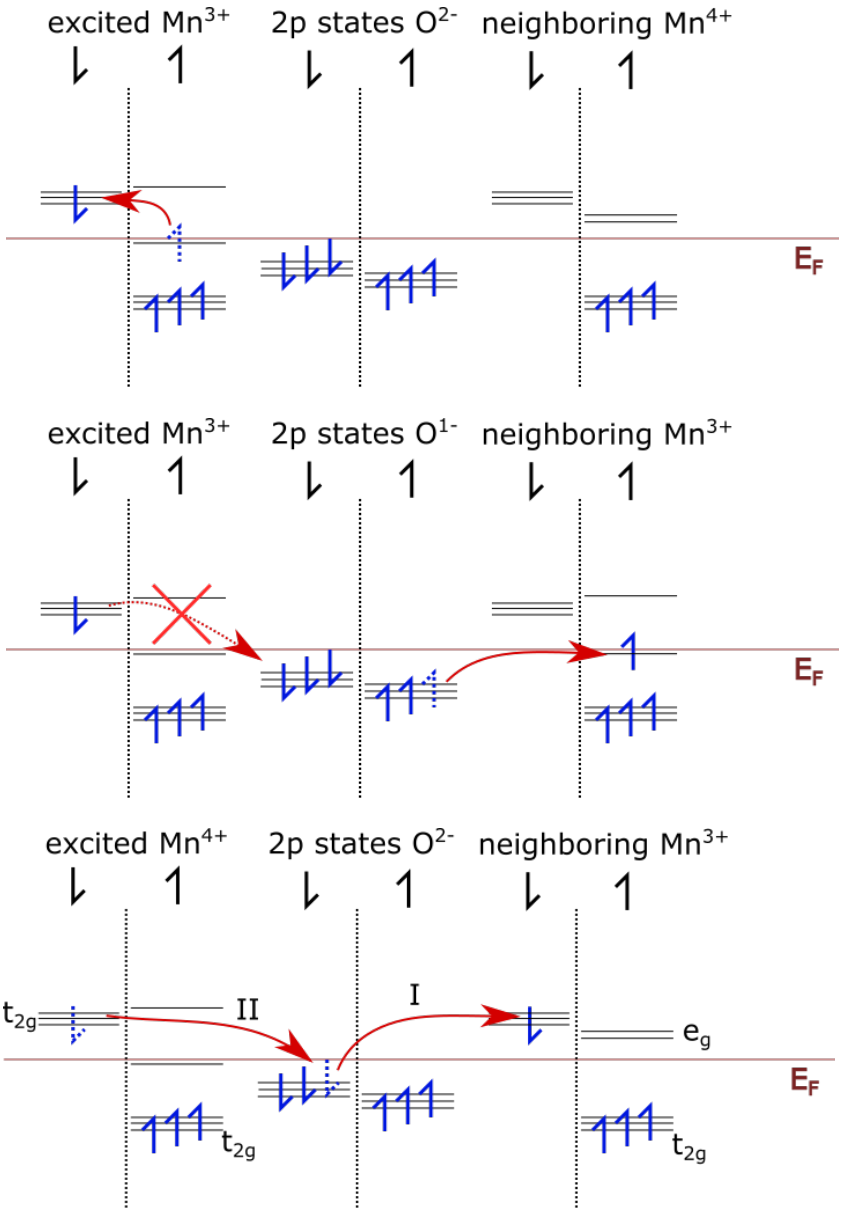

FIGURE 12.11: **Upper panel**: spin flip transition above the Fermi-energy at a Mn^{3+} site. **Middle panel**: initial step of a usual parallel spin hopping process - O2p into an unoccupied $e_{g,1}$ state in the majority channel. **Lower panel** initial step (I) of an antiparallel spin hopping process - O2p into an unoccupied t_{2g} state in the minority channel. And (II) a possible transition from the photo-excited Mn ion into the now free O2p state in the minority channel.

does not provide a minority state for the spin-flipped, excited electron to hop into. Only, if a spin-down electron from the O2p minority states vacates its state and expends more energy to

overcome the Hund's coupling energy, a hopping of the excited minority t_{2g} electron becomes possible.

Since, the electron-electron thermalization time is limited to the available phase space for electron-electron scattering, the overall, thermal behavior (see fig. 12.2) is dominated by the mobility of the conduction electrons. This time, the thermalization time decreases, when the resistivity increases driven by the increase of spin-down electrons in the Mn3d states, while approaching T_C. The hot or excited electrons' mobility contribute also to the scattering rate, thus, the systems reaction on the external stimuli can be explained. By applying a magnetic field to the sample, the Mn core spins align (stronger), since the spin splitting is enhanced. Therefore, the mobility of the hot electrons shrinks due to the less likely case of a neighbouring Mn ion with core spins pointing downwards (see fig. 12.11).

It is presumed, that the decreasing behavior of A_1 in dependence of an applied magnetic field is caused by the additional spin splitting.

In the spin-flip transition hypothesis, two effects explain the anomalous fluence dependence of the first process. First, the more electrons undergo a spin-flip transition, the greater is number of electrons close to the Fermi energy, which become relatively immobility due to their antiparallel spin, with respect to the total number of electrons which are able to contribute to e-e-scattering. Secondly, if the number of Mn^{3+} ions in low spin configuration increases, the mobility of $e_{g,1,\uparrow}$ electrons shrinks, too, since the occupation of $e_{g,1,\uparrow}$ states corresponding to a former low-spin Mn^{3+} requires a formation of a Mn^{2+} ion, which is energetically unfavorable. Therefore, when the probability increases due to more photons, the thermalization time and, thereby, τ_1 slows down.

In summary, the expectations of the spin-flip transition reaction on external stimuli explains the found observations as discussed previously. Again, the expectations are summarized in a tabular form see 12.3.

As visible in fig. 12.12, the expectations for the dependence of τ_1 on the external stimuli change by B and F for the case of a photo-induced spin-flip process, see table 12.3, match with the fit results pf τ_1 as visible in fig. 12.12 (b) and (c). Furthermore, the decrease which is

TABLE 12.3: Expected reactions of a photo-induced spin-flip transition:

	τ_1	A_1
temperature	decrease χ	slight decrease ✓
caused by	generally decreasing mobility	the thermal expansion
fluence	increase ✓	increase ✓
caused by	larger number of anti-parallel aligned hot electrons and therefore, reduction of the general mobility	more photons parallel alignment between
magnetic field	increase ✓	decrease ✓
caused by	generally decreasing mobility of hot electrons	larger spin splitting

found for the MOKE response, see fit. 12.12 (d), is explainable within this hypothesis. The spin-flip transition induces a change of the spin system and therefore lead to a demagnetization on the ultrafast ($\lesssim 450$ fs).

Nevertheless, the expectation of a spin-flip scenario does not match for the temperature-dependent results (fig. 12.12 (a)). To point out, the photo-induced spin-flip is most likely not the only light induced transition, which happens within the measurements. Spin-flipping transitions, which are introduced by a magnetic dipole transition, are much weaker than electric dipole transitions [21, 22, 23, 24]. Hence, if electric dipole transitions happen next to the spin-flip, the general thermal dependence is dominated by the response of this additional electric dipole transitions. In contrast, the other two external stimuli impact the thermalization time of the spin-flipped electrons much stronger since the phase space for electron-electron scattering of a spin-flipped e_g electron is reduced quite strongly. Here, it is suggested that the imprint of the spin-flip transition on the thermalization time is disproportionately large compared to other contributing transitions.

12.1.5 Discussion Summary of the Initial Increase in the psTR Data

In conclusion, three different types of initial excitation processes, charge transfer, intersite and optically induced hopping, are suggested in literature and a photon-induced spin-flip process was suggested as additional hypothesis in this thesis. Within the assumption of

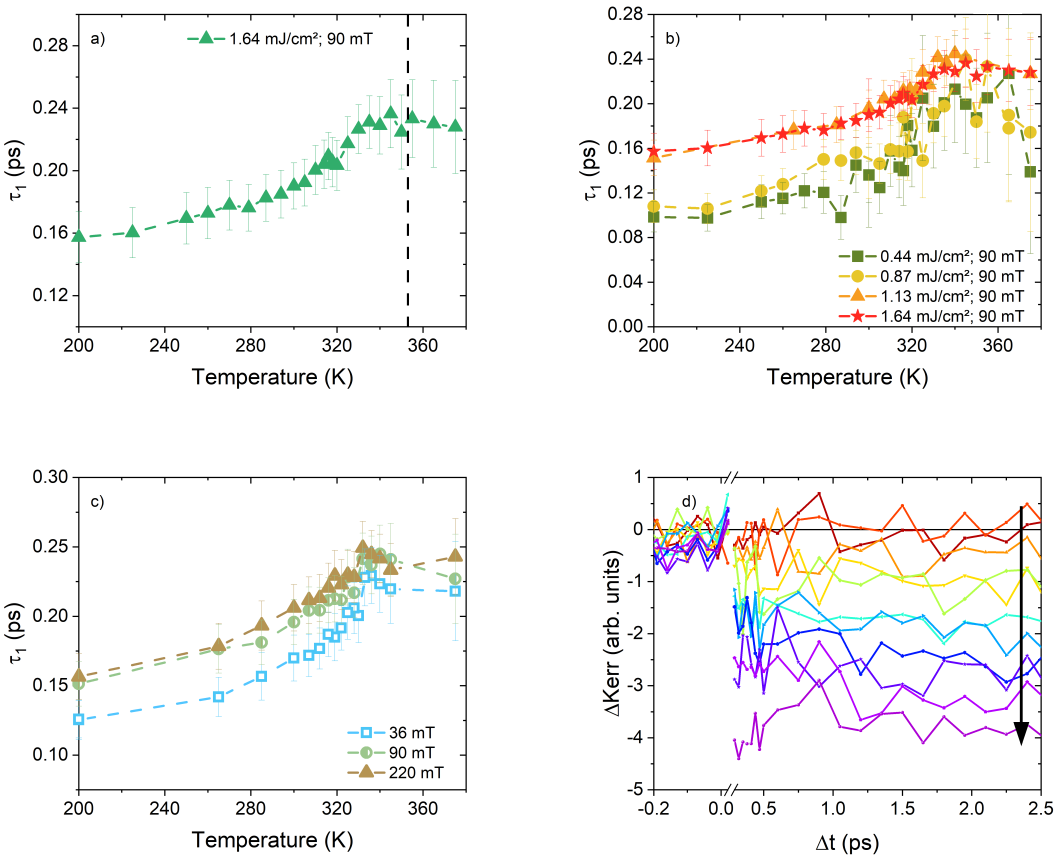

FIGURE 12.12: Dependencies of the time constant τ_1 on the (**a**) temperature, (**b**) fluence, and (**c**) the applied magnetic field of the transient reflectivity. (**d**) depicts the change in the TRMOKE signal when decreasing the temperature.

the ionic-picture, an hypothesis of the main excitation step was set up. The fit results for the τ_1-process, which are discussed in this section, exclude a transition type, which either enhance the mobility of the conduction electrons or leave it roughly unchanged, justified on the changes τ_1 in the psTR as well as in the TRMOKE measurements with the changes of the external stimuli, $T,\ F,\ B$. Hence, a charge transfer type excitation, an intersite transition as well as a photon-induced hopping process do not explain the experimental observations.

Therefore, the psTR and TRMOKE data in external stimuli dependence suggest that the excitation of the initial step, τ_1, is dominated by a photo-induced spin-flip. Nevertheless, it is

recommended to review this hypothesis using time-resolved ab-initio calculations since the arguments are based on the rough assumption of an ionic-picture.

12.2 Feature No. 2 - Coherent Optical Phonon Excitation

The initial excitation step, which consists of the occupation of a former unoccupied Mn3d orbital as well as a most likely depopulation of an former occupied Mn3d orbital, requires a rearrangement of the surrounding oxygen octahedron(/octahedra). In order to do so, optical phonons are needed to be excited. Therefore, in accordance with literature [105, 118, 151] the oscillation which occur at the hundreds of femtoseconds timescale are assigned to the excitation of coherent optical phonons (COP).

12.3 Feature No. 3 and No. 4 - Second Electron-Phonon Coupling and Brillouin Scattering

The first two features suggested an excitation and thermalization process of electrons which lead to a disturbance of the established JT distortions caused by the occupancy of a Mn(3d) state above the Fermi-energy. Here, the strong electron-phonon coupling of the manganite empowered the first step, τ_1, by enabling the transferability of the excited electron into an additional Mn(3d) state via the excitement of coherent optical phonons and, thereby, the activation of the surrounding oxygen octahedron. Note, that the activation of the oxygen octahedron is not equivalent with the thermalization of the electrons with the entire lattice. In other words, the absorbed energy is now stored in the occupation of the higher energy level and in the disturbance of the JT distortions, which existed before the pump-pulse. Thus, the question is now, how does the dynamics go on?

In LPCMO, similar two features are found, see section 9.3: a second exponential increase, τ_2, as well as a peak-like structure, which is identified as coherent acoustic phonon excitation. It is suggested for LPCMO that τ_2 represents a second electron-phonon interaction based

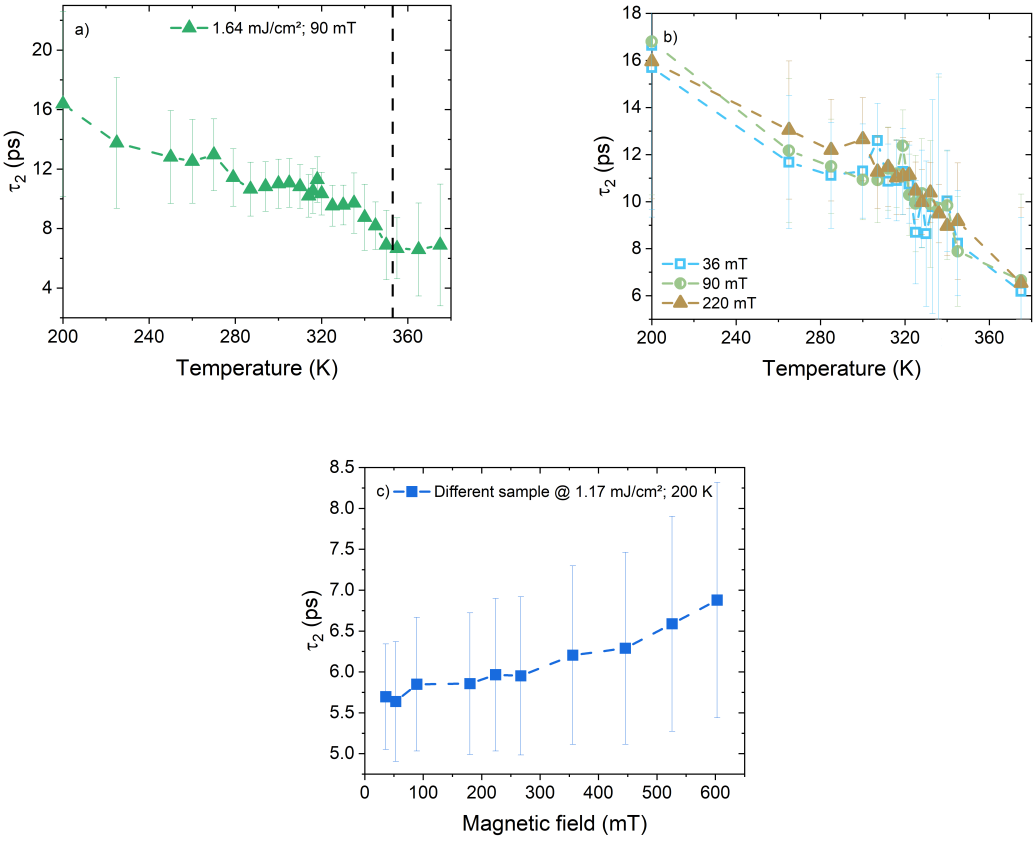

FIGURE 12.13: The fit results of τ_2 (**a**) temperature dependence; (**b**) three temperature-dependent series for different magnetic fields and (**c**) magnetic field-dependent series at $T = 200$ K. The color-matched lines as guide to the eye. The errors are calculated from the fit.

on the observed appearance in all magnetic phases within $\Delta\mathcal{R}$ and an invisibility of it in the transient Kerr signal. A similar behavior of τ_2 is observed for the LSMO dynamics, see fig. 12.13. A temperature dependence is found, but the fit results of the second increase are rather independent on the external magnetic field. Furthermore, there is no indication of a transient change at a comparable timescale in the TRMOKE signal. The second increase in the transient reflectivity data exhibits a time constant which increases from ~ 8 ps to ~ 16 ps when the base temperature is decreased an persists across the phase transition, as shown in fig. 12.13 (a). In contrast, no further decrease (or an increase) is visible in the TRMOKE signal (see fig. 12.14) at the delay times which are under debate.

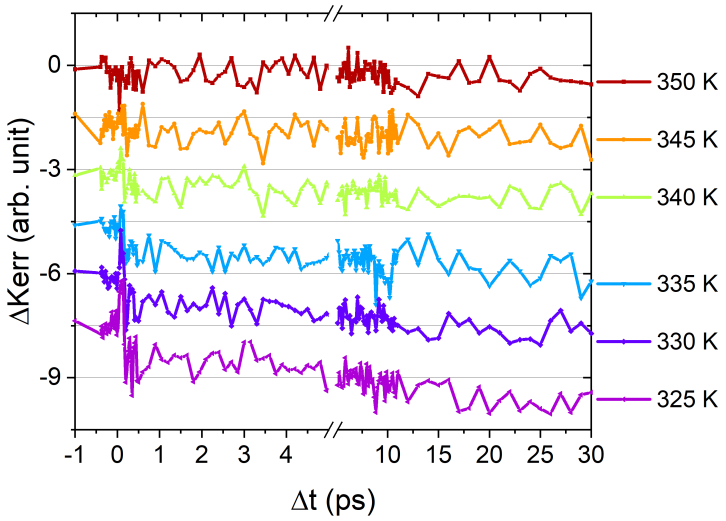

FIGURE 12.14: A selection of TRMOKE data at a time scale up to $\Delta t = 30$ ps which are y-shifted in order to demonstrate that no dynamics of about $\tau \approx 12$ ps persists in the TRMOKE data.

Again, the investigation of Li and co-workers [118], where they observe a second timescale for the lattice dynamics in $La_{0.84}Sr_{0.16}MnO_3$ using femtosecond electron diffraction, confirms the hypothesis of a second electron-phonon energy dissipation channel. For a more detailed discussion see section 9.3.

Therefore, the feature No. 3, the second exponential increase, is suggested to reflect a second coupling between the electrons and the lattice.

Following the progress of the psTR-data, a second exponential increase, feature No. 3, is found to overlap with the feature No. 4, similar to the LPCMO case (see sec. 9.3). In contrast to the LPCMO data, distinct oscillations are visible in a number of the LSMO data in addition to the first peak, which is described by the Gaussian peak in eq. 8.1, see fig. 12.15. Thus, feature No. 4 is strongly recommended to be the first maximum of Brillouin scattering.

Brillouin scattering, in general, is possible in every part of the sample, in a thin layer as well as in the substrate. Ren et al. [164] have investigated BS in similar sample systems, LSMO grown on STO, in more detail. Following the frequency calculations in this paper for STO,

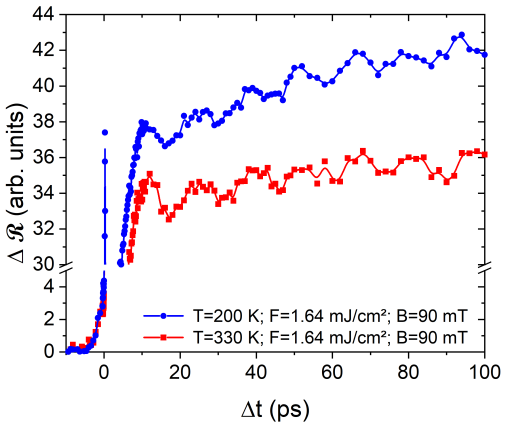

FIGURE 12.15: Exemplary psTR traces which show distinct Brillouin scattering. Two different temperatures of the same measurement series at $F = 1,64$ mJ/cm^2 and $B = 90$ mT are plotted: $T_1 = 200$ K in blue and $T_2 = 330$ K in red. The color-matched lines as guide to the eye.

the expected oscillation frequency of $f_{Lit} \approx 70$ GHz [164] matches quite well the oscillation frequency, which is found in the data here, e.g., see fig. 12.15, $f \approx 68$ GHz.

The frequency of the Brillouin scattering can theoretically be calculated by [164]:

$$f = \frac{2vn(\lambda_{probe})}{\lambda_{probe}}.$$

With the literature value of the sound velocity of STO, $v_{\text{STO}} = 7800$ m/s [164], and the reflective index, $n_{\text{STO}} = 2.4597$ [165] at $\lambda_{probe} = 515$ nm, the frequency is calculated to $f_{theo} = 74.5$ GHz. Therefore, the feature No. 4 is assigned to Brillouin scattering in the STO substrate.

12.4 Feature No. 5 - Spin-Lattice Relaxation

In the case of LPCMO, it is shown in sec. 9.4 that the third exponential increase, which corresponds to the feature No. 5, can be assigned to the spin-lattice relaxation. In the current case of LSMO, this fifth feature in fig. 11.1 shows a comparable behavior depending on the external stimuli, but with the difference of an off-set, as it is going to be discussed in the following. Therefore, the time constant τ_3 is going to be attributed to the spin-lattice interaction also for LSMO. This means it is connected to the thermally driven spin(-flip)-dynamics. Note that, if the hypothesis of a photon-induced spin-flip in section 12.1 is correct, then the spin-phonon scattering, which is assumed to be the underlying process of the feature No. 5, would be a second, dynamical step which changes the magnetic order of the system.

But, we start with the discussion of the impacts of the external stimuli, $T,\ F,\ B$, on the third, exponential increase of the transient reflectivity signal.

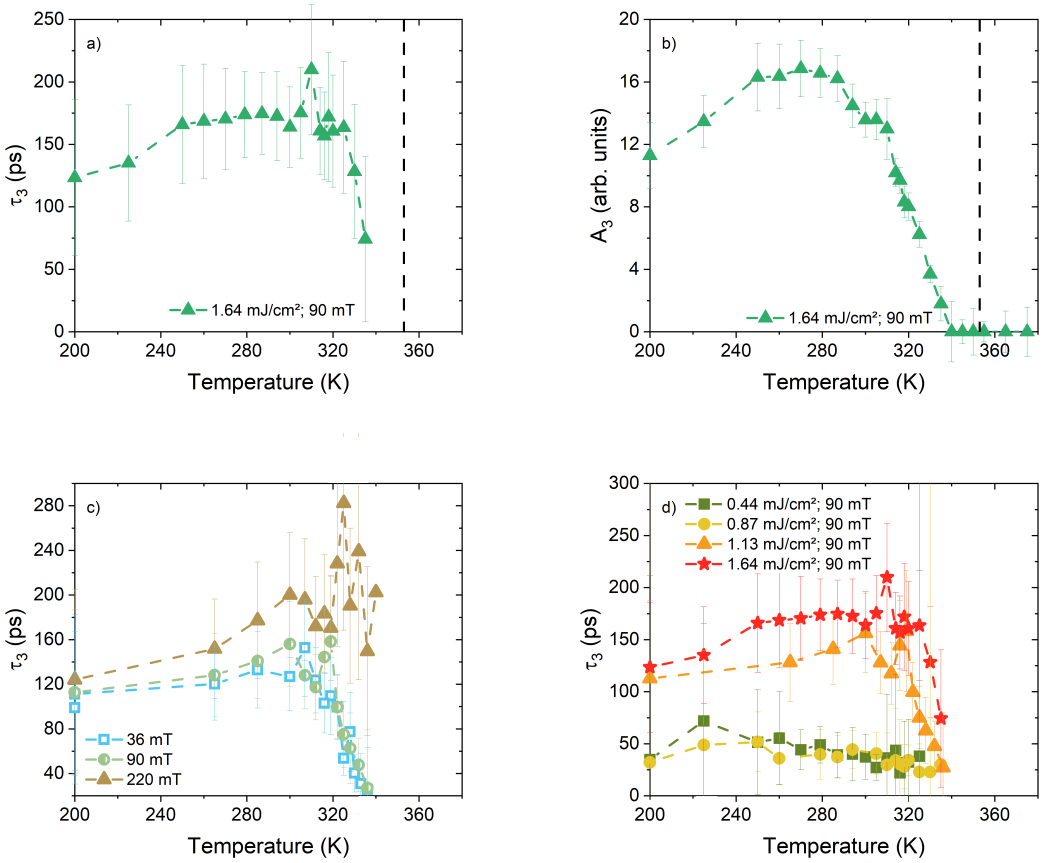

FIGURE 12.16: Dependencies of the third exponential process on (**a**) the temperature (τ_3), (**b**) the temperature (A_3), (**c**) the magnetic field (τ_3), and (**d**) the fluence (τ_3). The errors are calculated from the fit. The color-matched lines as guide to the eye.

The most conspicuous development of τ_3 is its vanishing for high temperatures. Note, that it does not vanish at about the static T_C, as it was shown in the LPCMO case, but it disappears at $90 \sim 96\ \%$ of T_C for LSMO. This fact is going to be discussed after the changes which are introduced by varying the external stimuli.

As visible in fig. 12.16, the temperature where the third exponential increase vanishes shifts towards higher temperatures when a stronger magnetic field is applied. These behaviours

strongly suggests a strong connection of τ_3 to the magnetic (base) state of the sample: when forcing the spin system to align in an external magnetic field, and thereby, shifting the static transition temperature to higher values, then the DSWT, which is the reason why the spin dynamics is visible in the transient reflectivity data, emerges at higher temperatures already. Within the measured fluence range, the vanishing point of the τ_3-process shifts towards higher temperatures by increasing the pump fluence. In the theoretical picture of the three temperature model, this behavior seems to be counterintuitive: Injecting more energy into the electron system during the pump-process leads to a hotter electron system, the energy of which is transmitted onto the phonon system during the electron-phonon thermalization. Finally, more energy is transferred in to the spin system and in its disordering. Hence, the expected consequence is a total demagnetization at lower base temperatures already. This described behavior is found also for LPCMO, see. chapter 9.4.

However in LSMO, the amplitude, A_3, vanishes at slightly lower temperatures as the transition temperature; it disappears at $90 \sim 96\ \%T_C$ already, see fig. 12.16. To clarify whether the model, which is explained in the previous paragraph, is incorrect for LSMO or if something else happened, e.g., in the fit, which let the vanishing point of A_3 seems to appear at lower T as it actually happens, the MOKE data should be considered. Regarding the fit, two other explanations might be possible, too. First, the used fluences are quite low compared to, e.g., the ones used for LPCMO, thus the reached amplitudes in the psTR data are relatively small. Combining this with the distinctly visible Brillouin scattering, which occurs more pronounced and slightly later than in the LPCMO measurements[5], might lead to an underestimation of A_3 for lower fluences within the fit. If this is true, an overestimation of A_2 as well as τ_2 would be the consequence.

A second, explanation might be the following. If the demagnetization process becomes so slow and weak that it is overlapped by the relaxation process, τ_4, so that it is invisible by eye within the scope of the scanned pump-probe delay range. Testing this hypothesis, three sets of simultaneously measured TRMOKE and psTR data are plotted together in 12.17. For each trace, the turning point is marked by a vertical line where the demagnetization process

[5]Main, fitted position of the Gaussian peak for LPCMO is ~ 8.5 ps versus ~ 10.2 ps for LSMO.

or the relaxation process become dominant in the TRMOKE and the transient reflectivity measurements, respectively. For $T = 355$ K and $T = 350$ K, a huge difference between the appearance of the relaxation process (earlier) in the psTR data and the appearance of the demagnetization (later) in the TRMOKE exists. Decreasing the temperature further, the difference is reversed for $T = 345$ K. But the demagnetization is still too weak to lead to a change in the reflectivity signal, which is visible as an increase of the data. Following this finding, the hypothesis, that the contribution of the demagnetization to the reflectivity signal are too weak to be visible as a further increase of the signal, seems to be plausible. Since the strength of the demagnetization dependents on the pump-fluence [16, 142, 163], the appearance of a non-vanishing A_3 within the fit is shifted towards lower temperatures when pumping the system with a weaker fluence.

In conclusion, the appearance of the feature No. 5, which is strongly influenced by external stimuli, strongly suggests a process which is dependent on the static situation magnetization of the LSMO. In combination with the found time constants of $\tau_3 \sim 50$ - 250 ps, the feature No. 5 described by the third exponential function, $A_3,\ \tau_3$, is assigned to the spin-lattice relaxation, which manifest itself as demagnetization process in the TRMOKE data.

12.5 Feature No. 6 - Relaxation Back into the Ground State

The feature No. 6 is the only decreasing, exponential function in $\Delta\mathcal{R}$, which is found within the scope of the experiments. Therefore, τ_4 is assumed to represent the relaxation back to the ground state.

Following the development of τ_4 with T, see 12.18 (a), a massive imprint of the PT is visible, namely a critical slowing down peak of the time constant, which has been assigned to the spin-specific heat in earlier works, e.g., [102]. Therefore, a small reminder of the concept of critical slowing down (CSD) shall be given before starting the discussion of τ_4; for more details, see also section 9.5.
Thinking about a system close to a phase transition (first or second order), the entropy of

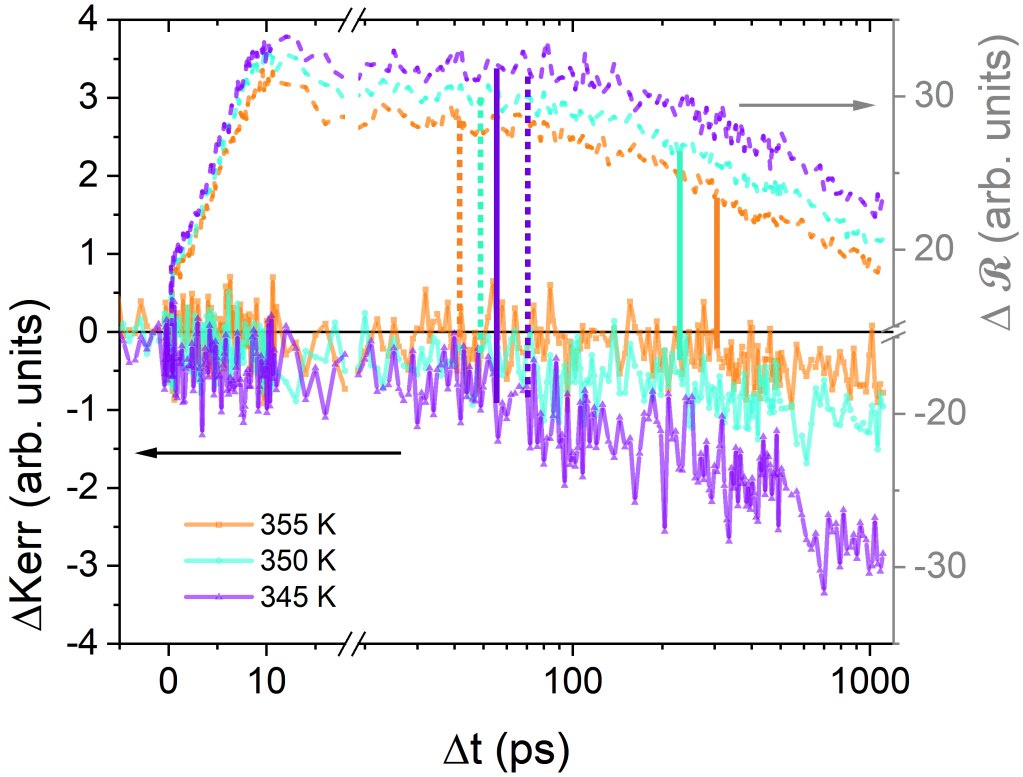

FIGURE 12.17: TRMOKE signal and $\Delta\mathcal{R}$ plotted together for three different temperatures below T_C where the fitted amplitude is not existing $A_3 = 0$ in the fit of the psTR. The solid measurement data correspond to the TRMOKE signal; the dotted data correspond to the transient reflectivity. The vertical solid (dotted) lines mark the times when the demagnetization process (relaxation process) becomes dominant.

the system increases more or less suddenly at the critical temperature, T_C. In the case of a magnetic PT, this means that the previous arrangement of the spin system loses (a part of) the ordering when entering the new magnetic phase, e.g., paramagnetic phase in case of LSMO. Since the difference in the entropy is connected to the specific heat via:

$$\Delta S = \int_{T_1}^{T_2} \frac{C \mathrm{d}T}{T}, \tag{12.1}$$

the specific heat shows a spike-like behavior at T_C. This spike leads to the fact, that an energy barrier of the so called latent heat needs to be overcome before entering the new, more

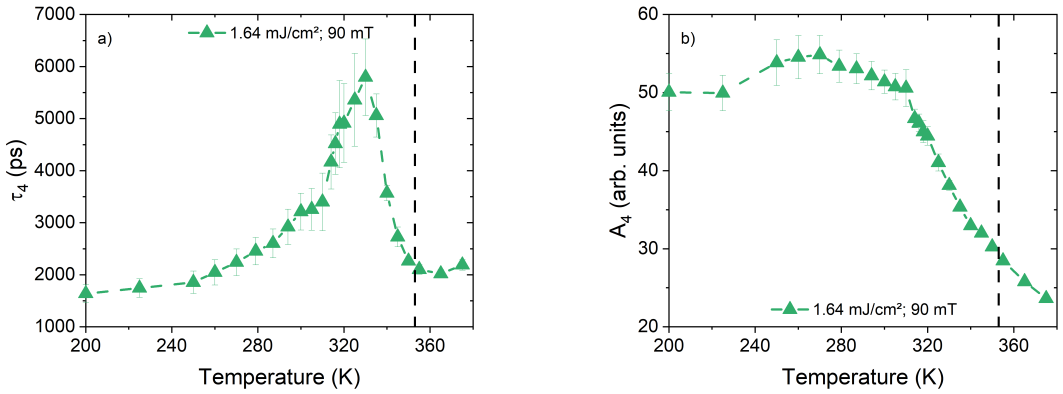

FIGURE 12.18: Temperature-dependent fit results for $\Delta\mathcal{R}$ of the fourth exponential functions from eq. 8.1: (**a**) τ_4, and (**b**) A_4, measured at an applied magnetic field of $B = 90$ mT and a fluence of $F \approx 1.64$ mJ/cm^2. The errors are calculated from the fit. The color-matched lines as guide to the eye. The vertical, dashed, black line marks the statically determined $T_C = 353$ K of the LSMO sample.

disordered phase. Now, this disordering leads to a dramatic slowing down in the recovery step after a phase transition was fully or partially crossed within a pump-probe experiment, since the order needs to be rearranged during the recovery. Note, that the FM/PM PT is a second order phase transition, thus a slowing down behavior is observed already close to the transition temperature and not just only at $T = T_C$.
The results of this thesis underscore that hypothesis, as explained in the following.

The evaluation of the peak in τ_4 with respect to the magnetic stimuli, which are represented by the results of the Asym2Sig fit in fig. 12.19 (a) - (d), shows trends which underscores the critical behavior perfectly. When forcing the spin system to align to an higher external field, the dynamic transition temperature, see fig. 12.19 (a), is shifted to higher values, whereas the general shape of the peak becomes broader, see fig. 12.19 (c), and less pronounced, see fig. 12.19 (b). If the peak in τ_4 is directly connected to the spin specific heat, the area beneath the curve should be connected to the entropy change of the system, see eq. 12.1. Hence, the reduction of the ordering is less strong for higher, applied, magnetic fields when integrating

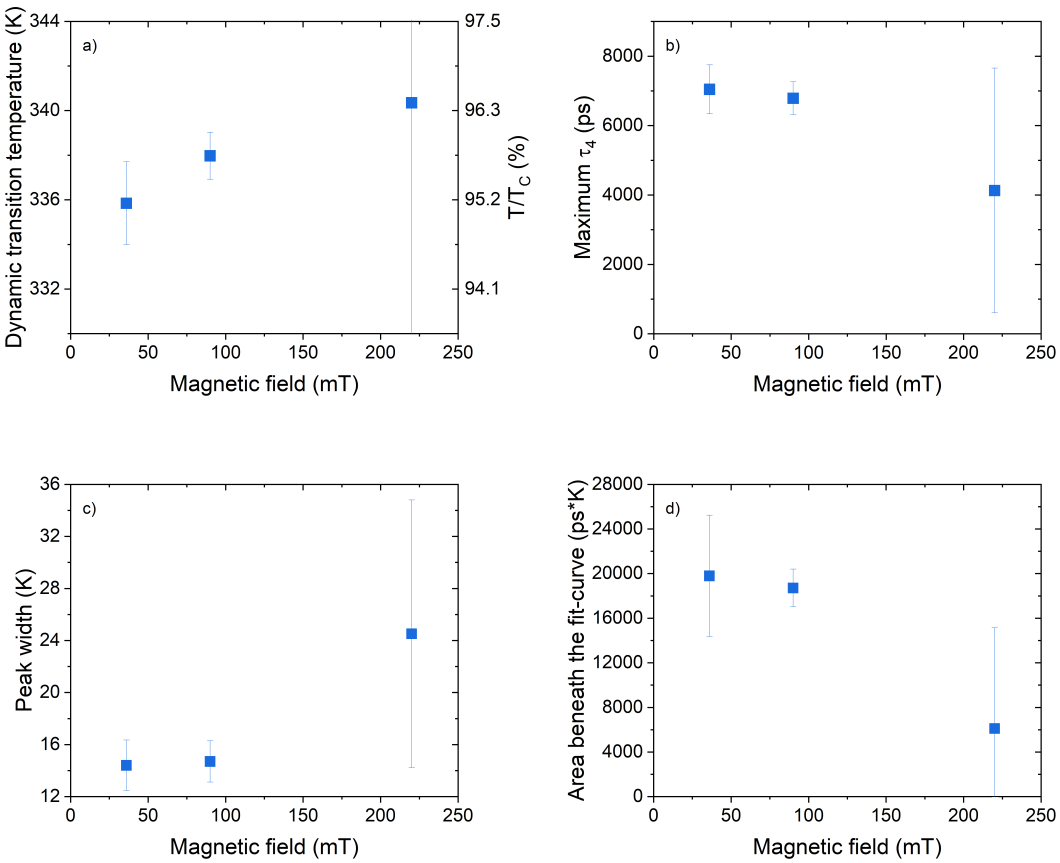

FIGURE 12.19: Results of the Asym2Sig fit for τ_4 in magnetic field dependence measured at $F = 1.13$ mJ/cm^2: (**a**) peak position, (**b**) maximum of the fit, (**c**) the width, and (**d**) area underneath the curve. The errors are calculated from the fit.

over the same temperature range.

When thinking of the fluence as energy which is injected into the sample system during the pump process, the fig. 12.20 (a) fulfils the expectations of the CSD hypothesis with the downward trend while increasing the fluence. If the system is pumped harder, the phase transition is crossed during the excited dynamics already when starting from a lower base temperature.

Also the narrowing of the peak in fig. 12.20 (c) is explainable in the CSD hypothesis. If more energy is injected into the system, the enforced change is higher, hence, the difference in the

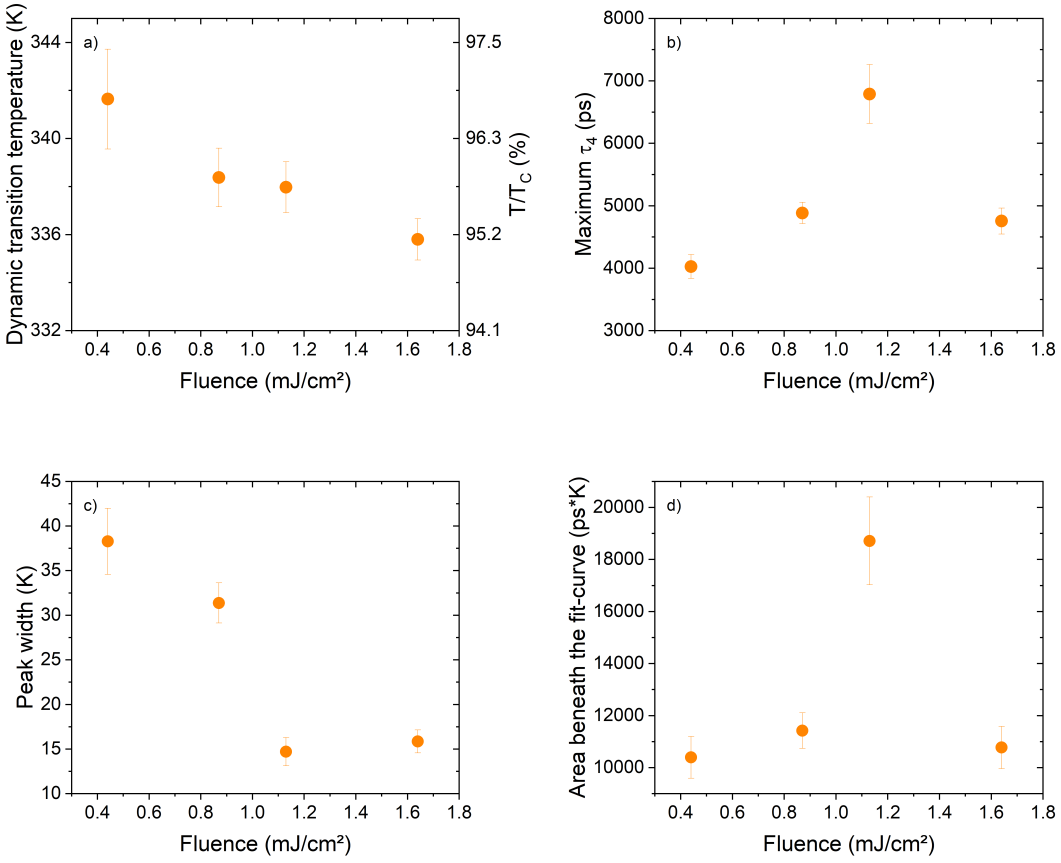

FIGURE 12.20: Results of the Asym2Sig fit for τ_4 in fluence dependence measured at $B = 90$ mT: (**a**) peak position, (**b**) maximum of the fit, (**c**) the width, and (**d**) area underneath the curve. The errors are calculated from the fit.

repelling energy potential is stronger at the beginning of the relaxation process.

Since, the CSD peak in τ_4 is broad compared to the T-step sizes between two measurements (see fig. 12.18), one would expect the area underneath the peak to be more or less independent on the fluence. As before, if the peak in τ_4 is directly connected to C_S, the area beneath the curve should be connected to ΔS, see eq. 12.1. This entropy change is expected to be independent of the pump-fluence, if the excitation process is assumed to be of the same kind for all fluences (varying in strength, only). In fig. 12.20 (d), the area results for three of the four fluences are in line with this theory within the error bars. The only contradiction point is the on of the value for $F \approx 1.1$ mJ/cm^2. Unfortunately, only four data points are not enough to exclude an measurement error, e.g., in the measurement series under the conditions $F = 1.13$

mJ/cm^2 and $B = 90$ mT. Thus, it stays a point of speculation, whether the energy dissipation path changes at a certain fluence or if the previously named series contains measurement errors.

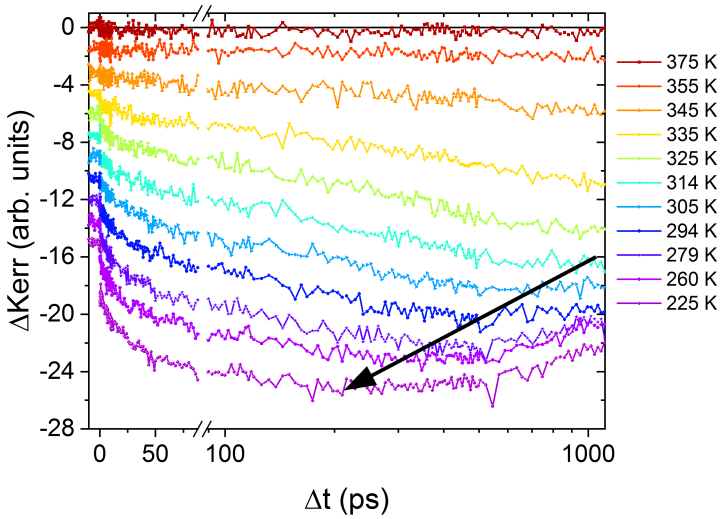

FIGURE 12.21: A selection of TRMOKE data to visualize the remagnetization behavior depending on the temperature. The black arrow indicates the shift of the turning point in the dynamics.

The TRMOKE data point towards a critical slowing down of the spin subsystem close to the phase transition, too. As the black arrow indicates in fig. 12.21, the turning point from demagnetization to remagnetization process migrates towards earlier timescales when the base temperature of the sample is cooled down. Unfortunately, it is not possible to directly compare the remagnetization time and the relaxation of the transient reflectivity signal, τ_4 since the remagnetization process is too slow to be measurable by using the setup described in chapter 10.

12.6 Discussion Summary of the Dynamics in LSMO

The time-resolved reflectivity signal of LSMO thin films grown on a STO substrates is measured simultaneously with the TRMOKE signal for different external stimuli, T, B, F. Six different features are identified in the transient reflectivity traces as depicted in fig. 12.22. Five of them are fitted by the equation 8.1:

$$\Delta\mathcal{R} = G \cdot exp(-(t - t_P)^2/2 \cdot \omega) - \sum_{i=1}^{4} A_i \cdot exp(-\Delta t/\tau_i).$$

Based on the found dependencies of the six features on the three varied external stimuli, T, B, and F, the processes, which cause these features, are discussed in the previous sections of this chapter. The processes are assigned as follows starting with feature No. 1, the excitation

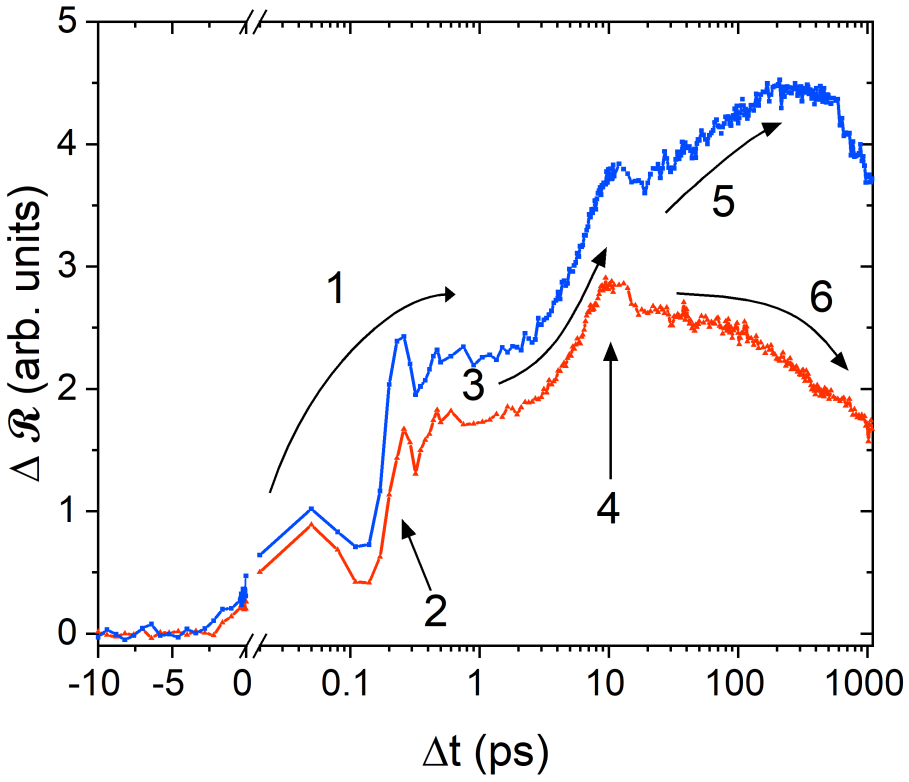

FIGURE 12.22: Labeling of the 6 features, which are observed in chapter 11 and discussed in chapter 12 of the transient reflectivity signal.

of the electronic system.

Feature No. 1, the excitation and thermalization process is found to show unexpected dependencies on the changes of the external magnetic field and the pump fluence. Inter alia, if the phase space for electron-electron scattering is increased by the larger number of hot electrons due to a higher pump-fluence, the thermalization time is expected to decrease. In contrast, an increase of τ_1 is observed for low fluences. To explain the discrepancy between expectations and the experimental findings, a trapping of the hot electrons is suggested which is caused by a spin-flip of the hot electron during the excitation step. Due to the double exchange in LSMO, a hopping of a minority electron is less probable. The hot minority electron is trapped by the Pauli-principle and the fact that the minority O2p states are almost fully occupied. This leads to a reduction of the phase space for electron-electron scattering even though more electrons might be excited.
Therefore, a photo-induced spin-flip transition is suggested as part of the excitation process. The spin-flip transition is expected to be not the only photo-induced transition but one of at least two.

Enforced by the excitation of electron into Mn3d states above the Fermi energy, coherent optical phonons are excited in order to minimize the Coulomb energy of the excited and the surrounding electrons. The imprint of these phonons with a frequency in the THz regime is visible as feature No. 2 in the transient reflectivity traces.

On longer timescales, $\tau_2 \sim 12$ ps, a second increase of the psTR signal is found. In fig. 12.22, this feature is labeled as No. 3. The two facts that it is found independently on the magnetic ground state of the sample and that it is not observed in the magneto-optical time traces exclude the spin-lattice relaxation as reason for this energy dissipation path. In stead, a second electron-phonon interaction is suggested; according to the debated timescale, the feature No. 3 might be connected to the energy exchange between electrons and acoustic phonons. Femtosecond electron diffraction studies by Li and co-workers [118] on orthorhombic LSMO and by Abreu et al. [155] on $TbMnO_3$ demonstrated that lattice dynamics of this timescale

appear in manganites.

In the order of ~ 10 ps an oscillating behavior, feature No. 4, is visible in transient reflectivity traces. Already in earlier studies, see [164], coherent acoustic phonon excitation in LSMO thin films grown on STO substrates were investigated. Thus, the ~ 68 GHz oscillations are assigned to Brillouin scatting in the STO substrate.

The feature No. 5, a third increase which is described by the amplitude, A_3, and the time constant, τ_3, is found to appear in the ferromagnetic phase only; but dynamics of comparable time constants are observed in both signals, transient reflectivity and TRMOKE. Therefore, feature No. 5 is assigned to the spin-lattice relaxation, leading to a thermally driven demagnetization of the sample.

Finally, the feature No. 6, the relaxation of the transient reflectivity signal, which is described by the fourth exponential function, A_4, τ_4, is assigned to the relaxation back to the ground state. It is shown that the strength of the introduced disorder in the spin subsystem by the previous process has a big impact on the time which is needed to relax the sample system back to the ground state. An explanation for this is the shrinking of the repelling energy potential when approaching the phase transition from below in the base temperature and pushing only slightly the system across the PT during the pump-probe experiment.

Part 4

Final Thoughts

CHAPTER 13

Summary

In this thesis, the ultrafast dynamics of $La_{0.7}Sr_{0.3}MnO_3$ and $(La_{0.6}Pr_{0.4})_{0.7}Ca_{0.3}MnO_3$ thin films were individually shown and discussed. Wide similarities between both films were observed, such as the over all signal development of the psTR, the critical slowing down close to the magnetic phase transitions (see section 9.5 and 12.5), coherently excited optical (section 9.2 and 12.2) and acoustical phonons (section 9.3 and 12.3), as well as a long lasting, thermal demagnetization (section 9.4 and 12.4) being dominant after roughly $\Delta t \gtrsim 10$ ps beneathe T_C. Moreover, a distinct dynamic spectral weight transfer is found in both systems when crossing the PT, which manifests itself most impressively in the emergence of the third time constant, τ_3, which was clearly assigned to the spin-lattice interaction (section 9.4 and 12.4). All these similarities make it possible to evaluate all data sets by the use of the same fit function:

$$\Delta\mathcal{R} = G \cdot exp(-(t - t_P)^2/2 \cdot \omega) - \sum_{i=1}^{4} A_i \cdot exp(-\Delta t/\tau_i)$$

which is the necessary requirement for a comparison of both manganite systems. Thereby, the different features (see fig. 12.1 and 12.1) of the psTR traces are suggested to be assigned as follows:

Feature No. 1: (A_1, τ_1) initial excitation and thermalization of the electrons,

Feature No. 2: (neglected in the fit) coherent optical phonon excitation,

Feature No. 3: (A_2, τ_2) second electron-phonon interaction,

Feature No. 4: (G, ω, t_P) first maximum of the Brillouin scattering,

Feature No. 5: (A_3, τ_3) spin-lattice relaxation, and

Feature No. 6: (A_4, τ_4) relaxation back to the ground state.

Nevertheless, next to manifold accordances, a number of differences are visible within the data sets, which leads to the hypothesis that, to some extend, different processes are excited by pumping LPCMO or LSMO, respectively. The greatest contrast is found at the (sub-)ps timescale of the TRMOKE data, where LSMO behaves normally, i. e., a decrease of the signal within the ferromagnetic phase (see fig. 11.15); whereas LPCMO shows a rather unexpected increase of the magneto-optical rotation at a comparable timescale (see fig. 8.15). Even more remarkable is the fact, that this part of the signal is quasi-independent of the magnetization state of the LPCMO film, in that sense, that it is present even deep in the paramagnetic phase, more than 100 K above T_C. Regardless of that, the intensity seems to depend on both the externally applied and the internally existing magnetic field.

Together with the difference in the fluence and magnetic field dependence of both pump-experiments, these signals suggest to correspond to two different kinds of excitation pathways. In the case of LPCMO, the nonlinear dependence of the excitation amplitude, A_1, on the pump fluence (see fig. 9.2 (a)) points towards a two photon excitation. Thinking of an excitation process of $\Delta E = 2.4$ eV, static optical spectroscopy suggests a charge transfer transition [67, 91, 147]. Within this hypothesis, the increase in the TRMOKE signal at the sub-ps timescale is explained by a change of the total angular momentum, J, and a resulting in a change off ϵ'_{xy} and ϵ''_{xy}. In contrast, the increase of τ_1 in LSMO when increasing the fluence suggests a reduction of the phase space for electron-electron scattering (see fig. 5(a)). Both the magnetic field dependence and the TRMOKE response of LSMO suggest a demagnetization at the ultrafast timescales. Due to momentum and energy conservation reasons, the simplest explanation for a demagnetization during the excitation process in a double-exchange coupled perovskite manganite is a photo induces spin-flip. Spin-flip processes based on electron-electron scattering would either break the conservation laws or would require a number of intermediate steps which is incompatible with the fs-timescale at which the ultrafast demagnetization is executed. Since a magnetic dipole transition is usually much weaker than an electric dipole transition, the photo-induced spin-flip is suggested to be just a percentage of the excitation process among others.

Turning to the question of differences and analogies in the energy dissipation pathways

after the initial excitation, the coherent excitation of optical phonons is suggested to be a first electron-phonon interaction in order to rearrange the Jahn-Teller distortions of the oxygen octahedron surrounding the Mn ions which provided the initial or final states for the electron excitation.
The following second increase of the transient reflectivity signal is suggested as a second electron-lattice energy transfer due to the persistence through out all magnetic states and leak of visibility in the TRMOKE traces. This second increase is overlapped by the coherent acoustic phonon excitation, the Brillouin scattering. It is demonstrated with the help of FDTD simulations that acoustic phonons in the LPCMO film are excited. The oscillation frequency in the LSMO case points towards a strain wave in the STO substrate.

In both sample systems the quasi-equilibrium is finally reached by spin-lattice interaction and the resulting thermal demagnetization of the films. This process is limited to the ferromagnetic state, what explains the disappearance of the third increase in the transient reflectivity signal above the Curie temperature. The spin-lattice relaxation time, τ_3, depends quite strongly on the external stimuli, $T,\ B,\ F$, and varies roughly between 25 ps and 200 ps.

A critical slowing down of the relaxation time back into the ground state, τ_4, is found for both manganites. For LPCMO, FDTD simulations based on different approaches are calculated and underline the connection of the critical slowing down to the spin specific heat. The needed information about the temperature-dependent changes in the thermal diffusion are provided by 3ω measurements.

CHAPTER 14

Outlook

14.1 LPCMO

14.1.1 Review on the Two Photon Excitation Hypothesis

The idea for the assignment of a two photon process as part of the excitation process, A_1, τ_1, is suggested due to the non-linearity which is found in the fluence-dependent results, which are measured directly at the phase transition. Two critical remarks need to be considered here:
(i) it is believed that the cryostat window was damaged during the fluence-dependent measurements for fluences higher than 7 mJ/cm^2. Based on this estimation, the parabolic fit of the A_1 fluence dependence is limited to the lower fluence regime, < 6 mJ/cm^2. It might be possible that the exact point at which the fluence became too high and damaged the window is estimated wrongly. Hence, it is possible that the interpretation of a nonlinear fluence dependence is wrong and, instead, e.g., a linear behavior is found. In this case, a two photon process would not be dominant.
(ii) the only fluence-dependent series was measured in the phase transition region, close to the statically determined T_C. Close to T_C, the fluctuations of the spin system are large [166, 167, 168]. It might be possible that these fluctuations enhance transition probabilities for certain transitions. If this is the case, a measurement at a temperature close to T_C is not representative for the material's behavior far away from the critical temperature.

In order to review the two-photon hypothesis, two kinds of measurements are suggested. Of course, the fluence-dependent series should be remeasured and checked whether the quadratic

behavior can be confirmed. Here, it is recommended to add measurement points in the range between 1 and 6 mJ/cm^2 in regards to a fit. Additionally, the transmittance of the cryostat window should be measured before and after the measurement series in order to check for beam damages. Furthermore, it is suggested to add measurement points below 1 mJ/cm^2. The intention of this is the comparison between LPCMO and LSMO.[1]

The second kind of suggested measurements is to utilize a second nonlinear-optics beam line, e.g., an optical parametric amplifier, in order to pump the LPCMO with the frequency-doubled 2.4 eV and probe the system by using an even higher photon energy. If a two-photon process was observed in the previous measurements, the dynamics which are induced by the photon energy of 2.4 eV and by 1.2 eV should consistent.

Taking the critical remark (ii) into account, it is recommended to perform additional fluence-dependent series which are measured at $T < T_C$ and $T << T_C$, e.g., $T = 175$ K and $T = 100$ K, and at $T > T_C$ and $T >> T_C$, e.g., $T = 215$ K and $T = 300$ K.

Furthermore, theoretical support by ab-initio calculations, e.g., TDDFT, should be consulted in order to clarify the hypothesis of a light-induced phase transition as reason for the non-linearity of the fluence dependence of A_1. As described in the section 9.1, a discussion of a possibly existing hidden phase is not expedient by the experimental data only.

14.1.2 Further Development on a Theoretical Model for Transient Optical Spectroscopy

In order to show the connection of the strong increase in the relaxation time, τ_4 to the critical slowing down of the spin subsystem below the Curie temperature, FDTD simulation were utilized to simulate the reflectivity signal for different temperatures across the phase transition. Different models were used to check what is needed to be taken into account in order to reproduce the enormous increase. All of them considered the coupling constants $g_{el,la}$ and

[1] Measurements of higher fluences than ~ 3 mJ/cm^2 on LSMO are not recommended. Every time when LSMO is measured at higher fluence, a modification of the sample and in the time-resolved traces was observed. These changes vanishes a couple of days after the sample has been removed from the cryostat. This behavior points strongly to a temporal laser induced change of the material. Therefore, high fluence measurement data of LSMO might not be comparable to the LPCMO measurements.

$g_{la,sp}$ as constant as function of temperature. But experimental findings [8, 80] suggest an change in these parameters when turning from one into the other phase.
To improve the describing model, variable $g_{el,la}(T)$ and $g_{la,sp}(T)$ should be consider. Unfortunately, these parameters are hardly to measure. Usually, they are determined by time-resolved measurements which are modeled by a 3TM. Since using parameters which have been determined by a 3TM as input parameter for a 3TM would lead to no gain of knowledge, another theoretical approach should be considered: time-dependent density functional theory (TDDFT) [35, 36, 37]. Connected to the challenges of "static" DFT for manganite systems [44], e.g., a suitable reduction of the computational time for doped manganite systems, a time-dependent version of it might be even more challenging.

An experimental answer to the question, if and how long-living polaronic quasi-particles are involved as part of the relaxation dynamics, might be given by time-resolved electron diffraction techniques, e.g., femtosecond electron diffraction. But in contrast to the studies which are available in literature [117, 118, 155], delay times up to more than ~ 1 ns are needed in order to observe a relaxation of the lattice which is not caused by the spin-lattice relaxation / the demagnetization. Since correlated polarons are detectable by x-ray diffraction [71, 72], a time-resolved x-ray diffraction technique might also gain knowledge about metastable polaronic quasiparticles.

14.2 LSMO

14.2.1 Review on the Photo-Induced Spin-Flip Hypothesis

The suggested hypothesis of a photo-induced spin-flip is based on a thought experiment only up to now. Whether a magnetic dipole transition is resonant at 1.2 eV is not known so far, thus the transition matrix element for such a transition is needed to be calculated.
A measurement technique which is potentially capable to detect a spin-flip which is caused by an exciting photon is the time- and spin-resolved photoemission spectroscopy. Two challenges might be considered in context. (i) the needed integration time for a time-resolved trace

which should detect an event which is $\sim 10^5$ times less probable than excitations by an electric dipole transition [22, 23, 24] might be too long compared to the stability of fs-pulsed laser systems. (ii) photoemission is a quite surface-sensitive technique [169, 170] due to the inelastic mean free path of the electrons. Unfortunately, the surface layers of manganites tend to show surface properties which differ from the bulk behavior. A demonstration regarding the density of states is given in the DFT studies of LSMO by Pruneda et al. [85]. Here, the spin projected density of states is calculated for the bulk material and the surface layer. This means for the photoemission experiments, that it might be possible that no magnetic dipole transition is available even though it might be the case for bulk sensitive experiments.

14.3 Further Comparison of LPCMO and LSMO

The motivation of investigating the two different manganite systems, LPCMO and LSMO, was to study the impact of the different electron-phonon couplings of both systems on the ultrafast energy dissipation processes. As result, hypothesis of quite different excitation processes are set up based on the observations in both materials: For LPCMO, a charge transfer transition (from O2p state to Mn3d state in spin-up configuration) is suggested to appear via a two-photon absorption; the findings in LSMO point towards a photo-induced spin-flip transition. In both cases, the results are relatively unexpected. In a first approach, a single-photon electric dipole transition was anticipated for both systems; both a photo-induced spin-flip [22, 23, 24] and a nonlinear optical [171, 172] response mostly show weak intensities compared to single-photon electric dipole transitions due to a lower transition probability. Due to these quite different excitation processes, a comparison of the following dynamics with respect to the *direct* imprint of the electron-phonon coupling is not possible since the follow-up energy dissipation of two different kine of excitations is expected to result in different dynamics.

If the hypothesis of both excitation processes in LPCMO and LSMO can be confirmed, it is suggested to repeat the time-resolved studies on LSMO but with a pump energy of about 2.4 eV [92] and an even higher probe energy. Due to the suggested two-photon process in LPCMO, this pump-energy might excite related transitions in both materials.

Bibliography

[1] *United Nations Millennium Development Goals*. 14.08.2022. URL: https://www.un.org/millenniumgoals/.

[2] *THE 17 GOALS | Sustainable Development*. 13.08.2022. URL: https://sdgs.un.org/goals#history.

[3] NobelPrize.org. *The Nobel Prize in Chemistry 2019*. 14.08.2022. URL: https://www.nobelprize.org/prizes/chemistry/2019/summary/.

[4] San Ping Jiang. 'Development of lanthanum strontium manganite perovskite cathode materials of solid oxide fuel cells: a review'. In: *Journal of Materials Science* 43.21 (2008), pp. 6799–6833. ISSN: 0022-2461. DOI: 10.1007/s10853-008-2966-6.

[5] Urushibara, Moritomo, Arima, Asamitsu, Kido and Tokura. 'Insulator-metal transition and giant magnetoresistance in La1-xSrxMnO3'. In: *Physical review. B, Condensed matter* 51.20 (1995), pp. 14103–14109. ISSN: 0163-1829. DOI: 10.1103/PhysRevB.51.14103.

[6] A. Belenchuk, O. Shapoval, V. Roddatis, V. Bruchmann-Bamberg, K. Samwer and V. Moshnyaga. 'Ruddlesden-Popper interface in correlated manganite heterostructures induces magnetic decoupling and dead layer reduction'. In: *Applied Physics Letters* 109.23 (2016), p. 232405. ISSN: 0003-6951. DOI: 10.1063/1.4971833.

[7] M. Huijben, L. W. Martin, Y.-H. Chu, M. B. Holcomb, P. Yu, G. Rijnders, D. H. A. Blank and R. Ramesh. 'Critical thickness and orbital ordering in ultrathin La0.7Sr0.3MnO3 films'. In: *Physical Review B* 78.9 (2008), p. 094413. ISSN: 1098-0121. DOI: 10.1103/PhysRevB.78.094413.

[8] V. Moshnyaga et al. 'Intrinsic antiferromagnetic coupling underlies colossal magnetoresistance effect: Role of correlated polarons'. In: *Physical Review B* 89.2 (2014), p. 024420. ISSN: 1098-0121. DOI: 10.1103/PhysRevB.89.024420.

[9] Cinja Seick, Karen Stroh, Tim Titze, Vitaly Bruchmann-Bamberg, Andreas Weisser, Stefan Mathias, Vasily Moshnyaga, Henning Ulrichs and Daniel Steil. 'Energy Relaxation in $(La_{0.6}Pr_{0.4})_{0.7}Ca_{0.3}MnO_3$ Films across the metal-insulator transition'. In: *Phys. Rev. B* 107 (2023), p. 085115. DOI: 10.1103/PhysRevB.107.085115.

[10] T. Pincelli et al. 'Quantifying the critical thickness of electron hybridization in spintronics materials'. In: *Nature communications* 8 (2017), p. 16051. DOI: 10.1038/ncomms16051.

[11] M. Cesaria, A. P. Caricato, G. Maruccio and M. Martino. 'LSMO – growing opportunities by PLD and applications in spintronics'. In: *Journal of Physics: Conference Series* 292 (2011), p. 012003. DOI: 10.1088/1742-6596/292/1/012003.

[12] Martin Wahler, Nico Homonnay, Tim Richter, Alexander Müller, Christian Eisenschmidt, Bodo Fuhrmann and Georg Schmidt. 'Inverse spin Hall effect in a complex ferromagnetic oxide heterostructure'. In: *Scientific reports* 6.1 (2016), p. 28727. DOI: 10.1038/srep28727.

[13] Jijie Huang, Han Wang, Xing Sun, Xinghang Zhang and Haiyan Wang. 'Multifunctional La0.67Sr0.33MnO3 (LSMO) Thin Films Integrated on Mica Substrates toward Flexible Spintronics and Electronics'. In: *ACS applied materials & interfaces* 10.49 (2018), pp. 42698–42705. DOI: 10.1021/acsami.8b16626.

[14] B. Koopmans, H.H.J.E. Kicken, M. van Kampen and W.J.M. de Jonge. 'Microscopic model for femtosecond magnetization dynamics'. In: *Journal of Magnetism and Magnetic Materials* 286 (2005), pp. 271–275. ISSN: 03048853. DOI: 10.1016/j.jmmm.2004.09.079.

[15] C. L. Kane and E. J. Mele. 'Z2 topological order and the quantum spin Hall effect'. In: *Physical review letters* 95.14 (2005), p. 146802. ISSN: 0031-9007. DOI: 10.1103/PhysRevLett.95.146802.

[16] B. Koopmans, G. Malinowski, F. Dalla Longa, D. Steiauf, M. Fähnle, T. Roth, M. Cinchetti and M. Aeschlimann. 'Explaining the paradoxical diversity of ultrafast laser-induced demagnetization'. In: *Nature materials* 9.3 (2010), pp. 259–265. ISSN: 1476-1122. DOI: 10.1038/NMAT2593.

[17] D. Steiauf and M. Fähnle. 'Elliott-Yafet mechanism and the discussion of femtosecond magnetization dynamics'. In: *Physical Review B* 79.14 (2009). ISSN: 1098-0121. DOI: 10.1103/PhysRevB.79.140401.

[18] A. J. Schellekens, W. Verhoeven, T. N. Vader and B. Koopmans. 'Investigating the contribution of superdiffusive transport to ultrafast demagnetization of ferromagnetic thin films'. In: *Applied Physics Letters* 102.25 (2013), p. 252408. ISSN: 0003-6951. DOI: 10.1063/1.4812658.

[19] M. Battiato, K. Carva and P. M. Oppeneer. 'Superdiffusive spin transport as a mechanism of ultrafast demagnetization'. In: *Physical review letters* 105.2 (2010), p. 027203. DOI: 10.1103/PhysRevLett.105.027203.

[20] M. Battiato, K. Carva and P. M. Oppeneer. 'Theory of laser-induced ultrafast superdiffusive spin transport in layered heterostructures'. In: *Physical Review B* 86.2 (2012). ISSN: 1098-0121. DOI: 10.1103/PhysRevB.86.024404.

[21] Claude Cohen-Tannoudji, Bernard Diu and Franck Laloë. *Quantum mechanics: Volume II*. [Nachdr.] Vol. 2. A Wiley-Interscience publication. New York: Wiley, 2003. ISBN: 0471164348.

[22] Sinan Karaveli and Rashid Zia. 'Spectral tuning by selective enhancement of electric and magnetic dipole emission'. In: *Physical review letters* 106.19 (2011), p. 193004. DOI: 10.1103/PhysRevLett.106.193004.

[23] Vladimir M. Shalaev. 'Optical negative-index metamaterials'. In: *Nature Photonics* 1.1 (2007), pp. 41–48. ISSN: 1749-4885. DOI: 10.1038/nphoton.2006.49.

[24] Harald Giessen and Ralf Vogelgesang. 'Physics. Glimpsing the weak magnetic field of light'. In: *Science (New York, N.Y.)* 326.5952 (2009), pp. 529–530. DOI: 10.1126/science.1181552.

[25] B. F. Jones and W. S. Moore. 'Lattice-ion interactions of Ti3+ in corundum II. The experimentally observed effects of electric fields'. In: *Journal of Physics C: Solid State Physics* 2.11 (1969), pp. 1964–1969. ISSN: 00223719. DOI: 10.1088/0022-3719/2/11/308.

[26] P. Abdul Azeem, M. Kalidasan, K. Rama Gopal and R. R. Reddy. 'Spectral analysis of Eu3+:B2O3–Al2O3–MF2 (M=Zn, Ca, Pb) glasses'. In: *Journal of Alloys and*

Compounds 474.1-2 (2009), pp. 536–540. ISSN: 09258388. DOI: 10.1016/j.jallcom.2008.06.134.

[27] S. I. Anisimov, B. L. Kapeliovich and T. L. Perel'man. 'Electron emission from metal surfaces exposed to ultrashort laser pulses'. In: 66 (1974), pp. 776–781. URL: http://www.jetp.ras.ru/cgi-bin/dn/e_039_02_0375.pdf.

[28] E. Beaurepaire, J.-C. Merle, A. Daunois and J.-Y. Bigot. 'Ultrafast spin dynamics in ferromagnetic nickel'. In: *Physical review letters* 76.22 (1996), pp. 4250–4253. DOI: 10.1103/PhysRevLett.76.4250.

[29] Ji-Wan Kim, Kyeong-Dong Lee, Jae-Woo Jeong and Sung-Chul Shin. 'Ultrafast spin demagnetization by nonthermal electrons of TbFe alloy film'. In: *Applied Physics Letters* 94.19 (2009), p. 192506. ISSN: 0003-6951. DOI: 10.1063/1.3130743.

[30] M. Hofherr et al. 'Speed and efficiency of femtosecond spin current injection into a nonmagnetic material'. In: *Physical Review B* 96.10 (2017), p. 100403. ISSN: 1098-0121. DOI: 10.1103/PhysRevB.96.100403.

[31] B. Koopmans, J. J. M. Ruigrok, F. Dalla Longa and W. J. M. de Jonge. 'Unifying ultrafast magnetization dynamics'. In: *Physical review letters* 95.26 (2005), p. 267207. DOI: 10.1103/PhysRevLett.95.267207.

[32] B. Y. Mueller, T. Roth, M. Cinchetti, M. Aeschlimann and B. Rethfeld. 'Driving force of ultrafast magnetization dynamics'. In: *New Journal of Physics* 13.12 (2011), p. 123010. DOI: 10.1088/1367-2630/13/12/123010.

[33] B. Y. Mueller and B. Rethfeld. 'Relaxation dynamics in laser-excited metals under nonequilibrium conditions'. In: *Physical Review B* 87.3 (2013). ISSN: 1098-0121. DOI: 10.1103/PhysRevB.87.035139.

[34] B. Y. Mueller and B. Rethfeld. 'Thermodynamic μT model of ultrafast magnetization dynamics'. In: *Physical Review B* 90.14 (2014), p. 144420. ISSN: 1098-0121. DOI: 10.1103/PhysRevB.90.144420.

[35] Erich Runge and E. K. U. Gross. 'Density-Functional Theory for Time-Dependent Systems'. In: *Physical review letters* 52.12 (1984), pp. 997–1000. ISSN: 0031-9007. DOI: 10.1103/PhysRevLett.52.997.

[36] S. A. Sato, K. Yabana, Y. Shinohara, T. Otobe and G. F. Bertsch. 'Numerical pump-probe experiments of laser-excited silicon in nonequilibrium phase'. In: *Physical Review B* 89.6 (2014), p. 064304. ISSN: 1098-0121. DOI: 10.1103/PhysRevB.89.064304.

[37] K. Krieger, J. K. Dewhurst, P. Elliott, S. Sharma and E. K. U. Gross. 'Laser-induced demagnetization at ultrashort time scales: predictions of TDDFT'. In: *Journal of chemical theory and computation* 11.10 (2015), pp. 4870–4874. DOI: 10.1021/acs.jctc.5b00621.

[38] John Kay Dewhurst, Peter Elliott, Sam Shallcross, Eberhard K. U. Gross and Sangeeta Sharma. 'Laser-Induced Intersite Spin Transfer'. In: *Nano letters* 18.3 (2018), pp. 1842–1848. DOI: 10.1021/acs.nanolett.7b05118.

[39] Florian Siegrist et al. 'Light-wave dynamic control of magnetism'. In: *Nature* 571.7764 (2019), pp. 240–244. DOI: 10.1038/s41586-019-1333-x.

[40] Daniel Steil et al. 'Efficiency of ultrafast optically induced spin transfer in Heusler compounds'. In: *Physical Review Research* 2.2 (2020). DOI: 10.1103/PhysRevResearch.2.023199.

[41] Sangeeta Rajpurohit, Christian Jooss and Peter E. Blöchl. 'Evolution of the magnetic and polaronic order of Pr1/2Ca1/2MnO3 following an ultrashort light pulse'. In: *Physical Review B* 102.1 (2020). ISSN: 1098-0121. DOI: 10.1103/PhysRevB.102.014302.

[42] Elbio Dagotto, Takashi Hotta and Adriana Moreo. 'Colossal magnetoresistant materials: the key role of phase separation'. In: *Physics Reports* 344.1-3 (2001), pp. 1–153. ISSN: 03701573. DOI: 10.1016/S0370-1573(00)00121-6.

[43] Takashi Hotta. 'Orbital ordering phenomena in d- and f-electron systems'. In: *Reports on Progress in Physics* 69.7 (2006), pp. 2061–2155. ISSN: 0034-4885. DOI: 10.1088/0034-4885/69/7/R02.

[44] Mohsen Sotoudeh, Sangeeta Rajpurohit, Peter Blöchl, Daniel Mierwaldt, Jonas Norpoth, Vladimir Roddatis, Stephanie Mildner, Birte Kressdorf, Benedikt Ifland and Christian Jooss. 'Electronic structure of Pr1−xCaxMnO3'. In: *Physical Review B* 95.23 (2017). ISSN: 1098-0121. DOI: 10.1103/PhysRevB.95.235150.

[45] John C. Tully. 'Mixed quantum–classical dynamics'. In: *Faraday Discussions* 110 (1998), pp. 407–419. ISSN: 13596640. DOI: 10.1039/A801824C.

[46] A. D. McLachlan. 'A variational solution of the time-dependent Schrodinger equation'. In: *Molecular Physics* 8.1 (1964), pp. 39–44. ISSN: 0026-8976. DOI: 10.1080/00268976400100041.

[47] Y. Tokura and Y. Tomioka. 'Colossal magnetoresistive manganites'. In: *Journal of Magnetism and Magnetic Materials* 200.1-3 (1999), pp. 1–23. ISSN: 03048853. DOI: 10.1016/S0304-8853(99)00352-2.

[48] Koichi Momma and Fujio Izumi. 'VESTA 3 for three-dimensional visualization of crystal, volumetric and morphology data'. In: *Journal of Applied Crystallography* 44.6 (2011), pp. 1272–1276. ISSN: 0021-8898. DOI: 10.1107/S0021889811038970.

[49] E. O. Wollan and W. C. Koehler. 'Neutron Diffraction Study of the Magnetic Properties of the Series of Perovskite-Type Compounds [(1−x)La, xCa]MnO3'. In: *Physical Review* 100.2 (1955), pp. 545–563. ISSN: 0031-899X. DOI: 10.1103/PhysRev.100.545.

[50] M. Paraskevopoulos, F. Mayr, C. Hartinger, A. Pimenov, J. Hemberger, P. Lunkenheimer, A. Loidl, A. A. Mukhin, V.Yu. Ivanov and A. M. Balbashov. 'The phase diagram and optical properties of La1−xSrxMnO3 for x0.2'. In: *Journal of Magnetism and Magnetic Materials* 211.1-3 (2000), pp. 118–127. ISSN: 03048853. DOI: 10.1016/S0304-8853(99)00722-2.

[51] J. Hemberger, A. Krimmel, T. Kurz, H.-A. Krug von Nidda, V. Yu. Ivanov, A. A. Mukhin, A. M. Balbashov and A. Loidl. 'Structural, magnetic, and electrical properties of single-crystalline La1−xSrxMnO3(0.4<x<0.85)'. In: *Physical review. B, Condensed matter* 66.9 (2002), p. 094410. ISSN: 0163-1829. DOI: 10.1103/PhysRevB.66.094410.

[52] P. D. Battle, T. C. Gibb and C. W. Jones. 'The structural and magnetic properties of SrMnO3: A reinvestigation'. In: *Journal of Solid State Chemistry* 74.1 (1988), pp. 60–66. ISSN: 00224596. DOI: 10.1016/0022-4596(88)90331-3.

[53] Marco Molinari, David A. Tompsett, Stephen C. Parker, Feridoon Azough and Robert Freer. 'Structural, electronic and thermoelectric behaviour of CaMnO 3 and CaMnO

(3−δ)'. In: *J. Mater. Chem. A* 2.34 (2014), pp. 14109–14117. ISSN: 2050-7488. DOI: 10.1039/C4TA01514B.

[54] Z. Jirák, S. Krupička, Z. Šimša, M. Dlouhá and S. Vratislav. 'Neutron diffraction study of Pr1 − xCaxMnO3 perovskites'. In: *Journal of Magnetism and Magnetic Materials* 53.1-2 (1985), pp. 153–166. ISSN: 03048853. DOI: 10.1016/0304-8853(85)90144-1.

[55] T. Kimura, T. Goto, H. Shintani, K. Ishizaka, T. Arima and Y. Tokura. 'Magnetic control of ferroelectric polarization'. In: *Nature* 426.6962 (2003), pp. 55–58. DOI: 10.1038/nature02018.

[56] T. Goto, T. Kimura, G. Lawes, A. P. Ramirez and Y. Tokura. 'Ferroelectricity and giant magnetocapacitance in perovskite rare-earth manganites'. In: *Physical review letters* 92 (2004), p. 257201. DOI: 10.1103/PhysRevLett.92.257201.

[57] Vasily Moshnyaga and Konrad Samwer. 'Polaronic Emergent Phases in Manganite-based Heterostructures'. In: *Crystals* 9.10 (2019), p. 489. DOI: 10.3390/cryst9100489.

[58] Sayani Majumdar and Sebastiaan van Dijken. 'Pulsed laser deposition of La 1− x Sr x MnO 3 : thin-film properties and spintronic applications'. In: *Journal of Physics D: Applied Physics* 47.3 (2014), p. 034010. ISSN: 0022-3727. DOI: 10.1088/0022-3727/47/3/034010.

[59] H. A. Jahn and E. Teller. 'Stability of polyatomic molecules in degenerate electronic states - I—Orbital degeneracy'. In: *Proceedings of the Royal Society of London. Series A - Mathematical and Physical Sciences* 161.905 (1937), pp. 220–235. ISSN: 0080-4630. DOI: 10.1098/rspa.1937.0142.

[60] Cesare Franchini, Michele Reticcioli, Martin Setvin and Ulrike Diebold. 'Polarons in materials'. In: *Nature Reviews Materials* 6.7 (2021), pp. 560–586. DOI: 10.1038/s41578-021-00289-w.

[61] T. Holstein. 'Studies of polaron motion: Part II. The "small" polaron'. In: *Annals of Physics* 8.3 (1959), pp. 343–389. ISSN: 00034916. DOI: 10.1016/0003-4916(59)90003-X.

[62] T. Holstein. ‘Studies of Polaron Motion: Part I. The Molecular-Crystal Model’. In: *Annals of Physics* 281.1-2 (1959), pp. 706–724. ISSN: 00034916. DOI: 10.1006/aphy.2000.6020.

[63] H. Fröhlich, H. Pelzer and S. Zienau. ‘XX. Properties of slow electrons in polar materials’. In: *The London, Edinburgh, and Dublin Philosophical Magazine and Journal of Science* 41.314 (1950), pp. 221–242. ISSN: 1941-5982. DOI: 10.1080/14786445008521794.

[64] H. Fröhlich. ‘Electrons in lattice fields’. In: *Advances in Physics* 3.11 (1954), pp. 325–361. ISSN: 0001-8732. DOI: 10.1080/00018735400101213.

[65] Ch. Hartinger, F. Mayr, J. Deisenhofer, A. Loidl and T. Kopp. ‘Large and small polaron excitations in La2/3(Sr/Ca)1/3MnO3 films’. In: *Physical Review B* 69.10 (2004), p. 100403. ISSN: 1098-0121. DOI: 10.1103/PhysRevB.69.100403.

[66] Ch. Hartinger, F. Mayr, A. Loidl and T. Kopp. ‘Polaronic excitations in colossal magnetoresistance manganite films’. In: *Physical Review B* 73.2 (2006), p. 024408. ISSN: 1098-0121. DOI: 10.1103/PhysRevB.73.024408.

[67] M. Quijada, J. Černe, J. R. Simpson, H. D. Drew, K. H. Ahn, A. J. Millis, R. Shreekala, R. Ramesh, M. Rajeswari and T. Venkatesan. ‘Optical conductivity of manganites: Crossover from Jahn-Teller small polaron to coherent transport in the ferromagnetic state’. In: *Physical review. B, Condensed matter* 58.24 (1998), pp. 16093–16102. ISSN: 0163-1829. DOI: 10.1103/PhysRevB.58.16093.

[68] Sebastian Hühn. ‘Kationen-Ordnung in ferri/ferromagnetischen perowskitischen Dünnfilmen’. Dissertation. Göttingen: Georg-August-Universität, 2015.

[69] Dai, Fernandez-Baca, Wakabayashi, Plummer, Tomioka and Tokura. ‘Short-range polaron correlations in the ferromagnetic La1-xCaxMnO3’. In: *Physical review letters* 85.12 (2000), pp. 2553–2556. ISSN: 0031-9007. DOI: 10.1103/PhysRevLett.85.2553.

[70] Adams, Lynn, Mukovskii, Arsenov and Shulyatev. ‘Charge ordering and polaron formation in the magnetoresistive oxide La0.7Ca0.3MnO3’. In: *Physical review letters* 85.18 (2000), pp. 3954–3957. ISSN: 0031-9007. DOI: 10.1103/PhysRevLett.85.3954.

[71] T. Y. Koo, V. Kiryukhin, P. A. Sharma, J. P. Hill and S-W. Cheong. 'Magnetic-field-induced collapse of charge-ordered nanoclusters and the colossal magnetoresistance effect in Nd0.7Sr0.3MnO3'. In: *Physical review. B, Condensed matter* 64.22 (2001). ISSN: 0163-1829. DOI: 10.1103/PhysRevB.64.220405.

[72] S. Shimomura, T. Tonegawa, K. Tajima, N. Wakabayashi, N. Ikeda, T. Shobu, Y. Noda, Y. Tomioka and Y. Tokura. 'X-ray diffuse scattering study on charge-localized states of Pr1−xCaxMnO3(x=0.35,0.4,0.5)'. In: *Physical review. B, Condensed matter* 62.6 (2000), pp. 3875–3878. ISSN: 0163-1829. DOI: 10.1103/PhysRevB.62.3875.

[73] V. Kiryukhin, T. Y. Koo, H. Ishibashi, J. P. Hill and S-W. Cheong. 'Average lattice symmetry and nanoscale structural correlations in magnetoresistive manganites'. In: *Physical review. B, Condensed matter* 67.6 (2003), p. 064421. ISSN: 0163-1829. DOI: 10.1103/PhysRevB.67.064421.

[74] P. W. Anderson. 'Antiferromagnetism. Theory of Superexchange Interaction'. In: *Physical Review* 79.2 (1950), pp. 350–356. ISSN: 0031-899X. DOI: 10.1103/PhysRev.79.350.

[75] G. H. Jonker and J. H. van Santen. 'Ferromagnetic compounds of manganese with perovskite structure'. In: *Physica* 16.3 (1950), pp. 337–349. ISSN: 00318914. DOI: 10.1016/0031-8914(50)90033-4.

[76] Clarence Zener. 'Interaction between the d -Shells in the Transition Metals. II. Ferromagnetic Compounds of Manganese with Perovskite Structure'. In: *Physical Review* 82.3 (1951), pp. 403–405. ISSN: 0031-899X. DOI: 10.1103/PhysRev.82.403.

[77] P. W. Anderson and H. Hasegawa. 'Considerations on Double Exchange'. In: *Physical Review* 100.2 (1955), pp. 675–681. ISSN: 0031-899X. DOI: 10.1103/PhysRev.100.675.

[78] P.-G. de Gennes. 'Effects of Double Exchange in Magnetic Crystals'. In: *Physical Review* 118.1 (1960), pp. 141–154. ISSN: 0031-899X. DOI: 10.1103/PhysRev.118.141.

[79] Hwang, Cheong, Radaelli, Marezio and Batlogg. 'Lattice effects on the magnetoresistance in doped LaMnO3'. In: *Physical review letters* 75.5 (1995), pp. 914–917. DOI: 10.1103/PhysRevLett.75.914.

[80] V. Moshnyaga and K. Samwer. 'Electron-lattice correlations and phase transitions in CMR manganites'. In: *Annalen der Physik* 523.8-9 (2011), pp. 652–663. ISSN: 00033804. DOI: 10.1002/andp.201100040.

[81] Dinesh Kumar, Narendra Kumar Verma, Chandra Bhal Singh and Akhilesh Kumar Singh. 'Crystallite size strain analysis of nanocrystalline La0.7Sr0.3MnO3 perovskite by Williamson-Hall plot method'. In: *AIP Conference Proceedings* 1942 (2018), p. 050024. DOI: 10.1063/1.5028655.

[82] Sayani Majumdar, H. Huhtinen, H. S. Majumdar, R. Laiho and R. Österbacka. 'Effect of La0.67Sr0.33MnO3 electrodes on organic spin valves'. In: *Journal of Applied Physics* 104.3 (2008), p. 033910. ISSN: 0021-8979. DOI: 10.1063/1.2963814.

[83] CRYSTAL GmbH. *CRYSTAL GmbH - Crystal Technology: Substrates/Wafers, Optical Components, Laser Crystals*. 2022. URL: https://crystal-gmbh.com/en/products/substrates/a-z.php.

[84] J. R. Sun, H. W. Yeung, H. K. Wong, T. Zhu and B. G. Shen. 'Effects of vacuum annealing on the transport property of La $_{0.67}$ Sr $_{0.33}$ MnO $_{3-\delta}$ films'. In: *The European Physical Journal B* 35.4 (2003), pp. 481–491. ISSN: 1434-6028. DOI: 10.1140/epjb/e2003-00301-6.

[85] J. M. Pruneda, V. Ferrari, R. Rurali, P. B. Littlewood, N. A. Spaldin and Emilio Artacho. 'Ferrodistortive instability at the (001) surface of half-metallic manganites'. In: *Physical review letters* 99.22 (2007), p. 226101. DOI: 10.1103/PhysRevLett.99.226101.

[86] Makoto Izumi, Yasushi Ogimoto, Takashi Manako, Masashi Kawasaki and Yoshinori Tokura. 'Interface Effect and Its Doping Dependence in La 1- x Sr x MnO 3 /SrTiO 3 Superlattices'. In: *Journal of the Physical Society of Japan* 71.11 (2002), pp. 2621–2624. ISSN: 0031-9015. DOI: 10.1143/JPSJ.71.2621.

[87] J. Volger. 'Further experimental investigations on some ferromagnetic oxidic compounds of manganese with perovskite structure'. In: *Physica* 20.1-6 (1954), pp. 49–66. ISSN: 00318914. DOI: 10.1016/S0031-8914(54)80015-2.

[88] M. Uehara, S. Mori, C. H. Chen and S.-W. Cheong. 'Percolative phase separation underlies colossal magnetoresistance in mixed-valent manganites'. In: *Nature* 399.6736 (1999), pp. 560–563. DOI: 10.1038/21142.

[89] S. Hühn, M. Jungbauer, M. Michelmann and et al. 'Modeling of colossal magnetoresistance in La0.67Ca0.33MnO3/Pr0.67Ca0.33MnO3 superlattices: Comparison with individual (La1−yPry)0.67Ca0.33MnO3 films'. In: *Journal of Applied Physics* 113.17 (2013), p. 17D701. ISSN: 0021-8979. DOI: 10.1063/1.4793711.

[90] V. Moshnyaga, L. Sudheendra, O. I. Lebedev, S. A. Köster, K. Gehrke, O. Shapoval, A. Belenchuk, B. Damaschke, G. van Tendeloo and K. Samwer. 'A-site ordering versus electronic inhomogeneity in colossally magnetoresistive manganite films'. In: *Physical review letters* 97.10 (2006), p. 107205. DOI: 10.1103/PhysRevLett.97.107205.

[91] S. Yamaguchi, Y. Okimoto, K. Ishibashi and Y. Tokura. 'Magneto-optical Kerr effects in perovskite-type transition-metal oxides: La1−xSrxMnO3 and La1−xSrxCoO3'. In: *Physical review. B, Condensed matter* 58.11 (1998), pp. 6862–6870. ISSN: 0163-1829. DOI: 10.1103/PhysRevB.58.6862.

[92] R. Rauer, M. Rübhausen and K. Dörr. 'Magnetic-order induced spectral-weight redistribution in La0.7(Sr,Ca)0.3MnO3'. In: *Physical Review B* 73.9 (2006). ISSN: 1098-0121. DOI: 10.1103/PhysRevB.73.092402.

[93] T. Ishikawa, K. Ookura and Y. Tokura. 'Optical response to orbital and charge ordering in a layered manganite: La1/2Sr3/2MnO4'. In: *Physical review. B, Condensed matter* 59.13 (1999), pp. 8367–8370. ISSN: 0163-1829. DOI: 10.1103/PhysRevB.59.8367.

[94] Y. Okimoto, T. Katsufuji, T. Ishikawa, A. Urushibara, T. Arima and Y. Tokura. 'Anomalous variation of optical spectra with spin polarization in double-exchange ferromagnet: La1-xSrxMnO3'. In: *Physical review letters* 75.1 (1995), pp. 109–112. DOI: 10.1103/PhysRevLett.75.109.

[95] M. van Kampen, J. T. Kohlhepp, W. J. M. de Jonge, B. Koopmans and R. Coehoorn. 'Sub-picosecond electron and phonon dynamics in nickel'. In: *Journal of Physics:*

Condensed Matter 17.43 (2005), pp. 6823–6834. ISSN: 0953-8984. DOI: 10.1088/0953-8984/17/43/004.

[96] E. Carpene, E. Mancini, C. Dallera, M. Brenna, E. Puppin and S. de Silvestri. 'Dynamics of electron-magnon interaction and ultrafast demagnetization in thin iron films'. In: *Physical Review B* 78.17 (2008), p. 174422. ISSN: 1098-0121. DOI: 10.1103/PhysRevB.78.174422.

[97] U. Atxitia, O. Chubykalo-Fesenko, J. Walowski, A. Mann and M. Münzenberg. 'Evidence for thermal mechanisms in laser-induced femtosecond spin dynamics'. In: *Physical Review B* 81.17 (2010), p. 174401. ISSN: 1098-0121. DOI: 10.1103/PhysRevB.81.174401.

[98] Ahmed I. Lobad, Richard D. Averitt, Chuhee Kwon and Antoinette J. Taylor. 'Spin–lattice interaction in colossal magnetoresistance manganites'. In: *Applied Physics Letters* 77.24 (2000), pp. 4025–4027. ISSN: 0003-6951. DOI: 10.1063/1.1329324.

[99] M. Fiebig, K. Miyano, Y. Tomioka and Y. Tokura. 'Sub-picosecond photo-induced melting of a charge-ordered state in a perovskite manganite'. In: *Applied Physics B* 71.2 (2000), pp. 211–215. ISSN: 0946-2171. DOI: 10.1007/s003400000338.

[100] Ahmed I. Lobad, A. J. Taylor, C. Kwon, S. A. Trugman and T. R. Gosnell. 'Laser induced dynamic spectral weight transfer in La0.7Ca0.3MnO3'. In: *Chemical Physics* 251.1-3 (2000), pp. 227–236. ISSN: 03010104. DOI: 10.1016/S0301-0104(99)00297-9.

[101] Ahmed I. Lobad, Richard D. Averitt and Antoinette J. Taylor. 'Picosecond dynamics of the spin-lattice relaxation in La0.7Ca0.2MnO3: Magnetic-field dependence'. In: *Physical review. B, Condensed matter* 63.6 (2001). ISSN: 0163-1829. DOI: 10.1103/PhysRevB.63.060410.

[102] T. Ogasawara, M. Matsubara, Y. Tomioka, M. Kuwata-Gonokami, H. Okamoto and Y. Tokura. 'Photoinduced spin dynamics in La0.6Sr0.4MnO3 observed by time-resolved magneto-optical Kerr spectroscopy'. In: *Physical review. B, Condensed matter* 68.18 (2003), p. 180407. ISSN: 0163-1829. DOI: 10.1103/PhysRevB.68.180407.

[103] Y. H. Ren, M. Ebrahim, Z. A. Xu and G. Lüpke. 'Ultrafast quasi-particle dynamics of charge/orbital ordered and ferromagnetic clusters in La 0.7 Ca 0.3 MnO 3'. In: *New*

Journal of Physics 11.11 (2009), p. 113013. DOI: 10.1088/1367-2630/11/11/113013.

[104] Y. H. Ren, H. B. Zhao, G. Lüpke, C. S. Hong, N. H. Hur, Y. F. Hu and Qi Li. 'Ultrafast photoinduced reflectivity transients in doped manganite'. In: *The Journal of chemical physics* 121.1 (2004), pp. 436–440. ISSN: 0021-9606. DOI: 10.1063/1.1755661.

[105] J. Bielecki, R. Rauer, E. Zanghellini, R. Gunnarsson, K. Dörr and L. Börjesson. 'Two-component heat diffusion observed in LaMnO3 and La0.7Ca0.3MnO3'. In: *Physical Review B* 81.6 (2010). ISSN: 1098-0121. DOI: 10.1103/PhysRevB.81.064434.

[106] C. L. Kane and E. J. Mele. 'Quantum spin Hall effect in graphene'. In: *Physical review letters* 95.22 (2005), p. 226801. ISSN: 0031-9007. DOI: 10.1103/PhysRevLett.95.226801.

[107] Gregg Jaeger. 'The Ehrenfest Classification of Phase Transitions: Introduction and Evolution'. In: *Archive for History of Exact Sciences* 53.1 (1998), pp. 51–81. ISSN: 0003-9519. DOI: 10.1007/s004070050021.

[108] D. Kim, B. Revaz, B. L. Zink, F. Hellman, J. J. Rhyne and J. F. Mitchell. 'Tricritical point and the doping dependence of the order of the ferromagnetic phase transition of La1-xCaxMnO3'. In: *Physical review letters* 89.22 (2002), p. 227202. DOI: 10.1103/PhysRevLett.89.227202.

[109] K. Ghosh, C. J. Lobb, R. L. Greene, S. G. Karabashev, D. A. Shulyatev, A. A. Arsenov and Y. Mukovskii. 'Critical Phenomena in the Double-Exchange Ferromagnet La0.7Sr0.3MnO3'. In: *Physical review letters* 81.21 (1998), pp. 4740–4743. ISSN: 0031-9007. DOI: 10.1103/PhysRevLett.81.4740.

[110] D. Kim, B. L. Zink, F. Hellman and J. M. D. Coey. 'Critical behavior of La0.75Sr0.25MnO3'. In: *Physical review. B, Condensed matter* 65.21 (2002), p. 214424. ISSN: 0163-1829. DOI: 10.1103/PhysRevB.65.214424.

[111] Ch.V Mohan, M. Seeger, H. Kronmüller, P. Murugaraj and J. Maier. 'Critical behaviour near the ferromagnetic–paramagnetic phase transition in La0.8Sr0.2MnO3'. In: *Journal of Magnetism and Magnetic Materials* 183.3 (1998), pp. 348–355. ISSN: 03048853. DOI: 10.1016/S0304-8853(97)01095-0.

[112] Gerd Wedler. *Lehrbuch der Physikalischen Chemie*. 5th ed. WILEY-VCH, 2004. ISBN: 978-3-527-31066-1.

[113] Rudolf Gross and Achim Marx. *Festkörperphysik*. Oldenburg Verlag München, 2012. ISBN: 978-3-486-71294-0.

[114] Takasu Hashimoto, Taisuke Miyoshi and Hideaki Ohtsuka. 'Investigation of the relaxation process in the Cu3 Au-alloy order-disorder phase transition near the transition point'. In: *Physical Review B* 13.3 (1976), pp. 1119–1122. ISSN: 1098-0121. DOI: 10.1103/PhysRevB.13.1119.

[115] F. Schrettle, P. Lunkenheimer, J. Hemberger, V. Yu Ivanov, A. A. Mukhin, A. M. Balbashov and A. Loidl. 'Relaxations as key to the magnetocapacitive effects in the perovskite manganites'. In: *Physical review letters* 102.20 (2009), p. 207208. ISSN: 0031-9007. DOI: 10.1103/PhysRevLett.102.207208.

[116] Takeshi Ogasawara, Katsuhiro Tobe, Tsuyoshi Kimura, Hiroshi Okamoto and Yoshinori Tokura. 'Photo-Induced Dynamics of Charge/Orbital Order in Perovskite Manganite Nd 0.5 Ca 0.5 MnO 3'. In: *Journal of the Physical Society of Japan* 71.10 (2002), pp. 2380–2383. ISSN: 0031-9015. DOI: 10.1143/JPSJ.71.2380.

[117] Junjie Li, Xuan Wang, Haidong Zhou, Jun Zhou, J. G. Cheng and Jianming Cao. 'Direct and real time probe of photoinduced structure transition in colossal magnetoresistive material'. In: *Applied Physics Letters* 109.4 (2016), p. 041905. ISSN: 0003-6951. DOI: 10.1063/1.4960100.

[118] Junjie Li et al. 'Dichotomy in ultrafast atomic dynamics as direct evidence of polaron formation in manganites'. In: *npj Quantum Materials* 1.1 (2016). DOI: 10.1038/npjquantmats.2016.26.

[119] T. Ogasawara, T. Kimura, T. Ishikawa, M. Kuwata-Gonokami and Y. Tokura. 'Dynamics of photoinduced melting of charge/orbital order in a layered manganite La0.5Sr1.5MnO4'. In: *Physical Review B* 63.11 (2001), p. 113105. ISSN: 1098-0121. DOI: 10.1103/PhysRevB.63.113105.

[120] B. Kressdorf et al. 'Orbital-order phase transition in Pr1−xCaxMnO3 probed by photovoltaics'. In: *Physical Review B* 103.23 (2021), p. 235122. ISSN: 1098-0121. DOI: 10.1103/PhysRevB.103.235122.

[121] Hirohiko Ichikawa et al. 'Transient photoinduced 'hidden' phase in a manganite'. In: *Nature materials* 10.2 (2011), pp. 101–105. ISSN: 1476-1122. DOI: 10.1038/nmat2929.

[122] Jingdi Zhang, Xuelian Tan, Mengkun Liu, S. W. Teitelbaum, K. W. Post, Feng Jin, K. A. Nelson, D. N. Basov, Wenbin Wu and R. D. Averitt. 'Cooperative photoinduced metastable phase control in strained manganite films'. In: *Nature materials* 15.9 (2016), pp. 956–960. ISSN: 1476-1122. DOI: 10.1038/nmat4695.

[123] Samuel W. Teitelbaum, B. K. Ofori-Okai, Yu-Hsiang Cheng, Jingdi Zhang, Feng Jin, Wenbin Wu, Richard D. Averitt and Keith A. Nelson. 'Dynamics of a Persistent Insulator-to-Metal Transition in Strained Manganite Films'. In: *Physical review letters* 123.26 (2019), p. 267201. ISSN: 0031-9007. DOI: 10.1103/PhysRevLett.123.267201.

[124] David G. Cahill. 'Thermal conductivity measurement from 30 to 750 K: the 3ω method'. In: *Review of Scientific Instruments* 61.2 (1990), pp. 802–808. ISSN: 0034-6748. DOI: 10.1063/1.1141498.

[125] V. Moshnyaga, I. Khoroshun, A. Sidorenko, P. Petrenko, A. Weidinger, M. Zeitler, B. Rauschenbach, R. Tidecks and K. Samwer. 'Preparation of rare-earth manganite-oxide thin films by metalorganic aerosol deposition technique'. In: *Applied Physics Letters* 74.19 (1999), pp. 2842–2844. ISSN: 0003-6951. DOI: 10.1063/1.124032.

[126] M. Buchner, K. Höfler, B. Henne, V. Ney and A. Ney. 'Tutorial: Basic principles, limits of detection, and pitfalls of highly sensitive SQUID magnetometry for nanomagnetism and spintronics'. In: *Journal of Applied Physics* 124.16 (2018), p. 161101. ISSN: 0021-8979. DOI: 10.1063/1.5045299.

[127] Quantum Design GmbH. *Magnetic Property Measurement System: SQUID VSM User's Manual*. 2009.

[128] Jacques I. Pankove. *Optical Processes in Semiconductors*. 1975. ISBN: 9780486602752.

[129] A. S. Hassanien and Alaa A. Akl. 'Effect of Se addition on optical and electrical properties of chalcogenide CdSSe thin films'. In: *Superlattices and Microstructures* 89 (2016), pp. 153–169. ISSN: 07496036. DOI: 10.1016/j.spmi.2015.10.044.

[130] Enrico Nichelatti. 'Complex refractive index of a slab from reflectance and transmittance: analytical solution'. In: *Journal of Optics A: Pure and Applied Optics* 4.4 (2002), pp. 400–403. ISSN: 14644258. DOI: 10.1088/1464-4258/4/4/306.

[131] S. Y. El-Zaiat. 'Determination of the complex refractive index of a thick slab material from its spectral reflectance and transmittance at normal incidence'. In: *Optik* 124.2 (2013), pp. 157–161. ISSN: 00304026. DOI: 10.1016/j.ijleo.2011.11.039.

[132] Henning Ulrichs, Dennis Meyer, Markus Müller, Maria Mansurova and Florian Döring. 'Numerical calculation of laser-induced thermal diffusion and elastic dynamics'. In: *AIP Conference Proceedings* 1763 (2016), p. 040004. DOI: 10.1063/1.4961352.

[133] Hassakorn Wattanasarn and Tosawat Seetawan. 'Studies Thermophysical Properties of MgO by First Principle Simulation'. In: *Advanced Materials Research* 802 (2013), pp. 139–143. DOI: 10.4028/www.scientific.net/AMR.802.139.

[134] R. I. Hickson, S. I. Barry, G. N. Mercer and H. S. Sidhu. 'Finite difference schemes for multilayer diffusion'. In: *Mathematical and Computer Modelling* 54.1-2 (2011), pp. 210–220. ISSN: 08957177. DOI: 10.1016/j.mcm.2011.02.003.

[135] R. D. Averitt, A. I. Lobad, C. Kwon, S. A. Trugman, V. K. Thorsmølle and A. J. Taylor. 'Ultrafast conductivity dynamics in colossal magnetoresistance manganites'. In: *Physical review letters* 87.1 (2001), p. 017401. DOI: 10.1103/PhysRevLett.87.017401.

[136] M. Quintero, J. Sacanell, L. Ghivelder, A. M. Gomes, A. G. Leyva and F. Parisi. 'Magnetocaloric effect in manganites: Metamagnetic transitions for magnetic refrigeration'. In: *Applied Physics Letters* 97.12 (2010), p. 121916. ISSN: 0003-6951. DOI: 10.1063/1.3491175.

[137] Markus Michelmann. 'Temperatur- und Magnetfeldabhängigkeit der elastischen Konstanten eines (La,Pr,Ca)-Manganats'. Diplomarbeit. Göttingen: Georg-August-Universität, 2010.

[138] Neeraj Kumar, H. Kishan, Ashok Rao and V. P. S. Awana. 'Structural, electrical, magnetic, and thermal studies of Cr-doped La0.7Ca0.3Mn1−xCrxO3 ($0 \leq x \leq 1$) manganites'. In: *Journal of Applied Physics* 107.8 (2010), p. 083905. ISSN: 0021-8979. DOI: 10.1063/1.3342462.

[139] 'Magnesium Oxide (MgO)'. In: *Handbook on Physical Properties of Semiconductors: Volume 3: II–VI Compound Semiconductors*. Boston, MA: Springer US, 2004, pp. 1–24. ISBN: 978-1-4020-7821-7. DOI: 10.1007/1-4020-7821-8_1.

[140] Olivier Deparis. 'Poynting vector in transfer-matrix formalism for the calculation of light absorption profile in stratified isotropic optical media'. In: *Optics letters* 36.20 (2011), pp. 3960–3962. DOI: 10.1364/OL.36.003960.

[141] R. E. Stephens and I. H. Malitson. 'Index of refraction of magnesium oxide'. In: *Journal of Research of the National Bureau of Standards* 49.4 (1952), p. 249. ISSN: 0091-0635. DOI: 10.6028/jres.049.025.

[142] Yuting Liu et al. 'Ultrafast magnetization dynamics of Mn-doped L10 FePt with spatial inhomogeneity'. In: *Journal of Magnetism and Magnetic Materials* 502 (2020), p. 166477. ISSN: 03048853. DOI: 10.1016/j.jmmm.2020.166477.

[143] Hiroyuki Yada, Masakazu Matsubara, Hiroyuki Matsuzaki, Hiroyuki Yamada, Akihito Sawa and Hiroshi Okamoto. 'Discrimination between photodoping- and heat-induced magnetization changes in Nd 0.52 Sr 0.48 MnO 3 using a heterostructure with SrTiO 3'. In: *Physical Review B* 84.4 (2011), p. 045114. ISSN: 1098-0121. DOI: 10.1103/PhysRevB.84.045114.

[144] Hiroyuki Yada, Masakazu Matsubara, Hiroyuki Yamada, Akihito Sawa, Hiroyuki Matsuzaki and Hiroshi Okamoto. 'Ultrafast control of magnetization by photocarrier injection in La 0.9 Sr 0.1 MnO 3 /SrTiO 3 heterostructures'. In: *Physical Review B* 83.16 (2011). ISSN: 1098-0121. DOI: 10.1103/PhysRevB.83.165408.

[145] T. Pincelli et al. 'Transient quantum isolation and critical behavior in the magnetization dynamics of half-metallic manganites'. In: *Physical Review B* 100.4 (2019), p. 045118. ISSN: 1098-0121. DOI: 10.1103/PhysRevB.100.045118.

[146] Alexandr Tikhii, Vladimir Gritskih, Svetlana Kara–Murza, Natalia Korchikova, Yuri Nikolaenko and Igor Zhikharev. 'Optical conductivity of LSMO films on Al 2 O 3 substrates'. In: *physica status solidi c* 10.4 (2013), pp. 673–676. ISSN: 1862-6351. DOI: 10.1002/pssc.201200858. URL: https://onlinelibrary.wiley.com/doi/10.1002/pssc.201200858.

[147] M. Cesaria, A. P. Caricato, G. Leggieri, M. Martino and G. Maruccio. 'Optical response of oxygen deficient La 0.7 Sr 0.3 MnO 3 thin films deposited by pulsed laser deposition'. In: *Thin Solid Films* 545 (2013), pp. 592–600. ISSN: 00406090. DOI: 10.1016/j.tsf.2013.07.071.

[148] Taka-hisa Arima and Yoshinori Tokura. 'Optical Study of Electronic Structure in Perovskite-Type RM O 3 (R =La, Y; M =Sc, Ti, V, Cr, Mn, Fe, Co, Ni, Cu)'. In: *Journal of the Physical Society of Japan* 64.7 (1995), pp. 2488–2501. ISSN: 0031-9015. DOI: 10.1143/JPSJ.64.2488.

[149] Sebastian Merten. 'Polaronic behaviour at manganite interfaces studied by advanced Raman scattering techniques'. PhD thesis. Göttingen: Georg-August-Universität, 2019.

[150] S. Merten, O. Shapoval, B. Damaschke, K. Samwer and V. Moshnyaga. 'Magnetic-Field-Induced Suppression of Jahn-Teller Phonon Bands in (La0.6Pr0.4)0.7Ca0.3MnO3: the Mechanism of Colossal Magnetoresistance shown by Raman Spectroscopy'. In: *Scientific reports* 9.1 (2019), p. 2387. DOI: 10.1038/s41598-019-39597-1.

[151] D. Lim, V. Thorsmølle, R. Averitt, Q. Jia, K. Ahn, M. Graf, S. Trugman and A. Taylor. 'Coherent optical and acoustic phonon generation correlated with the charge-ordering phase transition in La1−xCaxMnO3'. In: *Physical Review B* 71.13 (2005). ISSN: 1098-0121. DOI: 10.1103/PhysRevB.71.134403.

[152] J.-H. Park, C. T. Chen, S.-W Cheong, W. Bao, G. Meigs, V. Chakarian and Y. U. Idzerda. 'Electronic aspects of the ferromagnetic transition in manganese perovskites'. In: *Physical review letters* 76.22 (1996), pp. 4215–4218. DOI: 10.1103/PhysRevLett.76.4215.

[153] S. A. McGill, R. I. Miller, O. N. Torrens, A. Mamchik, I-Wei Chen and J. M. Kikkawa. 'Dynamic Kerr effect and the spectral weight transfer of the manganites'. In: *Physical review letters* 93.4 (2004), p. 047402. DOI: 10.1103/PhysRevLett.93.047402.

[154] Nai Fei Ren and Wei Feng Jin. 'Investigation of Nonequilibrium Dynamics of Nickel Film Excitated by Femtosecond Laser'. In: *Advanced Materials Research* 97-101

(2010), pp. 652–655. DOI: 10.4028/www.scientific.net/AMR.97-101.652.

[155] Elsa Abreu et al. *Photoinduced structural dynamics of multiferroic $TbMnO_3$*. 2022. URL: https://arxiv.org/pdf/2201.10009.

[156] Markus Jungbauer. 'Gestaltung der elektronischen Korrelationen in Perowskit- Heterostrukturen auf atomarer Skala'. Dissertation. Göttingen: Georg-August-Universität, 2015. DOI: 10.53846/goediss-5462.

[157] Georg M. Müller et al. 'Spin polarization in half-metals probed by femtosecond spin excitation'. In: *Nature materials* 8.1 (2009), pp. 56–61. ISSN: 1476-1122. DOI: 10.1038/NMAT2341.

[158] G. Banach and W. M. Temmerman. 'Delocalization and charge disproportionation in La(1−x)SrxMnO3'. In: *Physical Review B* 69.5 (2004), p. 054427. ISSN: 1098-0121. DOI: 10.1103/PhysRevB.69.054427.

[159] S. Picozzi, C. Ma, Z. Yang, R. Bertacco, M. Cantoni, A. Cattoni, D. Petti, S. Brivio and F. Ciccacci. 'Oxygen vacancies and induced changes in the electronic and magnetic structures of La0.66Sr0.33MnO3 : A combined ab initio and photoemission study'. In: *Physical Review B* 75.9 (2007). ISSN: 1098-0121. DOI: 10.1103/PhysRevB.75.094418.

[160] Zhaoliang Liao, Fengmiao Li, Peng Gao, Lin Li, Jiandong Guo, Xiaoqing Pan, R. Jin, E. W. Plummer and Jiandi Zhang. 'Origin of the metal-insulator transition in ultrathin films of La2/3Sr2/3MnO3'. In: *Physical Review B* 92.12 (2015). ISSN: 1098-0121. DOI: 10.1103/PhysRevB.92.125123.

[161] W. E. Pickett and D. J. Singh. 'Electronic structure and half-metallic transport in the La1-xCaxMnO3 system'. In: *Physical review. B, Condensed matter* 53.3 (1996), pp. 1146–1160. ISSN: 0163-1829. DOI: 10.1103/PhysRevB.53.1146.

[162] D. J. Singh and W. E. Pickett. 'Pseudogaps, Jahn-Teller distortions, and magnetic order in manganite perovskites'. In: *Physical review. B, Condensed matter* 57.1 (1998), pp. 88–91. ISSN: 0163-1829. DOI: 10.1103/PhysRevB.57.88.

[163] Tianqi Li, Aaron Patz, Leonidas Mouchliadis, Jiaqiang Yan, Thomas A. Lograsso, Ilias E. Perakis and Jigang Wang. 'Femtosecond switching of magnetism via strongly

correlated spin-charge quantum excitations'. In: *Nature* 496.7443 (2013), pp. 69–73. DOI: 10.1038/nature11934.

[164] Y. H. Ren, M. Trigo, R. Merlin, Venimadhav Adyam and Qi Li. 'Generation and detection of coherent longitudinal acoustic phonons in the La0.67Sr0.33MnO3 thin films by femtosecond light pulses'. In: *Applied Physics Letters* 90.25 (2007), p. 251918. ISSN: 0003-6951. DOI: 10.1063/1.2751130.

[165] *CRC Handbook of Laser Science and Technology, Volume IV Edited by M.J. Weber (CRC Press, 1986)*. Vol. 12. 1987. DOI: 10.1557/S0883769400068238.

[166] O. Gunnarsson. 'Band model for magnetism of transition metals in the spin-density-functional formalism'. In: *Journal of Physics F: Metal Physics* 6.4 (1976), pp. 587–606. ISSN: 0305-4608. DOI: 10.1088/0305-4608/6/4/018.

[167] P. Mohn and E. P. Wohlfarth. 'The Curie temperature of the ferromagnetic transition metals and their compounds'. In: *Journal of Physics F: Metal Physics* 17.12 (1987), pp. 2421–2430. ISSN: 0305-4608. DOI: 10.1088/0305-4608/17/12/016.

[168] J. M. Marín Ramírez, E. Oblak, P. Riego, G. Campillo, J. Osorio, O. Arnache and A. Berger. 'Experimental exploration of dynamic phase transitions and associated metamagnetic fluctuations for materials with different Curie temperatures'. In: *Physical review. E* 102.2-1 (2020), p. 022804. DOI: 10.1103/PhysRevE.102.022804.

[169] Stefan Hüfner. *Photoelectron Spectroscopy: Principles and Applications*. Third Revised and Enlarged Edition. Springer eBook Collection. Berlin and Heidelberg: Springer, 2003. ISBN: 978-3-642-07520-9. DOI: 10.1007/978-3-662-09280-4.

[170] Marius Keunecke. 'Ultrafast electron dynamics measured with a novel time-resolved high-repetition rate momentum microscopy setup'. Dissertation. Göttingen: Georg-August-Universität, 2021.

[171] P. A. Franken, A. E. Hill, C. W. Peters and G. Weinreich. 'Generation of Optical Harmonics'. In: *Physical review letters* 7.4 (1961), pp. 118–119. ISSN: 0031-9007. DOI: 10.1103/PhysRevLett.7.118.

[172] Aimo Winkelmann, Vahit Sametoglu, Jin Zhao, Atsushi Kubo and Hrvoje Petek. 'Angle-dependent study of a direct optical transition in the sp bands of Ag(111) by

one- and two-photon photoemission'. In: *Physical Review B* 76.19 (2007), p. 195428. ISSN: 1098-0121. DOI: 10.1103/PhysRevB.76.195428.

[173] Maurizio Martino, Maura Cesaria, Anna Paola Caricato, Giuseppe Maruccio, Adriano Cola and Isabella Farella. 'La 0.7 Sr 0.3 MnO 3 thin films deposited by pulsed laser ablation for spintronic applications'. In: *physica status solidi (a)* 208.8 (2011), pp. 1817–1820. ISSN: 18626300. DOI: 10.1002/pssa.201084037.

[174] D. L. Niu, X. J. Liu, Q. J. Huang and S. Y. Zhang. 'Thermal diffusivity of La 0 .6Sr 0 .4MnO 3 thin film investigated by transient thermal grating technique'. In: *Journal de Physique IV (Proceedings)* 125 (2005), pp. 249–251. ISSN: 1155-4339. DOI: 10.1051/jp4:2005125059.

APPENDIX A

Time-Resolved Optical Spectroscopy Setup

A1 Ultrafast Optical Spectroscopy Setup

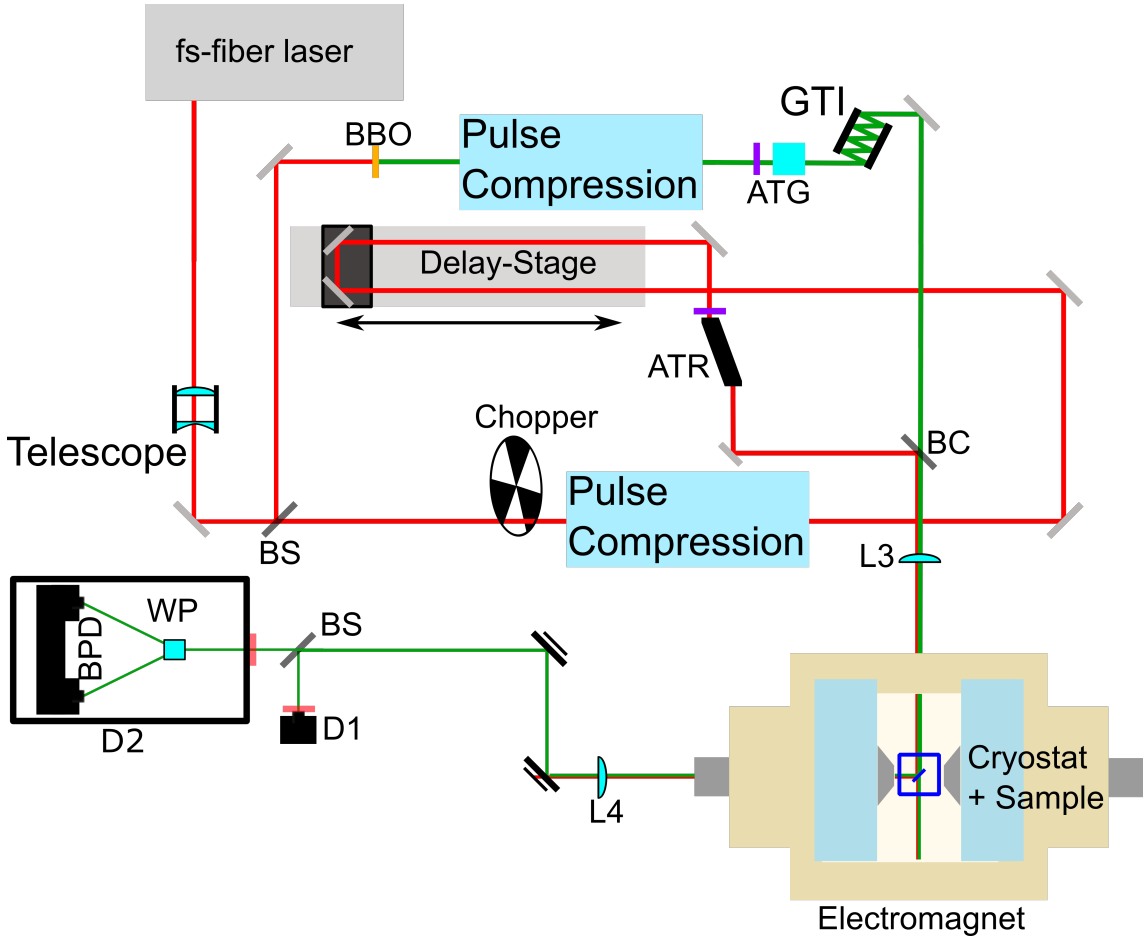

FIGURE A.1: Sketch of the optical spectroscopy setup which has been used for the time-resolved data (MOKE as well as reflectivity) of LPCMO thin films, which are measured under a $45°$-angle with respect to the external magnetic field and to the incident laser light.

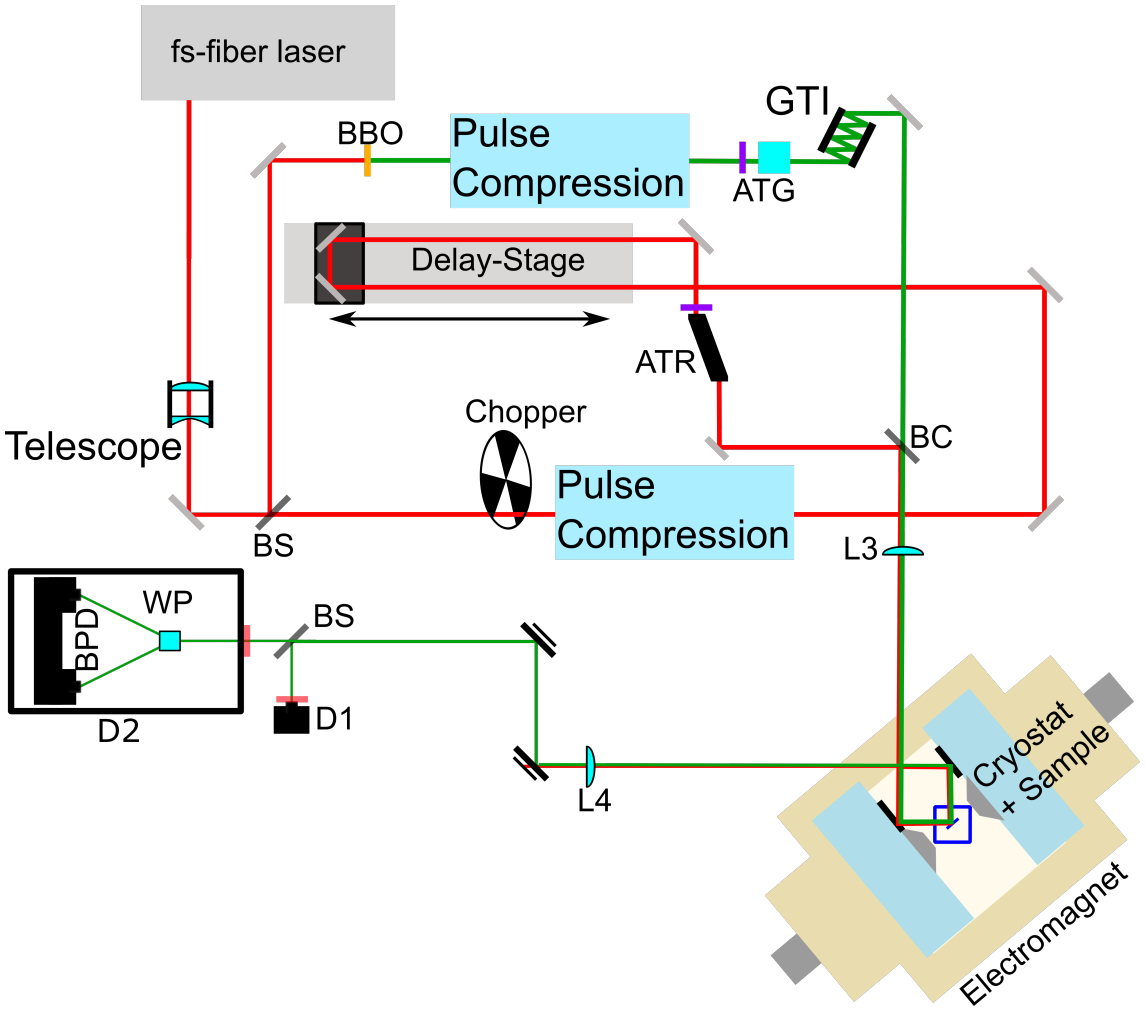

FIGURE A.2: Sketch of the optical spectroscopy setup which has been used for the time-resolved data (MOKE as well as reflectivity) of LSMO thin films, which is installed parallel to the external magnetic field and under a $\sim 45°$-angle with respect to the incident laser light.

The IR-laser beam, which is coupled into the setup, is directly splitt in such way that about 20 % of the intensity is transmitted through a β-barium-borate crystal to generate the second harmonic. This bichromatic implementation ($\lambda_{pump} = 1030$ nm and $\lambda_{probe} = 515$ nm) allows a nearly colinearity of the pump and probe beam at the sample position.

After the interaction with the sample, the beams are reflected from dielectric mirrors, which are designed to be highly reflective for the probe beam and almost transparent for the pump. A beamsplitter by Thorlabs allows to measure the time-resolved magneto-optical Kerr effect (TRMOKE) and the transient reflectivity (psTR) simultaneously with the help of two detectors.

The reflectivity detector is a single Si-photo diode with an integrated, tunable amplification by Thorlabs. On the other hand, a balanced-bridge detector is applied to measure the MOKE-signal.

A temporal delay between both the pump and the probe pulse is created by sending the pump-beam though a piezo-controlled stage before the beam hits the sample. The positioning of the delay stage (*M-521* by *Physik Instromente*) enables a scanning range of more than 1.1 ns and the drive ensures a bidirectional repeatability of $\sigma_{\Delta t} = 0.2$ µm.

Finally, the environmental control is achieved by a variable-gap electromagnet and a ^{4}He cryostat in between the gap, both by Lake Shore. For the measurements on LSMO, the samples are positioned in such way that the in-plane component of the thin film magnetization lies parallel to the magnetic field lines of the electromagnet. The laser light is reflected in a 45°-angle. In this way, environmental conditions of $T = 150 - 380$ K and $B = 0 \sim 800$ mT as well as $F =$ mJ/cm^2 were applied to the samples. [1]

A2 Signal Processing

The pre-amplified signals from the psTR-PD as well as from the MOKE-detector were coupled into a lock-in amplifier to detect only the changes in signal induced by the pump pulse which was triggered by the pump chopper frequency of $f = 534$ Hz.

A3 Absorbed Fluence Range and Estimation of the Number of Excited Electrons

Since the absorbed fluence, $\mathcal{F}$, cannot be measured directly, the incoming fluence, F, is given in the chapters regarding the measured data. Nevertheless, an estimation shall be given here about the number of excited electrons per pulse.

[1] Due to a lack of space inside the cryostat and close to it - in between the pole shoes - it was not possible to measure the pressure at the sample position within the cryostat. But it is estimated that the samples are exposed to $p \approx 10^{-4} - 10^{-5}$ mbar.

From the maximal and minimal incoming F of the central pump wavelength $\lambda = 1030$ nm, the number of incoming photons per area of a pseudo-cubic unit cell can be estimated, assuming that wavelength distribution is more or less symmetrically centered, by:

$$N_{photons} \approx 16 \frac{1}{\text{pulse} \cdot \text{stack of UCs}}. \tag{A.1}$$

Since N is the number of photons which hits the thin film sample at the surface within the area of a pseudo-cubic unit cell, it needs to be taken into account how many UC are part of the underlying stack. From this, the averaged number of photons which are absorbed by the electronic structure[2] can be estimated using the Beer-Lambert law with a literature value of $\alpha \sim 10^7$ m^{-1} [173, 174] for LSMO and combined with a roughly rounded number of ~ 130 UC within the stack:

$$\mathcal{F}_{min} \approx 0.01 \frac{photons}{UC},$$
$$\mathcal{F}_{max} \approx 0.05 \frac{photons}{UC}.$$

[2] It is assumed that all absorbed photons contribute to the direct excitation of the electronic system.

APPENDIX B

Additional Ultrafast Dynamics Data

B1 LPCMO

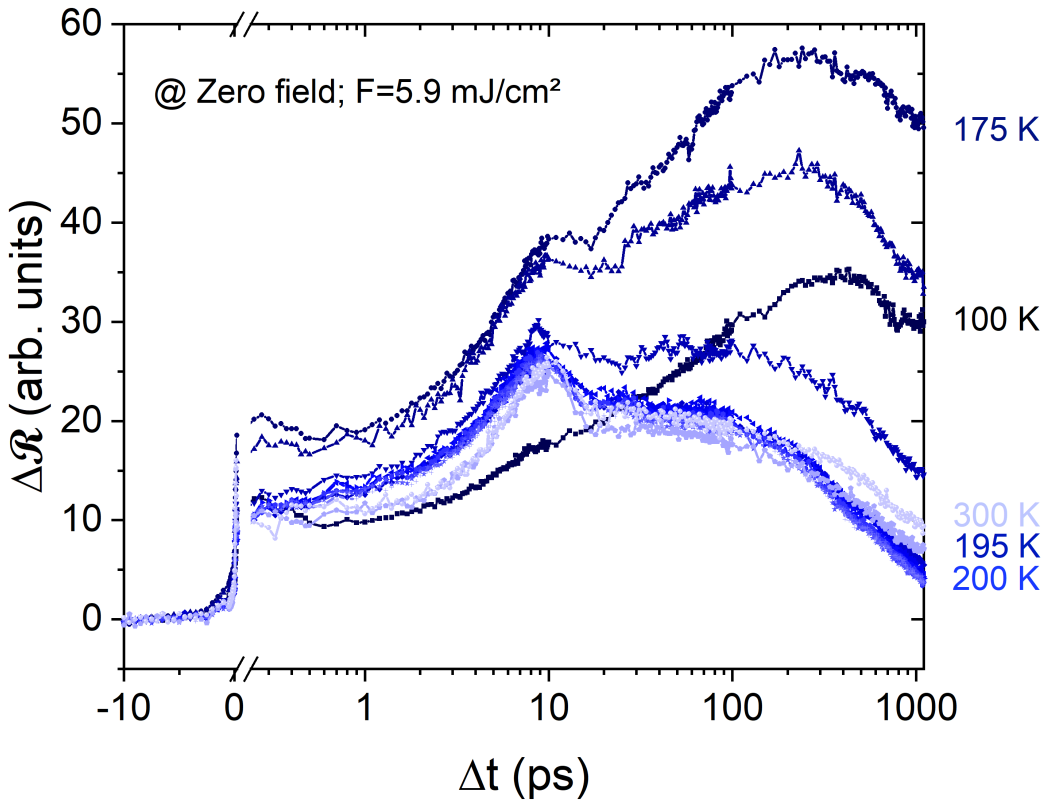

FIGURE B.1: The full set of psTR traces belonging to the ZFW cycle in the figures 8.1. The color code: tints correspond to higher temperature, shades correspond to lower temperatures. Note the logarithmic x-scale.

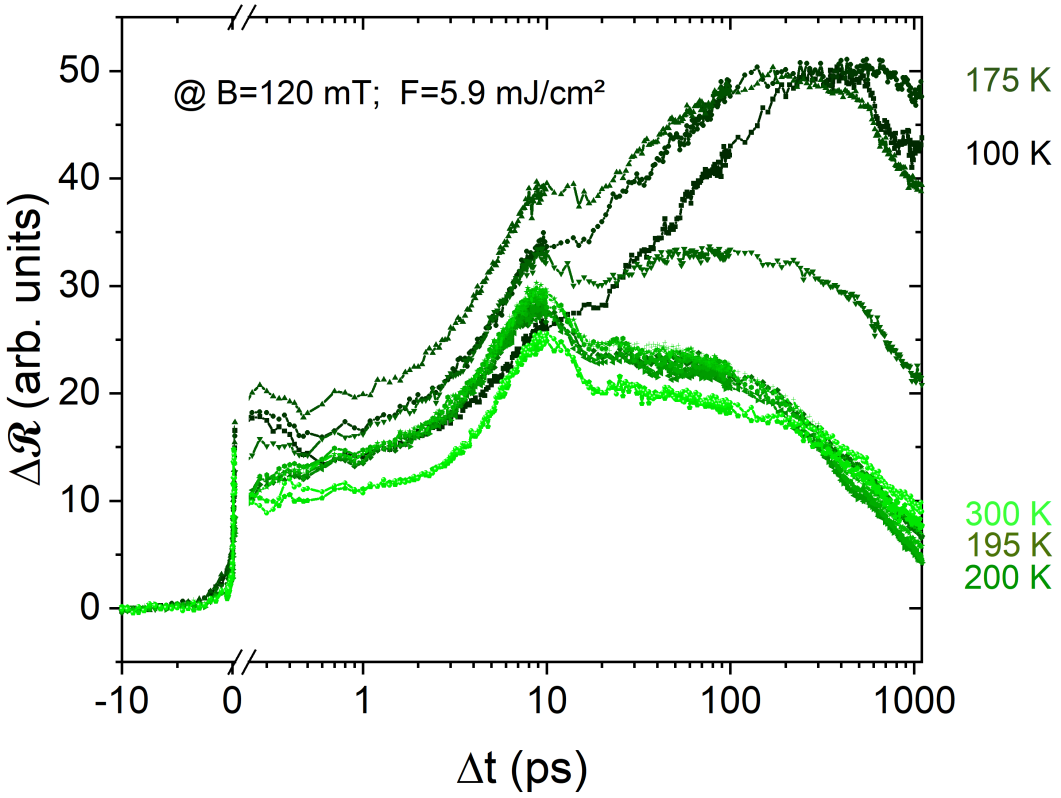

FIGURE B.2: The full set of psTR traces belonging to the 120 mT cycle in the figures 8.1. The color code: tints correspond to higher temperature, shades correspond to lower temperatures. Note the logarithmic x-scale.

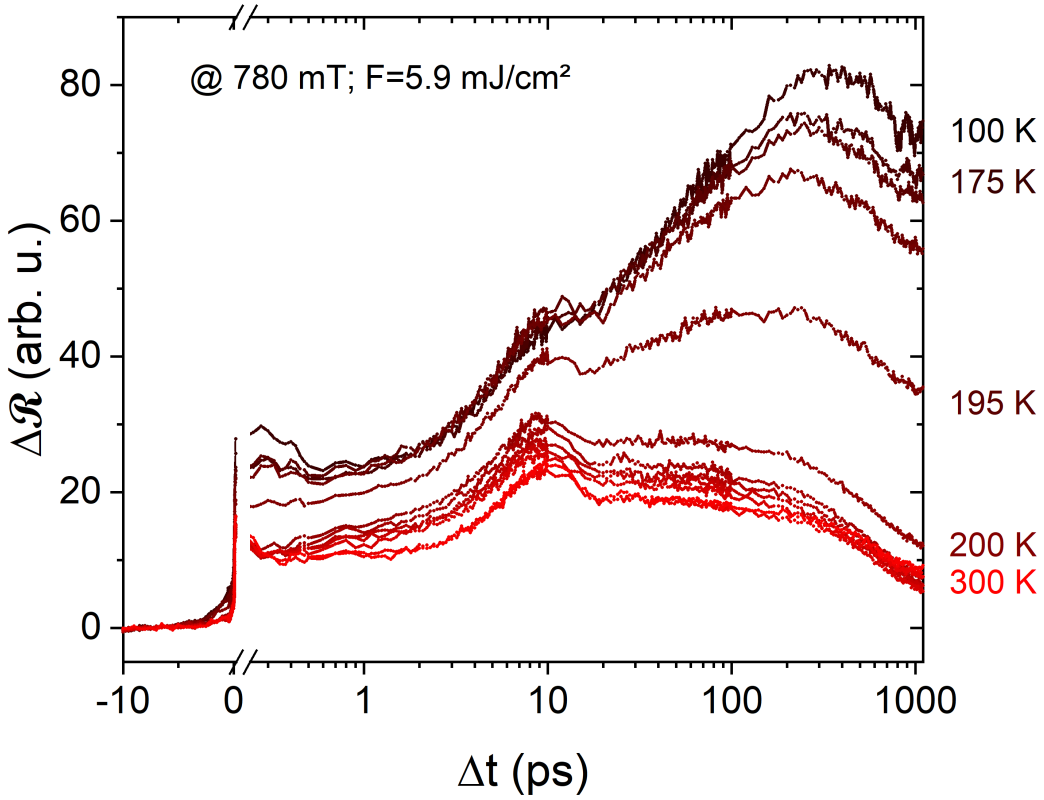

FIGURE B.3: The full set of psTR traces belonging to the 780 mT cycle in the figures 8.1. The color code: tints correspond to higher temperature, shades correspond to lower temperatures. Note the logarithmic x-scale.

B2 LSMO

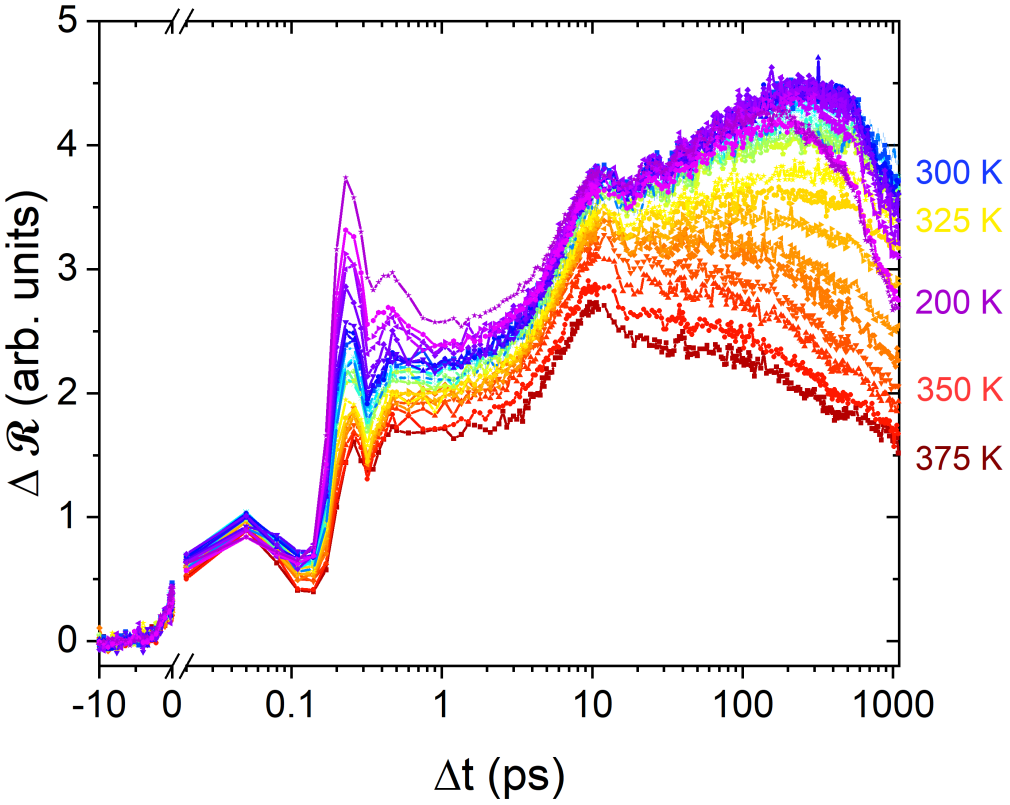

FIGURE B.4: The psTR traces belonging to the results in the figures 11.2, 11.4 and 11.5. The data were measured with $F = 1.64$ mJ/cm^2 and $B = 90$ mT. The color code matches the temperatures: high temperatures correspond to more reddish/warmer colors and lower temperatures are represented in bluish/colder colors. Note the logarithmic x-scale.

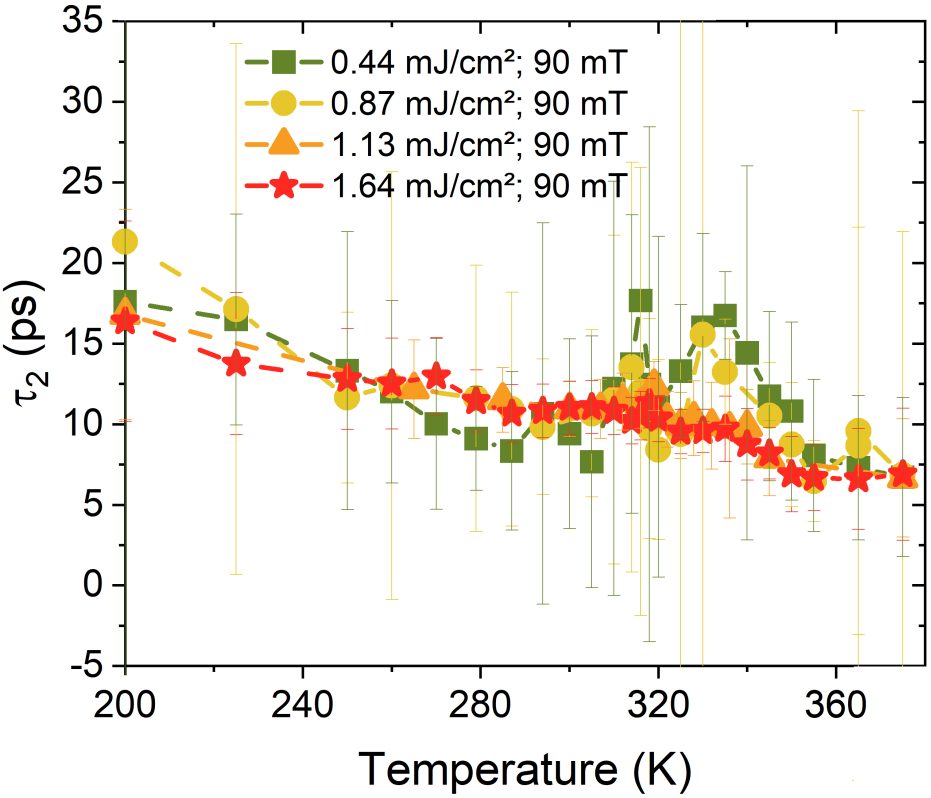

FIGURE B.5: Figure 11.6 (b) including the error bars, which were calculated by the fit eq. 8.1.

APPENDIX C

Static Characterization

C1 Magnetization and Resistivity

Generell schreiben wie ausgewertet: z.b logdT, Hintergrundabzug für LSMO
The transition temperatures for the magnetic as well as for the electronic phase are determined by the minimum of the logarithmic derivative of the temperature-dependent magnetization or resistance curve, respectively.

C1.1 LPCMO

The transition temperatures of LPCMO are plotted in fig. C.1 for different, external magnetic fields. The minimum of the logarithmic derivative of the temperature-dependent data is defined as the transition temperature here. Three different kinds of experiments are summarized in this graph: measurements by SQUID-magnetometer in black, by PPMS with parallel applied field in red, and by PPMS with perpendicularly applied field in blue. The found Curie-temerautre, $T_C \approx 195$ K
The two electronic experiments differ by $\Delta T = 1 - 3$ K. ΔT shows a tendency to increase with higher magnetic fields. This gives rise to the idea, that the difference might be explained by the tilt of the magnetic moment of the film out of its easy, magnetic axis. Mustermann and co-workers showed that LPCMO thin films, which are comparable to this one, have their magnetic, easy axis along the steps of the MgO-substrates. This means for the perpendicular case, that the effective field (the component of the magnetic moment which is parallel to the electronic measurement direction) is smaller than the externally applied value. Thus, a lower transition temperature is expected.

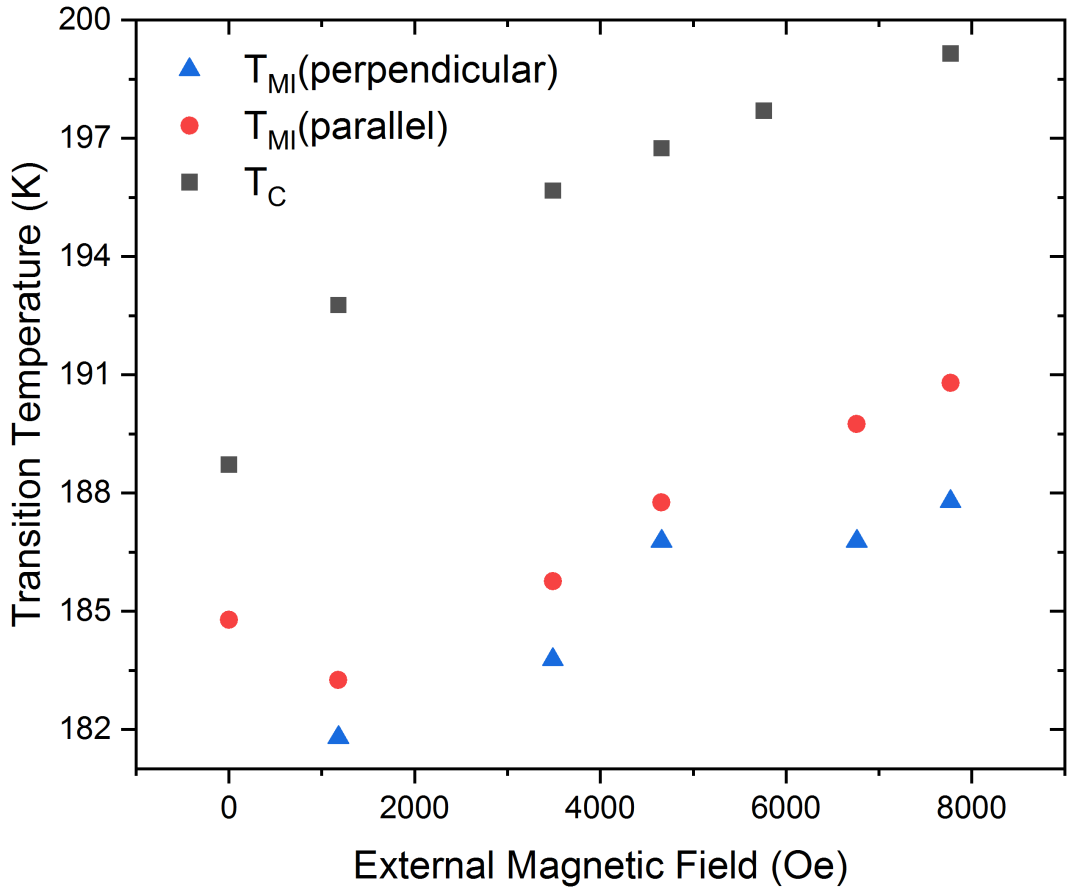

FIGURE C.1: The transition temperatures are plotted against the statically applied magnetic field. The black squares represent the Curie-temperature measured by SQUID. The red circle and the blue triangle belong to data collected by PPMS for two different geometries: external magnetic field was parallel (red) and perpendicularly (blue) applied with respect to the surface of the thin film.

Whereas, a temperature difference of $\Delta T \approx 10$ K between the transition measured with the magnetometer and the ones measured electronically with a four-point measuring exsits with the exception of the zero field data[1].

[1]For zero-field measurements, it is known, that a rest field is always applied. Even with newer generations of SQUID-magnetometer (or PPMS), where companies have developed particular low-field measurement modes, an unanticipated, small magnetic moment is left after the calibration procedure. Thus, it is likely that the so-called ZF-data points do not belong to the same external magnetic fields, but vary by a small, undefined value. Which might explain the smaller difference between the transition temperatures at 0 Oe in comparison to the differences at higher fields.

C1.2 LSMO

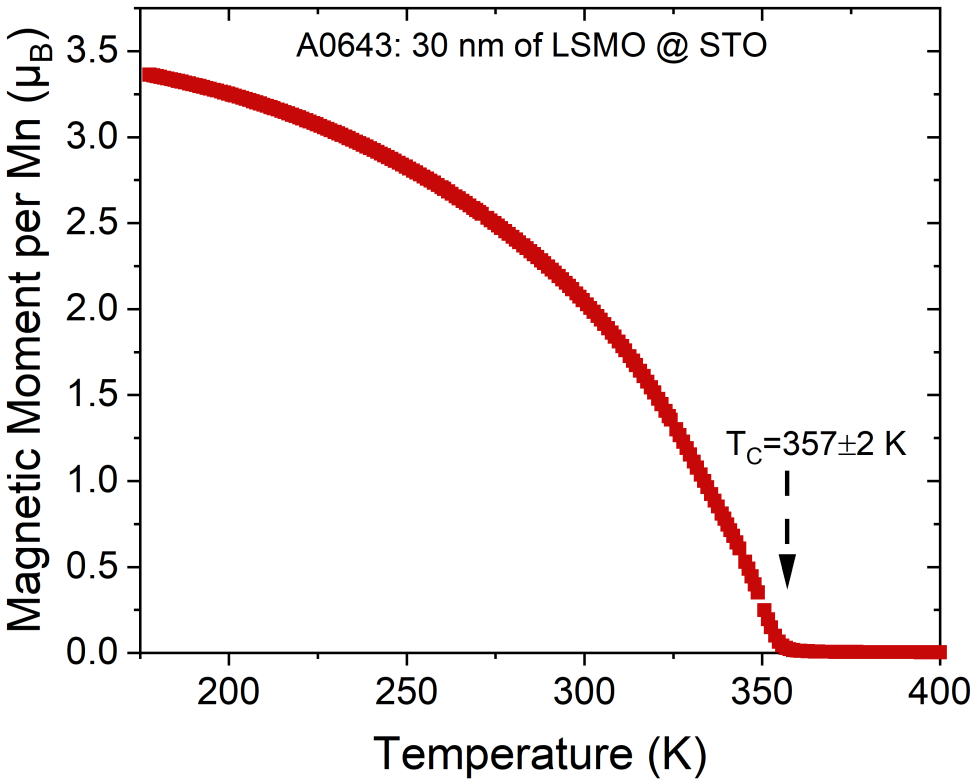

FIGURE C.2: SQUID-measurement of the static $M(T)$ of LSMO.

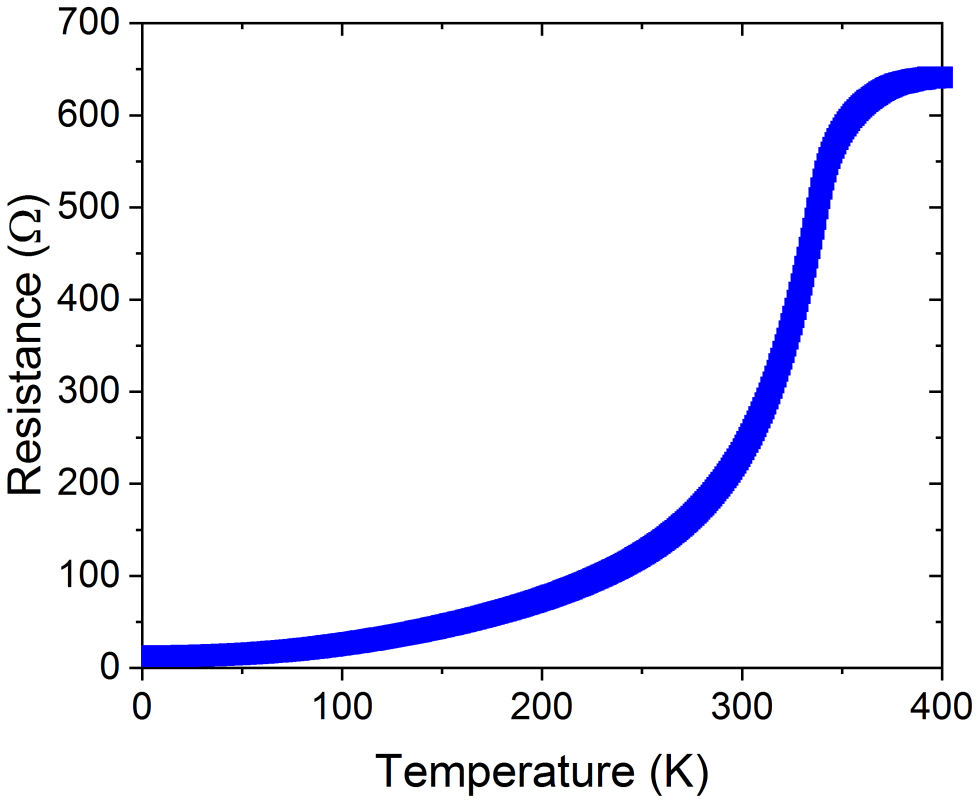

FIGURE C.3: PPMS-measurement of the static $R(T)$ of LSMO.